SECURITY CLASSIFICATION OF THIS PAGE *(When Data Entered)*

REPORT DOCUMENTATION PAGE		READ INSTRUCTIONS BEFORE COMPLETING FORM
1. REPORT NUMBER Report 3	2. GOVT ACCESSION NO.	3. RECIPIENT'S CATALOG NUMBER
4. TITLE *(and Subtitle)* A Study of the Coherent Structures in the Viscous Wall Region of a Turbulent Flow		5. TYPE OF REPORT & PERIOD COVERED Technical 6. PERFORMING ORG. REPORT NUMBER
7. AUTHOR*(s)* Christos Nikolaides and Thomas J. Hanratty, Project Supervisor		8. CONTRACT OR GRANT NUMBER*(s)* N00014-88-82-K-0324
9. PERFORMING ORGANIZATION NAME AND ADDRESS Department of Chemical Engineering University of Illinois Urbana, Illinois 61801		10. PROGRAM ELEMENT, PROJECT, TASK AREA & WORK UNIT NUMBERS NR 657-728
11. CONTROLLING OFFICE NAME AND ADDRESS Office of Naval Research Fluid Dynamics Program - Dr. M. M. Reischman Arlington, VA 22217		12. REPORT DATE November, 1983 13. NUMBER OF PAGES 339
14. MONITORING AGENCY NAME & ADDRESS*(if different from Controlling Office)*		15. SECURITY CLASS. *(of this report)* Unclassified 15a. DECLASSIFICATION/DOWNGRADING SCHEDULE
16. DISTRIBUTION STATEMENT *(of this Report)* Approved for public release; distribution unlimited		
17. DISTRIBUTION STATEMENT *(of the abstract entered in Block 20, if different from Report)*		
18. SUPPLEMENTARY NOTES		
19. KEY WORDS *(Continue on reverse side if necessary and identify by block number)* turbulence viscous wall region		
20. ABSTRACT *(Continue on reverse side if necessary and identify by block number)* see reverse side		

DD FORM 1 JAN 73 1473 EDITION OF 1 NOV 65 IS OBSOLETE

SECURITY CLASSIFICATION OF THIS PAGE *(When Data Entered)*

Conditionally averaged measurements of the flow in the viscous wall region showed that strong spanwise flows at $y^+=40$ are related to strong spanwise flows at the wall that are of the opposite sign. At $y^+=20$ the spanwise flows are always in phase with the flows at the wall.

The characteristics of the dominant eddies at the wall were explored by performing numerical computations using a fixed cell in space. Close to the edge of the viscous sublayer ($y^+=15$) the use of a single spatial harmonic ($\lambda^+=100$) was found to be adequate in predicting all the important features of turbulence.

At the edge of the viscous wall layer two spatial harmonics were found to be necessary for the description of the flow field. The longer scale outer flow eddies produce most of the spanwise mixing in the wall region. The smaller scale $\lambda^+=100$ eddies can account for momentum transport, Reynolds stress production and the creation of $\overline{u^2}$ and $\overline{v^2}$ energy in this region.

The physical picture of the flow that results from the interaction of the wall with the outer layer is the following. The mean flow engergy is primarily produced in the outer layer by the mean pressure gradient and is subsequently transferred into the viscous wall region. All the turbulent kinetic energy is produced by the v-w flow in the wall layer and is concentrated in the streamwise component of the velocity. This energy is convected out of the wall layer into the core region, where part of it is transferred to the motion of the y-z plane. The cycle of events completes with the transport of $\overline{v^2}$ energy into the wall region and the set-up of the v-w field, whereby energy is transferred from the v to the w component of the velocity by means of pressure-velocity gradient interactions.

A STUDY OF THE COHERENT STRUCTURES IN THE VISCOUS WALL REGION OF A TURBULENT FLOW

LIBRARY
RESEARCH REPORTS DIVISION
NAVAL POSTGRADUATE SCHOOL
MONTEREY, CALIFORNIA 93943

PREPARED BY
C. NIKOLAIDES
T. J. HANRATTY, PROJECT SUPERVISOR

FOR
THE OFFICE OF NAVAL RESEARCH, ARLINGTON, VA 22217
CONTRACT N00014-88-82-K-0324
PROJECT NR 657-728

REPORT 3

DEPARTMENT OF CHEMICAL ENGINEERING
UNIVERSITY OF ILLINOIS
URBANA, ILLINOIS
61801

NOVEMBER 1983

APPROVED FOR PUBLIC RELEASE, DISTRIBUTION UNLIMITED

A STUDY OF THE COHERENT STRUCTURES IN THE VISCOUS WALL REGION OF A TURBULENT FLOW

Prepared by

Christos Nikolaides
Thomas J. Hanratty, Project Supervisor

for

The Office of Naval Research, Arlington, VA 22217
Contract N00014-88-82-K-0324
Project NR 657-728

Report 3

Department of Chemical Engineering
University of Illinois
Urbana, Illinois
61801

November, 1983

Approved for public release, distribution unlimited

TABLE OF CONTENTS

Chapter — Page

1. INTRODUCTION 1

2. LITERATURE SURVEY 11

I. Turbulence measurements and coherent structures 13

A. Measurements of turbulence properties in the viscous wall region ... 13

1. Mean velocity measurements 13

2. Intensities of velocity fluctuations 14

3. Probability distributions and higher order moments 15

4. Reynolds stress 16

5. Correlation measurements 17

6. Spectral measurements 21

B. Coherent structures in wall turbulence 22

1. Visual and instrumental studies 22

2. Measurements of the streak spacing, λ, and the bursting period T_B 34

II. Computational methods for turbulent flows 36

A. Reynolds averaging 36

1. Zero-equation models 36

2. One-equation models 37

3. Two-equation models 37

4. Stress-equation models 38

B. Large-Eddy Simulations (LES) 39

C. Simple eddy modelling of the viscous wall region 47

3. EXPERIMENTAL METHODS 49

4. THEORY 52

I. Conditional averaging scheme 52

II. Eddy model for the viscous wall region 59

A. Continuum equations and boundary conditions 59

B. Numerical methods 65

1. ADI-scheme 65

2. Semi-implicit scheme 73

3. Pressure solution 77

C. Selection of model parameters 79

D. Vorticity dynamics and energy balance for the model flow 98

5. RESULTS 114

I. Analysis of experimental data 114

A. Relation of wall patterns to transverse velocity fluctuations in the fluid 114

B. Streamwise variation of the eddy structure 119

C. Coherency normal to the wall 125

II. Numerical computations 128

A. Upper boundary at $y_o^+ = 40$ 130

1. One harmonic in the spanwise direction 130

2. Two harmonics in the spanwise direction 199

B. Upper boundary at $y_o^+ = 15$ 225

6. ENERGY CALCULATIONS FOR THE MODEL FLOW 252

7. SCALING FOR THE MODEL FLOW 260

8. DISCUSSION 264

I. Conditional averaging 264

II. Numerical computations 267

9. CONCLUSIONS 285

LIST OF REFERENCES 287

NOMENCLATURE 295

APPENDIX

A. COMPUTER PROGRAM 304

B. PULSATING FLOW AT THE UPPER BOUNDARY OF THE VISCOUS WALL REGION (Moving cell runs) 329

C. SHIFTING OF THE $\lambda^+ = 100$ WALL EDDIES (Moving cell runs) 338

VITA 340

LIST OF FIGURES

Figure		Page
1	Idealized coherent eddy structure	4
2	Plot of the detection function $\hat{S}_{d_k}$ vs T^+	55
3	Example of how the detection scheme works	57
4	Percentage of closed flow	87
5	Conditionally averaged data for positive transverse flows at the wall; the fluid probe at $y^+ = 20$	115
6	Conditionally averaged data for positive transverse flows at the wall; the fluid probe at $y^+ = 40$	116
7	Measurements of $R_{us_z}(x^+, 40, 0; \tau^+)$ and $R_{ws_z}(x^+, 40, 0; \tau^+)$	120
8	Measurements of $R_{us_z}(x^+, 20, 0; \tau^+)$ and $R_{ws_z}(x^+, 20, 0; \tau^+)$	122
9	Conditionally averaged data for positive transverse flows at the wall; arrows indicate conditionally averaged transverse velocity, $<w>$, at $y^+ = 40$ (right side of figure) and $y^+ = 20$ (the left side of figure). Arrow length of +750 indicates $<w>/(\overline{w^2})^{1/2}$ equal to +1	124
10	Measurements of $R_{us_z}(-25, 40, z^+; \tau^+)$, $R_{ws_z}(-25, 40, z^+; \tau^+)$, $R_{us_z}(-25, 40, z^+; \tau^+)$ and $R_{ws_z}(-25, 40, z^+; \tau^+)$	126
11	Measurements of $R_{us_z}(-25, 20, z^+; \tau^+)$, $R_{ws_z}(-25, 20, z^+; \tau^+)$, $R_{us_z}(-25, 20, z^+; \tau^+)$ and $R_{ws_z}(-25, 20, z^+; \tau^+)$	127
12	Streamline contours for a single harmonic run at $t^+ = 5$ and 10; upper boundary at $y_o^+ = 40$	132
13	Streamline contours for a single harmonic run at $t^+ = 15$ and 20; upper boundary at $y_o^+ = 40$	133
14	Streamline contours for a single harmonic run at $t^+ = 25$ and 30;	

upper boundary at $y_o^+ = 40$ 134

15 Streamline contours for a single harmonic run at $t^+ = 35$ and 40; upper boundary at $y_o^+ = 40$ 135

16 Streamline contours for a single harmonic run at $t^+ = 45$ and 50; upper boundary at $y_o^+ = 40$ 136

17 Streamline contours for a single harmonic run at $t^+ = 55$ and 60; upper boundary at $y_o^+ = 40$ 137

18 Streamline contours for a single harmonic run at $t^+ = 65$ and 70; upper boundary at $y_o^+ = 40$ 138

19 Streamline contours for a single harmonic run at $t^+ = 75$ and 80; upper boundary at $y_o^+ = 40$ 139

20 Streamline contours for a single harmonic run at $t^+ = 85$ and 90; upper boundary at $y_o^+ = 40$ 140

21 Streamline contours for a single harmonic run at $t^+ = 95$ and 100; upper boundary at $y_o^+ = 40$ 141

22a Plots of the spanwise velocity gradient at the wall versus z^+ from $t^+ = 4$ to $t^+ = 40$ 143

22b Plots of the spanwise velocity gradient at the wall versus z^+ from $t^+ = 44$ to $t^+ = 80$ 144

22c Plots of the spanwise velocity gradient at the wall versus z^+ from $t^+ = 84$ to $t^+ = 100$ 145

23 Plot of the $R_{s_i s_i}$ correlation versus Δz^+; single harmonic run 146

24 Streamwise vorticity contours for a single harmonic run at $t^+ = 5$ and 10; upper boundary at $y_o^+ = 40$ 148

25 Streamwise vorticity contours for a single harmonic run at $t^+ = 15$ and 20; upper boundary at $y_o^+ = 40$ 149

26 Streamwise vorticity contours for a single harmonic run at $t^+ = 25$ and 30; upper boundary at $y_o^+ = 40$ 150

27 Streamwise vorticity contours for a single harmonic run at $t^+ = 35$

and 40; upper boundary at $y_o^+ = 40$ 151

28 Streamwise vorticity contours for a single harmonic run at $t^+ = 45$ and 50; upper boundary at $y_o^+ = 40$ 152

29 Streamwise vorticity contours for a single harmonic run at $t^+ = 55$ and 60; upper boundary at $y_o^+ = 40$ 153

30 Streamwise vorticity contours for a single harmonic run at $t^+ = 65$ and 70; upper boundary at $y_o^+ = 40$ 154

31 Streamwise vorticity contours for a single harmonic run at $t^+ = 75$ and 80; upper boundary at $y_o^+ = 40$ 155

32 Streamwise vorticity contours for a single harmonic run at $t^+ = 85$ and 90; upper boundary at $y_o^+ = 40$ 156

33 Streamwise vorticity contours for a single harmonic run at $t^+ = 95$ and 100; upper boundary at $y_o^+ = 40$ 157

34 Instantaneous streamwise velocity contours for a single harmonic run at $t^+ = 10$ and 20; upper boundary at $y_o^+ = 40$ 158

35 Instantaneous streamwise velocity contours for a single harmonic run at $t^+ = 30$ and 40; upper boundary at $y_o^+ = 40$ 159

36 Instantaneous streamwise velocity contours for a single harmonic run at $t^+ = 50$ and 60; upper boundary at $y_o^+ = 40$ 160

37 Instantaneous streamwise velocity contours for a single harmonic run at $t^+ = 70$ and 80; upper boundary at $y_o^+ = 40$ 161

38 Instantaneous streamwise velocity contours for a single harmonic run at $t^+ = 90$ and 100; upper boundary at $y_o^+ = 40$ 162

39 Plots of v^+ versus t^+ at $z^+ = 42$. Single harmonic run; upper boundary at $y_o^+ = 40$ 164

40 Plots of w^+ versus t^+ at $z^+ = 30$. Single harmonic run; upper boundary at $y_o^+ = 40$ 165

41 Plots of u^+ versus t^+ at $z^+ = 42$. Single harmonic run; upper boundary at $y_o^+ = 40$ 166

42 Plots of ζ^+ versus t^+ at $z^+=30$. Single harmonic run; upper boundary at $y_o^+=40$ 167

43 Plots of u/u' versus t^+ at $y^+=10$. Single harmonic run; upper boundary at $y_o^+=40$ 169

44 Plots of v/v' versus t^+ at $y^+=20$. Single harmonic run; upper boundary at $y_o^+=40$ 170

45 Plots of w/w' versus t^+ at $y^+=20$. Single harmonic run; upper boundary at $y_o^+=40$ 171

46 Plots of ζ/ζ' versus t^+ at $y^+=5$. Single harmonic run; upper boundary at $y_o^+=40$ 172

47a Plots of ζ^+ versus y^+ at $z^+=18$ from $t^+=4$ to $t^+=40$. Single harmonic run; upper boundary at $y_o^+=40$ 173

47b Plots of ζ^+ versus y^+ at $z^+=18$ from $t^+=44$ to $t^+=80$. Single harmonic run; upper boundary at $y_o^+=40$ 174

47c Plots of ζ^+ versus y^+ at $z^+=18$ from $t^+=84$ to $t^+=100$. Single harmonic run; upper boundary at $y_o^+=40$ 175

48a Plots of w^+ versus y^+ at $z^+=18$ from $t^+=4$ to $t^+=40$. Single harmonic run; upper boundary at $y_o^+=40$ 176

48b Plots of w^+ versus y^+ at $z^+=18$ from $t^+=44$ to $t^+=80$. Single harmonic run; upper boundary at $y_o^+=40$ 177

48c Plots of w^+ versus y^+ at $z^+=18$ from $t^+=84$ to $t^+=100$. Single harmonic run; upper boundary at $y_o^+=40$ 178

49a Plots of v^+ versus y^+ at $z^+=42$ from $t^+=4$ to $t^+=40$. Single harmonic run; upper boundary at $y_o^+=40$ 179

49b Plots of v^+ versus y^+ at $z^+=42$ from $t^+=44$ to $t^+=80$. Single harmonic run; upper boundary at $y_o^+=40$ 180

49c Plots of v^+ versus y^+ at $z^+=42$ from $t^+=84$ to $t^+=100$. Single harmonic run; upper boundary at $y_o^+=40$ 181

50a Plots of u^+ versus y^+ at $z^+=42$ from $t^+=4$ to $t^+=40$. Single harmonic run; upper boundary at $y_o^+=40$ 182

50b Plots of u^+ versus y^+ at $z^+ = 42$ from $t^+ = 44$ to $t^+ = 80$. Single harmonic run; upper boundary at $y_o^+ = 40$ 183

50c Plots of u^+ versus y^+ at $z^+ = 42$ from $t^+ = 84$ to $t^+ = 100$. Single harmonic run; upper boundary at $y_o^+ = 40$ 184

51 Trajectories of fluid particles in the cell. Single harmonic run 187

52 Streaklines for a single harmonic run. Injection point at $z_i^+ = 25$, $y_i^+ = 1.25$ 188

53 Mean streamwise velocity for a single harmonic run; upper boundary at $y_o^+ = 40$ 190

54 Reynolds stress and $-\overline{uv}/u'v'$ correlation for a single harmonic run; upper boundary at $y_o^+ = 40$ 191

55 Intensity of streamwise velocity fluctuations for a single harmonic run; upper boundary at $y_o^+ = 40$ 192

56 Intensities of the normal and spanwise velocity fluctuations for a single harmonic run; upper boundary at $y_o^+ = 40$ 193

57 Skewness and flatness of streamwise velocity fluctuations for a single harmonic run; upper boundary at $y_o^+ = 40$ 194

58 Plots of v/v' versus t^+ at $y^+ = 10$. Signals at $y_o^+ = 40$ contain a wide range of frequencies 196

59 Plots of u/u' versus t^+ at $y^+ = 10$. Signals at $y_o^+ = 40$ contain a wide range of frequencies 197

60 Trajectories of fluid particles in the cell. Signals at $y_o^+ = 40$ contain a wide range of frequencies 198

61 Streamline contours for a double harmonic run at $t^+ = 10$, 20, 30 and 40; upper boundary at $y_o^+ = 40$ 200

62 Streamline contours for a double harmonic run at $t^+ = 50$, 60, 70 and 80; upper boundary at $y_o^+ = 40$ 201

63 Streamline contours for a double harmonic run at $t^+ = 90$, 100, 110 and 120; upper boundary at $y_o^+ = 40$ 202

64 Streamline contours for a double harmonic run at $t^+ = 130,140,150$ and 160; upper boundary at $y_o^+ = 40$ 203

65 Streamline contours for a double harmonic run at $t^+ = 170,180,190$ and 200; upper boundary at $y_o^+ = 40$ 204

66 Streamline contours for a double harmonic run at $t^+ = 210,220,230$ and 240; upper boundary at $y_o^+ = 40$ 205

67 Streamline contours for a double harmonic run at $t^+ = 250,260,270$ and 280; upper boundary at $y_o^+ = 40$ 206

68 Streamline contours for a double harmonic run at $t^+ = 290,300,310$ and 320; upper boundary at $y_o^+ = 40$ 207

69 Streamline contours for a double harmonic run at $t^+ = 330,340,350$ and 360; upper boundary at $y_o^+ = 40$ 208

70 Streamline contours for a double harmonic run at $t^+ = 370,380,390$ and 400; upper boundary at $y_o^+ = 40$ 209

71 Plot of the $R_{s_1 s_2}$ correlation versus Δz^+; double harmonic run 212

72 Plots of v^+ versus t^+ at $z^+ = 40$. Double harmonic run; upper boundary at $y_o^+ = 40$ 213

73 Plots of w^+ versus t^+ at $z^+ = 32$. Double harmonic run; upper boundary at $y_o^+ = 40$ 214

74 Plots of u^+ versus t^+ at $z^+ = 40$. Double harmonic run; upper boundary at $y_o^+ = 40$ 215

75 Plots of ς^+ versus t^+ at $z^+ = 16$. Double harmonic run; upper boundary at $y_o^+ = 40$ 216

76 Plots of v/v' versus t^+ at $y^+ = 20$. Double harmonic run; upper boundary at $y_o^+ = 40$ 217

77 Plots of w/w' versus t^+ at $y^+ = 20$. Double harmonic run; upper boundary at $y_o^+ = 40$ 218

78 Plots of u/u' versus t^+ at $y^+ = 10$. Double harmonic run; upper boundary at $y_o^+ = 40$ 219

79 Plots of ς/ς' versus t^+ at $y^+ = 5$. Double harmonic run; upper boundary at $y_o^+ = 40$ 220

80a Plots of w^+ versus y^+ at $z^+ = 32$ from $t^+ = 10$ to $t^+ = 100$. Double harmonic run; upper boundary at $y_o^+ = 40$ 221

80b Plots of w^+ versus y^+ at $z^+ = 32$ from $t^+ = 110$ to $t^+ = 200$. Double harmonic run; upper boundary at $y_o^+ = 40$ 222

80c Plots of w^+ versus y^+ at $z^+ = 32$ from $t^+ = 210$ to $t^+ = 300$. Double harmonic run; upper boundary at $y_o^+ = 40$ 223

80d Plots of w^+ versus y^+ at $z^+ = 32$ from $t^+ = 310$ to $t^+ = 400$. Double harmonic run; upper boundary at $y_o^+ = 40$ 224

81 Trajectories of fluid particles in the cell. Double harmonic run 226

82 Streaklines for a double harmonic run. Injection point at $z_i^+ = 100$, $y_i^+ = 1.25$ 227

83 Mean streamwise velocity for a double harmonic run; upper boundary at $y_o^+ = 40$ 228

84 Reynolds stress and $-\overline{uv}/u'v'$ correlation for a double harmonic run; upper boundary at $y_o^+ = 40$ 229

85 Intensity of streamwise velocity fluctuations for a double harmonic run; upper boundary at $y_o^+ = 40$ 230

86 Intensitites of the normal and spanwise velocity fluctuations for a double harmonic run; upper boundary at $y_o^+ = 40$ 231

87 Skewness and flatness of streamwise velocity fluctuations for a double harmonic run; upper boundary at $y_o^+ = 40$ 232

88 Streamline contours for a single harmonic run at $t^+ = 10$ and 20; upper boundary at $y_o^+ = 15$ 233

89 Streamline contours for a single harmonic run at $t^+ = 30$ and 40; upper boundary at $y_o^+ = 15$ 234

90 Streamline contours for a single harmonic run at $t^+ = 50$ and 60; upper boundary at $y_o^+ = 15$ 235

91 Streamline contours for a single harmonic run at $t^+=70$ and 80; upper boundary at $y_o^+=15$ 236

92 Streamline contours for a single harmonic run at $t^+=90$ and 100; upper boundary at $y_o^+=15$ 237

93 Streamwise vorticity contours for a single harmonic run at $t^+=10$ and 20; upper boundary at $y_o^+=15$ 239

94 Streamwise vorticity contours for a single harmonic run at $t^+=30$ and 40; upper boundary at $y_o^+=15$ 240

95 Streamwise vorticity contours for a single harmonic run at $t^+=50$ and 60; upper boundary at $y_o^+=15$ 241

96 Streamwise vorticity contours for a single harmonic run at $t^+=70$ and 80; upper boundary at $y_o^+=15$ 242

97 Streamwise vorticity contours for a single harmonic run at $t^+=90$ and 100; upper boundary at $y_o^+=15$ 243

98 Plots of u/u' versus t^+ at $z^+ = 6$. Single harmonic run; upper boundary at $y_o^+=15$ 244

99 Plots of v/v' versus t^+ at $z^+ = 6$. Single harmonic run; upper boundary at $y_o^+=15$ 245

100 Plots of w/w' versus t^+ at $z^+ = 30$. Single harmonic run; upper boundary at $y_o^+=15$ 246

101 Plots of ς/ς' versus t^+ at $z^+ = 30$. Single harmonic run; upper boundary at $y_o^+=15$ 247

102 Mean streamwise velocity for a single harmonic run; upper boundary at $y_o^+=15$ 248

103 Reynolds stress and $-\overline{uv}/u'v'$ correlation for a single harmonic run; upper boundary at $y_o^+=15$ 249

104 Intensity of streamwise velocity fluctuations for a single harmonic run; upper boundary at $y_o^+=15$ 250

105 Intensities of the normal and spanwise components of the velocity for a single harmonic run; upper boundary at $y_o^+=15$ 251

106 Balance of the streamwise component of the turbulent kinetic energy 253

107 Balance of the normal component of the turbulent kinetic energy 255

108 Balance of the spanwise component of the turbulent kinetic energy 256

109 Pressure-velocity gradient correlation coefficient 257

110 Balance of the turbulent kinetic energy 259

111 Mean streamwise velocity profiles for single and double harmonic runs; upper boundary at $y_o^+ = 40$ 276

112 Reynolds stress and $-\overline{uv}/u'v'$ correlation for single and double harmonic runs; upper boundary at $y_o^+ = 40$ 277

113 Intensity of streamwise velocity fluctuations for single and double harmonic runs; upper boundary at $y_o^+ = 40$ 278

114 Intensities of the normal and spanwise components of the velocity for single and double harmonic runs; upper boundary at $y_o^+ = 40$ 279

115 Skewness and flatness of streamwise velocity fluctuations for single and double harmonic runs; upper boundary at $y_o^+ = 40$ 280

116 Energy and vorticity transport from interaction of the wall and the outer layer 283

B-1 Plot of the $R_{s_1 s_1}(\Delta z)$ correlation versus Δz^+. Moving cell run; upper boundary at $y_o^+ = 40$ 332

B-2 Mean streamwise velocity for a moving cell run; upper boundary at $y_o^+ = 40$ 333

B-3 Reynolds stress and $-\overline{uv}/u'v'$ correlation for a moving cell run; upper boundary at $y_o^+ = 40$ 334

B-4 Intensity of streamwise velocity fluctuations for a moving cell run; upper boundary at $y_o^+ = 40$ 335

B-5 Intensities of the normal and spanwise components of the velocity for a moving cell run; upper boundary at $y_o^+ = 40$ 336

B-6 Skewness and flatness of the streamwise velocity fluctuations for a moving cell run; upper boundary at $y_o^+ = 40$ 337

CHAPTER 1

INTRODUCTION

The discovery in the late 50's of coherent eddy structures in the viscous wall region of a bounded turbulent shear flow, using visualization techniques, opened up new horizons for both the theoretical and the experimental worker in the field. Dye-as well as hydrogen bubble techniques (Beatty et al (Corrsin 1956), Kline et al 1967) revealed the existence of a streaky structure in the viscous sub-layer region. These streaks were found to alternate in the spanwise direction and to be characterized by a low streamwise velocity fluid, whereas the regions between successive streaks were observed to carry an excess of streamwise momentum. As these streaks migrate downstream, at the same time, they lift away from the wall and when they reach a critical distance they start to oscillate and break-up into chaotic motions. The most important finding is that during the eruption of the low momentum fluid away from the wall a great deal of turbulent kinetic energy is produced. Due to the violence of the eruption these streaks were given the name "turbulent bursts". It was also found that, if the spanwise spacing between the wall streaks and the frequency of occurrence of the turbulent bursts are made dimensionless with wall parameters (friction velocity u_* and viscosity ν), they remain constant over a wide range of Reynolds numbers (Kim et al 1971).

The impact of this discovery was twofold:

1) It was realized that there is a need for reliable measurements close to the wall

2) There was a need to develop statistical analysis methods that would be able to retain the "phase information" in a turbulent signal. It was realized that the conventional long term averaging techniques "smear out" all the characteristic features of turbulence. It was this realization that led to the development of "conditional averaging" techniques.

A number of research groups have been involved in investigating the coherent structures in the viscous wall region. A review of their work, the differences in their experimental methodologies and their results will be presented in the next chapter. A detailed summary of the work on turbulent boundary layer research has also been given by Laufer (1972) and Willmarth (1975).

Many attempts have been made to describe analytically the structure in the viscous wall region. Taylor (1936) solved the truncated linearized momentum equation and related the velocity field to the pressure field. Linearized analyses have also been conducted by Sternberg (1962), Schubert and Corcos (1967), Gurkham and Kader (1970) and by Hatziavramidis (1978). These analyses don't take into account the Reynolds stress terms and thus fail to characterize the energy containing motions in the viscous sublayer region.

Bakewell and Lumley (1967) suggested that the wall streaks result from counterrotating pairs of eddies homogeneous in the flow direction. Sirkar and Hanratty (1970a) also suggested that the flow in the wall region is dominated by

a secondary pattern homogeneous in the flow direction that is of the type shown in Figure 1a. According to the model, the streaks observed when dye is injected from a wall slot result from the sweeping action of the secondary flow in the transverse direction close to the wall.

Fortuna and Hanratty (Fortuna 1971, Hanratty et al 1977) assumed that, on average, the streamlines in the secondary flow have the shape shown in Figure 1a, and used a pseudosteady state assumption to calculate the streamwise velocity component. They pictured the secondary flow to bring high momentum fluid to the wall at A, to exchange momentum with the wall as it moved fluid in the transverse direction from A and B and to remove low momentum fluid from the wall at B. According to this picture, the streamwise, s_x, and the spanwise, s_z, components of the velocity gradient at the wall should have the phase relation shown in Figures 1b and 1c.

Hatziavramidis and Hanratty (1979) undertook a computational study to explore how the viscous wall region would respond to transverse velocity fluctuations at its outer boundary, $y_o^+ \approx 30$–40. The basic model was similar to the one used by Fortuna (1971) but it was recognized that his pseudosteady state assumption overlooks important aspects of the flow. The flow field in the viscous wall region was pictured to be coherent and to be associated with flow deviations in a well mixed outer region. The transverse flow at $y_o^+ \approx 30$–40 was taken as $w = w_L \sin 2\pi z/\lambda \cos 2\pi t/T_B$, where λ is the spacing of the dye streaks, T_B, the period between bursts and w_L, a constant. Good agreement was obtained

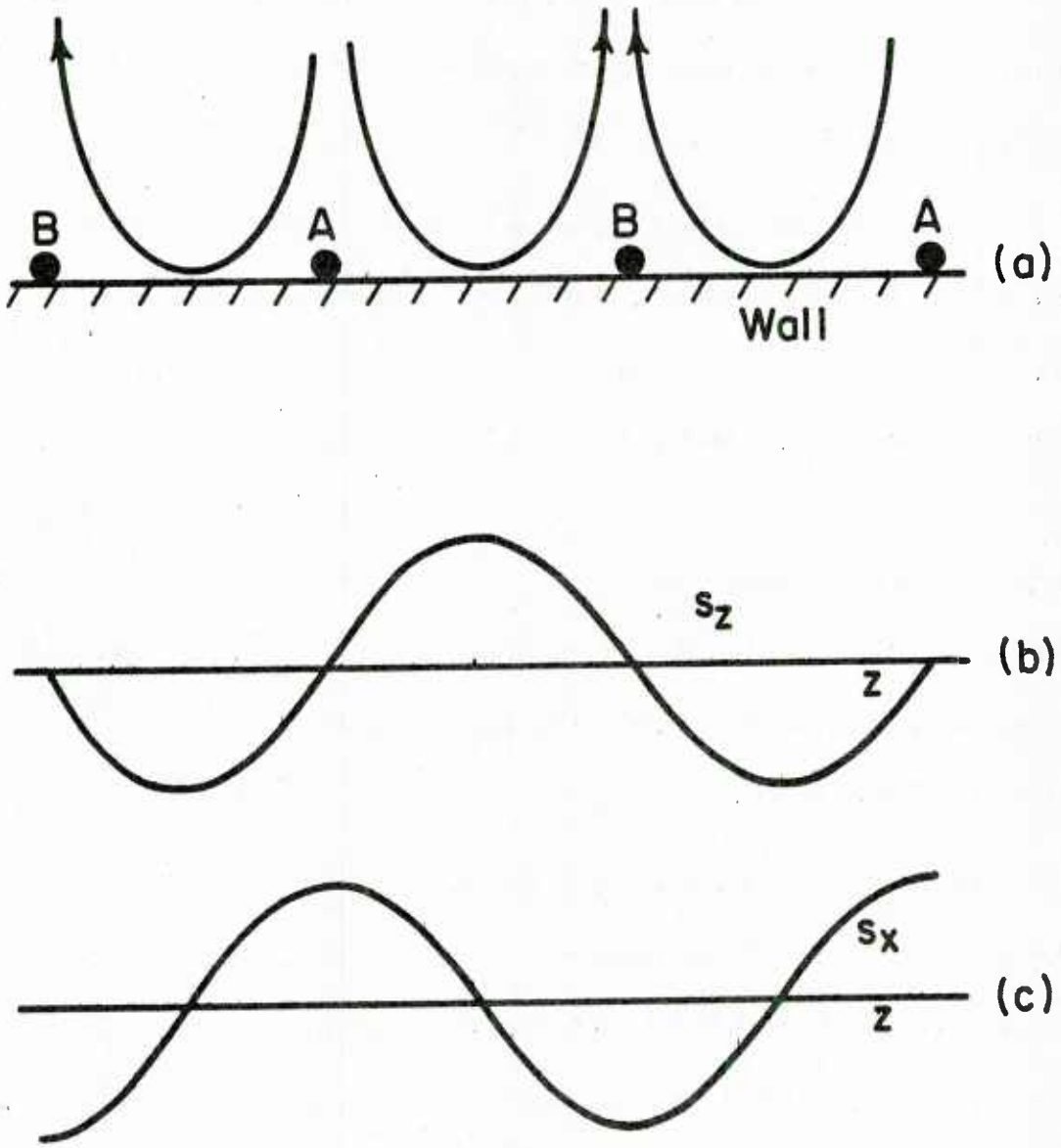

Figure 1 Idealized coherent eddy structure.

between the calculated flow field and experimental results, especially for $y^+ < 15$.

The initial motivation for the model in Figure 1a was provided by measurements of s_x and s_z obtained by Sirkar and Hanratty (1970b) by studying the mass transfer rates to a pair of rectangular electrodes mounted in a chevron arrangement flush with the wall. The results of these experiments showed that the transverse flow at the wall is quite large, s_z being about $0.1S_x$.

Lee, Eckelmann and Hanratty (1974) used an array of electrode pairs to measure s_x and s_z simultaneously at a number of locations on the wall. Their experiments support the existence of a secondary flow pattern of the type visualized by Sirkar and Hanratty (1970a) and the proposal of Fortuna (1971) regarding the influence of this secondary flow on the streamwise velocity fluctuations. In particular, it was found that the s_z variation in the spanwise direction can, on average, be adequately described by a sinusoidal variation of the type shown in Figure 1b. It was also shown that the s_z pattern is accompanied by a spatial variation of s_x that is out of phase by $\lambda/4$. Their measurements of λ are in good agreement with results of the visual studies, cited above.

These results of Lee et al established the patterns of s_x and s_z at the wall which are associated with the wall eddies, but left unanswered the question of how well, if at all, events at the wall are related to phenomena occurring at distances away from the wall. For this purpose, conditionally averaged velocity measurements are needed which reflect in a direct way the relation of the velocity field to changes in the eddy structure and which give information on how the

eddy structure and velocity field evolve in time. One way of doing this would be to combine instrumental measurements of the velocity field with dye pattern measurements. A different approach has been taken in two recent experiments performed by Hogenes (1979,1982) and by Lau (1980).

Measurements of s_z at a number of z-locations are compared with the pattern shown in Figure 1b to determine whether a strong eddy exists. Probes which are mass transfer analogues of the hot film anemometer are located over the center of this array, defined as $z=0$, in order to measure properties of the velocity field. Four aspects of strong wall eddies are defined. Negative or positive values of ds_z/dz at $z=0$ indicate respectively that a strong outflow or inflow would be sampled by the fluid probes. Maxima or minima in $s_z(z)$ at a fixed time indicate strong positive or negative spanwise flows and, on average, a coupled inflow and outflow at distances of $\Delta z^+ \approx 25$ from the center of the wall probe array.

Hogenes and Hanratty (1982) examined the influence of these eddies, defined in terms of the $s_z(z)$ pattern, on the axial velocity component by studying how the $s_z(z)$ pattern and the streamwise velocity profile at $z=0$ are associated with changes in the eddy pattern. They were able to show that the $\lambda^+ \approx 100$ eddies are controlling the fluctuations of the streamwise velocity component in the viscous wall region.

Similar investigations have also been carried out by Blackwelder and Eckelmann (1978, 1979) and Kreplin and Eckelmann (1979a). Blackwelder and

Eckelmann (1978, 1979) studied the spanwise structure of the bursting phenomenon. They located a fluid probe, sensitive to streamwise velocity fluctuations, at $y^+=15$ in order to detect bursts and conditionally averaged measurements of s_x and s_z at one wall location as well as measurements of u and w at a fixed distance from the wall. Their detection scheme was a Variable Interval Time Averaging (V.I.T.A.) scheme that had been used by Kaplan and Laufer (1969) to study the intermittently turbulent region of a boundary layer. They concluded that the "bursting" phenomenon is associated with pairs of counterrotating vortices that seem to "pump" fluid away from the wall, thus forming a low speed streak. They also found that the streamwise momentum defect region is long and narrow, and that the velocity defect is terminated by a strong acceleration followed by a high speed region.

Kreplin and Eckelmann (1979a) investigated the propagation of perturbations in the wall region of a turbulent shear flow. They used a movable V-probe to measure the streamwise and spanwise components of the velocity at a certain distance from the wall. They also used a V-probe mounted on a wall plug at a wall distance of $y^+=2.3$ in order to measure the same components close to the wall. The movable V-probe was located at $x^+=0$ and $y^+=5$, 10, 20, 40 and the wall plug was positioned at $x^+=-108$, 0 and $+144$. From the correlation measurements, Kreplin and Eckelmann deduced that the wall region is dominated by pairs of inclined, counterrotating streamwise vortices. The average spanwise separation of their centers is about $z^+\approx 50$ and the length of the vortices was

estimated to be $x^+ \approx 1200$. As these vortices are convected downstream the angle of their plane of rotation was pictured to decrease and the average minimum distance of the vortex centre from the wall was estimated to be $y^+ \approx 30$.

The present work has two goals. One is to develop an effective conditional averaging scheme capable of detecting the wall eddy patterns. Using this scheme, then, the relation of the wall patterns to transverse velocity fluctuations is studied by determining the relation of the transverse velocity at different values of x, y and z to changes in the eddy structure. For this purpose the experimental measurements of Lau (1980) are used. In these experiments the longitudinal and spanwise components of the fluctuating velocity gradient at the wall of a pipe (s_x and s_z) and the fluctuating velocity at various distances from the wall (u and w) were simultaneously measured.

The second goal of this work is to explore a nonlinear model of the flow oriented eddies. Similar models have been explored by Chapman and Kuhn (1981) and by Hatziavramidis and Hanratty (1979). The difference between this work and the previous works is in the kind of the boundary conditions that are used at the edge of the viscous wall region. The secondary flow at $y_o^+ = 30$–50 is assumed to be characterized by two harmonics in the spanwise direction. The effect of these two spatial wavelengths on the properties of the time varying velocity field is investigated. The case in which one of the two harmonics of the spanwise velocity is of infinite wavelength is also analyzed.

The temporal variation of the secondary flow at the edge of the viscous wall region is characterized by single harmonics which are different for each wavelength. The case where the signal at the upper boundary contains a wide range of frequencies is also studied.

An attempt is also made to assess the effect of introducing a random phase to the signals at the outer boundary, which causes a shifting of the wall patterns.

Finally the effect of various boundary conditions at $y=y_o$ on the calculated dynamics is also explored.

An important contribution of this work is the development of a conditional averaging scheme that is able to capture the wall structures as they evolve in space and time. The application of this scheme to measurements of the spanwise velocity close to the wall and in the fluid revealed that the $\lambda^+ \approx 100$ wall eddies are associated with a very characteristic behavior of the spanwise velocity at $y^+ = 40$; that is, a flow reversal, with the return flow having the same magnitude as the flow that preceded it in time.

The most remarkable result of the computations in this work is that the use of a fixed cell model with two spatial harmonics can describe the important features of turbulence in the viscous wall region. It is shown that small wavelengths can account for the transfer of momentum to and from the wall and for the production of Reynolds stresses throughout the wall layer. In order to describe the intensity of the spanwise flows longer wavelengths become necessary, especially at the outer part of the wall region. As the distance from the wall

decreases, smaller wavelengths become more important and completely define the dynamics of turbulence in this region.

An important finding of this work is the process by which smaller wavelengths are generated by the wall. The mechanism for the generation of smaller scales appears to be the separation of the flow in the spanwise direction. This convective type motion creates small eddies by the non-linear interaction of larger scales.

Another striking discovery is a frequency filtering process according to which only low frequency velocity fluctuations in the plane perpendicular to the flow direction are effective in producing streamwise turbulence. Evidence for this selection process comes from an examination of the trajectories of inertia-free fluid particles within the wall region.

CHAPTER 2

LITERATURE SURVEY

In recent years there has been a growing interest in studying the coherent structures that are found in shear flow turbulence. Flow-visualization experiments have shown that many examples of boundary shear flows, including mixing layers or wakes, boundary layers and jets, have a coherent recurring structure. Statistical measuring techniques, however, only provide quantitative information on their time-averaged properties, so that much of the detail of such structures is lost. This is partly due to the fact that the repeating velocity patterns, when viewed at fixed points, are never sufficiently periodic to be clearly recognizable. It is also difficult to interpret information obtained at one or two fixed points as part of a somewhat complex moving structure. A much clearer picture is obtained if a series of transducers is used that can provide simultaneously spatial and temporal information about the structures.

Conditional averaging techniques have proved to be very powerful tools in providing more ordered information within which clearly defined patterns emerge. They normally depend on some automatic logical process for deciding which parts of the signal arise from the flow structures of immediate interest. Results obtained by following such procedures must naturally enough be accepted with caution unless the logical conditioning process is related to some clearly identifiable repetitive physical characteristic of the flow pattern.

An attempt to numerically calculate a turbulent flow field by solving the full 3-D time dependent Navier-Stokes equations is a very difficult task. The mesh-size of a three dimensional finite-difference grid that would be required to resolve the smallest turbulent eddies is so small that the computation is practically not feasible even on the largest supercomputers available today. It can be shown that for a pipe Reynolds number of 10^6 the number of grid points required to resolve the Kolmogorov microscale, which is the smallest eddy in a turbulent flow, is approximately 10^9.

The ways that the problem has been attacked so far are the following:

1) Reynolds averaging: This is the classical approach by O. Reynolds according to which the Navier- Stokes equations are averaged in time and one then is faced with the task of modelling the resulting Reynolds stresses.

2) Large-eddy simulations: These are time-dependent computations of the three-dimensional large eddy structure of turbulence. Due to the limitations on the mesh size the Navier-Stokes equations are spatially averaged and the small (subgrid) scale eddies have to be appropriatelly modelled.

3) Simple eddy modelling of the viscous wall region: According to this approach the time dependent Navier-Stokes equations are solved on a plane perpendicular to the flow direction that extends throughout the viscous wall region. The turbulent velocity boundary conditions have to be modelled at the outer boundary of the wall layer, then the time-dependent dynamics are computed and finally the results are time averaged. Thus (time) averaging is the last operation performed

on computed dynamics rather than the first operation performed on the dynamic equations as in the previous two approaches.

In section I of this chapter a review is presented of the available turbulence measurements in the viscous wall region and of the work on coherent eddy structures. An account is also given of the different conditional averaging techniques that were used in connection with these studies. Section II compiles the various computational methods for turbulent flows with an emphasis on the use of large computers for the time-dependent solution of the Navier-Stokes equations.

I. Turbulence measurements and coherent structures

A. Measurements of turbulence properties in the viscous wall region

The average statistical properties of the turbulent quantities in the viscous wall region have been measured quite extensively in many laboratories. These present themeselves in the form of average velocities, intensities and higher-order moments of velocity fluctuations, Reynolds stresses, correlations and spectral measurements.

1. Mean velocity measurements

The average streamwise velocity profile has been measured in various kinds of turbulent shear flows (boundary layer, pipe, channel). Laufer (1954) made measurements of the mean velocity $\overline{U}$ in a pipe. Ueda and Hinze (1975) carried out the same measurements in a plane boundary layer flow and Hussain and Reynolds (1975) in a fully developed turbulent channel flow.

All these measurements could well be represented by the relations:

$$\overline{U}^+ = y^+ \quad \text{for} \quad y^+ \leq 7$$

and

$$\overline{U}^+ = 2.44 ln y^+ + 4.9 \quad \text{for} \quad y^+ > 30$$

where the superscript + denotes quantities normalized with wall parameters (friction velocity u_*, viscosity ν).

In the buffer region $7 < y^+ < 30$ Van Driest's (1956) mixing length relation is widely used. Spalding (1971) has given a table of empirical formulas that fit the experimental data on the mean velocity in various regions of the flow.

2. Intensities of velocity fluctuations

The intensities of the fluctuating velocities are defined in terms of the root-mean-square (rms) of the fluctuating quantities:

$$u' = (\overline{u^2})^{1/2},$$
$$v' = (\overline{v^2})^{1/2},$$
$$w' = (\overline{w^2})^{1/2}.$$

The intensities of the two non-zero components of the velocity gradient at the wall are similarly defined as:

$$s_x' = (\overline{s_x^2})^{1/2} = \left[\left(\frac{\partial u}{\partial y} \mid_{y=0}\right)^2\right]^{1/2}$$
$$s_z' = (\overline{s_z^2})^{1/2} = \left[\left(\frac{\partial w}{\partial y} \mid_{y=0}\right)^2\right]^{1/2}$$

The intensities of the three components of the velocity have been measured by Ueda and Hinze (1975), Hussain and Reynolds (1975), Schildnecht et al (1979),

Kutateladze et al (1977), Clark (1968) and by Laufer both in a channel (1950) and in a pipe (1954).

The commom finding among the various measurements is that within the viscous wall region $u' > w' > v'$. The streamwise intensity $(u')^+$ reaches a maximum at $y^+ \approx$13–15 and the normal and spanwise intensities start leveling off for $y^+ \geq 25$.

Extensive measurements of s_x' and s_z' have been carried out in this laboratory (Eckelman 1971, Lee 1975, Hogenes 1979) and by other investigators (Py 1973, Eckelmann 1974, Kreplin 1973). The measurements with the electrochemical method show that $s_x'/\overline{S}_x \approx 0.3$ and $s_z'/\overline{S}_x \approx 0.1$ so that $s_x'/s_z' =$ca3. Measurements with hot-films give lower values for the streamwise intensity $(s_x'/\overline{S}_x = 0.205$–$0.25$ and the value of s_x'/s_z' has been reported by Kreplin and Eckelmann (1979b) to be 3.8.

3. Probability distributions and higher order moments

The probability density distributions have been measured by Klebanoff (1954), Zaric (1972), Eckelmann (1974), Ueda and Hinze (1975), Ueda and Mitzushina (1977), Elena et al (1979), and Kreplin and Eckelmann (1979b). The basic conclusion from these measurements is that the velocity fluctuations in the viscous wall region are non-Gaussian. The skewness of the streamwise velocity fluctuations is positive close to the wall, has a zero crossing at $y^+ =$13–15 and then becomes negative. Positive skewness means that the most pobable velocity is less than the mean which then implies that close to the wall the streamwise

velocity fluctuations will more often be negative than positive. At y^+ larger than 13–15, the opposite is true. The flatness of u-fluctuations has a minimum around the same y^+ where the skewness has a zero-crossing. A Gaussian-signal has a flatness of 3 and for larger values of the flatness the skirt of the probability density curve extends farther away from the average. The flatness is also a measure of the intermittency of the signal which then implies that the u-fluctuations are more intermittent close to the wall ($y^+ < 5$) and far away from the wall ($y^+ > 30$) than in the region $5 < y^+ < 30$.

The skewness of v is positive close to the wall (Kreplin and Eckelmann 1979b) and becomes zero for $y^+ \geq 15$. The flatness of v fluctuations shows a maximum where the flatness of u has a minimum (Ueda and Mitzushina 1977, Kreplin and Eckelmann 1979b). The skewness of the spanwise velocity fluctuations is zero throughout the viscous wall region and the flatness reaches a minimum of 3 around $y^+ = 25$ (Kreplin and Eckelmann 1979b).

The probability density distribution of the angles α, β between w, v and the flow direction has been measured by Kreplin and Eckelmann (1979c). They find that the most probable flow direction is toward the wall. They report $\alpha_{max} \approx 30^o$ ($\alpha_{min} \approx -30^o$) at $y^+ = 3.6$ and $\beta_{max} \approx 16^o$ at $y^+ = 3.4$ (away from the wall) $\beta_{min} \approx -10^o$ at $y^+ \approx 45$ (towards the wall).

4. Reynolds stress

Measurements of the Reynolds stress $-\overline{uv}$ have been carried out by Laufer (1954), Gupta and Kaplan (1972), Eckelmann (1974), Kutateladze et al (1977)

and by Schildnecht et al (1979).

The intermittency of the uv signal was confirmed by Gupta (1970) and Eckelmann (1974). The average $-\overline{uv}$ was found to be rather small compared to the peaks in the uv signal in the sublayer (peak/mean $\approx$30:1).

Willmarth and Lu (1972) and Wallace et al (1972) sorted the contributions to the uv product into the four quadrants of the uv-plane. The main contributions to the Reynolds stress $-\overline{uv}$ were from regions with $u<0$, $v>0$, and $u>0$, $v<0$ associated with ejections of low-speed fluid from the wall and inrushes of high-speed fluid from the outer flow. On the average ejections contribute 70% to the Reynolds stress, inrushes contribute another 70% and the rest -40% is taken up by motions that give a positive uv product (interactions).

Higher-order moments of the fluctuating uv product have been measured by Gupta and Kaplan (1972) and Antonia and Atkinson (1973). The skewness of uv is found to be negative throughout the viscous wall region and the flatness attains values up to 30-40 close to the wall. Wallace and Brodkey (1977) measured the joint probability density distribution $p(u,v)$ on the $u-v$ plane of a turbulent channel flow. They found that the largest contribution to $\overline{uv}$ is not produced by the most probable pair of velocities (u,v).

5. Correlation Measurements

The velocity correlation tensor for a stationary random process is defined as:

$$R_{u_i u_j}(\underline{x};\underline{r},\tau)=\frac{\overline{u_i(\underline{x},t)u_j(\underline{x}+\underline{r},t+\tau)}}{u_i'(\underline{x})u_j'(\underline{x}+\underline{r})}$$

If periodicity is also assumed in the streamwise (x) and spanwise (z) directions then the correlation becomes

$$R_{u_i u_j}(y;\,\Delta x,\,\Delta y,\,\Delta z,\,\tau)=\frac{\overline{u_i(x,\,y,\,z,\,t)u_j(x+\,\Delta x,\,y+\,\Delta y,\,z+\,\Delta z,\,\tau)}}{u_i'(y)u_j'(y+\,\Delta y)}$$

where $(u_1,\,u_2,\,u_3)\equiv(u,v,w)$.

The correlations of the fluctuating velocities in bounded turbulent shear flows have been measured by various turbulence researchers. Based on their measurements these investigators attempted to infer evidence about the existence of structure in the flow field. In what follows the correlation measurements are presented and the discussion of the conclusions reached by the investigators is postponed for part B of this section where the work on coherent eddy structures is discussed.

Grant (1958) was the first to obtain the nine correlations for a cylinder wake and for a turbulent boundary layer. His measurements of $R_{uu}(y;\underline{r})$,$R_{vv}(y;\underline{r})$ and $R_{ww}(y;\underline{r})$ at zero time delay in the inner part of the boundary layer are useful in supplying scaling information about the wall structures. They show that $R_{uu}(y_o^+;\,\Delta x^+,\,0,\,0)$ has a much longer tail than $R_{vv}(y_o^+;\,\Delta x^+,\,0,\,0)$ and $R_{ww}(y_o^+;\,\Delta x^+,\,0,\,0)$ where $y_o^+\approx$25–50. The correlations with a spanwise separation are also interesting in that they show that positive $R_{ww}(y_o^+;\,0,\,0,\,\Delta z^+)$ correlations occur for larger values of Δz^+ compared to $R_{uu}(y_o^+;\,0,\,0,\,\Delta z^+)$ and $R_{vv}(y_o^+;\,0,\,0,\,\Delta z^+)$, where now $y_o^+\approx$35. The latter

two correlations drop to zero around $\Delta z^+ \approx$60–90 and stay zero for longer Δz^+'s even though there is a hint for negative $R_{uu}(y_o^+;\, 0,\, 0,\, \Delta z^+)$ above $\Delta z^+ \approx$90.

Favre, Caviglio and Dumas (1957, 1958) have made extensive measurements of space-time correlations. Although these measurements are very detailed in their coverage of different separations in space and time, they are, on the other hand, restricted by being entirely of the type $R_{uu}(y;\Delta x,\, \Delta y,\, \Delta z,\, \tau)$.

Comte-Bellot (1961) carried out correlation measurements in a channel flow. The most interesting feature of her results are the negative values of $R_{uu}(y;\, 0,\, 0,\, \Delta z)$ and $R_{vv}(y;\, 0,\, 0,\, \Delta z)$, for sufficiently large Δz's, at the lowest y station where y/D=0.11 (D being the half-width of the channel) or y^+=550.

Tritton (1967) extended the work of Grant (1958). He measured various auto- and cross-correlations with an emphasis on $R_{uv}(y;\, \Delta x,\, \Delta y,\, \Delta z,\, 0)$. His $R_{vv}(y_o^+;\, 0,\, 0,\, \Delta z^+)$ measurements with y_o^+=40 give zero crossing at $\Delta z^+ \approx$20 and negative values extending out to $\Delta z^+ \approx$180 with a peak at $\Delta z^+ \approx$45. The same behavior was measured at y_o^+=174 and 414 with the zero crossing moving to larger Δz^+'s. These results were in agreement with Comte-Bellot's (1961) but contradict Grant's (1958) measurements for an unknown reason. Tritton's measurements of $R_{uv}(y;\, 0,\, 0,\, \Delta z)$ and $R_{uw}(y;\, 0,\, 0,\, \Delta z)$ are very interesting as a source of structural information for the coherent structures. His measurements of $R_{uv}(y_o^+;\, 0,\, 0,\, \Delta z^+)$ for y_o^+=10, 29 and 93 show zero crossings at $\Delta z^+ \approx$8, 38 and 85 with negative peaks at $\Delta z^+ \approx$35, 70 and 175 respectively and negative tails extending up to $\Delta z^+ \approx$400 for the largest of the above y_o^+'s. Tritton's

measurements of $R_{uw}(y_o^+; 0, \Delta y^+, \Delta z^+)$ show maxima at $\Delta z^+ \approx 52$ for $y_o^+ = 19$ and 32 and $\Delta y^+ = 4$ and -9 respectively (positive Δy^+ is in the direction away from the wall) and positive values extending up to $\Delta z^+ \approx 360$. The same behavior for $R_{uw}(19; \Delta x^+, 4, \Delta z^+)$ was measured with a longitudinal separation $\Delta x^+ \approx 237$.

Lee et al (1974) measured simultaneously the two components of the velocity gradient at the wall S_x and s_z and obtained correlations of the form $R_{s_z s_z}(\Delta z)$, $R_{s_x s_x}(\Delta z)$ and $R_{s_z s_x}(\Delta z, \tau)$. Their results show that the s_z pattern is accompanied by a spatial variation of s_x which is out of phase by $\lambda/4$. The development of the s_x pattern was found to lag behind the development of the s_z pattern, indicating that the streamwise flow at the wall is largely controlled by the spanwise velocity field.

Kreplin and Eckelmann (1979a) studied the propagation of perturbations in the viscous wall region and calculated correlations of the form $R_{us_x}(\Delta y, \tau)$ $R_{ws_x}(\Delta y, \tau)$. They interpreted their measurements as being associated with vortical flow structures, inclined to the wall, that travel downstream. The spanwise distance between these structures was found to be $\Delta z^+ \approx 50$ and they could be observed over a streamwise distance of $\Delta x^+ > 1000$. They also attributed the antisymmetry of the $R_{ws_x}(-40, \tau)$ correlation to the fact that the vortex centre moves below $y^+ = 40$ as it is convected downstream.

6. Spectral measurements

The energy spectrum tensor for a stationary random process that is homogeneous in the x and z directions is given as the Fourier transform of the corresponding correlation tensor:

$$\Phi_{u_i u_j}(y; \underline{k}, \omega) = \frac{1}{(2\pi)^3} \int_{-\infty}^{\infty} \int\int R_{u_i u_j}(y; \underline{r}, \tau) e^{-i(\underline{k}\cdot\underline{r} + \omega\tau)} d\underline{r} d\tau$$

where $\underline{k}=(k_x, k_z)$, $\underline{r}=(x, z)$ and $d\underline{r}=dxdz$.

The frequency spectra of the streamwise fluctuating velocity within the viscous sublayer have been measured by Bakewell and Lumley (1967). The data, nondimensionalized by y^2w, define a single curve when plotted against $n^+=n\nu/u_*^2$.

The spectra of the fluctuating gradients at the wall, s_x and s_z, have been measured by Sirkar (1969) and Fortuna (1971) using electrochemical techniques. The median frequency of the wall spectra is $n^+\approx 0.01$ and most of the turbulent energy is contained in frequencies lower than that.

Morrison and Kronauer (1969) measured two-dimensional frequency wavenumber spectra $\Phi_{uu}(y^+; k_x^+, \omega^+)$ and $\Phi_{uu}(y^+; k_z^+, \omega^+)$ with y^+ covering the whole viscous wall region $0<y^+<40$–50. Their measurements, being limited on the streamwise velocity, are nevertheless useful in obtaining information about the relation between eddy size and lifetime in the wall region. As the distance y^+ from the wall increases, the ridge line of the $\Phi_{uu}(y^+; k_x^+, \omega^+)$ spectra exhibits a rotation from a vertical position to one forming an angle with the k_x^+ axis. At the same time the peak of Φ_{uu} shifts to smaller wavenumbers but the

corresponding circular frequency remains around $\omega^+ \approx 0.06$–0.08.

Morrison et al (1971) presented more extended measurements of $\Phi_{uu}(y^+; \omega^+, k_x^+)$ and $\Phi_{uu}(y^+; \omega^+, k_z^+)$ in the viscous sublayer. They found that the characteristic convection velocity is independent of the wavenumber and is the same at all positions in the layer ($c_x^+ \approx 8.0$). They concluded that sublayer turbulence is wave-like. The characteristic dimensions of the sublayer waves were found to be $\lambda_x^+ \approx 630$ and $\lambda_z^+ \approx 135$.

A summary of pressure spectral measurements at the wall is given by Willmarth (1975). These measurements are made with flush transducers or with pinhole microphones. Emmerling (1973) showed, for the first time, that the small-scale wall pressure fluctuations do scale with wall parameters. Bull (1967) plotted the variation of intensity of wall pressure fluctuations with Reynolds number. It was shown that the larger-scale wall pressure fluctuations scale on outer variables and increase in intensity with Reynolds number.

B. Coherent structures in wall turbulence

1. Visual and instrumental studies

The importance of coherent structures in understanding the mechanism that sustains turbulence has been emphasized in Colloquii and Workshops around the world. An account of the Colloquium on Coherent Structures on Turbulence held at Southhampton from 26-29 March 1974 has been given by Davies and Yule (1975). Summaries of the First and Second Research Specialists Workshops on Coherent Structures in Turbulent Boundary Layers have also been presented by

Kline (1978) and Kline and Falco (1979) respectively.

In these meetings the emphasis was placed on the following topics:

a) Presentation of experimental results

b) Reconciliation of the findings of the various laboratories

c) Posing of questions about the turbulent boundary layer structures.

In what follows a brief account of the work on coherent structures is presented. The first attempts in deducing information about the existence of eddy structures was based on correlation measurements as mentioned in part A of this section. The later development and use of conditional sampling and averaging techniques provided a more reliable method to extract structure out of a turbulent signal.

Townsend in a series of papers (1957, 1961, 1970) and in his book (1956) presented some novel ideas about the structure of turbulence. He suggested that a turbulent flow field has a double structure: a small scale or "active" motion which transfers momentum and produces Reynolds stress and a large scale or "inactive" motion which interacts with the active component at points farther from the wall where it can also contribute to Reynolds stress. The important point to emphasize here is that Townsend, for the first time, recognized the existence and importance of certain coherent structures having a characteristic length and time scale and formulated the problem in terms of these. Using the rapid distortion theory of Batchelor and Proudman (1954), Townsend (1970) calculated the nine correlations for a turbulent cylinder wake and compared them

with Grant's (1958) measurements. He concluded that the dominant structure is a double-roller eddy which can also be described as a section of a linear jet or as a diffused vortex-pair. He noted that this structure resembles closely the eddies studied in boundary-layer and pipe flow by Kline et al (1967).

Grant (1958) preferred to interpret his correlation measurements by postulating that there are stress releasing motions in the inner part of the boundary layer. He associated these with a series of jets lined up in the direction of the stream. Because of the short extent of $R_{vv}(y_o^+; 0, 0, \Delta z^+)$ he concluded that these motions are narrow in the z-direction and that the back-flow appears to be in the x-direction. He reconciled this notion with the negative values of $R_{ww}(y_o^+; 0, 0, \Delta z^+)$ by arguing that they are related to flows toward both sides of the displaced fluid.

Tritton (1967) did not succeed in formulating a simple model of the large eddies. He concluded though that his results do give further support to Townsend's hypothesis that the large eddies have a characteristic structure of their own. He also suggested that the description of the large eddies in the wall region as a coherent eruption from the viscous sublayer is unsatisfactory.

Bakewell and Lumley (1967) carried out an orthogonal decomposition of the correlation function of the streamwise velocity component with normal separation $R_{uu}(y; 0, \Delta y, 0)$ and postulated the existence of counterrotating eddies of streamwise extent that give rise to eruptions from the viscous sublayer which are coupled with more diffuse return flows.

Visualization techniques were extensively used by both the Stanford (Kline et al 1967, Kim et al 1971, Offen and Kline 1974) and the Ohio state group (Corino and Brodkey 1969, Nychas et al 1973, Praturi and Brodkey 1978). The results of these studies provided much information about the wall structures.

The Stanford group used dye injection through wall slots (Kline and Runstadler 1959, Runstadler et al 1963) or through a flattened Pitot tube placed in the outer flow (Offen and Kline 1974). Subsequent studies used the hydrogen bubble technique (Kline et al 1967, Kim et al 1971), since this method provides both qualitative and quantitative information. In this technique a single platinum wire is used as an electrode to generate small hydrogen bubbles. By pulsing the voltage applied to the wire, time lines can be generated, and, by insulating spanwise portions of the wire, streaks are formed. The experimental efforts of the Stanford group revealed a surprisingly organized structure close to the wall. It was found that the dye injected through the wall slots undergoes an indentifiable sequence of events: formation of a low-speed streak, lift-up of the low-speed streak, oscillatory growth and final breakup. This eruption of low axial momentum fluid away from the wall has been given the name "turbulent burst". The ejection of low-speed (u) fluid from the wall requires, from continuity, a return flow in the opposite direction. Such a wallward convective motion, called sweep or inrush was observed in almost every case just before the beginning of the oscillatory motion of the lifted wall streak. Two types of vortical motions were associated with a sweep. One is a transverse vortex that brings

fluid down toward the wall and then moves it forward in the mean flow direction. The other is an upward-tilted streawise vortex (Offen and Kline 1974).

The Ohio State group started an investigation of the wall flow structures (Corino and Brodkey 1969) by suspending solid particles of colloidal size in a liquid and photographing their motions with a high-speed motion picture camera moving with the flow. The most important characteristic of the wall region ($0 \leq y^+ \leq 30$) was found to be the intermittent ejection of discrete fluid elements outward from the wall. The actual ejection of fluid was only part of a sequence of events. The first of these events was a deceleration of the axial velocity of the fluid within a local region near the wall. Deficiencies as great as 50% of the local mean velocity were observed. While the field was thus decelerated, the next step occurred, which was an acceleration. This resulted from a mass of fluid coming from upstream with approximately the local mean velocity, that entered the retarded field, and then accelerated the fluid. This appeared to be a part of a large-scale disturbance carried by the mean flow. At various times an effect, called two-layer velocity, was observed. This was believed to be associated with the spanwise variation reported by Kline et al (1967) but of far smaller scale than implied by that observed for the boundary layer flow. The third event is an ejection i.e. an abrupt movement outward from the wall area of fluid originally within this region. At the time of ejection there is often a very sharp interface between accelerated and retarded fluid, creating a very high shear layer. The ejection phase ends with the entry from upstream of a stream of fluid directed

primarily in the axial direction; this is the sweep event.

Nychas et al (1973) photographed the outer region of a turbulent boundary layer along a flat plate. The single most important event observed was a large scale transverse vortex, which was transported downstream with an average velocity slightly smaller than the local mean. The transverse vortex appeared to be the result of a Helmholtz type of flow instability.

Praturi and Brodkey (1978) photographed the motions of small tracer particles in a turbulent boundary-layer flow using a stereoscopic medium-speed camera system moving with the flow. This technique allowed the three-dimensional aspects of the flow to be studied and in particular allowed axial vortex motions in the wall region to be identified. Their results indicated that bulges in the edge of the boundary layer are associated with transverse vortex motions. They suggested that the outer region motions give rise to conditions necessary for the dominant wall- region activity of ejections and axial vortex motions. These axial vortical motions were intense and lasted for a time short compared with the lifetime of outer-region transverse vortex motions. The results suggested that the wall-region vortex motions are a result of interaction between the incoming higher-speed fluid from the outer region and the outflowing low-speed wall- region fluid.

The interface separating the turbulent and non-turbulent regions of a fully developed turbulent boundary layer was explored by Kovasznay et al (1970). This was one of the first studies that utilized the concept of conditional sampling.

They used the following detector function:

$$I(t) = \begin{cases} 0 & \text{for non-turbulent flow} \\ 1 & \text{for turbulent flow} \end{cases}$$

Once $I(t)$ is known various conditional averages can be obtained. For example, the "turbulent zone average" of any fluctuating quantity is defined as

$$\overline{\overline{Q}} \equiv \lim_{t_1 \to \infty} \frac{1}{\gamma t_1} \int_{t_o}^{t_o + t_1} Q(t)\, I(t) dt \text{ where } \gamma = \lim_{t_1 \to \infty} \frac{1}{t_1} \int_{t_o}^{t_o + t_1} I(t) dt = \overline{I}$$

The use of this conditional averaging technique allowed Kovasznay et al to arrive to the following conclusions: 1) The non-turbulent flow moves slightly faster than the turbulent fluid adjacent to the surface, 2) The "front" of an interfacial bulge is steeper than the "back". This was consistent with the findings that the streamwise velocities at the "front" are higher on the average than those in the "back", 3) Conditional zone averages of the normal component of the velocity showed positive values in the turbulent and negative in the non-turbulent region.

Gupta et al (1971) used the VITA (Variable Interval Time Averaging Technique) to analyze measurements of the fluctuating streamwise velocity at various spanwise locations for $y^+ < 12$. According to this technique averages of fluctuating quantities are taken over short periods of time as follows:

$$\hat{Q}(x_i, t_o; T_s) = \frac{1}{T_s} \int_{t_o}^{t_o + T_s} Q(x_i, t) dt$$

In general $\hat{Q}$ is a random function of t_o. Using the above definition the correlation $R_{uu}(0, 0, \Delta z, t_o; T_s)$ was computed for various values of T_s keeping

t_o constant. For large T_o the correlation function behaves similarly to the one generated by the conventional long time averaging process. On the other hand for small T_o, large values of the correlation were observed for relatively large separation distances, suggesting a structure with a characteristic spanwise wavelength of $\lambda^+ \approx 100$.

Willmarth and Lu (1972) used conditionally sampled measurements of the product uv in order to study the structure of the Reynolds stress near the wall. They measured the fluctuating streamwise velocity u using a hot-wire at $y^+ = 16.2$ and the fluctuating uv product using an X-wire at $y^+ = 30$ located directly above the point where u was measured. The signal from the single hot-wire provided the triggering information for the conditional sampling process. When the value of u at $y^+ = 16.2$ crossed a given threshold level T with negative slope, the instantaneous uv product was recorded for a certain time interval before and after the sampling criteria were met. The fluctuating uv product is not the fluctuating stress caused by turbulence [which is $UV - \overline{U}\overline{V} = u\overline{V} + v\overline{U} + uv$] but the term ultimately contributing to the average of fluctuating stress i.e. the Reynolds stress ($= \overline{uv}$). So large values of the conditionally sampled $\tilde{uv}$ product would indicate large contributions to the Reynolds stress. Willmarth and Lu found $\tilde{uv} \approx 5\overline{uv}$ with $T = -2.15\, u'$ (where u' is the r.m.s. value of u) at $tU_\infty/\delta^* = 7$.

Blackwelder and Kaplan (1976) studied the wall structure of a turbulent boundary layer. They used two hot-wire rakes in order to study the variation of

the streawise velocity in the spanwise direction and the direction normal to the wall. They also used X-wires to measure the Reynolds stress. The detector probe was a single hot-wire sensitive to streamwise velocity fluctuations and located at $y^+=15$. They used the VITA technique in order to obtain a localized measure of the turbulent energy according to the relation:

$$\hat{\text{var}}(x_i,\ t,\ T)=\hat{u^2}(x_i,\ t,\ T)-[\hat{u}(x_i,\ t,\ T)]^2$$

where the $\hat{}$ denotes a VITA averaged quantity. The above quantity is a localized variance and is a positive-definite quantity. The detection function was defined as

$$D(t)=\begin{cases}1 & \text{if } \hat{\text{var}} > k\cdot u_{rms}^2\\ 0 & \text{otherwise}\end{cases}$$

where k is an appropriate threshold value. The conditional average of a quantity Q was then defined by

$$<Q(x_i,\ \tau)>_{y^+}=\frac{1}{N}\sum_{j=1}^{N} Q(x_i,\ t_j+\tau).$$

The quantities t_j are the points in time where detection occured. These were selected to be midway between the beginning and the end of the period during which $D(t)\neq 0$. Blackwelder and Kaplan found the detector function to be associated with large streamwise velocity accelerations. The conditionally averaged normal velocity was directed outwards in regions of strong streamwise-momentum deficit and inwards when the streamwise velocity exceeded its mean value. The conditionally averaged Reynolds shear stress was approximately an order of magnitude greater than its conventionally averaged value and decayed

slowly downstream.

Wallace et al (1977) used a pattern-recognition technique to detect a gradual deceleration from a local maximum followed by a strong acceleration in the u-signal. Their technique worked as follows: a short-time temporal average (referred to as TPAV) was taken to be the period from one maximum in du/dt to the next. TPAV was thus defined as TPAV $= \frac{1}{M-m} \sum_{n=m}^{M} u(n)$ where m and M are the first and last points in the pattern respectively. This value was subtracted from the u signal to obtain the fluctuating u velocity used in the pattern-recognition scheme. The basic requirement was for the slope of the u-signal during deceleration to be smaller than the slope during acceleration. Such patterns were found in over 65% of the total sample in the region of high Reynolds stress production. The unsmoothed data were subsequently normalized to an arbitrarily chosen unit time interval and stored. Conditionally averaged patterns of the v signal were found to be approximately 180^{o} out of phase with the u signal. Their interaction produces Reynolds stress in the wall region of a bounded turbulent shear-flow.

Eckelmann et al (1977) applied the above described pattern recognition technique to signals obtained from a five-sensor probe. Their results agreed with those obtained by Wallace et al (1977). They also obtained conditional averages of the instantaneous production term as defined by Brodkey et al (1973). The ejection-type motion was found to give the principal positive contribution to turbulence production. For $y^{+} < 30$ the sweep-type motion also contributes heavily

to positive production. In the outer region, however, the sweep motions are negative contributors to the production process.

Blackwelder and Eckelmann (1978) studied the spanwise structure of the bursting phenomenon. The bursts were detected at $y^+ \approx 15$ by using the VITA technique on the streamwise velocity component. Conditional averages with a time delay were obtained from wall elements having a spanwise spatial separation. They concluded that the bursting phenomenon is associated with pairs of counterrotating vortices that seem to "pump" fluid away from the wall, thus forming a low-speed streak. The length of these vortices was estimated to be $\Delta x^+ \approx 1000$.

Blackwelder and Eckelmann (1979) studied the vortex structure associated with the bursting phenomenon. Two wall elements were used to measure the two components of the velocity gradient at the wall. A characteristic function was defined as:

$$f^2(t) = \frac{u_1^2(t)}{\overline{u_1^2}} + \frac{w_1^2(t)}{\overline{w_1^2}} + \frac{u_2^2(t)}{\overline{u_2^2}} + \frac{w_2^2(t)}{\overline{w_2^2}}$$

where u_1, w_1 and u_2, w_2 are the signals from the two wall elements. This function is a measure of the energy associated with the fluctuations. If the coherent eddies are more energetic than the random fluctuations, their related velocity fluctuations will have excursions farther from the origin. The four signals from the probes define a single point in a four-dimensional space with each signal corresponding to one axis. The 16 different quadrants in this space correspond to

all combinations of the four signals. Blackwelder and Eckelmann applied a threshold level to the function $f^2(t)$ and by increasing it were able to show that the percentage of the time, spent in the quadrants associated with the streamwise vortices, increased.

Kreplin and Eckelmann (1979a) measured space-time correlations of the form $R_{ws_z}(\Delta y, \tau)$, $R_{ws_z}(\Delta y, \tau)$ and of the form $R_{uu}(y_o; \Delta x, \Delta y, \tau)$ and $R_{ww}(y_o; \Delta x, \Delta y, \tau)$. The two components of the velocity gradient at the wall were obtained from heated wall elements. The two components of the velocity u, w close to the wall were measured by a V-probe mounted on a wall plug at $y_o^+ = 2.3$ and $\Delta x^+ = -108$, 0 and $+144$. The same components in the fluid were measured by a movable V-probe at $\Delta y^+ = 5$, 10, 20, 40 and $\Delta x^+ = 0$. From these correlation measurements they deduced that the wall region is dominated by pairs of inclined, counterrotating streamwise vortices. Their centres were found at an average separation of $\Delta z^+ \approx 50$ and their lengths were estimated to be $\Delta x^+ \approx 1200$.

Hogenes and Hanratty (1982) carried out simultaneous measurements of the two components of the velocity gradient at multiple points on the wall and of the streamwise velocity at various distances from the wall. They studied the influence of the $\lambda^+ \approx 100$ wall eddies, defined in terms of the $s_z(z)$ pattern, on the axial velocity component. In order to identify maxima or minima and positive or negative slopes of the $s_z(z)$ profiles, they devised detection coefficients capable of detecting such characteristics of the spanwise variation of the s_z signal. These

coefficients were used to detect the wall events over the middle probe of the wall probe array and to define the triggering time for the conditional averaging process. Similar coefficients were used to study the temporal succession of wall patterns. Their results indicated that the $\lambda^+ \approx 100$ wall eddies are controlling the fluctuations of the streamwise velocity component in the viscous wall region. That provided further support for using the idealized eddy model of Sirkar and Hanratty (1970a) to describe momentum transport between the wall and the fluid and to account for the origin of the low momentum fluid that has been observed to emerge intermittently from the wall region.

2. Measurements of the streak spacing, λ, and the bursting period T_B

The spacing of the wall streaks in the spanwise direction, λ^+, can be determined either by visually counting the streaks in a large number of pictures or by determining the wavenumber k_z^+ that maximizes the spanwise spectra $\Phi_{uu}(k_z^+)$ of the streamwise velocity close to the wall. The spacing can also be inferred from correlation measurements (Lee et al 1974). Kim et al (1971) found $\lambda^+ = 100 \pm 20$. Coantic (1967) and Bakewell and Lumley (1967) used hot wire probes and calculated λ^+ from correlation measurements. Coantic found $\lambda^+ \approx 110$–130 and Bakewell and Lumley calculated $\lambda^+ \approx 100$. Gupta et al (1971) used a rake of hot-wires and obtained spanwise correlations of u below $y^+ = 12$. They found $\lambda^+ \approx 95$. Lee et al (1974) used electrochemical techniques to measure the spanwise correlation of both u and w at the wall. They measured $\lambda^+ \approx 105$–107. From measurements of Schraub and Kline (1965) the value of λ^+

appears to be insensitive to pressure gradient.

The mean period T_B between bursts has been measured for low Reynolds numbers. Two methods have been used for this purpose: 1) visual counting of the bursts and 2) the second mild maximum of the time autocorrelation of the streamwise velocity fluctuations. Kim et al (1971) presented a plot of T_B scaled with wall parameters versus Re_θ (momentum thickness Reynolds number) using the measurements of the Stanford group (Kim et al 1971-visual and autocorrelation measurements of T_B, Schraub and Kline 1965-visual measurement of F, Runstadler et al 1963-visual measurement of F, where F is a normalized burst rate per unit span). They also included measurements of T_B by Tu and Willmarth (1966) and by Rao et al (1971) who used the autocorrelation method. The resulting relation was $u_*^2\frac{T_B}{\nu}=0.65Re_\theta^{0.73}$. When the data were replotted as $U_\infty\frac{T_B}{\delta^*}$ versus Re_θ they fell on the line $U_\infty\frac{T_B}{\delta^*}\approx 30$ (or $U_\infty\frac{T_B}{\delta}\approx 5$) where δ^* is the displacement thickness and δ the thickness of the boundary layer. Kline et al (1967) plotted F^+ versus K(pressure gradient parameter $=\frac{\nu}{U_\infty^2}\frac{dU_\infty}{dx}$). For $K=0$ i.e. a zero pressure gradient turbulent boundary layer, $F^+\approx 120\times 10^{-6}$. The most reliable data appear to be from direct visual observations (Schraub and Kline 1965, Donohue et al 1972, Smith 1978). These are confined however to Re_θ values within a factor of two of $Re_\theta=10^3$. The scaling law for $\frac{T_B}{\lambda}$ has been a subject of controversy. During the past decade it generally has been thought

that $\frac{T_B}{\lambda}$ scales on outer variables U_∞ and δ but some recent measurements of Blackwelder and Haritonidis (1980) covering the range $10^3 < Re_\theta < 10^4$ have indicated that $\frac{T_B}{\lambda}$ scales on wall variables u_* and ν.

II. Computational methods for turbulent flows

As mentioned in the beginning of this chapter the solution of the full three-dimensional time-dependent Navier-Stokes equations is not possible due to the lack of computing power, even by the largest computers available today. A review of the methods that have been used so far, in order to get around this problem, is presented in what follows. Emphasis is given to the Large-Eddy Simulations (LES) and the newly developed approach of modelling the viscous wall region of a turbulent flow field. An extensive review of the Reynolds-averaging methods has been given by W.C. Reynolds (1976).

A. Reynolds averaging

According to this approach the Navier-Stokes equations are averaged in time and the resulting Reynolds stresses have to be modelled in order to close the problem. The various models that have been developed for this purpose are the following:

1. Zero-equation models

These models use only the pde's from the mean velocity field, and no turbulence pde's. They are mostly based on the eddy-viscosity and mixing length

concepts. According to these, the Reynolds stress is computed as: $-\overline{uv}=\nu_T\frac{\partial U}{\partial y}=l^2\mid\frac{\partial U}{\partial y}\mid\frac{\partial U}{\partial y}$ and so is completely specified by mean flow properties.

2. One-equation models

These models involve one pde relating to a turbulence velocity scale, in addition to the mean-flow pde's. The model equation for this velocity scale is provided by the turbulent kinetic energy equation.

The difference between zero-equation and one-equation models is that in the latter the eddy viscosity ν_T, instead of being related directly to the mean-flow scales, is modelled by $\nu_T=c_1 q\ l$ where q is the calculated rms turbulent kinetic energy and l is given by $l=Ky[1-\exp(-c_2 qy/\nu)]$ as in the zero equation models.

3. Two-equation models

These models use an additional pde related to a turbulence length scale. Most research groups have achieved considerable success using an equation for the isotropic dissipation D_{i_ϵ}. The equation relating D_{i_ϵ} to the length scale l can be taken to be the one proposed by Norris and Reynolds (1975) which works both in the viscous sublayer and the fully turbulent regions. According to this equation $D_{i_\epsilon}=c_1\frac{q^3}{l}\left[1+\frac{c_2}{ql/\nu}\right]$. At high turbulent Reynolds numbers (ql/ν) the limiting relation is $D_{i_\epsilon}=c_1\frac{q^3}{l}$ i.e. the dissipation is independent of viscosity and determined by the properties of the energy-containing eddies. At very low ql/ν

the limiting expression is : $D_{ij}=c_1 c_2\, \nu \frac{q^2}{l^2}$ i.e. there is dissipation in the large scales of the flow and is affected by the viscosity.

4. Stress-equation models

These models involve pde's for all components of the Reynolds stress tensor and in general for a length scale as well. The equations for $\overline{u_i u_j}$ can be formally written as: $\overline{u_i u_j}+ \overline{U_l}\ \overline{u_i u_j}_{,l}=P_{ij}+\phi_{ij}-J_{ijl,l}-D_{ij}$ where P_{ij} is the "generation tensor", ϕ_{ij} is the pressure-strain "redistribution tensor", D_{ij} is the "isotropic dissipation tensor" and J_{ijl} is the transport of $\overline{u_i u_j}$ (the subscript $,l$ denotes differentiation with respect to x_l). The redistribution term ϕ_{ij} has been the subject of most controversy and experimentation. In a flow without any mean strain, this term is responsible for the return to isotropy. However, in deforming flows the situation is much more complicated.

There is a basic difficulty in this general approach to turbulence models. One would like to model only terms that respond on time scales short compared to that of the computed quantities. In general, it seems that higher order statistical quantities take longer to reach steady state than lower order statistics. Any model obtained by truncation at some statistical order would suffer from this difficulty. What one really needs to do is truncate at some level of scale, and thereby take advantage of the fact that the smaller scales adjust faster to local conditions. Then, by truncating at smaller scales, one has at least hope of convergence, a hope that is at best dim when one truncates at higher and higher ord-

ers of statistical quantities that have comparable time scales. This is the idea behind the LES approach described below.

B. Large-Eddy Simulations(LES)

The idea is to do a three-dimensional time-dependent numerical computation of the large scale turbulence. It will always be impossible to compute the smallest scales in any real flow at high turbulence Reynolds numbers, so they must be modelled.

The first application of LES was made by Deardorff (1970) who in fact showed that a three-dimensional calculation is feasible. The idea of applying an averaging operator to the governing equations, with averaging typically being over the grid volume of the calculations to filter out the subgrid scale (SGS) motions, had been known since the early work of Reynolds (1895). This approach had been employed by several groups of meterologists (Smagorinsky et al 1965, Leith 1965) for the general circulation of the atmosphere. Deardorff actually tested this meteorological approach upon an interesting case of lab turbulence: plane Poiseuille flow (channel flow) driven by a uniform pressure gradient. He used 6,720 uniform grid intervals and simulated the subgrid scale effects using a suggestion of Smagorinsky et al (1965) and Lilly (1967) which is applicable only for large Reynolds numbers. With his pioneering work Deardorff demonstrated the potential of LES for use in basic studies of turbulence.

The grid-scale averaging operator was defined as:

$$\overline{u}(x,\,y,\,z,\,t)=\frac{1}{\Delta x\,\Delta y\,\Delta z}\int_{x-1/2\Delta x}^{x+1/2\Delta x}\int_{y-1/2\Delta y}^{y+1/2\Delta y}\int_{z-1/2\Delta z}^{z+1/2\Delta z}u(\xi,\,\eta,\,\varsigma,\,t)\,d\xi\,d\eta\,d\varsigma$$

A filtered variable, denoted by the overbar, is thus a continuous function of space and time. After applying the overbar operator the Navier-Stokes equations in flux form may be written as:

$$\frac{\partial\overline{u_i}}{\partial t}+\frac{\partial}{\partial x_j}(\overline{u_i}\;\overline{u_j})=-\frac{\partial}{\partial x_j}(\overline{u_i}\;\overline{u_j}+\overline{\overline{u_i}\,u_j'}+\overline{u_i'\,\overline{u_j}}+\overline{u_i'\,u_j'}-$$

$$\frac{1}{3}\delta_{ij}\overline{u_l'\,u_l'})-\frac{\partial}{\partial x_i}(\overline{p}+\frac{1}{3}\overline{u_l'\,u_l'})+\frac{1}{\mathrm{Re}}\nabla^2\overline{u_i}\qquad(2.1)$$

Here 1,2,3 correspond to x,y,z respectively and the prime quantities are given by: $u_i=\overline{u_i}+u_i'$ and represent deviations from local grid-volume means. Reynolds' averaging assumption

$$\overline{u_i\,u_j}=\overline{\overline{u_i}\;\overline{u_j}}+\overline{\overline{u_i}\,u_j'}+\overline{\overline{u_i}\,u_j'}+\overline{u_i'\,u_j'}=\overline{u_i}\;\overline{u_j}+\overline{u_i'\,u_j'}$$

can be used (otherwise it may be incorporated into later assumptions). If this assumption is used then the remaining as unknowns in (2.1) are the SGS Reynolds stresses $\overline{u_i'\,u_j'}-\frac{1}{3}\delta_{ij}\overline{u_l'\,u_l'}$. The method of evaluation used introduced SGS eddy coefficients as follows:

$$\overline{u_i'\,u_j'}-\frac{1}{3}\delta_{ij}\overline{u_l'\,u_l'}=-K(\frac{\partial\overline{u_i}}{\partial x_j}+\frac{\partial\overline{u_j}}{\partial x_i})$$

where K was modelled according to Smagorinsky's et al (1965) assumption:

$$K(x,y,z,t)=(c\Delta)^2\left[\frac{\partial\overline{u_i}}{\partial x_j}\left(\frac{\partial\overline{u_i}}{\partial x_j}+\frac{\partial\overline{u_j}}{\partial x_i}\right)\right]^{1/2}\qquad(2.2)$$

where c is a dimensionless constant and $\Delta=(\Delta x\cdot\Delta y\cdot\Delta z)^{1/3}$. If an inertial subrange exists on scales which encompass the grid interval, then the usual

dimensional arguments demand that

$$K = c^{4/3}\bar{\epsilon}^{1/3}\Delta^{4/3} \tag{2.3}$$

where $\bar{\epsilon}$ is the rate of dissipation within a local grid volume. But for homogeneous turbulence

$$\bar{\epsilon} = K\frac{\partial \overline{u_i}}{\partial x_j}\left(\frac{\partial \overline{u_i}}{\partial x_j} + \frac{\partial \overline{u_j}}{\partial x_i}\right) \tag{2.4}$$

Elimination of $\bar{\epsilon}$ between (2.3) and (2.4) gives (2.2). Lilly (1967) showed that if $c \approx 0.17$ then (2.2), (2.3) and (2.4) are compatible with the known value of Kolmogorov's universal constant for the inertial subrange. However, Deardorff found this value to be too large, causing motions to damp until excessively large mean shear built up. He, therefore, used the value $c = 0.10$ which seemed to be an optimum one.

The most distinguishing result of Deardorff's calculations was the discovery that the $\bar{u}$ eddies are more elongated in the downstream direction than the $\bar{v}$ or $\bar{w}$ eddies. The pressure eddies showed no indication of downstream elongation or tilt.

Leonard (1973) studied the energy cascade in large-eddy simulations of turbulent flows. He defined $\eta_{ij} = \overline{u_i' \bar{u}_j} + \overline{\bar{u}_i u_j'} + \overline{u_i' u_j'}$ and $\tau_{ij} = -(\eta_{ij} - \frac{1}{3}\eta_{kk}\delta_{ij})$. So now (2.1) becomes:

$$\frac{\partial \overline{u_i}}{\partial t} + \frac{\partial}{\partial x_j}(\overline{\bar{u}_i \bar{u}_j}) = -\frac{\partial}{\partial x_i}(\bar{p} + \frac{1}{3}\eta_{kk}) + \frac{\partial \tau_{ij}}{\partial x_j} + \frac{1}{\mathrm{Re}}\nabla^2 \overline{u_i}$$

One can now approximate $\overline{\bar{u}_i \bar{u}_j} \approx \overline{u_i}\ \overline{u_j}$ (Lilly , 1967) or lump the difference into the definition of η_{ij} and model τ_{ij} by an eddy viscosity hypothesis:

$\tau_{ij}=K(\frac{\partial \overline{u_i}}{\partial x_j}+\frac{\partial \overline{u_j}}{\partial x_i})$ where K is the same as Deardorff's (1970). Leonard studied the implications of the assumption $\overline{u_i\ u_j}=\overline{u_i}\ \overline{u_j}$. If $\overline{u_k}$ is constant over an averaging volume then one has to deal with a component u_k' which is effectively larger than that obtained when $\overline{u_k}$ is defined as a moving average over the grid volume. In the former case the modelling of the subgrid terms is clearly more critical. Leonard showed that appropriate handling of the term $\partial(\overline{u_i\ u_j})/\partial x_j$ can provide a significant portion of the large-scale dissipation besides the Reynolds stresses of the subgrid scale turbulence. He showed under certain assumptions that the dissipation rate due to $\partial(\overline{u_i\ u_j})/\partial x_j$, ϵ_{RS}, has a lower bound of $\epsilon_{RS}\geq 0.3\epsilon \pm 0.1\epsilon$ where ϵ is the total dissipation rate. The remainder of the losses must be taken up by the SGS term $\partial\tau_{ij}/\partial x_j$. He concluded that the variations of $\partial\overline{u_i}\ \overline{u_j}/\partial x_j$ within an averaging volume should be explicitly accounted for.

Schumann (1975) developed subgrid scale models for finite difference simulations of turbulent flows in plane channels and annuli. His finite difference equations were based on integral conservation equations for each grid volume. As a consequence the SGS stresses were defined as surface mean rather than grid volume mean values of the fluctuating velocity products. Schumann split the SGS stresses into two parts: one accounting for locally isotropic turbulence and the other for inhomogeneous effects. He wrote:

$$^j\overline{u_i'\ u_j'} = -^{ij}\mu(\overline{D_{ij}} - <\overline{D_{ij}}>) - {}^{ij}\mu^* <\overline{D_{ij}}> + \frac{1}{3}\delta_{ij}{}^k\overline{u_k'\ u_k'}$$

where $^j-$ means the average of any quantity over the surface whose unit normal

is in the j — direction. $\overline{D_{ij}}$ is the finite-difference analog of the strain tensor D_{ij}, ${}^{ij}\mu$ and ${}^{ij}\mu^*$ are eddy viscosities and the brackets $< >$ denote the time mean value. The locally isotropic part is set proportional to the fluctuating part of the strain tensor in order to get zero time mean values of the SGS stresses for $i \neq j$. The channel turbulence is inhomogeneous due to the nonzero components of the time mean strain. This is reflected by the inhomogeneous part of the above assumption. Schumann also developed a SGS kinetic energy transport equation which provided the velocity scale in his modelling of ${}^{ij}\mu$. He accounted for the anisotropy of the finite-difference scheme, used larger values for the periodicity lengths (x and z directions) and higher grid resolution (up to 65,536 grid volumes). His results for the mean velocity profile and the turbulent intensities were in better agreement with measurements by Laufer (1950) and Comte-Bellot (1965) than the previous calculations of Deardorff (1970).

Deardorff (1970) and Schumann (1975) were able to predict some of the features of turbulent channel flow with a fair amount of success. However, neither work treated the most important part of the flow, namely the region very near the wall. It is in this region that virtually all the turbulent energy production occurs. Both Deardorff and Schumann introduced artificial boundary conditions at some distance from the wall and, thus, effectively modelled the turbulence production mechanism in this region.

It was not until the joined efforts of Stanford University and the NASA Ames Research Center that the wall region was given its full credit in the LES

calculations of bounded turbulent shear flows. The availability of large and effective computing power (CDC 7600, Illiac IV) was very important for these calculations.

Moin et al (1978) calculated the three-dimensional time-dependent turbulence in a channel using the CDC 7600 computer and $16\times16\times65$ grid points. They employed arguments similar to Deardorff's (1970) for the modelling of the SGS Reynolds stresses. Their numerical scheme was a semi-implicit scheme that treats part of the diffusion terms and pressure implicitly, and the remaining terms explicitly. The time advancing uses the Adams-Bashforth method for the explicit terms and the Crank-Nicolson method for the implicit terms. The lengths of the computational box in the streamwise and spanwise directions were selected to include the important large scale eddies. For this purpose the measurements of Comte-Bellot (1963) were used. Due to storage limitations the mesh sizes were selected as: $\Delta x^+=251$ and $\Delta z^+=168$ which was inadequate for resolving the scales close to the wall, particularly in the spanwise direction. The initial conditions were provided from the governing equations of small disturbances used in hydrodynamic stability theory to obtain a velocity field with negative Reynolds stress. The value for c in equation (2.2) that they selected for the final calculations was $c=0.2$. The numerical results of Moin et al showed reasonable agreement with measurements. For the resolvable portion of the streamwise and spanwise intensities the agreement was good but it was only fair for the intensity of the normal velocity fluctuations. It was found that, especially in the

vicinity of the walls, a large fraction of the vertical turbulent intensity lies in the subgrid scale motions. The mean velocity profile agreed with measurements by Comte-Bellot (1963). A quantity of interest to turbulence modellers is the pressure-velocity gradient interaction. Moin et al's computations showed that over most of the channel the streamwise component of resolvable turbulence intensity transfers energy to the other components. In the vicinity of the wall ($y^+ < 30$) there is a large transfer of energy from the vertical component of turbulence intensity to the spanwise component.

Kim and Moin (1979) carried out a three-dimensional time-dependent calculation of turbulent flow in a channel using the ILLIAC IV computer and $64 \times 64 \times 64$ grid points. Their modelling of the eddy viscosity was similar to Moin et al's (1978). They used a semi-implicit finite difference scheme with implicit time advancement for all the viscous terms. The size of their computational box was the same as in Moin et al (1978) but because of the larger number of grid points the resolution in the streamwise and spanwise directions was better: $\Delta x^+ = 63$, $\Delta z^+ = 42$. Kim and Moin devised numerical tricks in order to efficiently manage the flow of data between the core memory and the disk memory where the entire data base resided. Due to core size limitations they had to develop a special algorithm for the solution of the block tridiagonal matrices resulting from the finite-difference formulation. The numerical results of Kim and Moin revealed most of the structure observed experimentally. They found the wall layer to consist of coherent structures of low-speed and high-speed

streaks alternating in the spanwise direction. Hot-spots, small localized regions of very large values of turbulent shear stress $\overline{uv}$ were frequently observed. No evidence of a direct relationship between streaks and streamwise vorticity ω_x was observed. Very close to the wall ω_x was not the result of large-scale revolving fluid motions but was rather due to the spanwise velocity gradient $\frac{\partial w}{\partial y}$. Though strong vortical regions were observed away from the wall ($y^+ \approx 30$) $(\overline{\omega_x^2})^{1/2}$ attained its maximum value at the wall. Their profiles for the pressure-velocity gradient interaction showed the same effect as calculated by Moin et al (1978); namely, a significant tranfer of energy from the normal to the spanwise component of turbulent kinetic energy in the immediate neighborhood of the wall ("splatting" effect).

Moin and Kim (1981) simulated fully developed turbulent flow in a channel using the ILLIAC IV computer and up to 516,096 grid points. They employed Schumann's (1975) modelling of the eddy viscosity but had to choose a value for ν_T^* (anisotropic eddy viscosity) from numerical experiments. They showed that the so called Leonard stress-term $\lambda_{ij} = \overline{\overline{u_i}\ \overline{u_j}} - \overline{\overline{u_i}}\ \overline{\overline{u_j}}$ can be quite significant, hence including it with τ_{ij} is not recommended. Their agreement of the computed mean velocity profile and turbulence statistics with experimental data was good. The regions of large-amplitude streamwise vorticity ω_x were found to be concentrated near the wall. Slightly above the wall, these regions contained revolving fluid elements induced by strong shear layers in the cross-stream plane. In the immediate neighborhood of the wall the "splatting" effect led to large magnitudes

of ω_z and instigated transfer of energy from the normal to the spanwise component of turbulence.

C. Simple eddy modelling of the viscous wall region

This newly developed approach focuses in the viscous wall region of a turbulent shear flow. The flow field is assumed to be homogeneous in the streamwise direction and the time-dependent Navier-Stokes equations are solved on a plane perpendicular to the mean flow.

Hatziavramidis (1978) was the first one to explore such a non-linear model of the $\lambda^+=100$ wall eddies. He visualized the flow to be coherent for $0 \leq y^+ \leq 40$ and well mixed for $y^+ > 40$. The boundary conditions, that were used at $y_o^+=40$, specified the fluctuating spanwise component of the velocity (w), zero stress ($\frac{\partial w}{\partial y}=0$) and zero intensity for the streamwise component of the velocity ($u'=0$). The period of the spanwise velocity fluctuations at $y_o^+=40$ was taken to be $T^+=100$.

The computed streamline patterns showed the flow field to alternate between strong convective motions (outflows and inflows) and periods of relative quiescence (streamwise vortices associated with low w- and v- velocities). The most interesting finding of the calculations was that the flow on the $y-z$ plane can create streamwise velocity fluctuations whose magnitude agrees with experimental measurements especially in the region $0 \leq y \leq 20$. The calculated mean streamwise velocity profile also agreed with measurements throughout the viscous

wall region. The intensities of the velocity fluctuations on the $y-z$ plane showed fair agreement with experiments. The calculated $(v')^+$ intensity attained higher values in the region $20 \leq y^+ \leq 40$ and the $(w')^+$ intensity exhibited lower values in the region $15 \leq y^+ \leq 35$.

These calculations showed for the first time, that by using simple boundary conditions at $y_o^+ = 40$ one can compute most of the important features of the viscous wall region i.e. momentum transport to and from the wall by the spatial and temporal coupling of inflows and outflows and creation of high intensity velocity fluctuations in the streamwise direction.

Chapman and Kuhn (1981) followed up the work of Hatziavramidis by using more realistic boundary conditions at $y_o^+ = 40$. The visualized the flow in the viscous wall region to result from the interaction of the $\lambda^+ = 100$ eddies with eddies that are associated with a "pulsating" type of flow at $y_o^+ = 40$, on a plane parallel to the wall. Their calculated Reynolds stress and intensity profiles showed better agreement with experiments than the computations of Hatziavramidis, especially in the region $20 \leq y^+ \leq 40$. The calculations of Chapman and Kuhn introduced for the first time the effect of outer flow eddies on the computed wall layer dynamics. However, the modelling of these eddies and the selection of the various model parameters are open to question and need to be improved with the help of more detailed experimental measurements in the viscous wall region.

CHAPTER 3

EXPERIMENTAL METHODS

The experimental results analyzed in this work were obtained by Lau (1980) in a 20 cm flow loop built by Sirkar (1969). Details about its construction and operation can be found in theses by Hogenes (1979) and Lau (1980).

The test section was made from an acrylic pipe, with an internal diameter of 20 cm and a length of 2 m. The fluid probe sensors were manufactured by TSI, Inc. Each pair was separated by a distance of 1 mm and was constructed from elements with a length of 1 mm and a diameter of 0.05 mm. Forty pairs of multiple V-shaped wall electrodes were aligned perpendicular to the mean flow direction. Only nine pairs were used in this work. Single V-shaped probes were located at various positions in the streamwise direction. A drawing of the test section and a schematic diagram of the arrangement of the measuring sensors can be found in Lau (1980).

All outputs from the electrode circuit were adjusted to have values between ± 5 volts. This was necessary because all analog signals were digitalized by an A/D converter having a resolution of only 16 bits. The A/D converter was controlled by an IBM 1800 computer. Before digitalization, the signals were filtered by a fourth order low pass Buttersworth filter with a cut-off frequency of 15 Hz, which corresponds to a dimensionless frequency of $n^+ = 1$. The sampling fre-

quency was 20 Hz and the sampling time 400 seconds. The data were stored in integer form in magnetic discs. Each disc has a capacity of approximately 400,000 words. These raw data were then transferred to magnetic tapes and analyzed in a CDC Cyber computer.

Both the wall and fluid probes were electrodes operated under conditions that the current flowing in the circuit is directly proportional to the rate of mass transfer to the electrodes. The electrolyte used in the experiments was a solution of iodine in potassium iodide with a concentration of 0.1 M KI and 0.001 M I_2. Details regarding these techniques can be found in theses by Lee (1975) and Hogenes (1979).

The mass-transfer rates to the wall were related to s_x and s_z through analytical expressions developed by Sirkar and Hanratty (1970b). Special calibration techniques had to be developed in order to describe the response of the wall electrodes to low flow rates (Nikolaides 1981). The relation of the mass transfer rates to fluid probes to the velocity components U and w was obtained empirically using the following expressions:

$$U=A(V_{1l}+V_{2l}),\quad w=A(V_{1l}-V_{2l}),$$

where A is a constant and V_{1l}, V_{2l} are the linearized voltage outputs from sensors 1 and 2; i.e., $V_{1l}=E_1^{\beta}$, $V_{2l}=E_2^{\beta}$, where E_1, E_2 are the voltage drops across the respective resistors. The calibration runs were carried out at the center of the pipe at different Reynolds numbers. The value of β obtained in this work is in agreement with the one measured by Hogenes (1979). It was found that, in

order to ensure that $\overline{uw} \approx 0$ and $\overline{w^3} \approx 0$, the angle formed by flow direction and the line that bisects the sensor- angle had to be readjusted approximately 2^o.

CHAPTER 4

THEORY

I. Conditional averaging scheme

Kaplan (1973) defines the process of conditional sampling as "the eduction of information about an event with respect to the time reference defined by its detection function." A detailed account of the various sampling techniques in turbulence measurements has been presented by Van Atta (1974). The importance of conditional averaging, as a way of extracting structure out of a turbulent signal, has been widely recognized among turbulence researchers. Several of the schemes that have already been used in studying the coherent structures of wall turbulence were presented in Chapter 2.

The development of an effective detection scheme requires knowledge of the general and specific features of the patterns that are to be conditionally sampled. In the case of the wall region of a bounded turbulent shear flow the situation is quite complicated. The wall structures evolve both in space and time and this has to be accounted for in the sampling procedure. Observations of the instantaneous signatures of the wall eddies, as characterized by the spanwise variation of s_z, show a number of interesting characteristics. There are periods of time that the wall is dominated by eddies that grow in size and wander back and forth in the spanwise direction. There are also time intervals during which nothing

spectacular occurs close to the wall.

Hogenes (1979, 1982) used the idealized sinusoidal variation of s_z shown in Figure 1b to define four distinct eddy patterns related to the midpoint of the wall probe array, MP. For two of them, the s_z profile exhibits a maximum or minimum above MP and, for the remaining two, it shows a zero crossing at MP with either a negative or positive slope.

We have adopted this same classification even though it is an extremely simplified approach to the problem. Since the patterns shift in the spanwise direction and the wavelength varies in time, the above selected eddy patterns represent limiting modes of the spanwise variation of s_z. The selection of the center of the probe array as a reference point for the classification of the eddy patterns is dictated by the fact that the fluid probe is located directly above MP.

In order to measure the strength of the eddy pattern the following function was employed:

$$\hat{S}_{d_k}=\sum_{i=1}^{9} \mid s_{z_i}(t_k) \mid - \mid \sum_{i=1}^{9} s_{z_i}(t_k) \mid ,$$

where i refers to the ith probe, k to the instant t_k in the data set, and s_{z_i} is made dimensionless using $(\overline{s_z^2})^{1/2}$. It is easily seen that $\hat{S}_{d_k} \geq 0$ for all t_k and that $\hat{S}_{d_k}=0$ when all the s_{z_i} are either positive or negative. An ideal eddy pattern similar to the one shown in Figure 1b with an amplitude equal to $(\overline{s_z^2})^{1/2} \approx 0.11$ and a wavelength of $\lambda^+ \approx 100$ would give a value of $\hat{S}_{d_k}$ approximately equal to 4.7.

The function $\hat{S}_{d_k}$ is plotted in Figure 2 for 1,000 data points or 1/8th of the data set. One can easily identify periods of activity associated with the peaks of $\hat{S}_{d_k}$ and periods of relative quiet when $\hat{S}_{d_k}$ decreases towards zero. If a threshold level $\tilde{S}_d$ is applied to $\hat{S}_{d_k}$, then for the time instants t_k that $\hat{S}_{d_k} \approx \tilde{S}_d$ a strong eddy pattern, similar to the one in Figure 1b, occurs over the wall probe array.

In order to be able to identify this eddy pattern with one of the four limiting modes of the s_z profile defined by Hogenes, additional information is needed. For this purpose, the product $P_k = s_{z_4}(t_k) \cdot s_{z_6}(t_k)$ is formed using the signals from probes 4 and 6 that are at equal distances from the middle probe 5 of the wall probe array. When $P_k > 0$, the sign of $s_{z_5}(t_k)$ is checked and, when $P_k < 0$, the difference $D_k = s_{z_4}(t_k) - s_{z_6}(t_k)$ is computed.

The objective of the scheme is to relax the stringent requirements, used in earlier efforts from this laboratory, of having a zero crossing of s_z or a maximum (minimum) exactly at probe 5. Four different aspects of the eddy motion are then recognized at probe 5:

(a) $P_k > 0, s_{z_5}(t_k) > 0$: positive transverse flow (PTF)

(b) $P_k > 0, s_{z_5}(t_k) < 0$: negative transverse flow (NTF)

(c) $P_k < 0, D_k > 0$: outflow

(d) $P_k < 0, D_k < 0$: inflow

For cases (a) and (b) when, also $s_{z_4}(t_k) \cdot s_{z_5}(t_k) < 0$ (or $s_{z_6}(t_k) \cdot s_{z_5}(t_k) < 0$), the smallest resolvable wavelength is detected.

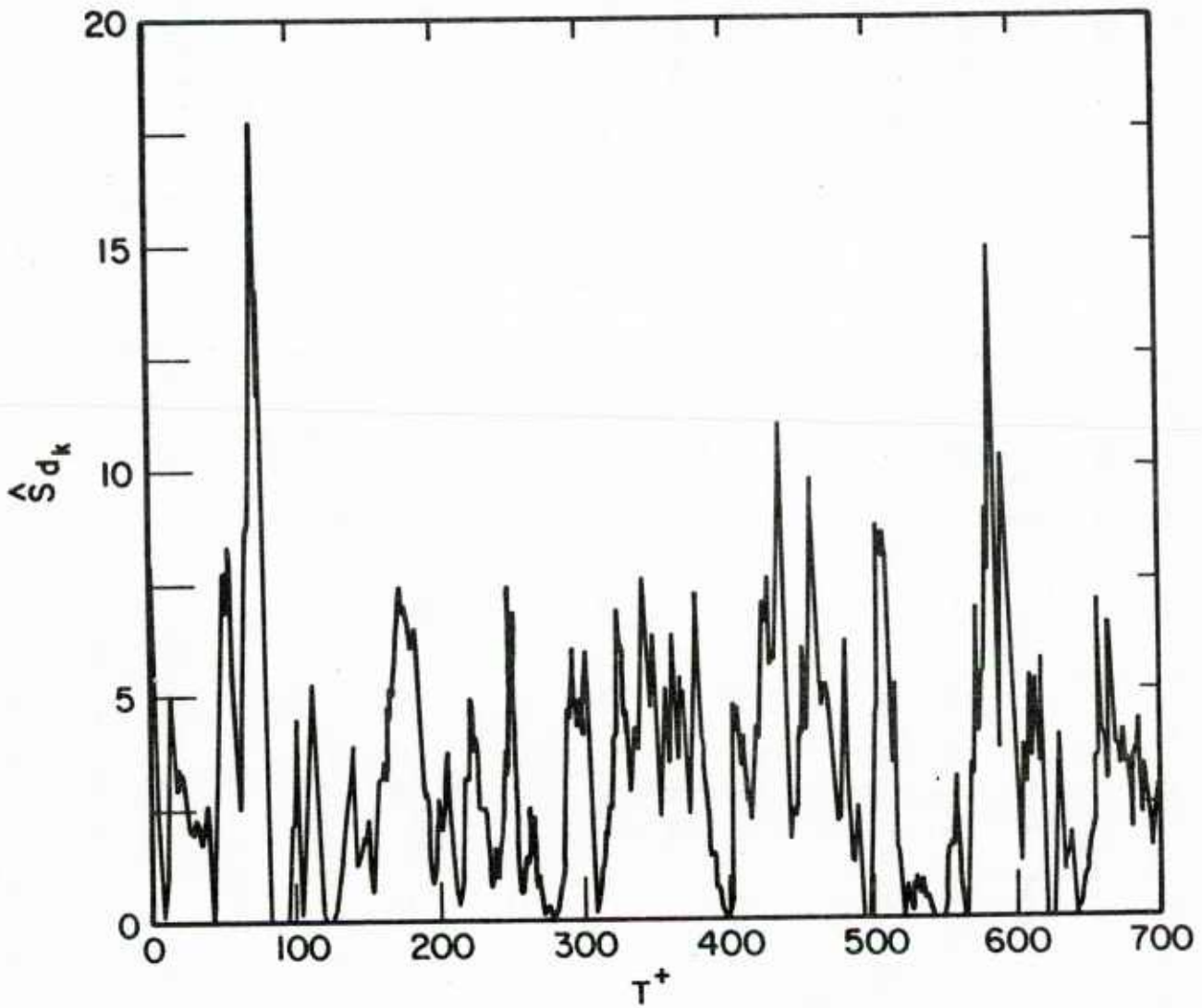

Figure 2 Plot of the detection function $\hat{S}_{d_k}$ vs T^+

It is clear that $\hat{S}_{d_k}$ defines a strong event and (a) through (d) distringuish the type of eddy pattern. The function $\hat{S}_{d_k}$ is similar to the one used by Kovasznay et al (1970) as a turbulence detector. The parameter $\hat{S}_{d_k}$ detects periods of time that the wall is dominated by strong eddy patterns and time intervals that the wall activity subsides. It is to be noted that $\hat{S}_{d_k}$ is not used to define any reference time for the conditional averaging procedure. Time zero for the averaging scheme is defined as the midpoint of the duration time of each pattern.

If, for example, $P_k>0$ and $s_{z_k}(t_k)>0$ for $t_m \leq t_k \leq t_n$ and $\hat{S}_{d_l}>\tilde{S}_d$ for some t_l, where $t_m \leq t_l \leq t_n$ and $\tilde{S}_d$ is a suitable threshold level, then a strong positive transverse flow occurs over the wall probe array and zero time is selected as $t_o=\frac{t_m+t_n}{2}$.

For an idealized eddy pattern $\hat{S}_{d_k}\approx 4.7$, as mentioned before. The average value $\hat{S}_{d_{av}}=\frac{1}{K}\sum_{k=1}^{K}\hat{S}_{d_k}\approx 4$ for all the experimental runs (K is the total number of data points). It seems reasonable to select a threshold level $\tilde{S}_d$ that is close to the above two characteristic values of the detection function $\hat{S}_{d_k}$. The effect of varying $\tilde{S}_d$ will be discussed later.

An example of how the conditional sampling scheme works is shown in Figure 3. It is seen that $P_k<0, D_k<0$ for $4.6<t^+<13.3$ and $P_k>0$, $s_{z_k}<0$ for $13.3<t^+<28$ where $t^+=0$ is some arbitrary time instant. If $\tilde{S}_d=4$, then $\hat{S}_{d_k}>\tilde{S}_d$

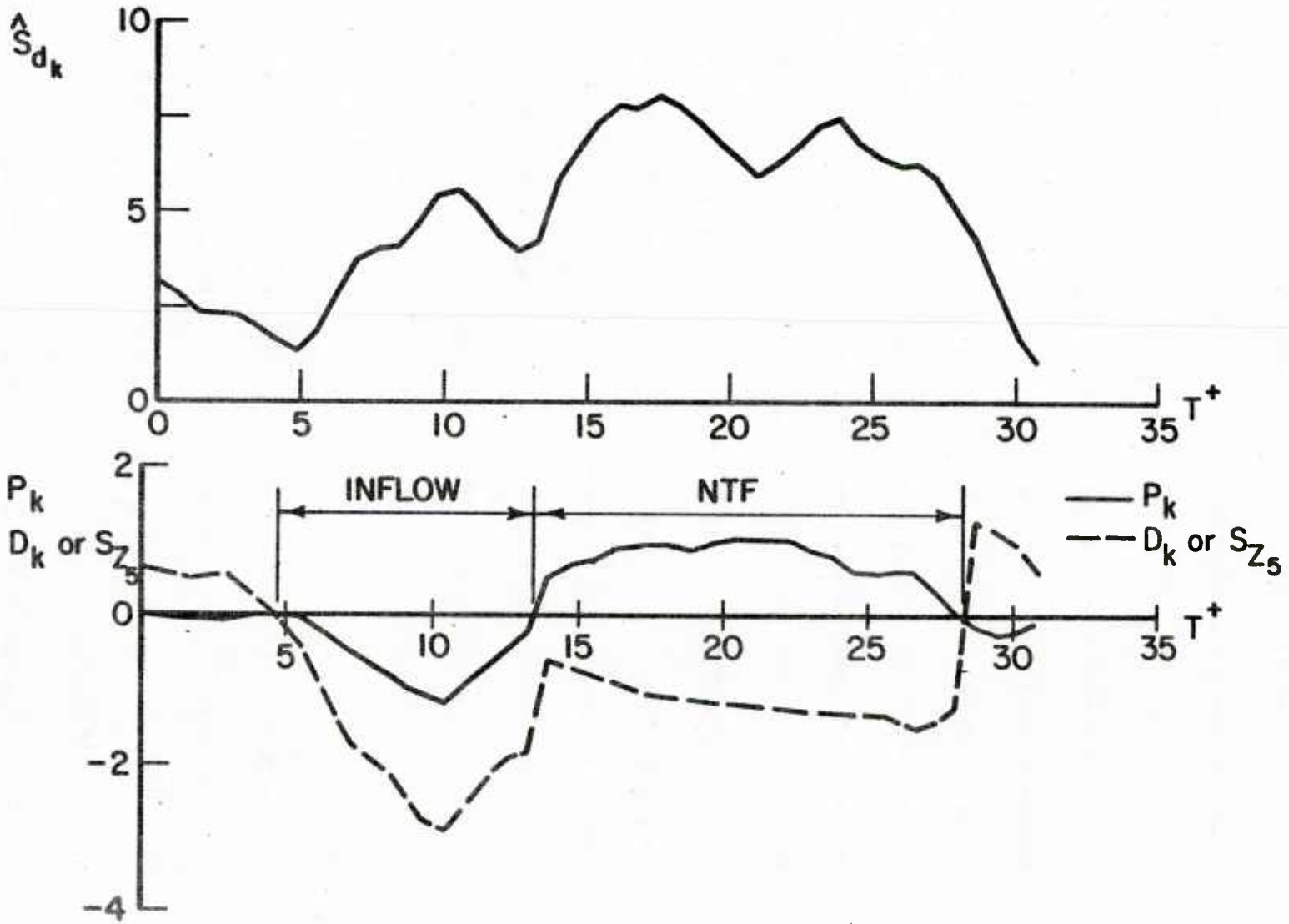

Figure 3 Example of how the detection scheme works.

for $8.5 < t^+ < 28.8$ and the scheme would detect an inflow followed by a negative transverse flow. Time zero for the inflow eddy pattern would be selected as $t_o^+ = 8.95$ and for the NTF pattern, $t_o^+ = 20.65$.

In previous work from this laboratory, Hogenes constructed a scheme to analyze multiple wall probe measurements which is quite different from what is presented above. Detection coefficients that are sensitive to the symmetry or antisymmetry of the eddy patterns, as characterized by the s_z variation, were used to conditionally sample strong eddies at the wall. The time instant that a detection coefficient attained its maximum value was defined as zero time.

The scheme described in the present work is considered to be an improvement over the one used previously by Hogenes for the following reasons: The strength and type of pattern are recognized by two independent processes. The use of conditions (a) through (d) eliminates the effect of the "shifting" of the eddy pattern and defines a reference time based on more than one time instant. The use of one threshold level on $\hat{S}_{d_4}$ gives equal weight to all four types of eddy motion.

Hogenes developed extra detection algorithms to study the temporal succession of the eddy patterns. This is avoided in the present detection scheme. Once the various modes of the s_z signature are isolated in the time axis it is easy to explore their temporal relation.

Some comments are also necessary regarding the number of events included in the conditional averaging procedure. When a positive (or negative) transverse

flow occurs over MP, an outflow takes place at a distance of approximately $\Delta z^+ \approx 25$ from MP. So it is seen that an outflow is associated with three of the four limiting modes of the s_z variation, as discussed above. If an attempt is made to relate outflows to the observed "bursts" (Runstadler et al 1963) one should recognize that not all outflows might eventually evolve into a burst. According to measurements by Kline et al (1967), the frequency of streak breakup per unit of span made dimensionless with wall parameters is approximately equal to 10^{-4} for flows with negligible pressure gradient. For a spanwise length of $\lambda^+ = 100$ the bursting frequency is thus $10^{-4} \cdot 100 \approx 0.01$.

Since the time duration of the experiments described in this study is $T^+ = 5600$ the number of bursts over the wall probe array should be equal to $5600 \times 0.01 = 56$. One would, therefore, expect that the sum of outflows, positive and negative transverse flows detected by the detection algorithm would at least be equal to 56.

These types of considerations provide an independent check on the number of the events selected for the averaging process. They would also help in constructing a technique for measuring the "bursting" frequency.

II. Eddy model for the viscous wall region

A. Continuum equations and boundary conditions

The eddy model in this work assumes that the flow in the viscous wall region is homogeneous in the axial direction and coherent on a plane perpendicu-

lar to the direction of the mean flow. Very close to the wall, where the low-speed dye-streaks have been observed, the eddies are characterized by certain length (λ) and time (T) scales. The characteristic length in the spanwise direction is the distance between dye-streaks ($\lambda^+ \approx 100$) and the characteristic period corresponds to the frequency of the most energetic velocity fluctuations close to the wall ($T^+ \approx 100$). As the distance from the wall increases, eddies with larger length and time scales become more important. These eddies, associated with the flow far away from the wall, interact with the wall eddies and their interaction completely specifies the dynamics of the viscous wall region.

In contrast to the model of Hatziavramidis (1978), where the flow outside the viscous wall region is assumed to be well-mixed, the present model attempts to define the interaction of the outer flow with the wall layer at a certain distance from the wall ($y_o^+ \approx 40$). The specification of this interaction, which results in the creation and maintenance of wall turbulence, is the most important part of the calculations is this work.

The continuum equations that describe the flow field are the time-dependent Navier-Stokes equations, for a flow homogeneous in the axial direction, along with the equation that describes conservation of mass (continuity equation):

$$\frac{\partial v}{\partial t} + \frac{\partial}{\partial y}(v^2/2) + \frac{\partial}{\partial z}(vw) = -\frac{\partial p}{\partial y} + \frac{1}{\mathrm{Re}}\left(\frac{\partial^2 v}{\partial y^2} + \frac{\partial^2 v}{\partial z^2}\right) \qquad (4.1)$$

$$\frac{\partial w}{\partial t} + \frac{\partial}{\partial y}(vw) + \frac{\partial}{\partial z}(w^2/2) = -\frac{\partial p}{\partial z} + \frac{1}{\mathrm{Re}}\left(\frac{\partial^2 w}{\partial y^2} + \frac{\partial^2 w}{\partial z^2}\right) \tag{4.2}$$

$$\frac{\partial U}{\partial t} + \frac{\partial}{\partial y}(vU) + \frac{\partial}{\partial z}(wU) = \frac{1}{\mathrm{Re}}\left(\frac{\partial^2 U}{\partial y^2} + \frac{\partial^2 U}{\partial z^2}\right) \tag{4.3}$$

$$\frac{\partial w}{\partial z} + \frac{\partial v}{\partial y} = 0 \tag{4.4}$$

All the variables above and in the rest of the work are dimensionless with respect to a characteristic length λ and a characteristic velocity U_c. These are selected so that $\lambda^+ = 100$ and $U_c^+ = 2(v')^+$ where $(v')^+$ is the rms value of the normal velocity fluctuations at $y = y_o$ expressed in wall variables. With these values, the Reynolds number is $\mathrm{Re} = \dfrac{U_c \cdot \lambda}{\nu} = U_c^+ \lambda^+ = 182$.

The boundary conditions that were used to solve the above system of equations are the following:

$$U = v = w = 0 \quad \text{(no slip condition)} \quad \text{at} \quad y = 0$$

$$w = 0, \quad \frac{\partial v}{\partial z} = 0, \quad \frac{\partial U}{\partial z} = 0 \quad \text{(symmetry conditions)} \quad \text{at} \quad \begin{cases} z = 0 \\ z = z_o \end{cases}$$

where $z_o = \lambda_2/2$ and λ_2 is the (dimensionless) wavelength of the outer flow eddies.

At the upper boundary of the computational domain ($y = y_o$) the following boundary conditions were prescribed:

$$w = w_{L1}(t)\sin\frac{2\pi z}{\lambda_{w_1}} + w_{L2}(t)\sin\frac{2\pi z}{\lambda_{w_2}} \tag{4.5}$$

$$v = v_{L1}(t)\cos\frac{2\pi z}{\lambda_{v_1}} + v_{L2}(t)\cos\frac{2\pi z}{\lambda_{v_2}} \tag{4.6}$$

$$u = u_{L1}(t)\cos\frac{2\pi z}{\lambda_{u_1}} + u_{L2}(t)\cos\frac{2\pi z}{\lambda_{u_2}} \tag{4.7}$$

and $U = \overline{U}(y_o) + u$, where u,v,w are the fluctuating components of the velocity at $y = y_o$ that are associated with the coherent flow and $\overline{U}(y_o)$ is the average streamwise velocity at the same location. The components with scales λ_{u_1}, λ_{v_1}, λ_{w_1} are associated with the $\lambda^+ \approx 100$ eddies, while the components with scales λ_{u_2}, λ_{v_2}, λ_{w_2} reflect the contribution of the outer flow eddies in the viscous wall region dynamics. The specification of the temporal part of u,v and w at $y = y_o$ and the selection of the relevant scales and the relative energies are discussed in part C of this section.

If the pressure gradient is elimated from (4.1) and (4.2) the following vorticity-stream function formulation of the problem is obtained:

$$\frac{\partial \varsigma}{\partial t} + \frac{\partial}{\partial z}(w\varsigma) + \frac{\partial}{\partial y}(v\varsigma) = \frac{1}{\mathrm{Re}}\left(\frac{\partial^2 \varsigma}{\partial z^2} + \frac{\partial^2 \varsigma}{\partial y^2}\right) \tag{4.8}$$

$$\nabla^2 \Psi = \varsigma \tag{4.9}$$

where $\varsigma = \frac{\partial w}{\partial y} - \frac{\partial v}{\partial z}$ and $w = \frac{\partial \Psi}{\partial y}$, $v = -\frac{\partial \Psi}{\partial z}$.

The advantage of the above (Ψ, ς) formulation as opposed to the primitive variable formulation (v,w,p) is that the pressure is eliminated from the problem. The system (4.8) and (4.9) can be solved for Ψ and ς and the velocites v,w can subsequently be obtained from the stream function. Another advantage of the (Ψ, ς) formulation is that the continuity equation (4.4) is satisfied by definition.

The implementation of the boundary conditions, however, is a more difficult task in the vorticity-stream function formulation. The way that the boundary conditions are translated from the (v,w,p) to the (Ψ, ς) formulation is as follows:

$$\Psi=0,\ \varsigma=\frac{\partial^2\Psi}{\partial y^2} \quad \text{at} \quad y=0$$

$$\Psi=0,\ \varsigma=0 \quad \text{at} \quad \begin{cases} z=0 \\ z=z_o \end{cases}$$

$$\Psi=-\int_o^z v(\xi,\ y_o,\ t)\,d\xi,\ \varsigma=\frac{\partial^2\Psi}{\partial y^2}-\frac{\partial v}{\partial z} \quad \text{at} \quad y=y_o$$

where ξ is a dummy variable.

It can be seen from (4.8) and (4.9) that the vorticity equation and the stream-function equation are coupled through the convective terms, which is a manifestation of the nonlinear character of the Navier-Stokes equations. It can also be seen from the boundary conditions that there is an extra coupling through the boundary vorticity, which is inherent in the vorticity-stream function formulation and would be absent if a primitive variable (v,w,p) formulation were used instead.

Once the velocities v and w are known, from the solution of (4.8) and (4.9), the streamwise velocity U can be obtained from the solution of equation (4.3) which is a linear partial-differential equation.

The initial conditions for the system (4.1), (4.2) and (4.4) were supplied by the inviscid-irrotational solution on the y–z plane. The initial profile for the

streamwise velocity component (equation (4.3)) was taken to be the Van-Driest profile for the time-averaged axial velocity in the viscous wall region (Hinze, 1975) $0 \leq y^+ \leq 40$.

The set of boundary conditions described above correspond to the case where the outer flow eddies have statistically definable length and time scales and finite energy. The case where all the energy of the velocity fluctuations in the viscous wall region is associated with the $\lambda^+ \approx 100$ eddies was also investigated. The results for these two cases are presented in Chapter 5. These calculations, where the nodes of the spanwise variation of the velocity components at $y=y_o$ are fixed in space, are referred to as "fixed cell runs".

Two other cases were studied during the course of this work. One is a pulsating type of flow on a plane parallel to the wall at $y=y_o$, that is associated with the outer flow eddies. The other one is a random shifting of the $\lambda^+ \approx 100$ eddies, with negligible energy attributed to the large scale eddies. In both cases, the nodes of the spanwise variation of the velocity components at $y=y_o$ are not fixed but vary in time. These calculations are referred to as "moving cell runs" and are presented in Appendices B and C.

Various boundary conditions, different from the ones described above, were also explored for the $\lambda^+ \approx 100$ eddies. These boundary conditions attempted to use a nondescript relation for the normal component of the velocity at $y=y_o$, by prescribing the vorticity or the flux of the vorticity along with the spanwise component of the velocity at the upper boundary of the computational domain. The

results of these calculations are discussed in Chapter 5.

B. Numerical methods

Two numerical schemes were used in this work for the time advancement of the vorticity equation. That used in the fixed cell runs was the Alternating Direction Implicit scheme, which is currently the most popular method for the solution of viscous fluid flow problems. The moving cell runs necessitated the development of a semi-implicit finite-difference scheme which is implicit in the viscous terms and explicit in the convective terms. The development of this method was also motivated by the desire to study the propagation of high frequencies in the secondary flow pattern, from the edge of the viscous wall region towards the wall, during the fixed cell runs.

1. ADI-scheme

A spatial and temporal discretization of (4.8) and (4.9) results in the following finite difference approximation for the vorticity-stream function formulation:

$$\frac{\varsigma_{ij}^{n+1/2}-\varsigma_{ij}^{n}}{(\Delta t/2)} = -\frac{(w\varsigma)_{i+1,j}^{n+1/2}-(w\varsigma)_{i-1,j}^{n+1/2}}{2\Delta z} - \frac{(v\varsigma)_{i,j+1}^{n}-(v\varsigma)_{i,j-1}^{n}}{2\Delta y} + \frac{1}{\mathrm{Re}}\left\{\frac{\varsigma_{i+1,j}^{n+1/2}-2\varsigma_{ij}^{n+1/2}+\varsigma_{i-1,j}^{n+1/2}}{\Delta z^2}+\frac{\varsigma_{i,j+1}^{n}-2\varsigma_{ij}^{n}+\varsigma_{i,j-1}^{n}}{\Delta y^2}\right\} \quad (4.10)$$

$$\frac{\varsigma_{ij}^{n+1}-\varsigma_{ij}^{n+1/2}}{(\Delta t/2)} = -\frac{(w\varsigma)_{i+1,j}^{n+1/2}-(w\varsigma)_{i-1,j}^{n+1/2}}{2\Delta z} - \frac{(v\varsigma)_{i,j+1}^{n+1}-(v\varsigma)_{i,j-1}^{n+1}}{2\Delta y} + \frac{1}{\mathrm{Re}}\left\{\frac{\varsigma_{i+1,j}^{n+1/2}-2\varsigma_{ij}^{n+1/2}+\varsigma_{i-1,j}^{n+1/2}}{\Delta z^2}+\frac{\varsigma_{i,j+1}^{n+1}-2\varsigma_{ij}^{n+1}+\varsigma_{i,j-1}^{n+1}}{\Delta y^2}\right\} \quad (4.11)$$

and

$$\frac{\Psi_{i+1,j}^{n+1} - 2\Psi_{ij}^{n+1} + \Psi_{i-1,j}^{n+1}}{\Delta z^2} + \frac{\Psi_{i,j+1}^{n+1} - 2\Psi_{ij}^{n+1} + \Psi_{i,j-1}^{n+1}}{\Delta y^2} = \varsigma_{ij}^{n+1} \quad (4.12)$$

Equation (4.10) can be solved for $\varsigma_{ij}^{n+1/2}$ and subsequently ς_{ij}^{n+1} can be obtained from (4.11). Then (4.12) can be inverted to give Ψ_{ij}^{n+1}. In order to solve equations (4.10) and (4.11), though, we need the values for the velocities $w_{i,j}^{n+1/2}$, $v_{i,j}^{n+1}$ and the values for the boundary vorticities $\varsigma_{1,j}^{n+1/2}$, $\varsigma_{M+1,j}^{n+1/2}$ and $\varsigma_{i,1}^{n+1}$,$\varsigma_{i,N+1}^{n+1}$, where M and N are the number of panels in which the computational domain is divided in the z and y directions respectively. It appears then that for the solution of the system of equations (4.10), (4.11), (4.12) an iterative scheme is required. According to this iterative procedure, the values for v,w and for the boundary vorticity would have to be guessed and then equations (4.10) and (4.11) would be solved for ς_{ij}^{n+1}. The stream function Ψ_{ij}^{n+1} could thus be obtained by solving (4.12) using the calculated values of ς_{ij}^{n+1}. The guessed values of v,w and the boundary vorticity can then be revised using the calculated values of Ψ_{ij}^{n+1} and the whole procedure is repeated until the values of Ψ_{ij}^{n+1} (or ς_{ij}^{n+1}) don't change between two successive iterations.

It has to be noted that the above procedure takes place within a given time step. In other words it takes a certain number of iterations to advance from time step n to time step $n+1$. This is important in unsteady state computations where the value of Ψ and ς at a given time t have to be accurately calculated.

The iteration pattern used in this work is described in what follows: It is noted that in the fixed cell runs the vorticity on the vertical boundaries is zero at

all times. So it is only the vorticity on the horizontal boundaries and the velocities v and w that have to be guessed during the iterative procedure. If the subscripts w and o denote the wall and the upper boundary of the computational domain, then the velocities v,w and the boundary vorticity are calculated as follows for each iteration:

$$(v^n)^{k+1} = -\frac{\partial \overline{\Psi}^{k+1}}{\partial z},\ (w^{n+1/2})^{k+1} = \frac{\partial \overline{\Psi}^{k+1}}{\partial y}$$

$$\text{and}\quad (v^{n+1})^{k+1} = -\frac{\partial \overline{\Psi}^{k+1}}{\partial z} \tag{4.13}$$

where $\overline{\Psi}^{k+1}$ is taken to be the arithmetic average of Ψ^n and the k-th iterate of Ψ^{n+1}: $\overline{\Psi}^{k+1}=1/2[\Psi^n+(\Psi^{n+1})^k]$ and:

$$(\varsigma_w^{n+1})^{k+1}=r(\varsigma_w^{n+1})^k+(1-r)(\nabla^2\Psi^{n+1})_w^k \tag{4.14}$$

$$(\varsigma_o^{n+1})^{k+1}=r(\varsigma_o^{n+1})^k+(1-r)(\nabla^2\Psi^{n+1})_o^k \tag{4.15}$$

It is to be noted that equations (4.13) are one of a number of possible alternatives for the approximation of v,w through the iteration procedure, as cited in Roache (1982). Peaceman and Rachford (1955) in their original formulation used $\overline{\Psi}^{k+1}=\frac{3}{4}\Psi^n+\frac{1}{4}(\Psi^{n+1})^k$ at the half-time step and $\overline{\Psi}^{k+1}=\frac{1}{4}\Psi^n+\frac{3}{4}(\Psi^{n+1})^k$ at the full-time step. Another alternative is to approximate the velocities as follows: $(v^n)^{k+1} = -\frac{\partial \Psi^n}{\partial z},\ (w^{n+1/2})^{k+1} = \frac{\partial \overline{\Psi}^{k+1}}{\partial y}$ and $(v^{n+1})^{k+1} = -\frac{\partial (\Psi^{n+1})^k}{\partial z}$ where $\overline{\Psi}^{k+1}$ is again given by: $\overline{\Psi}^{k+1} = \frac{1}{2}[\Psi^n+(\Psi^{n+1})^k]$. All the three aforementioned alternatives were investigated during the course of this work and it was found by numerical experiments that they don't influence the calculations. For the results

presented in this work the relations (4.13) were used.

The form of iteration (4.14) and (4.15) on the boundary vorticity has been suggested by Israeli (1970, 1972) and by Dorodnitsyn and Meller (1968). The relaxation constant r is introduced in order to smooth out any instabilities that could result from a poor guess of the boundary vorticity. In general r can be different at the two boundaries and can also change with the spanwise coordinate and from iteration to iteration. In this study r was chosen to be constant and the same for the two boundaries. Its optimum values were found to depend on the kind of boundary condition at $y=y_o$, on y_o and on the wavelength λ in the spanwise direction. These values were determined from numerical experiments and were subsequently used throughout the computational runs. When v and w were specified at $y=y_o$ then, for the range of wavelengths investigated, r was found to depend on y_o^+ according to the following table:

Table 1

y_o^+	r
40	0.35
20	0.65
15	0.73

The finite-difference approximation to (4.15) is obtained as follows:

$$(\nabla^2\Psi^{n+1})_o^k = \left(\frac{\partial^2\Psi^{n+1}}{\partial z^2} + \frac{\partial^2\Psi^{n+1}}{\partial y^2}\right)_o^k = \frac{\partial^2\Psi^{n+1}}{\partial y^2}\Big|_o^k - \frac{\partial v}{\partial z}\Big|_o^{n+1} \quad (4.16)$$

where $\frac{\partial v}{\partial z}\Big|_o^{n+1}$ is known and is obtained by differentiating the specified v

condition at $y=y_o$ with respect to z. The term $\frac{\partial^2\Psi^{n+1}}{\partial y^2} \mid_o^k$ is calculated at $y=y_o$ for the k-th iteration as follows: From a Taylor-series expansion at $y=y_o$ we get

$$\Psi_{i,N}^{n+1} = \Psi_{i,N+1}^{n+1} - \Delta y \frac{\partial \Psi^{n+1}}{\partial y} \mid_{i,N+1} + \frac{\Delta y^2}{2} \frac{\partial^2 \Psi^{n+1}}{\partial y^2} \mid_{i,N+1} + O(\Delta y^3),$$

where now o is replaced by $i,N+1$. By rearrangement we get:

$$\frac{\partial^2\Psi^{n+1}}{\partial y^2} \mid_{i,N+1}^k = 2\frac{(\Psi_{i,N}^{n+1})^k - (\Psi_{i,N+1}^{n+1})^k}{\Delta y^2} + 2\frac{w_{i,N+1}^{n+1}}{\Delta y} + O(\Delta y).$$

So (4.16) now becomes

$$(\nabla^2\Psi^{n+1})_o^k = 2\left[\frac{(\Psi_{i,N}^{n+1})^k - \Psi_o^{n+1}}{\Delta y^2} + \frac{w_o^{n+1}}{\Delta y}\right] - \frac{\partial v}{\partial z} \mid_o^{n+1} + O(\Delta y) \quad (4.17)$$

The finite-difference approximation to (4.14) is similarly obtained :

$$(\nabla^2\Psi^{n+1})_w^k = \frac{\partial^2\Psi^{n+1}}{\partial y^2} \mid_{i,1}^k \quad (4.18)$$

where w is now replaced by $i,1$.

From a Taylor-series expansion at $y=0$ we get

$$\Psi_{i,2}^{n+1} = \Psi_{i,1}^{n+1} + \Delta y \frac{\partial \Psi^{n+1}}{\partial y} \mid_{i,1} + \frac{\Delta y^2}{2} \frac{\partial^2 \Psi^{n+1}}{\partial y^2} \mid_{i,1} + \frac{\Delta y^3}{6} \frac{\partial^3 \Psi^{n+1}}{\partial y^3} \mid_{i,1} + O(\Delta y^4)$$

$$\Psi_{i,3}^{n+1} = \Psi_{i,1}^{n+1} + 2\Delta y \frac{\partial \Psi^{n+1}}{\partial y} \mid_{i,1} + \frac{4\Delta y^2}{2} \frac{\partial^2 \Psi^{n+1}}{\partial y^2} \mid_{i,1} + \frac{8\Delta y^3}{6} \frac{\partial^3 \Psi^{n+1}}{\partial y^3} \mid_{i,1} + O(\Delta y^4)$$

Eliminating $\frac{\partial^3\Psi^{n+1}}{\partial y^3} \mid_{i,1}$ results in

$$\Psi_{i,3}^{n+1} - 8\Psi_{i,2}^{n+1} = -7\Psi_{i,1}^{n+1} - 6\Delta y \frac{\partial \Psi^{n+1}}{\partial y} \mid_{i,1} - 2\Delta y^2 \frac{\partial^2 \Psi^{n+1}}{\partial y^2} \mid_{i,1} + O(\Delta y^4)$$

or

$$\frac{\partial^2 \Psi^{n+1}}{\partial y^2} \mid_{i,1}^{k} = \frac{-7\Psi_{i,1}^{n+1} + 8(\Psi_{i,2}^{n+1})^k - (\Psi_{i,3}^{n+1})^k}{2\Delta y^2} - \frac{3}{\Delta y} \frac{\partial \Psi^{n+1}}{\partial y} \mid_{i,1} + O(\Delta y^2)$$

Since $\Psi_{i,1}^{n+1} = \frac{\partial \Psi^{n+1}}{\partial y} \mid_{i,1} = 0$, equation (4.18) becomes

$$(\nabla^2 \Psi^{n+1})_w^k = \frac{8(\Psi_{i,2}^{n+1})^k - (\Psi_{i,3}^{n+1})^k}{2\Delta y^2} + O(\Delta y^2) \tag{4.19}$$

Using (4.17) and (4.19), equations (4.14) and (4.15) become:

$$(\varsigma_w^{n+1})^{k+1} = r(\varsigma_w^{n+1})^k + (1-r)\frac{8(\Psi_{i,2}^{n+1})^k - (\Psi_{i,3}^{n+1})^k}{2\Delta y^2} \tag{4.20}$$

$$(\varsigma_o^{n+1})^{k+1} = r(\varsigma_o^{n+1})^k +$$

$$(1-r)\left\{2\left[\frac{(\Psi_{i,N}^{n+1})^k - \Psi_o^{n+1}}{\Delta y^2} + \frac{w_o^{n+1}}{\Delta y}\right] - \frac{\partial v}{\partial z} \mid_o^{n+1}\right\} \tag{4.21}$$

where it is to be noted that the superscript k is absent from the terms Ψ_o^{n+1}, w_o^{n+1} and $\frac{\partial v}{\partial z} \mid_o^{n+1}$ since these terms don't change during the iteration procedure, being known for the time step $n+1$.

Equations (4.20), (4.21), and (4.13) are iterated along with (4.10), (4.11) and (4.12) until $\max_{i,j} \mid (\Psi_{ij}^{n+1})^{k+1} - (\Psi_{ij}^{n+1})^k \mid \leq \epsilon$, where ϵ is a prescribed tolerance. A tolerance of $\epsilon = 10^{-10}$ was used for all the runs described in this thesis. This value was found from trial runs to be adequate for the convergence of the boundary vorticity. Once convergence is attained, the same iteration procedure is repeated for the next time step. As it was mentioned before, since a steady-state solution is not sought, it is essential to make sure that we achieve

the desired convergence for a given time step.

Equations (4.10) and (4.11) are solved by inverting tridiagonal matrices. These matrices result from a rearrangement of (4.10) and (4.11) as follows:

Half-time step

$$A_i \varsigma_{i-1,j}^{n+1/2} + B_i \varsigma_{ij}^{n+1/2} + C_i \varsigma_{i+1,j}^{n+1/2} = D_i, \quad 2 \le i \le M$$

where:

$$A_i = \frac{\Delta z}{\Delta y}(\Psi_{i-1,j+1} - \Psi_{i-1,j-1}) + \frac{4}{\mathrm{Re}}$$

$$B_i = -8\left(\frac{1}{\mathrm{Re}} + \frac{\Delta z^2}{\Delta t}\right)$$

$$C_i = -\frac{\Delta z}{\Delta y}(\Psi_{i+1,j+1} - \Psi_{i+1,j-1}) + \frac{4}{\mathrm{Re}}$$

$$D_i = \left[\frac{\Delta z}{\Delta y}(\Psi_{i+1,j-1} - \Psi_{i-1,j-1}) - \frac{4}{\mathrm{Re}}\frac{\Delta z^2}{\Delta y^2}\right]\varsigma_{i,j-1}^{n} +$$

$$8\left(\frac{1}{\mathrm{Re}}\frac{\Delta z^2}{\Delta y^2} - \frac{\Delta z^2}{\Delta t}\right)\varsigma_{ij}^{n} - \left[\frac{\Delta z}{\Delta y}(\Psi_{i+1,j+1} - \Psi_{i-1,j+1}) + \frac{4}{\mathrm{Re}}\frac{\Delta z^2}{\Delta y^2}\right]\varsigma_{i,j+1}^{n}$$

or in matrix form

$$\begin{bmatrix} B_2 & C_2 & & & & \\ A_3 & B_3 & C_3 & & 0 & \\ & \ddots & \ddots & \ddots & & \\ & & & \ddots & & \\ 0 & & & A_{M-1} & B_{M-1} & C_{M-1} \\ & & & & A_M & B_M \end{bmatrix} \begin{bmatrix} \varsigma_{2,j} \\ \varsigma_{3,j} \\ \vdots \\ \varsigma_{M-1,j} \\ \varsigma_{M,j} \end{bmatrix} = \begin{bmatrix} D_2 - A_2\varsigma_{1,j}^{n+1/2} \\ D_3 \\ \vdots \\ D_{M-1} \\ D_M - C_M\varsigma_{M+1,j}^{n+1/2} \end{bmatrix}$$

Full-time step

$$A_j' \zeta_{i,j-1}^{n+1} + B_j' \zeta_{ij}^{n+1} + C_j' \zeta_{i,j+1}^{n+1} = D_j, \quad 2 \leq j \leq N$$

where :

$$A_j' = -\frac{\Delta z}{\Delta y}(\Psi_{i+1,j-1} - \Psi_{i-1,j-1}) + \frac{4}{\mathrm{Re}}\frac{\Delta z^2}{\Delta y^2}$$

$$B_j' = -8\left(\frac{1}{\mathrm{Re}}\frac{\Delta z^2}{\Delta y^2} + \frac{\Delta z^2}{\Delta t}\right)$$

$$C_j' = \frac{\Delta z}{\Delta y}(\Psi_{i+1,j+1} - \Psi_{i-1,j+1}) + \frac{4}{\mathrm{Re}}\frac{\Delta z^2}{\Delta y^2}$$

$$D_j' = -\left[\frac{\Delta z}{\Delta y}(\Psi_{i-1,j+1} - \Psi_{i-1,j-1}) + \frac{4}{\mathrm{Re}}\right]\zeta_{i-1,j}^{n+1/2} + 8\left(\frac{1}{\mathrm{Re}} - \frac{\Delta z^2}{\Delta t}\right)\zeta_{ij}^{n+1/2} +$$

$$\left[\frac{\Delta z}{\Delta z}(\Psi_{i+1,j+1} - \Psi_{i+1,j-1}) - \frac{4}{\mathrm{Re}}\right]\zeta_{i+1,j}^{n+1/2}$$

or in matrix form

$$\begin{bmatrix} B_2' & C_2' & & & & \\ A_3' & B_3' & C_3' & 0 & & \\ & \cdot & & & & \\ & & \cdot & & & \\ & & & \cdot & \cdot & \\ 0 & & A_{N-1}' & B_{N-1}' & C_{N-1}' & \\ & & & A_N' & B_N' & \end{bmatrix} \begin{bmatrix} \zeta_{i,2} \\ \zeta_{i,3} \\ \cdot \\ \cdot \\ \cdot \\ \zeta_{i,N-1} \\ \zeta_{i,N} \end{bmatrix} = \begin{bmatrix} D_2' - A_2' \zeta_{i,1}^{n+1} \\ D_3' \\ \cdot \\ \cdot \\ \cdot \\ D_{N-1}' \\ D_N' - C_N' \zeta_{i,N+1}^{n+1} \end{bmatrix}$$

It can be seen therefore that one iteration of the vorticity equation involves the solution of $(M-1)+(N-1)=M+N-2$ tridiagonal matrices where $M-1$ and $N-1$ are the number of interior points in the z and y directions respectively. The inversion of the tridiagonal matrices was implemented by the use of the subroutine LEQT1B from the IMSL package.

The values of Ψ_{ij}^{n+1} at the completion of each iteration, which are needed for the revision of the guessed velocities and boundary vorticities according to (4.20), (4.21) and (4.13), are obtained by inverting the Poisson equation (4.12). This was achieved by the use of the subroutine HWSCRT from the FISHPAK package developed at the National Center for Atmospheric Research in Colorado. This subroutine is a direct Poisson-solver and uses a cyclic-reduction scheme in order to invert the resulting block-tridiagonal matrix (Sweet, 1977).

In summary, then, the computational labor at a given time step and for k iterations involves the inversion of $k(M+N-2)$ tridiagonal matrices and the inversion of k Poisson equations.

The main advantage of the ADI-scheme is its unconditional stability with respect to the selection of the time step. It has to be pointed out though that a very long time step would result in an increased number of iterations and a loss of accuracy.

2. Semi-implicit scheme

As mentioned earlier in this chapter a semi-implicit scheme was developed in order to study the propagation of high frequencies in the viscous wall region for the fixed cell runs. The reason for developing a semi-implicit scheme is the desire to have a finite-difference approximation that preserves the speed of signal propagation in the continuum equation. For a pure convective motion as, for example, one characterized by the equation $\frac{\partial A}{\partial t} + U\frac{\partial A}{\partial x}=0$, a disturbance in

the scalar quantity A travels in the x-direction with a finite speed U. For pure viscous action as for example in $\frac{\partial A}{\partial t} = \alpha \frac{\partial^2 A}{\partial x^2}$ a disturbance in A propagates in the x-direction with infinite speed.

The ADI-scheme, being a fully implicit scheme, calculates all the velocities at a given time step simultaneously throughout the computational domain. This implies that a certain disturbance at the boundary affects all the calculated velocities at the same time. This is in agreement with the infinite speed of signal propagation for a purely viscous motion but contradicts the fact that a convective motion travels with finite speed in a continuum. According to the latter only the velocities that are in the neighborhood of the boundary should be affected by the disturbance within a given time step. From the above it is thus seen that a correct finite-difference approximation to the convective terms in the equation of motion would require an explicit formulation.

The semi-implicit scheme developed was used for the fixed cell runs when the boundary disturbances contained a wide-spectrum of frequencies. It was found that the results did not differ from the ones obtained with the ADI-scheme. All the fixed cell runs then were carried out with the ADI-scheme because of the freedom in selecting the time step.

The semi-implicit scheme was found to be necessary for the moving cell runs because the resulting numerical algorithms are simpler than those resulting from the ADI-scheme. In the case of periodic b.c's the use of the ADI-scheme

results in non-tridiagonal matrices for the inversion of which special splitting techniques would be required. Due to the unavailability, during the present work, of numerical codes that can effectively invert such matrices, all the moving cell runs were carried out using the semi-implicit scheme described below.

The time advancement of the vorticity equation is carried out by the use of the Adams-Bashforth formula for the convective terms and the Crank-Nicolson scheme for the viscous terms. Both are second-order schemes and the Adams-Bashforth method is both stable and accurate according to Lilly (1965). A similar semi-implicit scheme has been used by Kim and Moin (1979) and by Moin et al (1978) in their large-eddy simulations of incompressible turbulent channel flow.

The resulting finite difference approximation of the vorticity equation is:

$$\frac{\zeta^{n+1}-\zeta^{n}}{\Delta t} = -\left(\frac{3}{2}H^{n} - \frac{1}{2}H^{n-1}\right) + \frac{1}{2\mathrm{Re}}\left(\nabla^2\zeta^{n+1} + \nabla^2\zeta^{n}\right) + O(\Delta t^2) \quad (4.22)$$

where $H = \frac{\partial}{\partial z}(w\zeta) + \frac{\partial}{\partial y}(v\zeta)$. Rearrangement of (4.22) results in

$$\nabla^2\zeta^{n+1} - \frac{2\mathrm{Re}}{\Delta t}\zeta^{n+1} = \mathrm{Re}(3H^{n} - H^{n-1}) - \frac{2\mathrm{Re}}{\Delta t}\zeta^{n} - \nabla^2\zeta^{n}$$

$$\text{or} \quad \nabla^2\zeta^{n+1} - \frac{2\mathrm{Re}}{\Delta t}\zeta^{n+1} = Q \quad (4.23)$$

where $Q = \mathrm{Re}(3H^{n} - H^{n-1}) - \frac{2\mathrm{Re}}{\Delta t}\zeta^{n} - \nabla^2\zeta^{n}$ depends on time steps n and $n-1$. Equation (4.23) is a Helmholtz-equation and when discretized in space requires the inversion of a block tridiagonal matrix (Sweet 1977). As in the ADI-scheme the boundary vorticity is not known a-priori and has to be iterated. Since the convective terms are expressed in an explicit form the velocities don't need to be

iterated but one has to store both H^n and H^{n-1} in order to calculate the source term in (4.23).

The iteration pattern used with the semi-implicit scheme was exactly the same as with the ADI-scheme. The only difference is that equation (4.21) now becomes:

$$(\zeta_o^{n+1})^{k+1} = r(\zeta_o^{n+1})^k + (1-r)\left\{2\left[\frac{(\Psi_{i,N}^{n+1})^k - (\Psi_{i,N+1}^{n+1})^k}{\Delta y^2} + \frac{w_o^{n+1}}{\Delta y}\right] - \frac{\partial v}{\partial z} \mid_o^{n+1}\right\}$$

where the superscript k appears on $\Psi_{i,N+1}^{n+1}$ since the values of Ψ^{n+1} are not known a priori at $y=y_o$, for a moving cell, as it will be discussed in Appendix B.

The inversion of the discretized form of (4.23) was attained by the use of HWSCRT from FISHPAK, which was subsequently used to invert the Poisson stream-function equation. From numerical experiments it was also found that the optimum values of r are much smaller compared to the ones used in the ADI-scheme.

A disadvantage of the semi-implicit scheme is that there is a restriction on the allowable time step due to the explicit formulation of the convective terms. From linear analysis the following relation for the Courant number has to be satisfied: $C(t) = \Delta t\left\{\frac{w}{\Delta z} + \frac{v}{\Delta y}\right\} \leq 1$ (Roache, 1982).

For all the runs using the semi-implicit scheme a variable time step was used which was adjusted so that $C(t) = \max_{i,j}\left\{\frac{|\, w_{i,j}\,|}{\Delta z} + \frac{|\, v_{i,j}\,|}{\Delta y}\right\}\Delta t \leq 0.2$ was true for all time steps.

3. Pressure solution

It can be shown that by taking the y-derivative of (4.1) and the z-derivative of (4.2) and by adding the resulting equations, the following Poisson equation for the pressure is obtained:

$$\frac{\partial^2 p}{\partial y^2} + \frac{\partial^2 p}{\partial z^2} = 2\left[\left(\frac{\partial v}{\partial y}\right)\left(\frac{\partial w}{\partial z}\right) - \left(\frac{\partial v}{\partial z}\right)\left(\frac{\partial w}{\partial y}\right)\right] = S \qquad (4.24)$$

where again all the quantities are normalized with respect to U_c and λ. Since nature doesn't provide any boundary conditions for the pressure, these are obtained directly from the equations of motion applied at a specific boundary and are of the Neumann type.

Fixed cell

At $y=0$ (4.1) gives:

$$\frac{\partial p}{\partial y} = \frac{1}{\mathrm{Re}}\frac{\partial^2 v}{\partial y^2} = -\frac{1}{\mathrm{Re}}\frac{\partial \varsigma}{\partial z}.$$

At $y=y_o$ (4.1) results in : $\frac{\partial p}{\partial y} = \frac{1}{\mathrm{Re}}\left(\frac{\partial^2 v}{\partial y^2} + \frac{\partial^2 v}{\partial z^2}\right) - \frac{\partial v}{\partial t} - \left(v\frac{\partial v}{\partial y} + w\frac{\partial v}{\partial z}\right)$ or $\frac{\partial p}{\partial y} = -\frac{1}{\mathrm{Re}}\frac{\partial \varsigma}{\partial z} - \frac{\partial v}{\partial t} - \left(v\frac{\partial v}{\partial y} + w\frac{\partial v}{\partial z}\right)$ where $\frac{\partial v}{\partial t}$, v, w and $\frac{\partial v}{\partial z}$ are known and $\frac{\partial v}{\partial y} = -\frac{\partial w}{\partial z}$ is also known. At $z = 0$ and $z = z_o$ (4.2) gives $\frac{\partial p}{\partial z} = \frac{1}{\mathrm{Re}}\frac{\partial^2 w}{\partial z^2} = \frac{1}{\mathrm{Re}}\frac{\partial \varsigma}{\partial y} = 0.$

Moving cell

The boundary conditions at $y=0$ and $y=y_o$ are the same as for a fixed cell. At $z=0$ and $z=z_o$ periodicity is used: $p(z_o) = p(0)$.

It can be seen from (4.24) and from the boundary conditions that once Ψ and ς have been calculated for a given time step then p can be obtained by inverting (4.24). Inversion of (4.24) is not straightforward. It can be shown that a solution to (4.24) subject to Neumann conditions or to a combination of Neumann and periodic conditions does not exist in the usual sense but rather in a least squares sense (Swartztrauber, 1974).

The solution to (4.24) was obtained by using HWSCRT from the FISHPAK package. In order to ensure that a solution to the problem exists, the right side of (4.24) is perturbed by subtracting a constant c. The solution that HWSCRT returns is not unique since that solution plus any constant is also a solution. The solution can be checked by differencing it and comparing with the right-side S. For the runs reported in this work the constant c was found to be very small compared with the right hand side. In order to fix the constant of integration the pressure was arbitrarily specified to be zero ($p=0$) for a point at $z=z_o/2$.

All the computations were carried out on the University of Illinois CDC-CYBER 175 machine. A listing of the computer programs used is given in Appendix A. The mesh sizes used in the calculations were $\Delta z^+=4$ and $\Delta y^+=1.25$ in the spanwise and lateral directions respectively. The time step for the ADI-scheme runs was set to $\Delta t^+=1$ which was found to optimize the accuracy and the number of iterations per time step. For the semi-implicit scheme runs, Δt^+ was set so that $C(t)\leq 0.2$ where $C(t)$ is the Courant number. The resulting Δt^+ was approximately 0.1. The computations were carried out until

an equilibrium state was attained.

For the computational runs where the outer flow eddies have negligible energy this stationary state is reached after three cycles. When the large scale eddies have finite energy the time scale of the computations increases substantially due to the longer periods involved. In the present work the calculations were carried out for three cycles of the outer flow-eddies and the statistical results were obtained during the fourth cycle.

C. Selection of model parameters

The most important step of the calculations is the selection of the relevant parameters for the representation of the flow at the outer boundary ($y=y_o$) of the computational domain. These boundary conditions reflect the way in which the outer flow eddies interact with the eddies close to the wall, the net result being the creation of wall turbulence.

The way that the three components of the velocity are represented at $y=y_o$ is described by equations (4.5), (4.6) and (4.7) for a fixed cell. It can be seen from these equations that at any instant the fluctuating velocity components receive their energy from two spatial scales λ_{*1} and λ_{*2} where the subscript $*$ is one of u, v, w. The selection of these two scales and the specification of the temporal behavior of u, v and w can completely determine the fluctuating velocity field at $y=y_o$.

In selecting these parameters use is made of the available correlation and spectral measurements along with information from the work on coherent wall

structures. From these measurements it can be inferred that the selection of the model parameters should depend on y_o. For this reason two different positions of the outer boundary of the computational domain are considered in this work. The first one is right outside the edge of the viscous sublayer ($10 \leq y_o^+ \leq 20$) and the second one is farther away from the wall ($y_o^+ \approx 40$) where according to Kline et al (1967) the low-speed wall streaks break-up into chaotic motions. The selection of the model parameters for these two cases will be described in what follows. An important concern of the computations in this work is the agreement of calculated wall patterns with measurements from this laboratory (Eckelman 1971, Lau 1980).

For most of the computational runs, single harmonics were used in order to specify the temporal variation of u, v and w at $y=y_o$:

$$w_{L1}(t)=\hat{w}_{L1}\cos\frac{2\pi t}{T_{w1}},\quad w_{L2}(t)=\hat{w}_{L2}\cos\left(\frac{2\pi t}{T_{w2}}+\phi_{w2}\right)$$

$$v_{L1}(t)=\hat{v}_{L1}\cos\left(\frac{2\pi t}{T_{v1}}+\phi_{v1}\right),\quad v_{L2}(t)=\hat{v}_{L2}\cos\left(\frac{2\pi t}{T_{v2}}+\phi_{v2}\right)$$

$$u_{L1}(t)=\hat{u}_{L1}\cos\left(\frac{2\pi t}{T_{u1}}+\phi_{u1}\right),\quad u_{L2}(t)=\hat{u}_{L2}\cos\left(\frac{2\pi t}{T_{u2}}+\phi_{u2}\right)$$

By combining the above relations with (4.5), (4.6) and (4.7) we obtain:

$$w=\hat{w}_{L1}\cos\frac{2\pi t}{T_{w1}}\sin\frac{2\pi z}{\lambda_{w1}}+\hat{w}_{L2}\cos\left(\frac{2\pi t}{T_{w2}}+\phi_{w2}\right)\sin\frac{2\pi z}{\lambda_{w2}} \qquad (4.25)$$

$$v=\hat{v}_{L1}\cos\left(\frac{2\pi t}{T_{v1}}+\phi_{v1}\right)\frac{2\pi z}{\lambda_{v1}}+\hat{v}_{L2}\cos\left(\frac{2\pi t}{T_{v2}}+\phi_{v2}\right)\cos\frac{2\pi z}{\lambda_{v2}} \qquad (4.26)$$

$$u=\hat{u}_{L1}\cos\left(\frac{2\pi t}{T_{u1}}+\phi_{u1}\right)\frac{2\pi z}{\lambda_{u1}}+\hat{u}_{L2}\cos\left(\frac{2\pi t}{T_{u2}}+\phi_{u2}\right)\cos\frac{2\pi z}{\lambda_{u2}} \qquad (4.27)$$

and $U=\overline{U}(y_o)+u$.

The selection of the length scales, that are chosen to be representative of the wavenumber spectrum of the velocity fluctuations at $y=y_o$, is achieved with the use of measurements right at the wall and at $y^+\approx 40$. As it will be seen, the position of the outer boundary of the calculations affects the relative amount of energy in the outer flow eddies and the phases ϕ_{v1} and ϕ_{u1} in (4.26) and (4.27).

From measurements of the spanwise scale of the coherent wall structures (Kline et al 1967, Gupta et al 1971, Lee et al 1974) λ_{w1}, λ_{v1} and λ_{u1} are selected so that $\lambda^+_{w1}=\lambda^+_{v1}=\lambda^+_{u1}=100$. All the available correlation measurements indicate that there is an increase of the spanwise scale with increasing distance from the wall (Grant 1958, Comte-Bellot 1961, Tritton 1967). Even with a complete knowledge of the correlation function the form and distribution of the eddies cannot be calculated without some ambiguity (Townsend 1956). One can, nevertheless, infer from such correlations the existence of long or small scales, define a range for their size and examine their behavior with distance from the wall.

Grant's (1958) measurements at $y_o^+=35$ of $R_{ww}(y_o^+;\,0,\,0,\,\Delta z^+)$ indicate a zero crossing at $\Delta z^+\approx 175$ and weak negative values up to $\Delta z^+\approx 600$. Tritton (1967) did not measure $R_{ww}(y_o^+;\,0,\,0,\,\Delta z^+)$ but $R_{uu}(y_o^+;\,0,\,\Delta y^+,\,\Delta z^+)$ with $y_o^+=32$ and $\Delta y^+=-9$. His results show a maximum at $\Delta z^+\approx 52$ and positive

values persisting up to $\Delta z^+ \approx 400$. For a combination of two spatial harmonics as in (4.25), (4.26), (4.27) the correlation with spanwise separation will resume the value of 1 at $\Delta z^+ = \lambda_{*2}$ where $*$ is u, v or w. In reality the presence of a wide spectrum of wavenumbers with various phases smears out any such periodicity. If one attempts to extract length scales from the above measurements then an estimation of the range of eddy sizes can be obtained as follows: For single harmonics the auto-correlation with spanwise separation has a zero-crossing at $\lambda/4$ and the cross-correlation shows a maximum at $\lambda/4$, where λ is the wavelength. Grant's measurements would then indicate a wavelength of $4 \times 175 \approx 700$ and Tritton's a wavelength of $4 \times 52 \approx 208$. That means then that for the streamwise and spanwise components of the velocity at $y^+ = y_o^+$ there is appreciable amount of energy in eddies whose wavelength λ^+ ranges from 200 to 700 in wall units. These estimates are also supported by the measurements of Morrison and Kronauer (1969) of the streamwise velocity fluctuations that were outlined in Chapter 2. In particular their frequency-wavenumber spectra at $y^+ = 49$ and $y^+ = 27.8$ show that there is no appreciable energy for wavelengths smaller than $\lambda_z^+ = 160$ and $\lambda_z^+ = 70$ respectively, for any frequency. For the same y^+'s the peak of the $P(\omega^+, k_z^+)$ spectrum function occurs around $\lambda_z^+ \approx 400$, which lies in the middle of the range estimated from the correlations. It has to be noted, though, as pointed out by Morrison et al (1971), that there might be a Reynolds number effect on these measurements. Morrison et al compared their spectral measurements inside, and at the edge of, the viscous sublayer and concluded that

an increase of the Reynolds number has the effect of increasing the relative amount of low-frequency low-wavenumber (k_z^+) energy. From an analogous comparison of the position of the peak of $P(\omega^+, k_z^+)$, no appreciable Reynolds number effect can be seen. At positions farther away from the wall, examination of Morrison and Kronauer's data indicates that there is a small shift of the peak position to lower wavenumbers (k_z^+) with increasing Reynolds number, but this is rather inconclusive due to the small amount of data. So the estimate that the $\lambda_{u2}^+ = \lambda_{w2}^+ = 400$ eddies contain most of the energy on a plane parallel to the wall at $y^+ \approx 40$ appears to be substantiated by both correlation and spectral measurements.

In order to estimate the spanwise scale of the normal velocity fluctuations the measurements of Tritton (1967) are used. As mentioned in Chapter 2 his $R_{vv}(y_o^+; 0, 0, \Delta z)$ with $y_o^+ = 40$ shows a zero crossing at $\Delta z^+ \approx 20$. Using similar arguments as above, an estimate for the wavelength of v at $y_o^+ = 40$ is $4 \times 20 = 80$. The existence of long negative tails in the correlation would suggest that there is some energy in scales larger than $\lambda^+ \approx 80$.

So for a two wavelength spatial approximation of turbulence at $y_o^+ \approx 40$ as in (4.25), (4.26), (4.27) a large fraction of the $\overline{u^2}$ energy should be in the $\lambda_{u2}^+ = 400$ eddies, most of the $\overline{v^2}$ energy should be associated with the $\lambda_{v1}^+ = 100$ eddies and most of the $\overline{w^2}$ energy with the $\lambda_{w2}^+ = 400$ eddies. It should be noted that the wavelength $\lambda_{w2}^+ = 400$ should be taken more as a representative of a range and not as a very precise estimate of the size of the w-eddies in the spanwise

direction. As mentioned before, when the distance from the wall decreases the relative amount of energy associated with the outer flow eddies decreases. Thus it would be expected that, close to the edge of the viscous sublayer ($y_o^+ \approx 15$), most of the energy of the velocity fluctuations is associated with the $\lambda^+ = 100$ eddies, the outer flow eddies being unimportant in defining the dynamics of the flow.

The periods of the two scales (T_{u1}^+, T_{v1}^+, T_{w1}^+ and T_{u2}^+, T_{v2}^+, T_{w2}^+) can be estimated from various arguments. If it is assumed that, at distances away from the wall, where viscosity is not very important, the transient terms of the Navier-Stokes equations are of the same order of magnitude as the convective terms, we obtain

$$\frac{\partial w}{\partial t} \sim w \frac{\partial w}{\partial z} \Rightarrow \frac{u_*}{T_w} \sim \frac{u_*^2}{\lambda_w} \Rightarrow T_w^+ \sim \lambda_w^+$$

and

$$\frac{\partial v}{\partial t} \sim w \frac{\partial v}{\partial z} \Rightarrow \frac{u_*}{T_v} \sim \frac{u_*^2}{\lambda_v} \Rightarrow T_v^+ \sim \lambda_v^+$$

since all the velocity fluctuations scale with the friction velocity u_*.

So an estimate of the period of the velocity fluctuations on the y–z plane gives $T_w^+ (= T_v^+) \sim \lambda_w^+ (= \lambda_v^+)$. This indicates that the larger scales have longer periods and for the selected wavelengths at $y^+ = y_o^+$ we obtain $T_{u1}^+ = T_{v1}^+ = T_{w1}^+ \sim 100$ and $T_{u2}^+ = T_{v2}^+ = T_{w2}^+ \sim 400$.

The estimate $T^+ \sim 100$ for the small scale eddies agrees with measured frequency spectra of velocity fluctuations close to the wall. Bakewell and Lumley

(1967) measured the frequency spectra of streamwise velocity fluctuations at $y^+ = 1.25$, 2.50 and 5.00. Their measurements show that the normalized spectrum function data if plotted against ω^+ (where ω is the circular frequency) collapse on a single curve with a median frequency of $n^+ \approx 0.01$. The same results have been obtained by Fortuna (1971) for the fluctuations of the streamwise velocity gradient at the wall of a pipe and for Re=15,500, 16,100 and 17,000. Sirkar (1969) measured the s_x-spectra at Re=68,940 and 37,170 and obtained median frequencies of 7.61×10^{-3} and 8.54×10^{-3} respectively. He also measured the spectra of the spanwise velocity gradient fluctuations and found median frequencies of 7.75×10^{-3} and 1.1×10^{-2} for Re=68,940 and 37,750 respectively.

An estimate of the time scale of the $\lambda^+ = 100$ eddies can also be obtained from bursting frequency arguments. If it is assumed that throughout the viscous wall region the turbulent bursts, which contribute to the production of Reynolds stress, are associated primarily with the $\lambda^+ = 100$ eddies then equations (4.5) and (4.6) provide for two bursts through a period of $T^+ = T_{u1}^+ = T_{v1}^+$ and over a spanwise length of $\lambda^+ = \lambda_{u1}^+ = \lambda_{v1}^+ = 100$. The above assumption seems to be supported by the $R_{uv}(y_o^+; 0, 0, \Delta z^+)$ measurements of Tritton (1967) at $y_o^+ = 29$, that were described in Chapter 2. As indicated in the same chapter, Kline et al (1967) plotted the normalized burst rate F^+ versus $K = \frac{\nu}{U_\infty^2}\frac{dU_\infty}{dx}$ and obtained $F^+ \approx 120\times10^{-6}$ for $K=0$. F^+ is defined as

$$F^+ = \frac{(\#\text{ of bursts})}{(\text{time})(\text{span})}$$

so equations (4.5) and (4.6) give :

$$F^+ = \frac{2}{T^+\lambda^+} \Rightarrow T^+ = \frac{2}{F^+\lambda^+}$$

$$\text{or } T^+ = \frac{2}{120\times10^{-6}\times100} = 166.6 = T_{v1}^+ = T_{u1}^+$$

The above estimate of $T_{v1}^+ (=T_{u1}^+)$ is close to the ones obtained from order of magnitude analysis and spectral measurements, especially if one takes in account the experimental differences involved (spectral measurements-visual observations of bursts). For a coherent motion, one can finally take $T_{w1}^+ = T_{v1}^+ = T_{u1}^+$ for the specification of the periods of the velocity fluctuations that are associated with the $\lambda^+ \doteq 100$ eddies. Some thoughts related to the connection of T_{w1}^+ to the bursting frequency will be presented during the discussion of the results.

The estimation of T_{*2}^+ where $*$ is u, v or w from coherent structure experiments is a more difficult task. During the computational runs it was found that the value of $T_{v2}^+ (=T_{w2}^+)$ affects the intensities at the wall and especially the correlation $R_{v,v}(0, 0, \Delta z^+)$. With the rest of the parameters fixed, T_{*2}^+ could be varied so that the calculated $R_{v,v}$ agrees with experimental measurements (Eckelman 1971, Lau 1980). From streamwise auto-correlation data the mean period of the large scale u-eddies measured by Badri Narayanan and Marvin (1978) is $T^+ = 5\frac{\delta}{U_\infty}$. For a fully developed flow in a pipe, with $\delta = R$ (radius of the pipe) and $U_\infty = U_c$ (centerline velocity), it can be shown that the estimate $T^+ \approx 400$ from scaling arguments would correspond to a pipe Reynolds number

of 80,000 and that T^+ should increase with increasing Reynolds number. It is not certain, though, whether the eddies measured by Narayanan and Marvin correspond to the outer flow eddies of the present work.

With set values for the wavelengths λ_{u1}^+, λ_{v1}^+, λ_{w1}^+ and λ_{u2}^+, λ_{v2}^+, λ_{w2}^+ as well as for the periods T_{u1}^+, T_{v1}^+, T_{w1}^+ and T_{u2}^+, T_{v2}^+, T_{w2}^+, the remaining parameters in (4.25), (4.26), and (4.27), that are to be estimated, are the relative temporal phases and relative energies of the small and large eddies in each velocity component. As mentioned earlier these parameters depend on the position of the outer boundary ($y=y_o$) of the computational domain.

We define a $N\%$ closed flow in the wall region of a turbulent shear flow as the flow whose streamline pattern is similar to the one in Figure 4a for $N\%$ of the time and looks like the one in Figure 4b for (100–N)% of the time.

Figure 4a 100% closed flow

Figure 4b 0% closed flow

Figure 4 Percentage of closed flow.

So a 100% closed flow is represented by Figure 4a for 100% of the time while a 0% closed flow appears like Figure 4b for 100% of the time.

We will attempt to extract information about the type of flow (percentage of closed flow) of the wall and the outer flow eddies from long-term and conditionally averaged measurements. This information, under certain conditions, can be used to specify the relative phases between $w_{L1}(t)$, $v_{L1}(t)$ and $w_{L2}(t)$, $v_{L2}(t)$. The same measurements can also be used to estimate the percentage of $\overline{w^2}$ energy that is associated with the $\lambda^+ = 100$ eddies. We will also relate the phases ϕ_{v1} and $\phi'_{v2} = \phi_{v2} - \phi_{w2}$ to the slope of the $(v')^+$ intensity profile in order to obtain an additional constraint on the range of the selected variables. We will finally use Reynolds stress arguments in order to select the phases $\phi'_{u1} = \phi_{u1} - \phi_{v1}$ and $\phi'_{u2} = \phi_{u2} - \phi_{v2}$ as well as the percentage of $\overline{u^2}$ energy associated with the $\lambda^+ = 100$ eddies.

For the type of signals as in (4.25) and (4.26) the percentage of closed flow for each wavelength depends on the periods T_{v1}^+, T_{w1}^+ (or T_{v2}^+, T_{w2}^+) and the relative phase ϕ_{v1} (or $\phi'_{v2} = \phi_{v2} - \phi_{w2}$). For signals of the same period $T_{v1}^+ = T_{w1}^+$ (or $T_{v2}^+ = T_{w2}^+$) it is easy to show that the percentage of closed flow $N_1\%$ (or $N_2\%$) is given by :

$$N = 100 \times (1 - \frac{\phi}{\pi}) \tag{4.28}$$

where $N = N_1$ or N_2 and $\phi = \phi_{v1}$ or ϕ'_{v2}. It is thus seen that specification of N_1 and N_2 can provide us with the relative phases ϕ_{v1} and ϕ'_{v2} between

$v_{L1}(t)$, $w_{L1}(t)$ and $v_{L2}(t)$, $w_{L2}(t)$ respectively. For signals of different period, where $T_{w1}^{+} = MT_{w1}^{+}$ and M is an integer, the percentage of closed flow depends on M. It can be shown that if M=even integer, the flow is 50% closed for any ϕ_{w1} and if M=odd integer the percentage of closed flow varies between 33.3% and 66.6% depending on ϕ_{w1}.

Long-term correlation measurements by Kreplin and Eckelmann (1979a) and Nikolaides et al (1983) indicate that the spanwise flows at $y^{+} \approx 40$ show a weak negative correlation with spanwise flows close to the wall, at zero time delay. Similar correlations for $y^{+} \leq 20$ show strong positive values at zero time delay and exhibit maxima for positive values of the time delay. As it will be shown in Chapter 5, the use of conditional averaging techniques shows that the conditionally averaged spanwise velocity $<w>$ has a very characteristic temporal signature during the time that the $\lambda^{+}=100$ eddies are evolving at the wall. When the fluid probe is at $y^{+}=40$, the $<w>$ profile shows a reversal of sign of the same amplitude as the flow that preceded it in time, as can be seen in Figure 6. It is also seen that $<w>$ is of opposite sign to $<s_z>$ for most of the time that the $\lambda^{+}=100$ eddies are evolving at the wall. When the fluid probe is located at $y^{+}=20$, the conditionally averaged $<w>$ profile has the same sign with $<s_z>$ during most of the lifetime of the wall eddies. It has to be noted that the w and s_z profiles obtained from the application of the detection algorithm should show a loss of correlation for time instants for away from time zero. This is expected to have an effect on the calculated lifetimes of the conditionally

averaged $<w>$ and $<s_z>$ profiles and, subsequently, to affect the estimation of the percentage of closed flow of the $\lambda^+=100$ eddies from such measurements. A rough estimate from Figures 5 and 6 gives for N_1, as defined above, the following relations: At $y^+=40$, $N_1 \geq 70\%$ and at $y^+=20$, $N_1 \leq 20\%$. The percentage of closed flow at $y^+=y_o^+$ is the percentage of the time that the center of the eddy spends below $y^+=y_o^+$. Therefore, the above estimates of N_1 support the notion that the $\lambda^+ \approx 100$ eddies have their effective centres below $y^+=40$ for more than 70% of the time and below $y^+=20$ for less than 20% of the time. On an average, then, the "eye" of these eddies would lie in the region $20 \leq y^+ \leq 40$. Similar measurements, with the ones described above, are not available for the outer flow eddies. We visualize these eddies to have their effective centers very far from the wall, so that for any $y^+ \leq 40$, N_2, as defined above, is zero ($N_2 = 0\%$). Using, then, relation (4.28) we obtain the following estimates for the phases ϕ_{v1} and ϕ'_{v2}:

$$y^+=40 \quad : \quad 0 \leq \phi_{v1} \leq 54^o, \quad \phi'_{v2}=180^o$$

$$y^+=20 \quad : \quad 144^o \leq \phi_{v1} \leq 180^o$$

From the measurements of Nikolaides et al (1983), that are described in more detail in Chapter 5, the following estimate of the $\overline{w^2}$ energy associated the $\lambda^+=100$ eddies can be obtained: The amplitude (w_o) of the conditionally averaged $<w>$ profile at $y^+=40$ is $w_o=0.5\ w'$, where w' is the r.m.s. of the w-fluctuations. This value for w_o is expected to be lower than the amplitude of individual w profiles, that are selected to be conditionally averaged, since the

detection algorithm focuses on large amplitude s_z patterns at the wall. If $<w>$, then, is approximated by a single harmonic in time, the percentage of the energy E_{w1} associated with the $\lambda^+=100$ eddies would be:

$$E_{w1} = \frac{\frac{1}{2}w_o^2}{\overline{w^2}} = \frac{1}{2}(\frac{w_o}{w'})^2 = 12.5\%.$$

This value is, therefore, taken to provide a lower bound for the $\overline{w^2}$ energy contributed by the $\lambda^+=100$ eddies ($E_{w1}>12.5\%$). This estimate is consistent with the measurements of Grant (1958) and Tritton (1967) which indicate that at $y^+=40$ most of the energy is associated with eddies whose wavelengths are larger than $\lambda^+=100$.

The energy E_{v1} of the $\lambda^+=100$ eddies at $y^+=40$ cannot be estimated a priori due to the lack of appropriate measurements. The available correlation measurements of Tritton (1967) show that $R_{vv}(\Delta z^+)$ at $y^+=40$ show a zero crossing at $\Delta z^+\approx 20$, which would imply scales of $\lambda_z^+\approx 4\times 20=80$, but long negative tails out to $\Delta z^+\approx 180$ indicating the existence of scales longer than $\lambda^+=100$. The energy E_{v1} was found to have an effect on the profile of the spanwise intensity and on the wall turbulent characteristics. For $\lambda_{v2}^+ = \lambda_{w2}^+ = 400$ the value of $E_{v1}=75\%$ was found to give good agreement in relation to all the affected turbulent properties.

Outside the edge of the viscous sublayer ($y^+\approx 15$) we will assume that all the energy of the velocity fluctuations on a plane perpendicular to the flow is associated with the $\lambda^+=100$ eddies ($E_{v1} = E_{w1} = 100\%$).

It can be shown that, for the signals in (4.25) and (4.26), the slope of the $(v')^+$ profile is given by:

$$S = \frac{\partial (v')^+}{\partial y^+} = -\pi \frac{\dfrac{\hat{v}_{L1}^+ \hat{w}_{L1}^+}{\lambda_1^+} \cos\phi_{v1} + \dfrac{\hat{v}_{L2}^+ \hat{w}_{L2}^+}{\lambda_2^+} \cos\phi'_{v2}}{\sqrt{\hat{v}_{L1}^{+2} + \hat{v}_{L2}^{+2}}}$$

or

$$S = -\pi \left[\frac{\sqrt{E_{v1}}\, \hat{w}_{L1}^+}{\lambda_1^+} \cos\phi_{v1} + \frac{\sqrt{1-E_{v1}}\, \hat{w}_{L2}^+}{\lambda_2^+} \cos\phi'_{v2} \right] \tag{4.29}$$

For the selected parameters $\lambda_1^+ = 100$, $\lambda_2^+ = 400$, and $E_{v1} = 75\%$, $\phi'_{v2} = 180^\circ$ the following table gives values of S (in degrees) for pairs of ϕ_{v1}, E_{w1}

Table 2

$E_{w1}\%$	ϕ_{v1} (deg)			
	20	30	40	50
0	-1.25	-1.68	-2.04	-2.38
10	-1.22	-1.64	-2.01	-2.33
20	-1.14	-1.55	-1.89	-2.21
30	-1.01	-1.39	-1.71	-2.00
40	-0.84	-1.17	-1.46	-1.73
50	-0.62	-0.91	-1.16	-1.38

that fall in the ranges estimated before. The values of the slope S thus obtained appear to be close to the experiments, which show that the $(v')^+$ profile tends to level off for $y^+ \geq 30$. Close to the edge of the viscous sublayer where $E_{v1} = E_{w1} = 100\%$ (4.29) becomes $S = \dfrac{-2\pi (w')^+}{\lambda_1^+} \cos\phi_{v1}$ and for $\lambda_1^+ = 100$,

$(w')^+ = 1.06$ the following values of S are obtained (in degrees):

Table 3

ϕ_{v1}	S
150	3.30
160	3.58
170	3.75
180	3.81

The above values also appear to agree qualitatively with experiments, which show the $(v')^+$ profile to increase at the edge of the viscous sublayer, but with a slope rather higher than the ones calculated above. This would then indicate that smaller scales λ_1^+ would give higher values for S, a conclusion which is also discussed in Chapter 8.

For the signals in (4.26) and (4.27) the Reynolds stress is given by: $\overline{uv} = \frac{1}{4}(\hat{u}_{L1}\hat{v}_{L1}\cos\phi'_{u1} + \hat{u}_{L2}\hat{v}_{L2}\cos\phi'_{u2})$ where the overbar now denotes a space-time average and $\phi'_{u1} = \phi_{u1} - \phi_{v1}$, $\phi'_{u2} = \phi_{u2} - \phi_{v2}$. The correlation coefficient is given by:

$$C_{uv} = -\frac{\overline{uv}}{\sqrt{\overline{u^2}}\sqrt{\overline{v^2}}} \tag{4.30}$$

where again the overbar denotes a space-time average. Most of the available data (Laufer 1954, Kim et al 1971, Schildnecht et al 1979) indicate that $C_{uv} \approx 0.45$ for $10 \leq y^+ \leq 50$, but Kutateladze et al (1977) obtained lower values throughout the viscous wall region. For the signals in (4.26) and (4.27), then (4.30) becomes:

$$C_{uv} = -\frac{\hat{u}_{L1}\hat{v}_{L1}\cos\phi'_{u1} + \hat{u}_{L2}\hat{v}_{L2}\cos\phi'_{u2}}{\sqrt{\hat{u}_{L1}^2 + \hat{u}_{L2}^2}\sqrt{\hat{v}_{L1}^2 + \hat{v}_{L2}^2}} = 0.45 \tag{4.31}$$

If it is assumed that the $\lambda^+ = 100$ eddies contribute a fraction x of the Reynolds stress and that E_{u1} and E_{v1} are the $\overline{u^2}$ and $\overline{v^2}$ energy contributions of these eddies, equation (4.31) becomes:

$$\sqrt{E_{u1}}\sqrt{E_{v1}}\cos\phi'_{u1} + \sqrt{1-E_{u1}}\sqrt{1-E_{v1}}\cos\phi'_{u2} = -0.45 \tag{4.32}$$

or

$$\sqrt{E_{u1}}\sqrt{E_{v1}}\cos\phi'_{u1} = -0.45x \tag{4.33}$$

From the correlation measurements of Tritton (1967) we see that the $R_{uv}(y_o^+; 0, 0, \Delta z^+)$ correlation for $y_o^+ = 29$ shows a zero crossing at $\Delta z^+ \approx 38$. This would then indicate that most of the Reynolds stress production comes from eddies with wavelength $\lambda^+ = 100$, and that there is a small contribution from larger eddies. Wallace et al (1977) conditionally averaged the u and v signals, on the condition that there is a gradual deceleration in the u-signal followed by a strong acceleration. Their results indicate that the v-signal is approximately 180^o out of phase with the u-signal. This can be interpreted as $uv > 0$ for 100% of the time in an analogous fashion with the percentage of closed flow notion presented before. That means that the Reynolds stress producing eddies will be producing an ejection ($u < 0$, $v > 0$) for 50% of the time and a sweep ($u > 0$, $v < 0$) for the rest 50% of the time. If this is taken to be the case for the $\lambda^+ = 100$ eddies at $y^+ = 40$, then $\phi'_{u1} = 180$ and with $E_{v1} = 75\%$ we can use (4.32) to obtain pairs of E_{u1} and ϕ'_{u2} that satisfy this equation. Then from (4.33) we can calculate x. These values are shown in the following table:

Table 4

E_{u1} (%)	x	ϕ'_{u2} (deg)
5	.43	121.7
10	.61	111.8
15	.75	104.4
20	.86	98.1
25	.96	92.2

From the above table it can be seen that when E_{u1}=20%, for example, then 86% of the Reynolds stress comes from the λ^+=100 eddies and ϕ'_{u2}=98.1 ($u_{L2}(t)$ and $v_{L2}(t)$ are almost uncorrelated). There appears to be a contradiction between the data of Morrison and Kronauer (1969) and the correlation measurements of Tritton (1967) in that we need energies of $E_{u1} \geq 15\%$ in order to have the λ^+=100 eddies contribute more than 75% to the Reynolds stress at y^+=40. Nevertheless, there is qualitative agreement in that small energies E_{u1} can give an appreciable fraction of the Reynolds stress. Note that if x=1 (ϕ'_{u2}=90°) then E_{u1}=27% from (4.33).

The data of Willmarth and Lu (1972) that were discussed in Chapter 2 indicate that at y^+=30 the ejection and sweeps ($uv<0$) cover 65.11% of the time, whereas the interactions ($uv>0$) cover the rest 34.89% of the time. According to these measurements and using relations similar to the ones developed for an N% closed flow, it can be shown that ϕ'_{u1}=117.2° instead of 180°. For such a value of ϕ'_{u1} the values of E_{u1}, ϕ_{u2} and x that satisfy (4.32) and (4.33) are shown in the following table:

Table 5

$E_{u1}\%$	x	ϕ'_{u2} (deg)
10	0.28	133.2
20	0.39	127.6
30	0.48	123.9
40	0.56	121.0
50	0.62	118.8
60	0.68	117.0
70	0.74	115.7
80	0.79	115.4
90	0.83	118.1
95	0.86	125.0
97	0.87	134.0
98	0.87	145.3
100	0.88	no solution

It is thus seen, that in order to have the $\lambda^+=100$ eddies to contribute more than 75% of the Reynolds stress, E_{u1} should be greater than 70% which contradicts Morrison and Kronauer's data. So for the calculations in this work, when $y_o^+=40$ the following values are selected for $E_{u1}, \phi'_{u1}, \phi'_{u2}$: $E_{u1}=15\%$, $\phi'_{u1}=180^o$, $\phi'_{u2}=104.4$.

At $y^+\approx 15$ the situation is different. From Morrison and Kronauer's data we can argue that most of the energy is associated with the $\lambda^+=100$ eddies ($E_{u1}\approx 100\%$). We also assume, since there are no data available, that the Reynolds stress comes solely from the wall $\lambda^+=100$ eddies ($x=1$). Then since $E_{v1}=1$, as mentioned earlier, (4.33) gives $\cos\phi'_{u1}=-0.45 \Rightarrow \phi'_{u1}=116.7$ which is very close to the value obtained from the Willmarth and Lu (1972) data at $y^+=30$. There is also an indication in the data of Wallace et al (1977) that at

y^+=15 the u and v signatures have a phase difference less than 180° which can be clearly seen to be the case with their results at y^+=45. Wallace et al (1972) in an earlier paper calculated the auto-correlation of the classified stress (uv) with distance from the wall. Their results on the respective integral time scales are reproduced below:

Table 6

y^+	Total	Ejection	Sweep	Wallward interaction	Outward interaction
3.4	0.4	0.8	0.5	0.4	0.2
15	0.2	0.4	0.5	0.2	0.2
45	0.2	0.3	0.2	0.1	0.1
187	0.1	0.2	0.2	0.1	0.1

It can be seen that both the ejections and the sweeps are larger in their time scale and period of correlation than the interaction events. From these results, it is difficult to obtain an estimate of ϕ'_{u1} from the percentage of the time over which the interactions (or the sweeps and bursts) are important, because the respective time scales are not additive. Nevertheless, we can find a qualitative agreement between the assumption that E_{u1}=100% from Morrison and Kronauer's data at $y^+\approx$15 and the data of Wallace et al (1972) at y^+=15 and Willmarth and Lu (1972) at y^+=30. So for the calculations at $y^+\approx$15, E_{u1}=100% and ϕ'_{u1}=116.7.

downstream direction. Theodorsen argued that the "horseshoe" gives a positive production term in the balance equation for ω^2 and provides a mechanism for the most efficient macroscopic momentum exchange. Lighthill (1963) observed that flows towards and away from a wall would stretch and compress, respectively, the vortex lines close to the wall. Kline et al (1967) used Lighthill's arguments to suggest a plausible physical explanation for the formation of wall-layer streaks. Since the spanwise component of the vorticity is primarily due to $\frac{\partial U}{\partial y}$, the inflows (stretching) would act to increase the local U in the sublayer whereas the outflows (compression) would tend to decrease it. Hence a spanwise variation in U can develop naturally as a result of the inherent three-dimensionality of the coexisting turbulence. Kline et al argued that the streamwise vorticity thus generated accounts for the lifting of the low-speed wall-layer streaks observed experimentally prior to the breakup process.

Offen and Kline (1975) proposed that the streamwise and transverse vortices observed by Kim et al (1971) could merely indicate different parts of a stretched vortex. The hydrogen-bubble time-line experiments are essentially two dimensional (on a plane defined by the velocity vector and the wire). If the plane cuts the centre, or tip, of the stretched vortex, the time-lines will show a transverse vortex, whereas if it passes through one of the legs, the image will look like an upward-tilted streamwise vortex. Offen and Kline developed a model centered around a "lifting flow module" and pointed out its striking resemblance to some aspects of the "horseshoe structure" model proposed by Theodorsen (1952).

Recent experimental support about the existence of horseshoes vortices has been given by Head and Bandyopadhyay (1981). They used combined flow visualization and hot-wire measurements in a boundary layer at values of the momentum thickness Reynolds number (Re_θ) in the range 1000-7000. Over this range of Re_θ they found that the most significant feature of the boundary layer is the horseshoe (or hairpin) vortex postulated by Theodorsen (1952). They observed a general inclination of smoke-free fissures or smoke-filled filaments at a characteristic angle to the wall, which appeared to be in the region of 40^o. Their visual evidence suggested that this angle is characteristic of the flow in the outer part of the layer. Based on this observation they made measurements of the streamwise velocity at $y^+ \approx 40$ and at less than half the boundary layer thickness using two hot-wires in a staggered arrangement. Their measurements showed that the two signals were virtually identical supporting their visual observations that arrays of hairpin vortices, inclined at an angle of about 40^o to the surface, are being convected past the wires.

In what follows we will discuss the vorticity dynamics of the model flow, presented in part A of this section, and in particular we will focus on the vortex-stretching term of Equation (4.36). As mentioned earlier for a two dimensional flow (e.g. $U=0$, $\frac{\partial}{\partial x}=0$, $v,w\neq 0$) $P_x=P_y=P_z=0$ from (4.37), (4.38) and (4.39). If however $\frac{\partial}{\partial x}=0$ and $U,v,w\neq 0$, as in the model flow, we obtain from the same equations the following results:

$$P_x = \omega_y \frac{\partial U}{\partial y} + \omega_z \frac{\partial U}{\partial z} \tag{4.40}$$

$$P_y = \omega_y \frac{\partial v}{\partial y} + \omega_z \frac{\partial v}{\partial z} \tag{4.41}$$

$$P_z = \omega_y \frac{\partial w}{\partial y} + \omega_z \frac{\partial w}{\partial z} \tag{4.42}$$

where now $\omega_y = \frac{\partial U}{\partial z}$, $\omega_z = -\frac{\partial U}{\partial y}$ and the x-component of equation (4.36) is identical to equation (4.8) where now $\omega_x = \frac{\partial w}{\partial y} - \frac{\partial v}{\partial z} (= \varsigma)$.

Substituting these expressions in (4.40), (4.41) and (4.42) we get:

$$P_x = \frac{\partial U}{\partial z}\frac{\partial U}{\partial y} - \frac{\partial U}{\partial y}\frac{\partial U}{\partial z} = 0$$

$$P_y = \frac{\partial U}{\partial z}\frac{\partial v}{\partial y} - \frac{\partial U}{\partial y}\frac{\partial v}{\partial z} \neq 0 \tag{4.43}$$

$$P_z = \frac{\partial U}{\partial z}\frac{\partial w}{\partial y} - \frac{\partial U}{\partial y}\frac{\partial w}{\partial z} \neq 0 \tag{4.44}$$

It is thus seen that even though the model flow is three-dimensional (U, v, $w \neq 0$) the instantaneous vortex-stretching term in the streamwise vorticity equation is zero due to the assumption of homogeneity. Thus the model flow provides source terms only for the lateral and spanwise components of the vorticity. It is also interesting to note that at the sides of the cell ($z=0$ or z_o) where $\frac{\partial U}{\partial z} = \frac{\partial v}{\partial z} = \frac{\partial w}{\partial y} = 0$, equations (4.43) and (4.44) become:

$$P_y = 0, \; P_z = -\frac{\partial U}{\partial y}\frac{\partial w}{\partial z} = \omega_z \frac{\partial w}{\partial z}$$

where $\omega_z = -\frac{\partial U}{\partial y} < 0$ close to the wall.

This means that, for inflows, close to the wall where $\omega_z<0$ and $\frac{\partial w}{\partial z}>0$, $P_z<0$ and from (4.36) $\frac{\partial \omega_z}{\partial t}<0$ i.e. the spanwise vorticity is intensified (increases in magnitude). For outflows, $\frac{\partial w}{\partial z}<0$ and $P_z>0$, so $\frac{\partial \omega_z}{\partial t}>0$ and the spanwise vorticity decreases (in magnitude). So it can be seen that the "fixed cell" model flow provides for intensification or dampening of the spanwise vorticity at the sides of the cell and close to the wall as discussed by Lighthill (1963). It is also seen that there is no intensification of the lateral vorticity at the sides of the cell.

Let us now examine what the fluxes of the three components of the vorticity are at the boundary of our computational domain. If we consider the "fixed cell" model flow to define a control volume, then the fluxes at $y=0$, inside the control volume, are diffusional and given by:

$$\omega_x\text{-vorticity} \; : \; -\nu\frac{\partial \omega_x}{\partial y}\Big|_{y=0} = -\nu\frac{\partial^2 w}{\partial y^2}\Big|_{y=0} = -\frac{1}{\rho}\frac{\partial p}{\partial z}\Big|_{y=0}$$

$$\omega_y\text{-vorticity} \; : \; -\nu\frac{\partial \omega_y}{\partial y}\Big|_{y=0} = -\nu\frac{\partial S_x}{\partial z}$$

$$\omega_z\text{-vorticity} \; : \; -\nu\frac{\partial \omega_z}{\partial y}\Big|_{y=0} = \frac{1}{\rho}\frac{\partial P}{\partial x}\Big|_{y=0} = 0,$$

where S_x is the instantaneous streamwise velocity gradient at the wall and all the quantities are now dimensional. It is thus seen that the solid boundary is a source (or sink) of streamwise and lateral vorticity but does not allow the spanwise vorticity to diffuse inside or outside the control volume.

If we assume that the control volume extends over an even number of half-wavelengths, to assume periodicity, then it is easy to show that the net diffusional flux at the vertical sides of the control volume is zero and that the convective flux of vorticity ($w\vec{\omega}$) is zero because $w=0$ at $z=0$ or z_o.

At the outer boundary of the control volume the diffusional fluxes are negligible. The convective flux of vorticity is $v\vec{\omega}$ and for each component we obtain at $y=y_o$:

$$\omega_x\text{-vorticity} \; : \; v\left(\frac{\partial w}{\partial y} - \frac{\partial v}{\partial z}\right)$$

$$\omega_y\text{-vorticity} \; : \; v\frac{\partial U}{\partial z}$$

$$\omega_z\text{-vorticity} \; : \; -v\frac{\partial U}{\partial y}$$

So there is a convective flux of vorticity at the outer boundary of the computational domain that is associated with the normal component of the velocity.

In summary, then, the model flow, presented in part A of this section, provides the following picture regarding the vorticity dynamics of the viscous wall region: The spanwise and lateral components of the vorticity can be amplified due to vortex stretching but there is no source (or sink) for the streamwise component. The streamwise vorticity, then, for the model flow is created at the solid boundary and can also be convected inside the viscous wall region through the outer boundary at $y=y_o$. Since the pressure gradient in the x-direction is assumed to be negligible, there is no flux of spanwise vorticity through the wall.

It is thus seen that important elements of vortex-dynamics, that have been related to the existence of the wall streaks as discussed earlier, are not precluded by the model flow. It is also seen that the assumption of homogeneity does not affect the three-dimensional nature of the model as far as the vorticity dynamics picture is concerned.

We will now conclude this part of section II by deriving the balance equations for the mean flow energy, the non-zero components of the Reynolds stress tensor and for the turbulent kinetic energy in the model flow.

According to the classical theory of turbulence (Tennekes and Lumley, 1977) the internal dynamics of turbulence transfer energy from large scales to small scales. For a fully developed turbulent flow in a pipe (or channel) the energy supplied to the flow comes from the imposed pressure gradient. This energy is supplied to the mean flow eddies whose size is comparable to a characteristic dimension of the container (pipe radius or channel height). Turbulence, then, extracts energy from the mean flow eddies and by nonlinear interaction cascades it from large to small eddies, down to the Kolmogorov microscale eddies where the energy is dissipated into heat.

For a fully developed turbulent flow in a channel the following equation, describing the mean flow energy balance, can be obtained from Hinze's (1975) general expression, after eliminating all the terms that are equal to zero (all the variables are dimensionless):

$$\overline{U}\frac{d\overline{P}}{dx} = \overline{uv}\frac{d\overline{U}}{dy} + \frac{d}{dy}(-\overline{uv}\overline{U}) + \frac{1}{\mathrm{Re}}\frac{d}{dy}(\overline{U}\frac{d\overline{U}}{dy}) - \frac{1}{\mathrm{Re}}(\frac{d\overline{U}}{dy})^2 \qquad (4.45)$$

The term on the left hand side of equation (4.45) represents the rate of energy supply to the mean flow by the imposed pressure gradient ($\frac{d\overline{P}}{dx}$). The first term on the right hand side is the amount of energy extracted from the mean flow by the working of the Reynolds stress ($-\overline{uv}$) against the mean shear ($\frac{d\overline{U}}{dy}$). The last term on the r.h.s. is the energy that is directly dissipated from the mean flow into heat. The remaining two terms are transfer terms and redistribute the mean flow energy between different regions of the flow field. If equation (4.45) is integrated over half the cross-section of the channel (due to symmetry), the transfer terms drop out because $\overline{U}$ is zero on the boundaries and the following equation is obtained:

$$\frac{d\overline{P}}{dx}\int_0^H \overline{U}dy = \int_0^H \overline{uv}\frac{d\overline{U}}{dy}dy - \int_0^H \frac{1}{\mathrm{Re}}(\frac{d\overline{U}}{dy})^2 dy \qquad (4.46)$$

where H is the dimensionless half-height of the channel. Equation (4.46), then, shows that the total amount of energy given to the mean flow by the pressure gradient, goes partly into turbulent kinetic energy and partly into direct viscous dissipation. The implications of equation (4.46) can be made more clear if one divides the whole flow field into two regions: one extending from the wall to the edge of the viscous wall region ($y^+ \approx 40$) and the other extending from $y^+ \approx 40$ to the axis of the channel (core region). If now equation (4.45) is integrated separately over these two flow regions, the following equations are obtained:

$$\text{(core region)} \quad \frac{d\overline{P}}{dx}\int_{y_o}^{H}\overline{U}dy = [\overline{uv}\overline{U}]_{y=y_o}$$

$$\text{(viscous wall region)} \quad \frac{d\overline{P}}{dx}\int_{0}^{y_o}\overline{U}dy = \int_{0}^{y_o}\overline{uv}\frac{d\overline{U}}{dy}dy - [\overline{uv}\overline{U}]_{y=y_o} - \int_{0}^{y_o}\frac{1}{\mathrm{Re}}(\frac{d\overline{U}}{dy})^2dy$$

During the above integrations the following assumptions were made: 1) $\overline{uv}\frac{d\overline{U}}{dy}\approx 0$ in the core region because the mean shear is very small, 2) $\overline{uv}=0$ at $y=H$ and 3) the two viscous terms on the r.h.s. of equation (4.45) are negligible in the core region and at the edge of the viscous wall region. The above two equations can be rewritten as follows:

$$\text{(core region)} \quad \frac{d\overline{P}}{dx}(H-y_o)<\overline{U}>_c = [\overline{uv}\overline{U}]_{y=y_o} \tag{4.47}$$

$$\text{(wall region)} \quad \frac{d\overline{p}}{dx}y_o<\overline{U}>_{v.w.} = \int_{0}^{y_o}\overline{uv}\frac{d\overline{U}}{dy}dy - [\overline{uv}\overline{U}]_{y=y_o} - \int_{0}^{y_o}\frac{1}{\mathrm{Re}}(\frac{d\overline{U}}{dy})^2dy \tag{4.48}$$

where now $<\overline{U}>_c$ and $<\overline{U}>_{v.w.}$ are the average mean streamwise velocities in the core and the viscous wall region respectively. Since $H-y_o>>y_o$, especially for high Reynolds number, and $<\overline{U}>_c \; > \; <\overline{U}>_{v.w.}$ it is clear from (4.47) and (4.48) that most of the energy supply from the pressure gradient to the mean flow takes place in the core region. The very small amount of mean flow kinetic energy production in the viscous wall region justifies, then, the omission of the term $-\frac{\partial P}{\partial x}$ in equation (4.3). It can also be seen now that the term $[\overline{uv}\overline{U}]_{y=y_o}$ provides the link between equations (4.47) and (4.48). This term represents the total amount of energy transferred from the core region, where it is mainly produced, into the viscous wall region. It is also to be noticed that the sum of equa-

tions (4.47) and (4.48) gives back equation (4.46). So the picture that emerges for the balance of the mean flow kinetic energy is the following: Almost all of the mean flow kinetic energy is produced by the pressure gradient in the core region, according to equation (4.47). This energy is transferred by the term on the r.h.s. of equation (4.47) to the viscous wall region, where it is expended in two ways: Part of it is extracted by the turbulent motion and the rest of it goes into direct viscous dissipation.

In order to complete the picture for the energy balance of the flow field we have to consider the equation that expresses the conservation of turbulent kinetic energy. For this purpose we first develop the balance equations for the non-zero components of the Reynolds stress tensor. The equation for the turbulent kinetic energy can subsequently be obtained from the trace of the Reynolds stress tensor.

If we start from the N–S equations that describe the fluctuating flow field u_i and multiply both sides by the fluctuating velocity u_j we obtain the following equation:

$$\frac{\partial}{\partial t}\overline{u_i u_j} + \overline{U}_l \frac{\partial}{\partial x_l}\overline{u_i u_j} = -\left[\overline{u_j u_l}\frac{\partial \overline{U}_i}{\partial x_l} + \overline{u_i u_l}\frac{\partial \overline{U}_j}{\partial x_l}\right]$$
$$- \frac{\partial}{\partial x_l}\overline{u_i u_j u_l} - \frac{\partial}{\partial x_i}\overline{u_j p} - \frac{\partial}{\partial x_j}\overline{u_i p} + \overline{p\frac{\partial u_i}{\partial x_j}} + \overline{p\frac{\partial u_j}{\partial x_i}}$$
$$+ \frac{1}{\mathrm{Re}}\nabla^2\overline{u_i u_j} - \frac{2}{\mathrm{Re}}\overline{\frac{\partial u_i}{\partial x_l}\frac{\partial u_j}{\partial x_l}} \qquad (4.49)$$

where $u_i = U_i - \overline{U}_i$, $U_1 = U$, $U_2 = v$, $U_3 = w$. In this equation all the variables are dimensionless and the overbar denotes a quantity averaged both in space and

time. The first term on the r.h.s. of (4.49) is a production term and the last one is dissipative. The rest of the terms on the same side of the equation are transfer terms except $\overline{p(\frac{\partial u_i}{\partial x_j}+\frac{\partial u_j}{\partial x_i})}$. The diagonal terms of this tensor would be $2\overline{p\frac{\partial u_1}{\partial x_1}}$, $2\overline{p\frac{\partial u_2}{\partial x_2}}$ and $2\overline{p\frac{\partial u_3}{\partial x_3}}$ and the trace $2\overline{p\left(\frac{\partial u_1}{\partial x_1}+\frac{\partial u_2}{\partial x_2}+\frac{\partial u_3}{\partial x_3}\right)}$ is zero because of continuity. So this term does not contribute anything to the turbulent kinetic energy budget but redistributes the energy among the three components of the velocity. If, for example, $\overline{p\frac{\partial u_1}{\partial x_1}}<0$ and $\overline{p\frac{\partial u_2}{\partial x_2}}>0$, $\overline{p\frac{\partial u_3}{\partial x_3}}>0$ (so that continuity is satisfied) turbulent kinetic energy is transferred from the u_1 component of the velocity to the u_2 and u_3 components.

If, now, in (4.49) we substitute u,v and w for u_1,u_2 and u_3 and U, 0, 0 for U_1, U_2, U_3 respectively, and use the assumption of homogeneity, we obtain the following equations (stationary state) for $\overline{u^2}$,$\overline{v^2}$ and $\overline{w^2}$:

$$0=-\overline{uv}\frac{dU}{dy}-\frac{\partial}{\partial y}\overline{v\frac{u^2}{2}}+\frac{1}{\mathrm{Re}}\frac{\partial^2}{\partial y^2}\left(\frac{\overline{u^2}}{2}\right)-\frac{1}{\mathrm{Re}}\left[\overline{\left(\frac{\partial u}{\partial y}\right)^2}+\overline{\left(\frac{\partial u}{\partial z}\right)^2}\right] \tag{4.50}$$

$$0=-\frac{\partial}{\partial y}\overline{v\frac{v^2}{2}}-\frac{\partial}{\partial y}\overline{pv}+\overline{p\frac{\partial v}{\partial y}}+\frac{1}{\mathrm{Re}}\frac{\partial^2}{\partial y^2}\left(\frac{\overline{v^2}}{2}\right)-\frac{1}{\mathrm{Re}}\left[\overline{\left(\frac{\partial v}{\partial y}\right)^2}+\overline{\left(\frac{\partial v}{\partial z}\right)^2}\right] \tag{4.51}$$

$$0=-\frac{\partial}{\partial y}\overline{v\frac{w^2}{2}}+\overline{p\frac{\partial w}{\partial z}}+\frac{1}{\mathrm{Re}}\frac{\partial^2}{\partial y^2}\left(\frac{\overline{w^2}}{2}\right)-\frac{1}{\mathrm{Re}}\left[\overline{\left(\frac{\partial w}{\partial y}\right)^2}+\overline{\left(\frac{\partial w}{\partial z}\right)^2}\right] \tag{4.52}$$

and for the Reynolds shear stress $\overline{uv}$:

$$0 = -\overline{v^2}\frac{dU}{dy} - \frac{\partial}{\partial y}\overline{uv}\,v - \frac{\partial}{\partial y}\overline{pu} + p\overline{\frac{\partial u}{\partial y}} + \frac{1}{\mathrm{Re}}\frac{\partial^2}{\partial y^2}\overline{uv} - \frac{2}{\mathrm{Re}}\left[\overline{\frac{\partial u}{\partial y}\frac{\partial v}{\partial y}} + \overline{\frac{\partial u}{\partial z}\frac{\partial v}{\partial z}}\right]$$

So the model flow views the turbulent kinetic energy to be produced in the streamwise component of the velocity by the working of the Reynolds stress $-\overline{uv}$ on the mean shear $\frac{dU}{dy}$. Since the $p\overline{\frac{\partial u}{\partial x}}$ transfer term is absent, due to the assumption of homogeneity, there is no transfer of energy from the axial direction to the y–z plane. However, since $p\overline{\frac{\partial v}{\partial y}}$ and $p\overline{\frac{\partial w}{\partial z}} \neq 0$, there can be transfer of energy between these two components of the velocity. The Reynolds stress is produced by the term $-\overline{v^2}\frac{dU}{dy}$ which is negative because $\overline{uv} < 0$. At the outer boundary, $y = y_e$, of the model flow there are convective fluxes of $\overline{u^2}, \overline{v^2}$ and $\overline{w^2}$ energy ($\overline{vu^2}, \overline{v^3}, \overline{vw^2}$) as well as transfer of $\overline{v^2}$ energy by pressure diffusion ($\overline{pv}$). Since there is no $\overline{v^2}$ and $\overline{w^2}$ energy produced, the energy on the y–z plane should come from the outer boundary. There is, however, a significant transfer of energy from the normal to the spanwise component of the velocity through the transfer term $p\overline{\frac{\partial w}{\partial z}} = -p\overline{\frac{\partial v}{\partial y}}$, as will be seen in Chapter 6.

The balance equation for the turbulent kinetic energy can be obtained from Hinze's (1975) general expression when applied to the channel flow being considered. The same equation results after summing both parts of equations (4.50), (4.51) and (4.52), but we prefer to use the general expression in order to emphasize the different formulations of the terms that depend on the viscosity (Reynolds number). The resulting expression is the following:

$$0 = -\frac{\partial}{\partial y}\left[\overline{v\left(p + \frac{q^2}{2}\right)} - \overline{uv}\frac{d\overline{U}}{\partial y} + \frac{1}{\mathrm{Re}}\frac{\partial}{\partial x_j}\left[\overline{u_i\left(\frac{\partial u_i}{\partial x_j} + \frac{\partial u_j}{\partial x_i}\right)}\right] - \right.$$

$$\left.\frac{1}{\mathrm{Re}}\left[\overline{\frac{\partial u_i}{\partial x_j}\left(\frac{\partial u_i}{\partial x_j} + \frac{\partial u_j}{\partial x_i}\right)}\right]\right] \qquad (4.53)$$

where the last two terms have been kept in indicial notation in order to preserve the compactness of equation (4.53). In this equation $q^2 = u^2 + v^2 + w^2$ is twice the instantaneous turbulent kinetic energy. The explanation of each term of the above equation is the following: The second term on the r.h.s. represents the production of trubulent kinetic energy. This term appears with opposite sign in equation (4.45). The last term is the dissipation of turbulent kinetic energy into heat. The other two terms are transfer terms and redistribute the turbulent kinetic energy between different regions of the flow. Sometimes the last two terms in equation (4.53) are written as follows: $\frac{1}{\mathrm{Re}}\frac{\partial^2}{\partial x_j \partial x_j}\left(\frac{\overline{q^2}}{2}\right) - \frac{1}{\mathrm{Re}}\overline{\frac{\partial u_i}{\partial x_j}\frac{\partial u_i}{\partial x_j}}$ (Hinze, 1975). In this formulation the last term is not the true dissipation but the dissipation that would exist in an isotropic field and is thus called "isotropic" dissipation. The first term is similar to the one that would exist in a heat flow equation and, thus, represents viscous diffusion of turbulent kinetic energy. The same terms are obtained from a summation of (4.50), (4.51) and (4.52) because these equations were formulated in terms of the "isotropic" dissipation. From now on we will be using D to denote the true dissipation and D_{is} for the "isotropic" dissipation. By comparing the "isotropic" formulation of turbulent kinetic energy to the sum of (4.50), (4.51) and (4.52) we can see that for the model flow:

$$D_{is}=\frac{1}{\mathrm{Re}}\left[\overline{\left(\frac{\partial u}{\partial y}\right)^2}+\overline{\left(\frac{\partial u}{\partial z}\right)^2}+\overline{\left(\frac{\partial v}{\partial y}\right)^2}+\overline{\left(\frac{\partial v}{\partial z}\right)^2}+\overline{\left(\frac{\partial w}{\partial y}\right)^2}+\overline{\left(\frac{\partial w}{\partial z}\right)^2}\right]$$

If equation (4.53) is integrated over half the cross-section of the channel the following equation is obtained:

$$\int_0^H \overline{uv}\frac{d\overline{U}}{dy}dy=-\int_0^H \frac{1}{\mathrm{Re}}D\,dy \tag{4.54}$$

Equation (4.54) then shows that the total amount of turbulent kinetic energy produced is converted into heat by viscous dissipation. If now, in equation (4.46) we substitute the first term on the r.h.s. using equation (4.54) we obtain:

$$\frac{d\overline{P}}{dx}\int_0^H \overline{U}dy=-\int_0^H \frac{1}{\mathrm{Re}}D\,dy-\int_0^H \frac{1}{\mathrm{Re}}\left(\frac{d\overline{U}}{dy}\right)^2 dy$$

This equation expresses the fundamental conservation law that all the available energy from the pressure gradient is finally converted into heat by direct viscous dissipation and by dissipation through the turbulent motion.

A better insight into equation (4.53) can be obtained if we integrate it over the viscous wall region of the flow field. If the viscous transfer term is neglected at $y=y_o$, the following equation results:

$$0=\int_0^{y_o} -\overline{uv}\frac{d\overline{U}}{dy}dy-\int_0^{y_o}\frac{1}{\mathrm{Re}}D\,dy-\overline{v\left(p+\frac{q^2}{2}\right)}\;\Big|_{y=y_o}$$

This equation shows that the total amount of turbulent kinetic energy produced in the viscous wall region is partly dissipated and the rest is transferred to the core region by the last term on the r.h.s. This term represents a combined diffusion of kinetic energy by pressure-normal velocity interaction (pressure-

diffusion) and convection of energy by the v-component of the velocity.

In summary, then, the overall picture for the energy balance of the model flow is as follows: The mean flow kinetic energy is produced by the pressure gradient in the core region of the flow field. This energy is then transferred to the viscous wall region where part of it goes into turbulence and the rest is converted into heat by direct viscous dissipation. The turbulent kinetic energy is produced into the viscous wall region. The mean flow energy that is necessary to produce the turbulence does not result from a direct action of the pressure gradient but is transferred into the viscous wall region from the core where the pressure gradient produces almost all of the mean flow energy. Part, then, of the turbulent kinetic energy produced is dissipated into heat and the rest is transferred back to the core region.

CHAPTER 5

RESULTS

I. Analysis of experimental data

A. Relation of wall patterns to transverse velocity fluctuations in the fluid

Figures 5 and 6 show results of experiments in which the s_z patterns detected at the wall are associated with transverse velocity fluctuations in the fluid at $y^+=20$ and 40. The fluid probe was located at $\Delta x^+=25$, and this separation causes only a small delay time of $T^+\approx 1.5$ in detecting events at $x^+=0$ at the same y^+. Lag times between events at the fluid probe and the array of wall probes therefore can be associated primarily with the separation normal to the wall.

The s_z-patterns shown in Figures 5 and 6 were conditionally averaged for a positive transverse flow at $z^+=0$ using condition (a) of Chapter 4 with $\tilde{S}_d=4$. Data points were actually taken every $\Delta T^+=0.7$ but the results are presented every $\Delta T^+=2.1$. Fifty events were averaged for $y^+=40$ and forty-nine events for $y^+=20$. The effect of the threshold level $\tilde{S}_d$ on the number of events obtained is shown in Table 7.

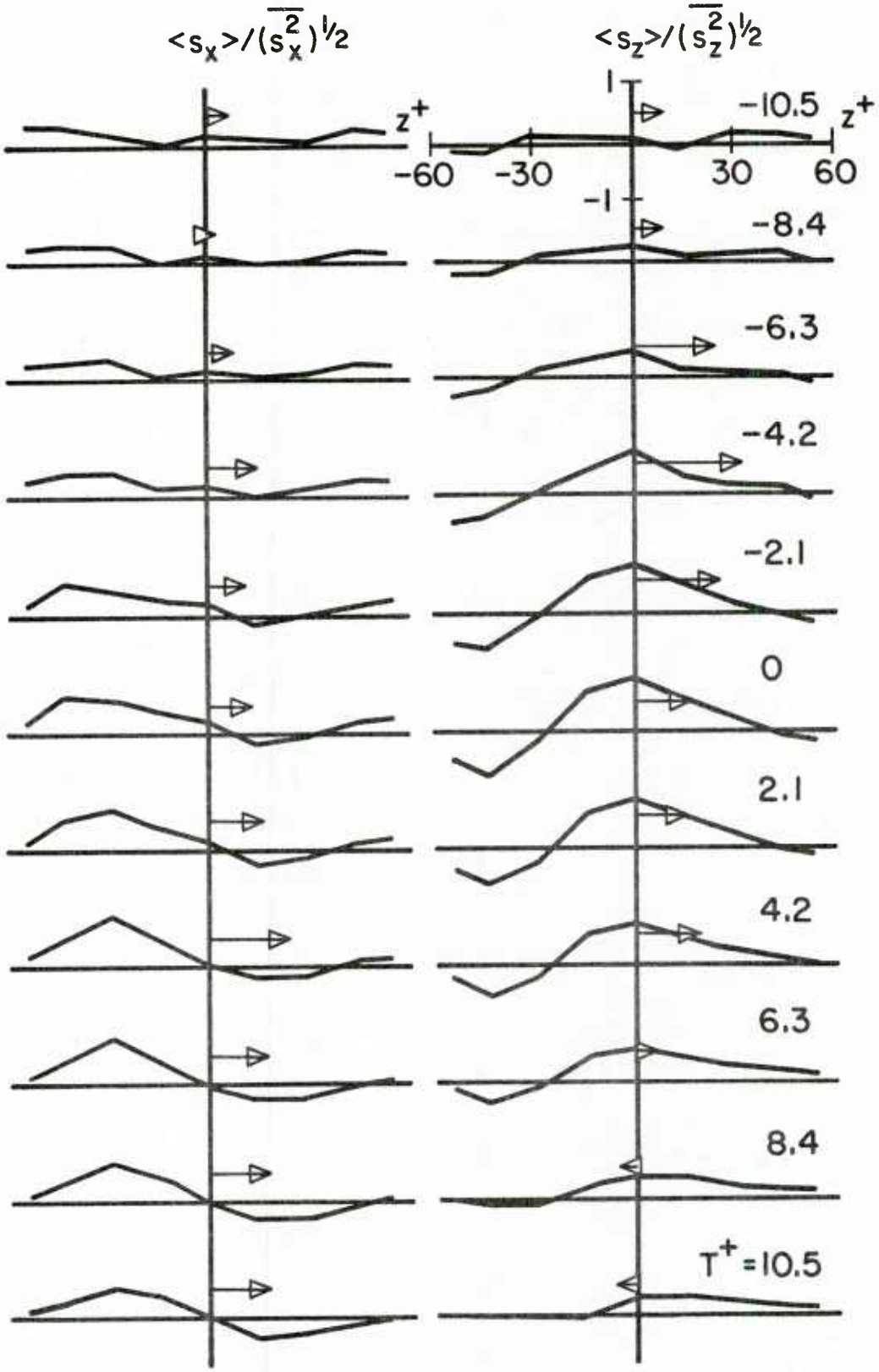

Figure 5 Conditionally averaged data for positive transverse flows at the wall; the fluid probe at $y^+ = 20$

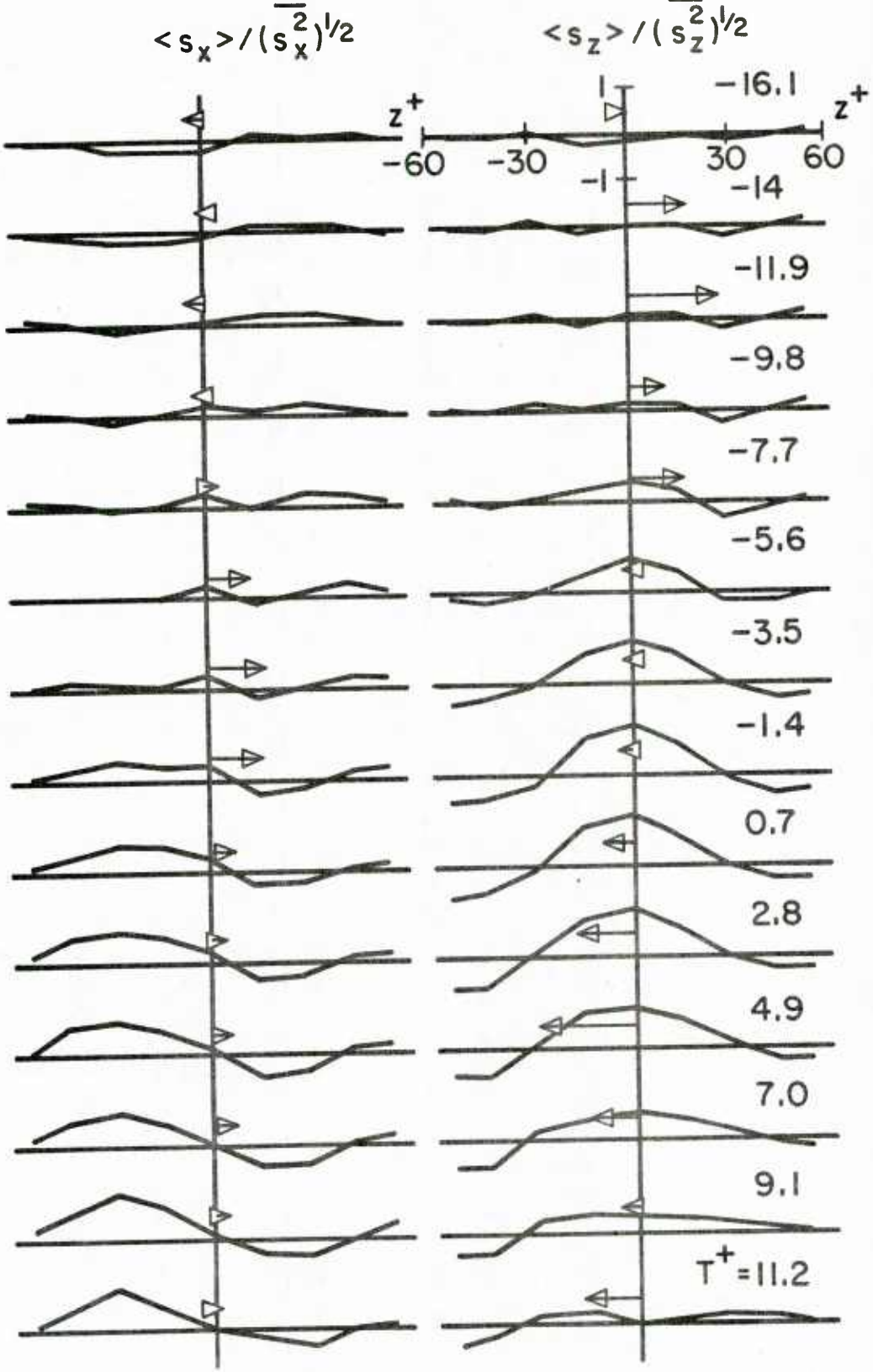

Figure 6 Conditionally averaged data for positive transverse flows at the wall; the fluid probe at $y^+ = 40$

Table 7

$\tilde{S}_d$	Fluid Probe at $y^+=40$		
	# of PTF's	# of NTF's	# of OUTFLOWS
3	59	62	59
4	50	56	52
5	43	42	44
6	37	38	38

It is seen that even large threshold levels one obtains a sufficient number of events according to arguments presented in Chapter 4.

As seen in the run with the fluid probe at $y^+=20$, a s_z profile with a maximum at $z^+=0$ and a wavelength of $\lambda^+\approx100$ starts to develop at $T^+=-9.1$, reaches its maximum amplitude of $1.0(\overline{s_z^2})^{1/2}$ at $T^+=0.7$ and dies out at $T^+=9.8$. It is to be noted that the s_x profiles lag the development of the s_z profiles by $\Delta T^+\approx7.7$. These are sine waves with a maximum at $z^+=-25$ and a minimum at $z^+=25$, corresponding to coupled inflows and outflows at these locations.

The arrows in Figures 5 and 6 represent the magnitude and direction of the conditionally averaged z and x velocity components at $y^+=20$ or 40. An arrow extending to $z^+=60$ indicates a value of $<w>/(\overline{w^2})^{1/2}$ or of $<u>/(\overline{u^2})^{1/2}$ of plus one. An arrow extending to $z^+=-60$ indicates a ratio of the conditionally averaged to the root mean squared fluctuating velocity component of minus one. It is noted that positive transverse flows at the wall are associated with positive transverse flows at $y^+=20$. The transverse flow at $y^+=20$ attains a maximum

value of $0.6(\overline{w^2})^{1/2}$ at $T^+ = -3.5$, indicating that the flow at the wall lags that at $y^+ = 20$. This is consistent with the finding by Hatziavramidis and Hanratty (1979) and by Kreplin and Eckelmann (1979a) that it takes a finite time for disturbances in the outer flow to propagate to the wall.

The conditionally averaged s_x and s_z profiles obtained in the run with the probe at $y^+ = 40$ are very similar to those shown in Figure 5, as would be expected if the experiments were reproducible. The arrows in Figure 6 represent the magnitude and direction of the conditionally averaged z and x velocity components at $y^+ = 40$. It is noted that at $y^+ = 40$ the conditionally averaged transverse component is positive before the flow at the wall starts to build up and has a maximum value of $0.5(\overline{w^2})^{1/2}$ at $T^+ = -12.6$. Around $T^+ = 0$ where s_z reaches its maximum amplitude of $1.15(\overline{s_z^2})^{1/2}$, the conditionally averaged w changes sign. We interpret these results as indicating that the flow at the wall is caused by transverse velocity fluctuations of the same sign at $y^+ = 40$. Because it takes a finite time for disturbances at $y^+ = 40$ to propagate to the wall the flow at $y^+ = 40$ has, on average, changed direction when activity at the wall is a maximum.

Kreplin and Eckelmann (1979a) made measurements of the correlation between s_z and the transverse component of the velocity at $y^+ = 5$, 10, 20, 40 and at $\Delta x^+ = -108$, 0, + 144. The results shown in Figure 6 agree with their measurements in that they found that disturbances propagate to the wall and that the correlations at $y^+ = 40$ are negative. However, Kreplin and Eckelmann

interpreted their results differently. As mentioned in Chapter 2, they deduced that the wall region is dominated by pairs of inclined, counterrotating streamwise vortices with an average transverse separation of their centers of about $z^+ \approx 50$ and a length of $x^+ \approx 1200$. They envisioned that as these vortices are convected downstream the angle of their plane of rotation decreases and that the average minimum distance of the vortex center from the wall is $y^+ \approx 30$.

B. Streamwise variation of the eddy structure

Correlations calculated from the measurements of Lau (1980) cover a much wider range of Δx^+ than the measurements of Kreplin and Eckelmann and do not agree with the physical picture of the wall eddies presented by them. The correlation coefficients were measured as a function of the three spatial coordinates (x^+, y^+, z^+) and time delay (τ^+). The origin of the coordinate system $(x^+=0, y^+=0, z^+=0)$ is the projection of the fluid probe on the wall. When $\tau^+ < 0$ the signal from the wall probe leads the one from the fluid probe and vice versa. The correlation coefficients $R_{uu_z}(-25, y^+, 0; \tau^+)$ and $R_{ww_z}(-25, y^+, 0; \tau^+)$ calculated for $y^+=20$ and 40 are in qualitative agreement with measurements by Kreplin and Eckelmann (1979a). The chief difference is that the peaks appear at smaller time delays because the probes are separated in the streamwise direction. The correlation $R_{ww_z}(-25, 40, 0; \tau^+)$ attained negative values during the period $-15 \leq \tau^+ \leq 2$ and a maximum value of 0.124 at $\tau^+ = 14.7$.

However, as shown in Figure 7 the correlation $R_{ww_z}(x^+, 40, 0; 0)$ is negative only for $x^+ = -25$ and is positive for all other values of x^+. When the fluid probe

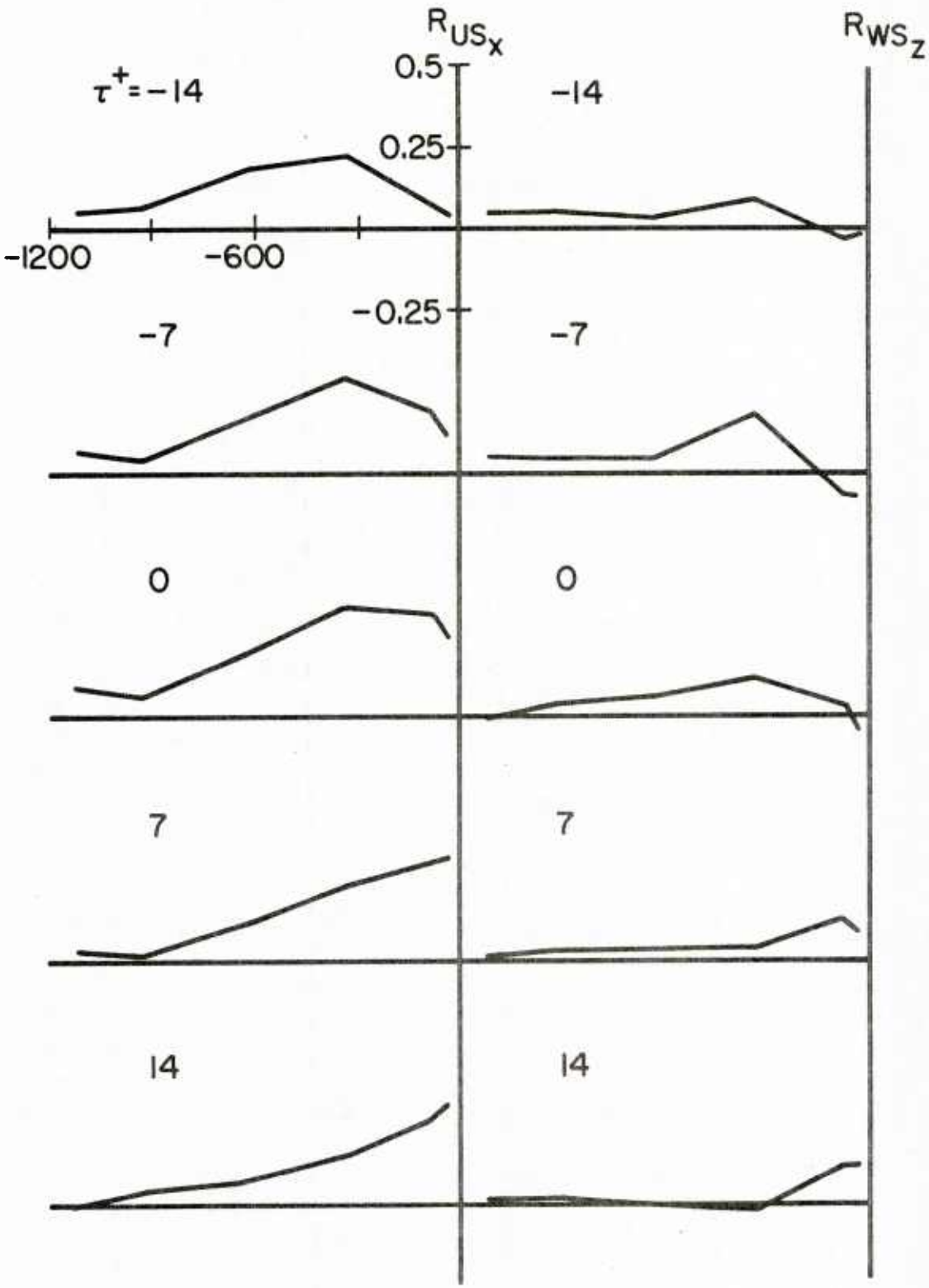

Figure 7 Measurements of $R_{us_x}(x^+, 40, 0; \tau^+)$ and $R_{ws_z}(x^+, 40, 0; \tau^+)$

is delayed negative values appear only at $x^+=75$ and $x^+=25$. When the wall probe is delayed ($\tau^+>0$) R_{ws_z} is positive at all x^+ stations. For the results shown in Figure 7 to be consistent with the vortex model it would be necessary for $R_{ws_z}(x^+, 40, 0; \tau^+)$ to be negative for a longer extent in the direction of the flow for $\tau^+<0$.

We prefer to interpret these correlation measurements by assuming that the flow at the wall is caused by flow disturbances in the same direction at $y^+\approx 40$. These disturbances have a convection velocity in the streamwise direction of $c_x^+\approx 15$ and in a direction normal to the wall of $c_y^+\approx 2$ at $y^+=40$, $c_y^+\approx 1.5$ at $y^+=20$ (Kreplin and Eckelmann, 1979a). According to this type of interpretation it takes a period of $\Delta T^+=20$ for a disturbance to travel from $y^+=40$ to the wall. Over this same period the disturbance would be convected downstream a distance of $\Delta x^+=300$. Thus it would be expected that large positive or negative transverse flows at $x^+=0$, $y^+=40$ would be associated with large positive or negative values of s_z at $x^+=-300$. The observed peak in $R_{ws_z}(x^+, 40, 0; \tau^+)$ shown in Figure 7 is consistent with this picture. The correlation coefficient $R_{us_z}(x^+, 40, 0; \tau^+)$ also shows a peak around $x^+=-300$ at $\tau^+=0$, which moves toward the fluid probe ($x^+=0$) for positive time delays.

Correlation measurements of $R_{us_z}(x^+, y^+, 0; \tau^+)$ and $R_{ws_z}(x^+, y^+, 0; \tau^+)$ with $y^+=20$ are shown in Figure 8. These show a similar behavior to those for $y^+=40$ in Figure 7. The only difference is that for $y^+=20$ R_{ws_z} is positive at all x^+ stations for any τ^+ and the peaks at $\tau^+=0$ appear closer to the origin. This

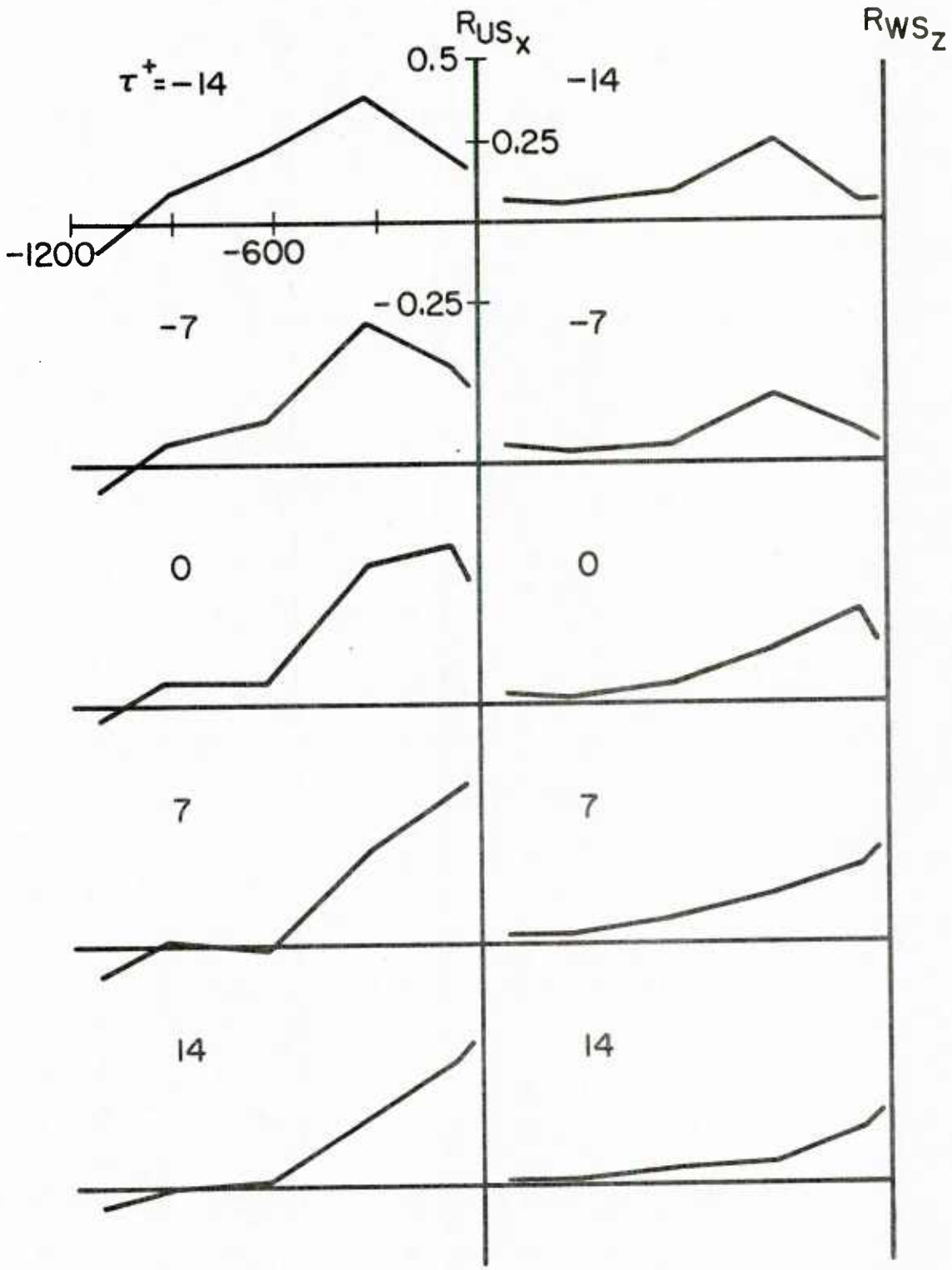

Figure 8 Measurements of $R_{us_z}(x^+, 20, 0; \tau^+)$ and $R_{ws_z}(x^+, 20, 0; \tau^+)$

is consistent with the above physical picture since it takes a shorter time, $\Delta T^+ \approx 13$, for disturbances at $y^+ = 20$ to propagate to the wall.

Measurements of the conditionally averaged streamwise variation of s_z shown in Figure 9 are consistent with the correlation measurements. The events that triggered the conditional averaging in Figures 5 and 6, a $s(z)$ profile at $x^+ = 0$ which indicated a strong positive transverse flow centered at $z^+ = 0$, were used to define $T^+ = 0$. The arrows indicate th magnitude and the direction of the transverse flow either at $y^+ = 20$ or $y^+ = 40$. An arrow length of + 750 indicates a value of $< w > / (\overline{w^2})^{1/2}$ or $< u > / (\overline{u^2})^{1/2}$ equal to plus one.

The salient feature of the conditionally averaged $s_z(o,x)$ profiles is the appearance of a peak which, as time progresses, moves to $x^+ = 0$ at a velocity given approximately by $c_x^+ = 15$.

It is seen that a strong transverse flow at the wall at $x^+ = 0$ is on average accompanied by a strong spanwise flow at $y^+ = 20$, $T^+ = -4.2$, $x^+ = -25$ and at $y^+ = 40$, $T^+ = -12$, $x^+ = -25$. As estimated earlier, disturbances at $y^+ = 40$ and $y^+ = 20$ require time intervals of $\Delta T^+ = 20$ and $\Delta T^+ = 13$ to reach the wall. Again, if it is assumed that the convection velocity in the streamwise direction is $c_x^+ = 15$, the maximum in $< w >$ at $y^+ = 40$, $T^+ = -12$; $y^+ = 20$, $T^+ = -4.2$ should be accompanied by maxima in s_z at $x^+ = -15 \times 20 = -300$ and at $x^+ = -15 \times 13 = -200$. This is in approximate agreement with the conditionally averaged measurements of $s_z(o,x)$.

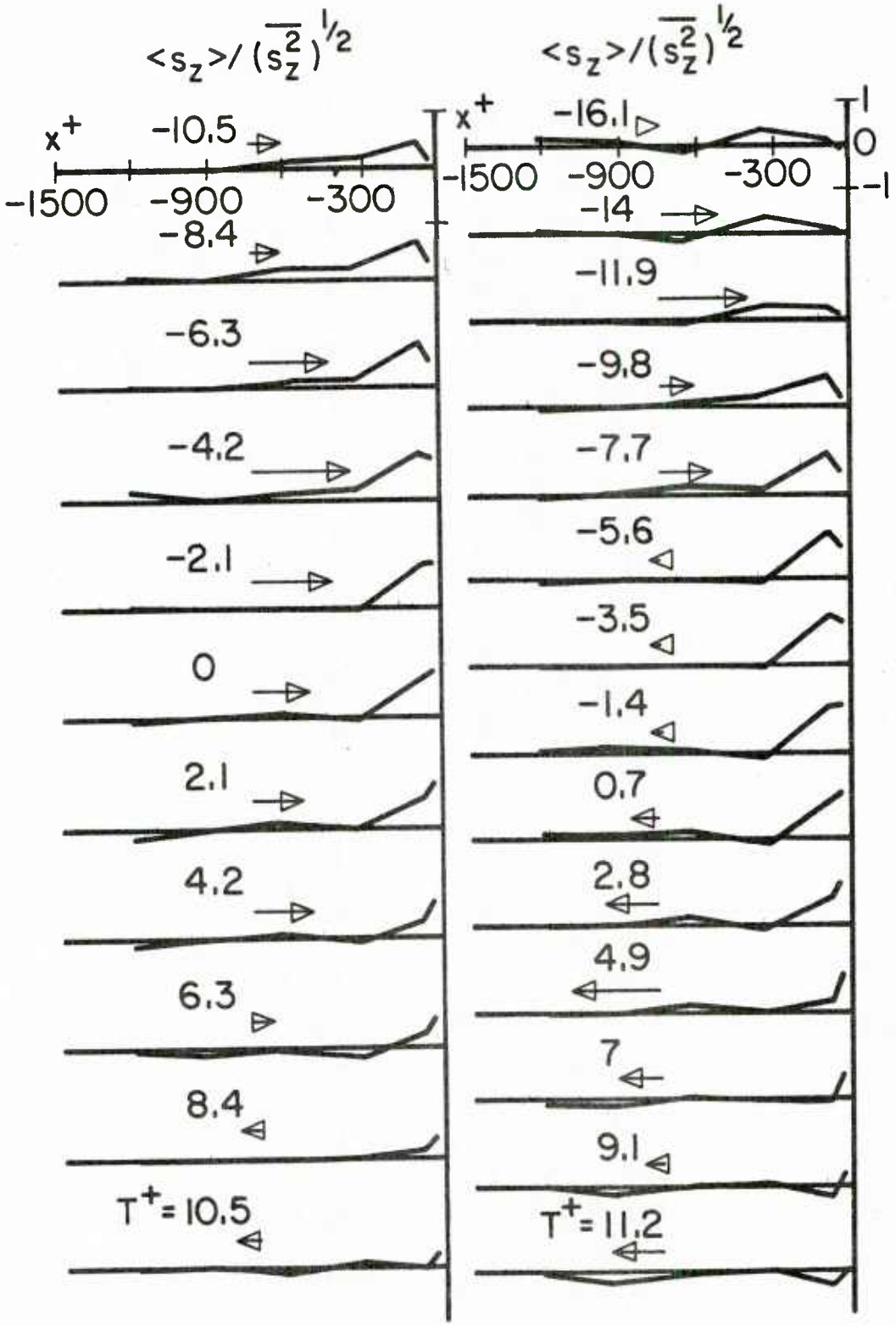

Figure 9 Conditionally averaged data for positive transverse flows at the wall; arrows indicate conditionally averaged transverse velocity, $<w>$, at $y^+=40$ (right side of figure) and $y^+=20$ (left side of figure). Arrow length of +750 indicates $<w>/(\overline{w^2})^{1/2}$ equal to +1

The flow reversal at $y^+=0$, $T^+\approx 0$ is not necessarily associated with a reversal of the flow at the wall. There is a hint of a negative flow developing at $x^+=-325$ for $-2.8\leq T^+\leq 4.2$ but this is not considered to be conclusive. The spatial variation of w in the spanwise direction at $y^+=40$, and not just its direction at a single point, determines the type of wall pattern seen by a fixed observerd at the wall. It is necessary for the flow at $y^+=40$ to reverse itself over a sufficient spanwise length in order that the spanwise flow at the wall will change its direction. Therefore, all positive transverse flows at the wall are not necessarily followed by negative transverse flows and vice versa.

C. Coherency normal to the wall

The correlation coefficients $R_{uu_z}(-25, y^+, z^+; \tau^+)$, $R_{ww_z}(-25, y^+, z^+; \tau^+)$, $R_{uu_z}(-25, y^+, z^+; \tau^+)$ and $R_{ww_z}(-25, y^+, z^+; \tau^+)$ for $y^+=40$ and 20 are shown in Figures 10 and 11 respectively. At $y^+=40$, R_{ww_z} shows again an interesting behavior. At zero time delay, the $R_{ww_z}(z^+)$ profile shows a wavelike variation with z^+, that has a wavelength of approximately $\Delta z^+\approx 90$. Negative values appear around $z^+=0$ at $\tau^+=0$, but at positive time delays the pattern reverses and positive values appear for all z^+'s. The wavelength is not so well defined for $\tau^+>0$; this is attributed to the fact that there is a certain amount of "jitter" associated with the wall patterns, as already mentioned in Chapter 4.

The cross correlations R_{uw_z} and R_{wu_z} are very well defined at $\tau^+=0$. They both show a wavelike variation with a wavelength of about 100 wall units and they are consistent with the flow picture presented in the previous part of this

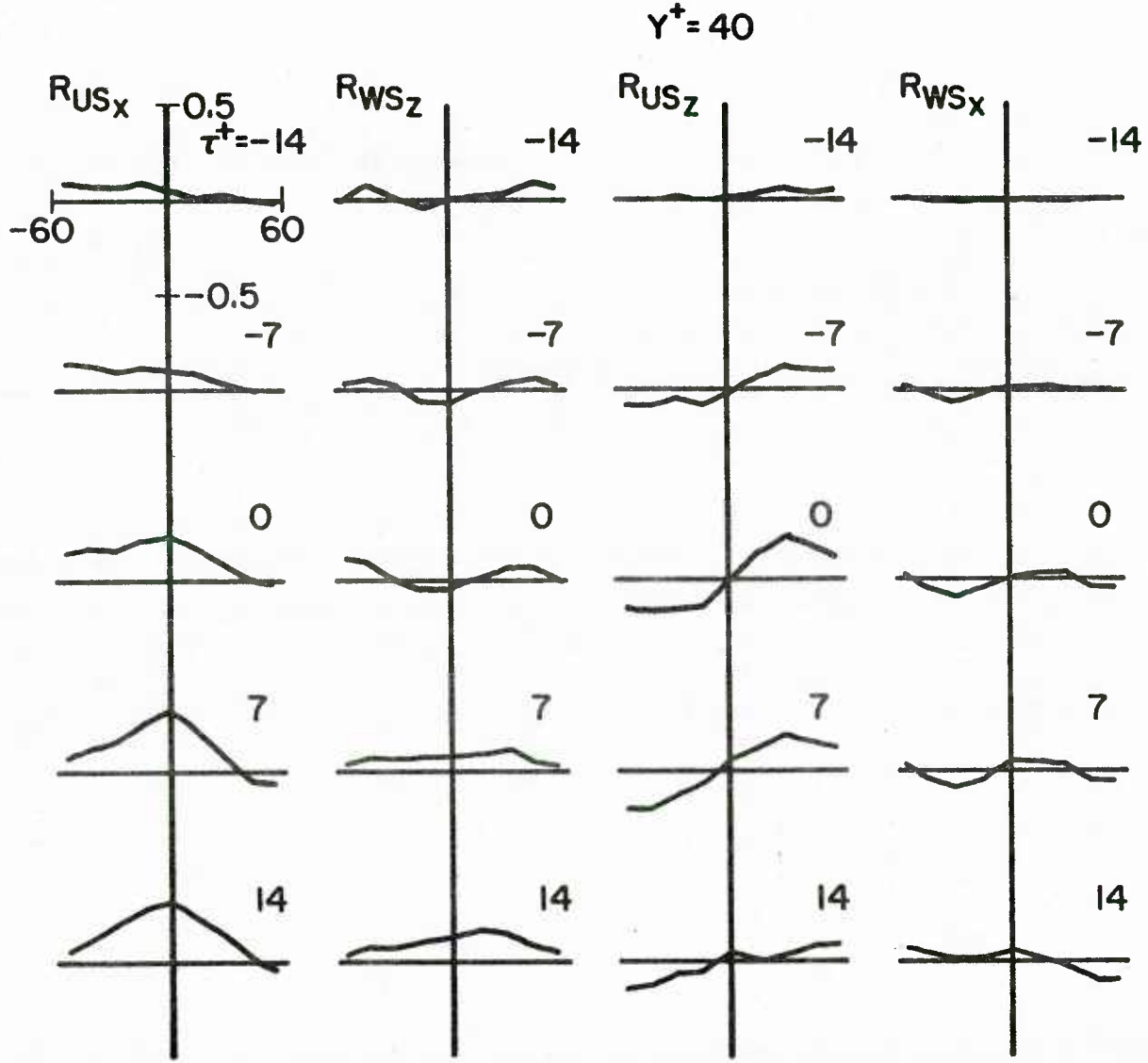

Figure 10 Measurements of $R_{uu_x}(-25, 40, z^+; \tau^+)$, $R_{ww_z}(-25, 40, z^+; \tau^+)$, $R_{uu_z}(-25, 40, z^+; \tau^+)$ and $R_{ww_x}(-25, 40, z^+; \tau^+)$

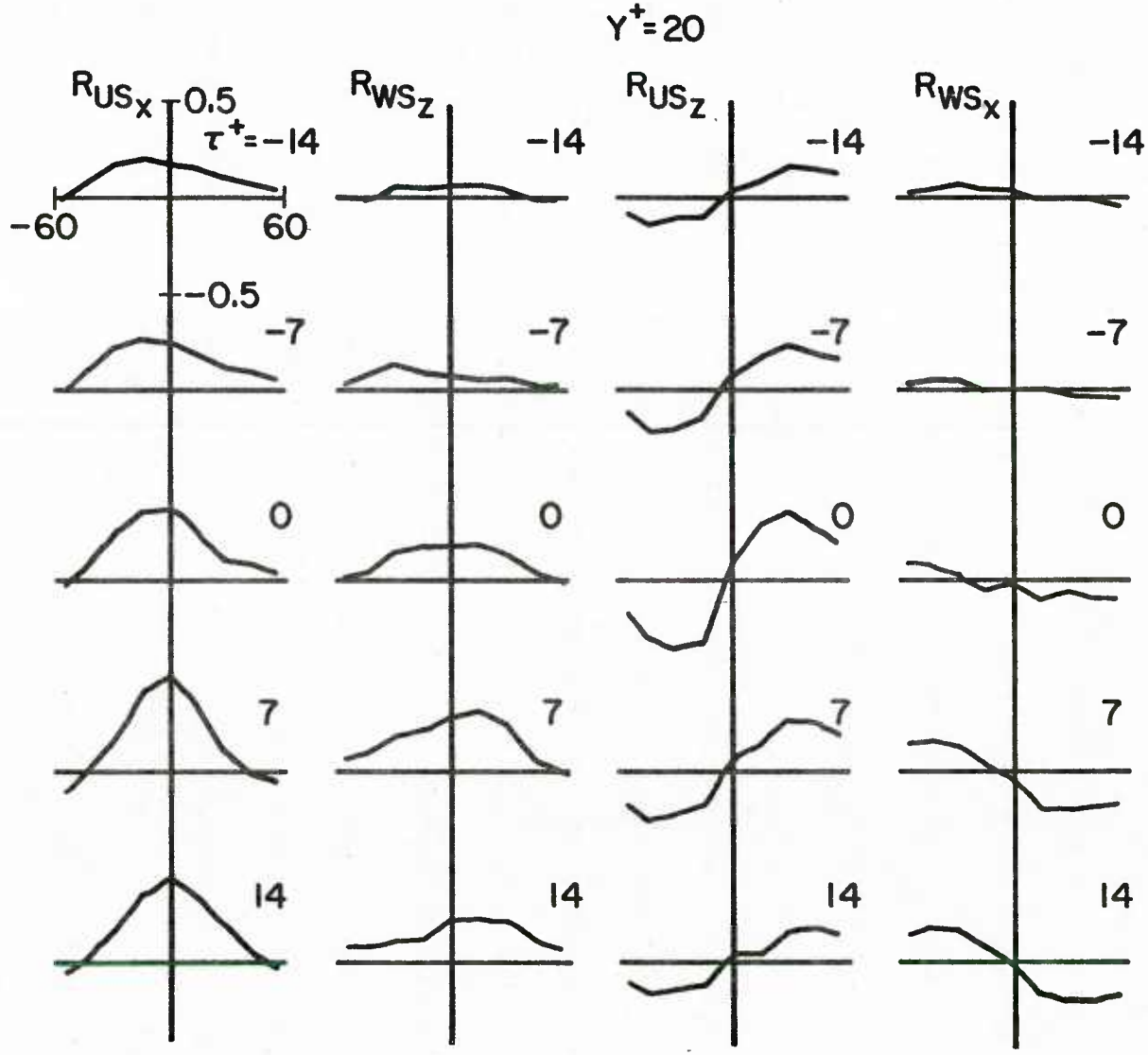

Figure 11 Measurements of $R_{uu_z}(-25, 20, z^+; \tau^+)$, $R_{ww_z}(-25, 20, z^+; \tau^+)$, $R_{uw_z}(-25, 20, z^+; \tau^+)$ and $R_{wu_z}(-25, 20, z^+; \tau^+)$

section. Notice the change in the R_{ws_z} pattern around $\tau^+ \approx 14$ which arises because w reverses direction at $y^+ = 40$.

At $y^+ = 20$, the situation is different. The correlation R_{ws_z} is positive for all z^+'s and time delays around $\tau^+ = 0$. The correlations R_{us_z} and R_{ws_z} are again well defined wavelike patterns and the difference in the R_{ws_z} pattern, from what was obtained with the probe at $y^+ = 40$, arises because w is in phase with the flow at the wall.

All the correlation coefficients are in agreement with the flow model presented in the previous section. In particular, the cross-correlation coefficients show a behavior that is similar to the one obtained at the wall. The present measurements agree well with measurements obtained by Lee et al (1974) using only wall probes (note that $R_{us_z}(-25, y^+, z^+; 0)$ is analogous to $R_{s_z s_z}(0, 0, z^+; 0)$ at the wall) supporting the assumption of coherency up to $y^+ = 40$.

Any conclusion about the wave-number variation of w at $y^+ = 40$ or 20 is not possible since the calculation of a correlation coefficient involves some sort of filtering (spatial filtering in this case). There is an indication that a wavelength selection occurs whose details are still unknown, and there is a definite need for an elucidation of this process.

II. Numerical computations

The solution of the vorticity and stream-function equations, subject to the boundary conditions (4.25), (4.26) and (4.27), is presented for $y_o^+ = 40$ and 15.

When the outer boundary of the computational domain is set at $y_o^+ = 40$, two cases are considered: In the first one, all the energy of the velocity fluctuations is associated with the $\lambda^+ = 100$ wall eddies. In the second case, a certain fraction of the $\overline{u^2}$, $\overline{v^2}$ and $\overline{w^2}$ energy at $y_o^+ = 40$ is attributed to the outer flow eddies. All the relative parameters that are needed to completely specify (4.25), (4.26) and (4.27) are selected according to arguments presented in Chapter 4.

For each case the results are presented in the following sequence: Contour plots of the stream-function, the streamwise vorticity and the streamwise component of the velocity are shown first for various points in time. Secondly, the three components of the velocity and the vorticity are cross-plotted for a fixed spanwise or lateral location in the cell as a function of time. Finally, space and time averaged statistical quantities are presented. Because of the unsteady nature of the calculations, path-line and streakline computations are also presented. The calculated path-lines are trajectories of inertia-free fluid particles in the cell. The streaklines, at each instant of time, constitute the locus of the endpoints of path-lines that originated from the same point, which will be referred to as "injection point". The calculated steaklines are, thus, helpful in comparing the numerical results of the present work with dye-visualization experiments.

The parameters that were used to specify the boundary conditions in the fixed cell runs presented below are summarized in Table 8.

Table 8

	y_o^+	T_{u1}^+	T_{u2}^+	T_{v1}^+	T_{v2}^+	T_{w1}^+	T_{w2}^+
Single harmonic	40	100	400	100		100	
Double harmonic	40	100	400	100	400	100	400
Single harmonic	15	100		100		100	

	E_{u1}	E_{v1}	E_{w1}	ϕ_{u1}	ϕ_{u2}	ϕ_{v1}	ϕ_{v2}	ϕ_{w2}
Single harmonic	.2025	1.00	1.00	252	150	72		
Double harmonic	.15	.75	.40	216	194.4	36	90	270
Single harmonic	1.00	1.00	1.00	269.7		153		

where the energies E_{u1}, E_{v1}, E_{w1} express the fraction of $\overline{u^2}, \overline{v^2}, \overline{w^2}$ energy respectively in the $\lambda^+ = 100$ eddies and all the phases are measured in degrees.

A. Upper boundary at $y_o^+ = 40$

1. One harmonic in the spanwise direction

In these calculations all the energy on the y–z plane is associated with the $\lambda^+ = 100$ eddies ($E_{v1}^+ = E_{w1}^+ = 1$). The outer flow eddies contain most of the energy of the streamwise velocity fluctuations and negligible amount of energy in the v and w components of the velocity. The outer flow u-eddies were assumed to have an infinite wavelength in the spanwise direction. Such eddies can be accommodated by a cell with $z_o^+ = 50$, which is sufficient to calculate the v–w motion, otherwise z_o^+ would have to be increased in order to account for u-eddies of finite wavelength longer than $\lambda^+ = 100$. This will be the case, when two harmonics are used in order to describe the flow on the y–z plane.

The temporal variation of the three components of the velocity was specified using a single harmonic in time. A case with a wide range of frequencies was also considered. In this case the velocites at $y_o^+=40$ were specified using the experimental data of Lau (1980).

When single frequencies are used for u,v and w the energy of the $\lambda^+=100$ u-eddies at $y_o^+=40$ can be calculated from Reynolds stress arguments, as shown in Chapter 4. Since in this case the outer flow eddies don't contribute to the Reynolds stress, the phase ϕ_{u2} cannot be estimated from similar arguments. It was found during the course of the computations that ϕ_{u2} affects the calculated skewness of the streamwise velocity fluctuations and the Reynolds stress close to the outer boundary $25\leq y^+\leq 40$. For ϕ_{u2} in the range 150°–200° the u-skewness and the Reynolds stress were found to have the best agreement with experimental data. It is to be noted that the value $\phi_{u2}=194.4$ calculated in Chapter 4, falls in the above range.

The results of the calculations are shown in the series of Figures 12 through 60. The evolution of the secondary flow pattern is shown for a period of time that is equal to the lifetime of the $\lambda^+=100$ eddies ($T^+=100$). Figures 12 through 21 show the streamline pattern of the flow for a case where the percentage of closed flow N_1 is 60%. It can be seen that, as expected, the flow at $y_o^+=40$ is closed during the periods $15\leq t^+\leq 45$ and $65\leq t^+\leq 95$, which constitute 60% of the total time. This closed flow is associated with a spinning mass of fluid which appears as a streamwise vortex. At $t^+=20$ the vortex occupies the whole cell in

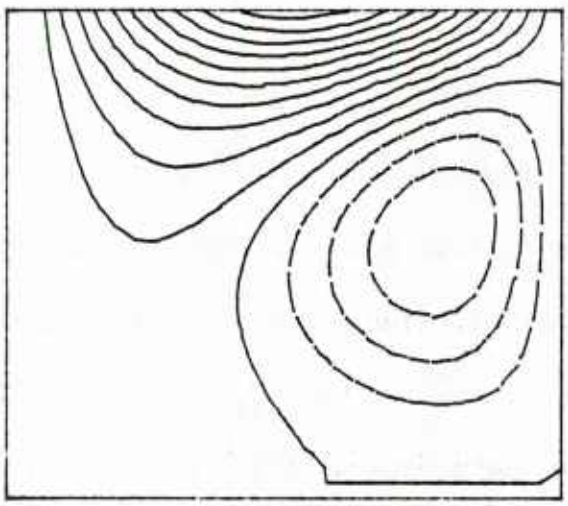

$t^+=5$

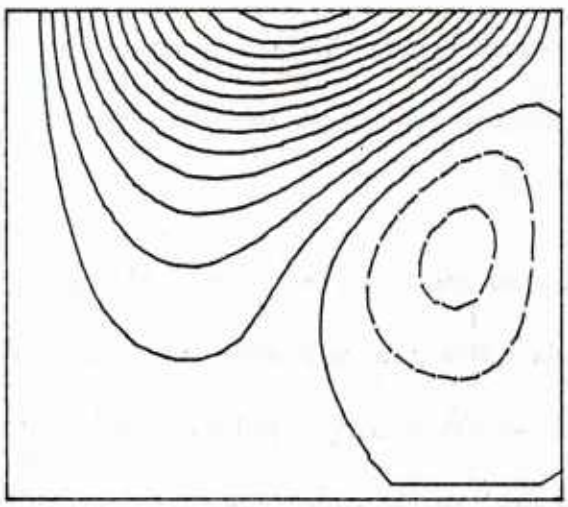

$t^+=10$

Figure 12 Streamline contours for a single harmonic run at $t^+ = 5$ and 10; upper boundary at $y_o^+ = 40$

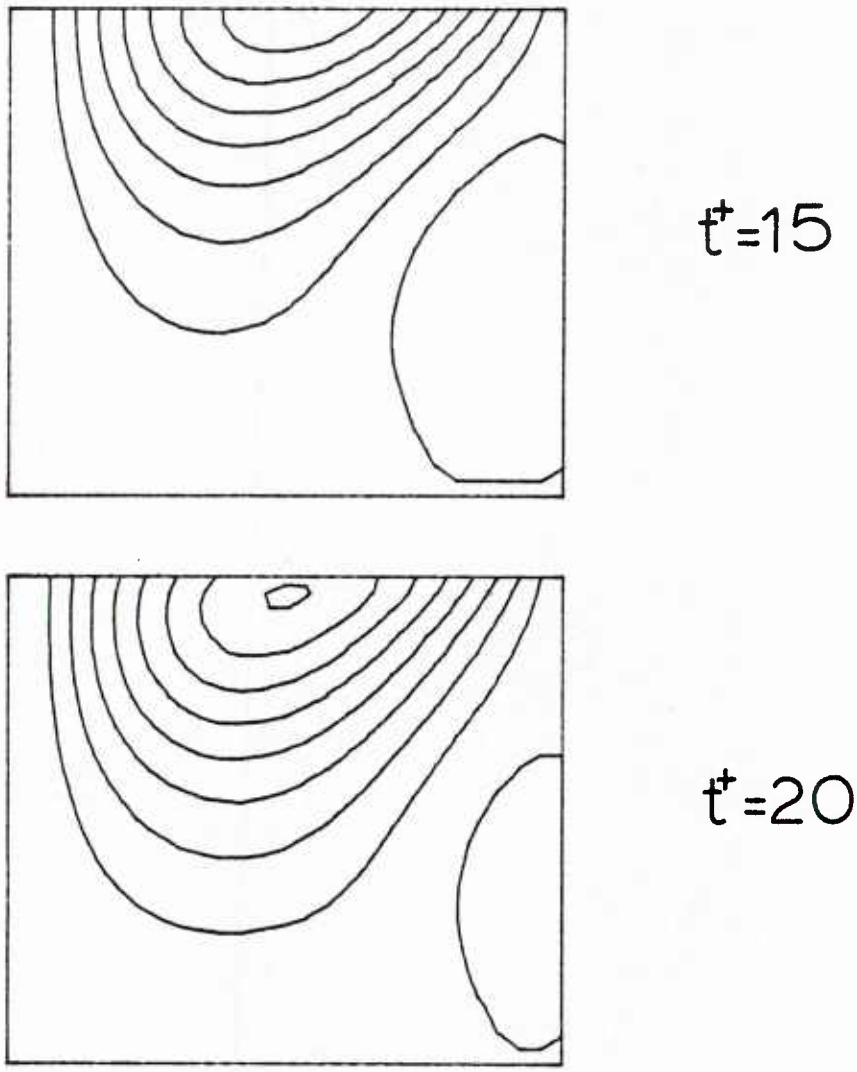

Figure 13 Streamline contours for a single harmonic run at $t^+ = 15$ and 20; upper boundary at $y_o^+ = 40$

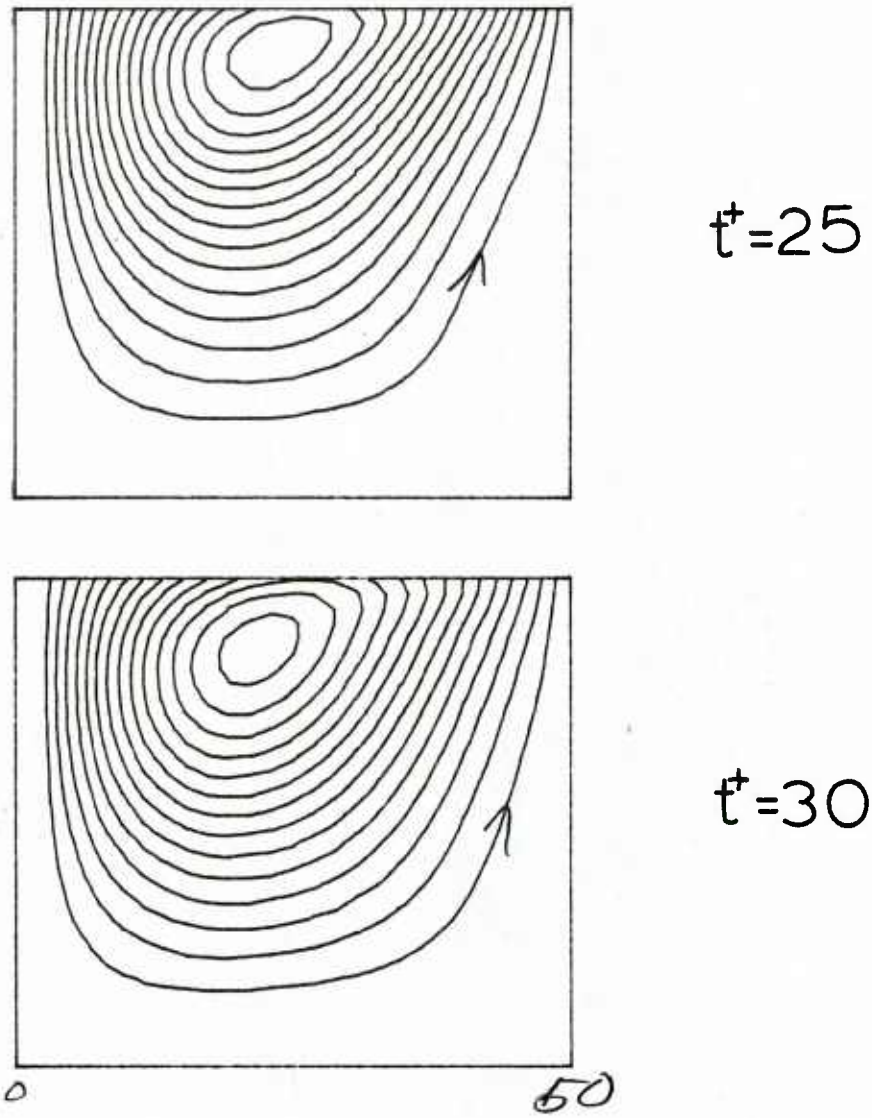

Figure 14 Streamline contours for a single harmonic run at $t^+ = 25$ and 30; upper boundary at $y_o^+ = 40$

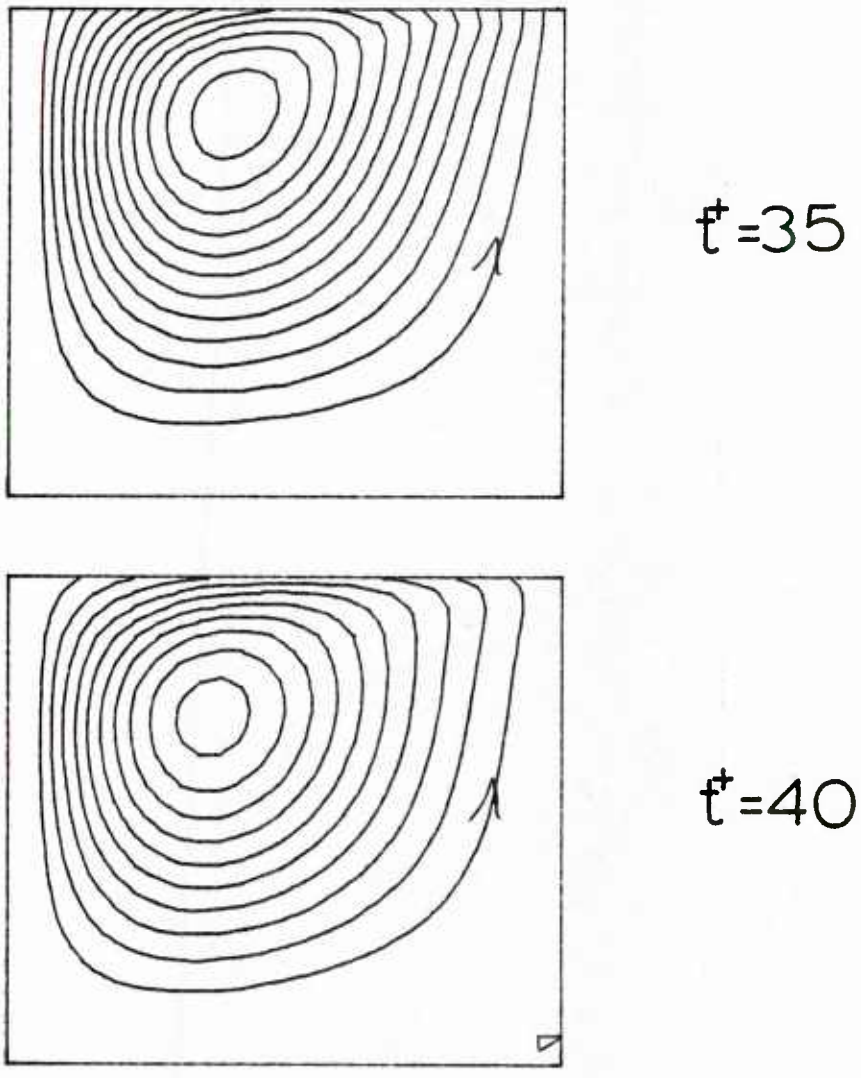

Figure 15 Streamline contours for a single harmonic run at $t^+ = 35$ and 40; upper boundary at $y_o^+ = 40$

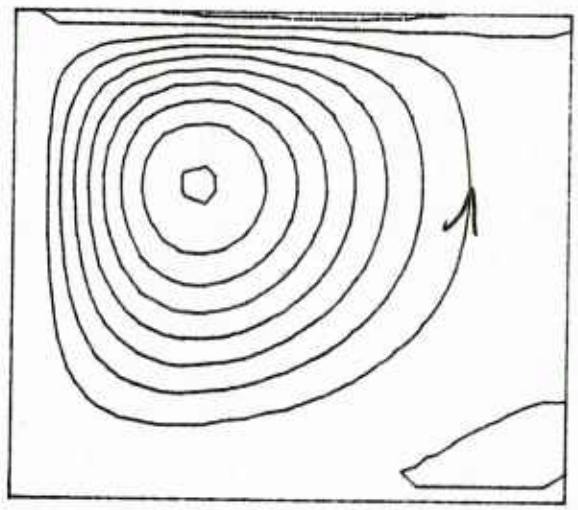

$t^+=45$

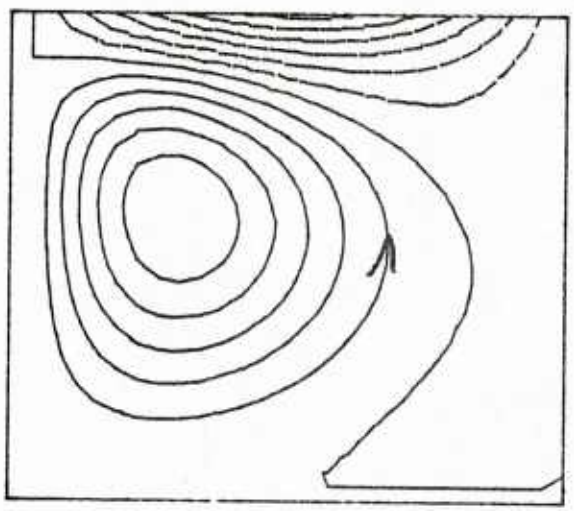

$t^+=50$

Figure 16 Streamline contours for a single harmonic run at $t^+ = 45$ and 50; upper boundary at $y_o^+ = 40$

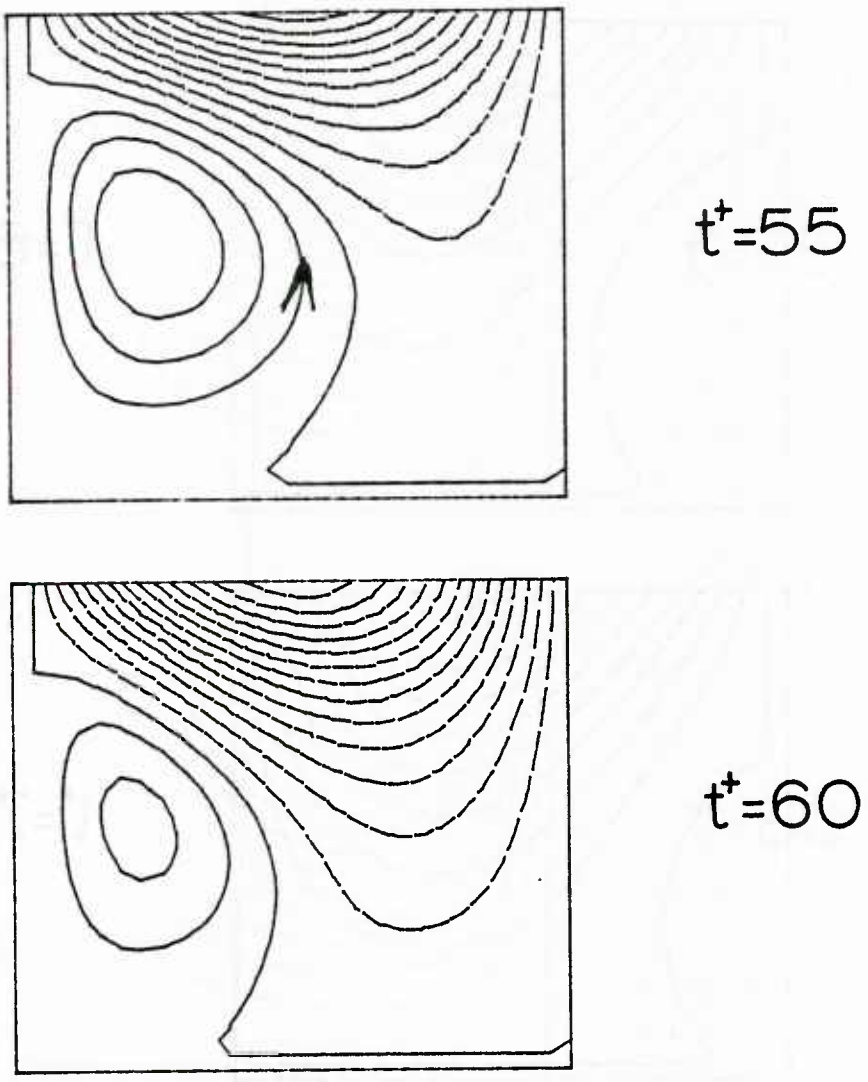

Figure 17 Streamline contours for a single harmonic run at $t^+ = 55$ and 60; upper boundary at $y_o^+ = 40$

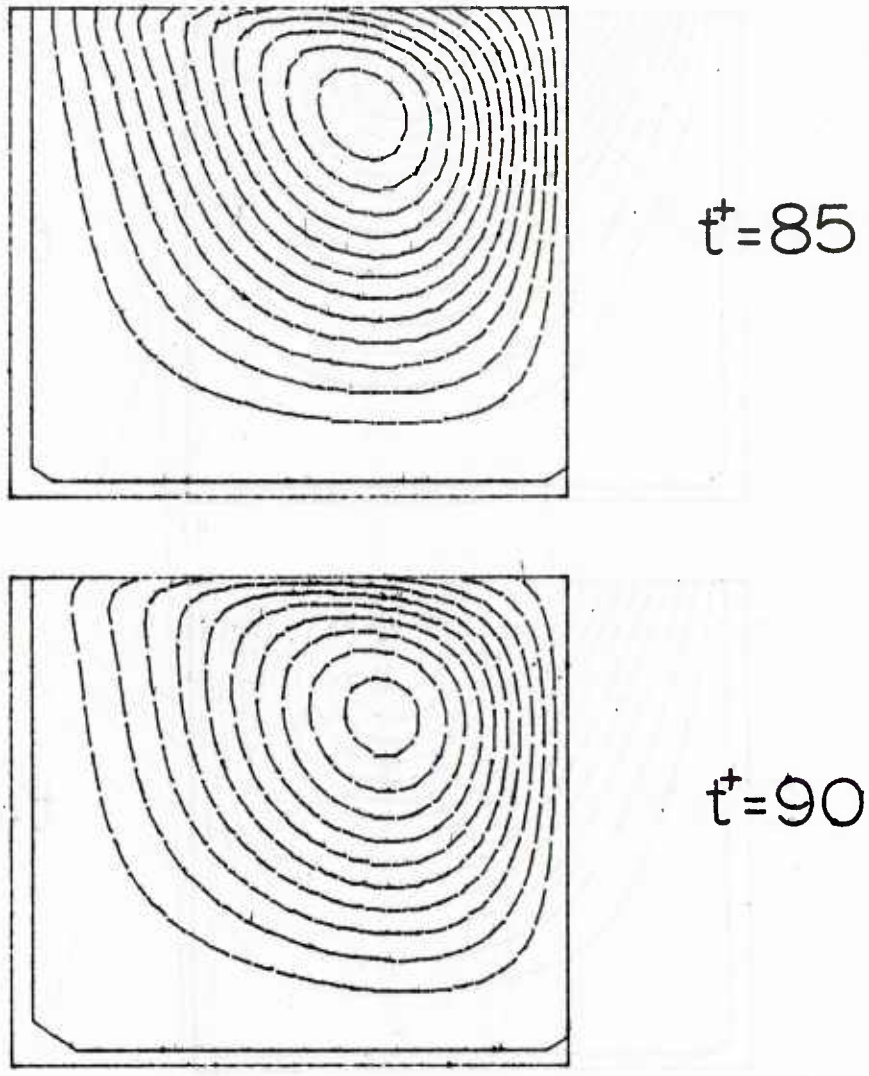

Figure 20 Streamline contours for a single harmonic run at $t^+ = 85$ and 90; upper boundary at $y_o^+ = 40$

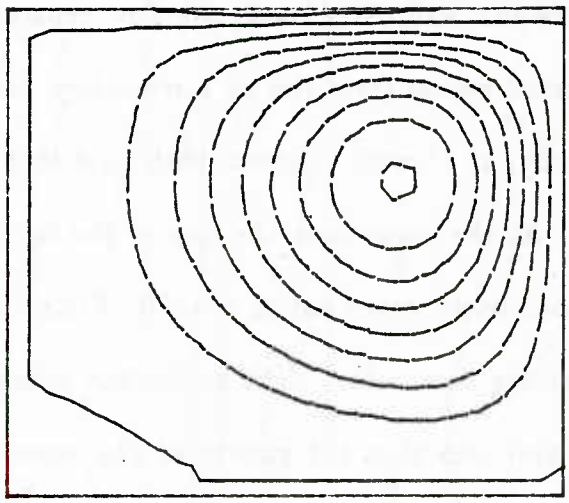

$t^+=95$

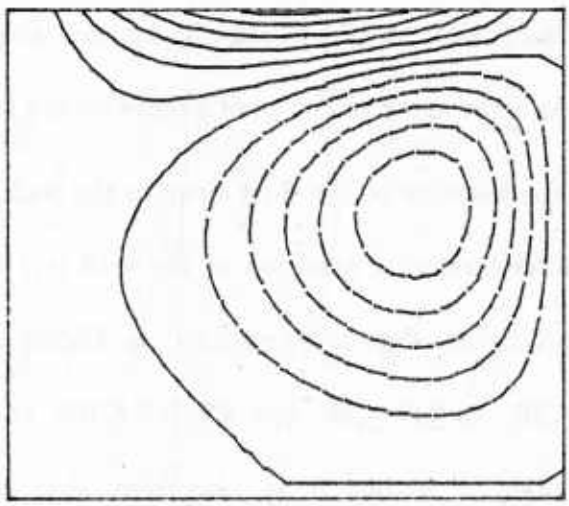

$t^+=100$

Figure 21 Streamline contours for a single harmonic run at $t^+ = 95$ and 100; upper boundary at $y_o^+ = 40$

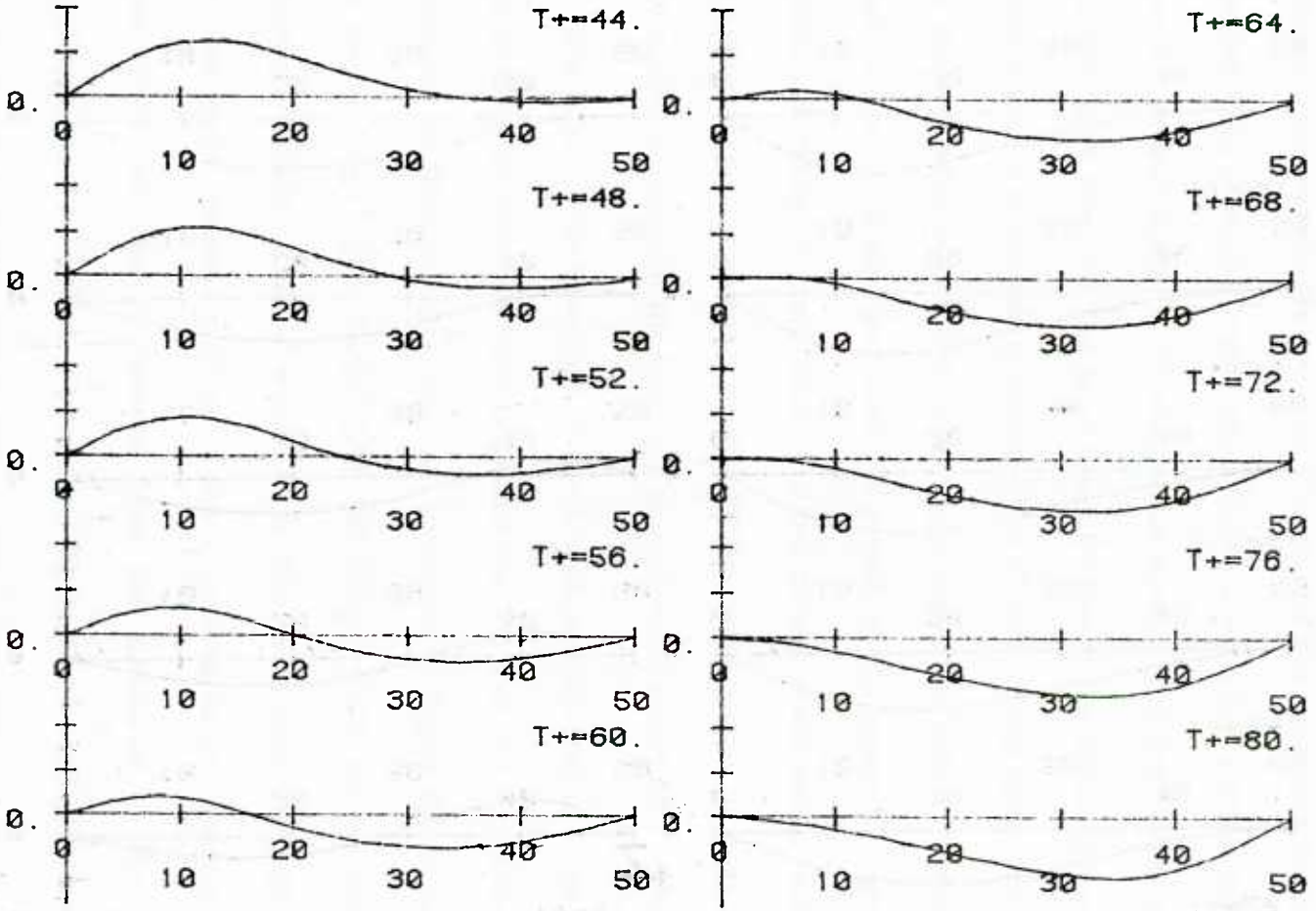

Figure 22b Plots of the spanwise velocity gradient at the wall versus z^+ from $t^+=44$ to $t^+=80$

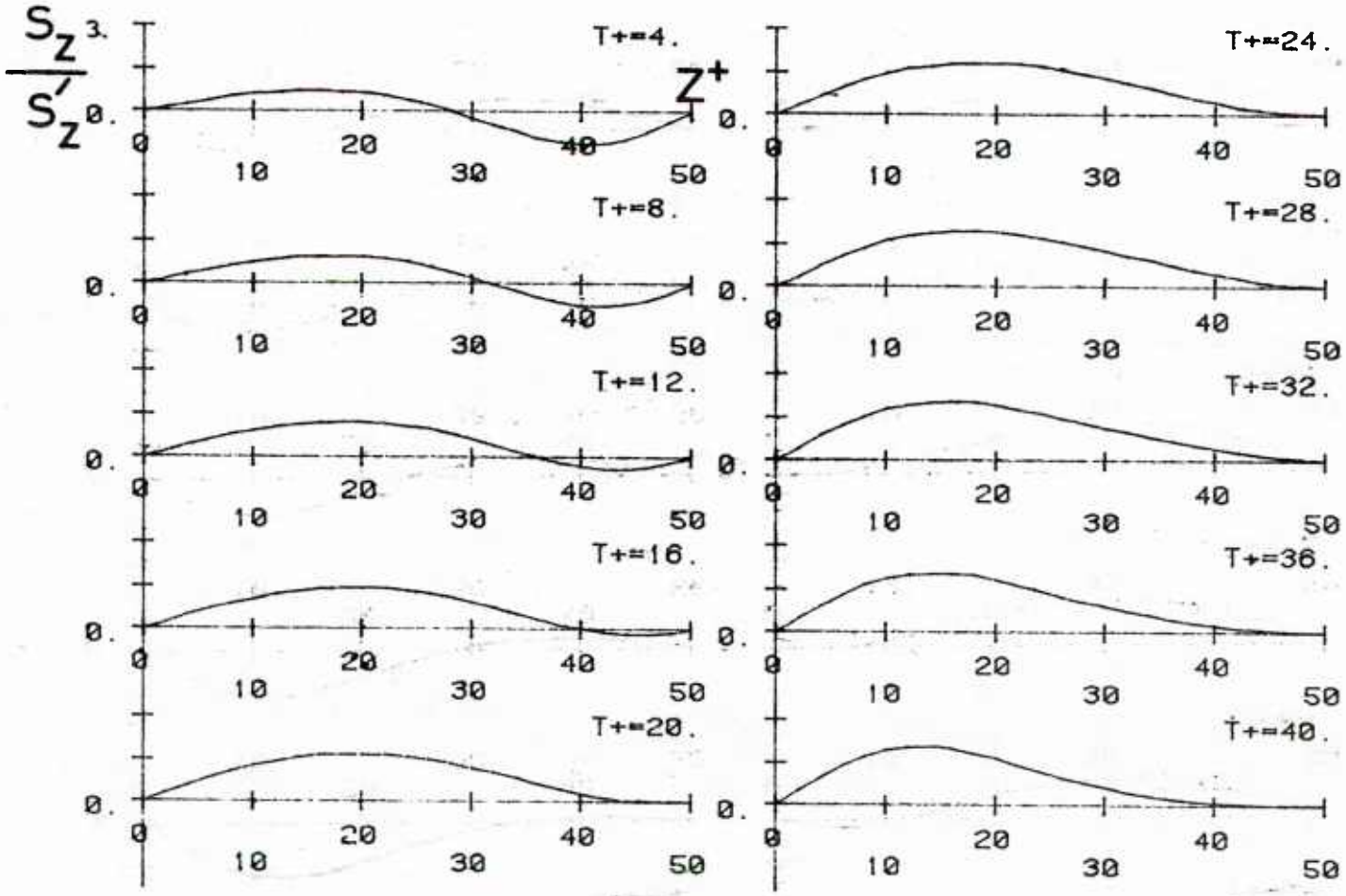

Figure 22a Plots of the spanwise velocity gradient at the wall versus z^+ from $t^+=4$ to $t^+=40$

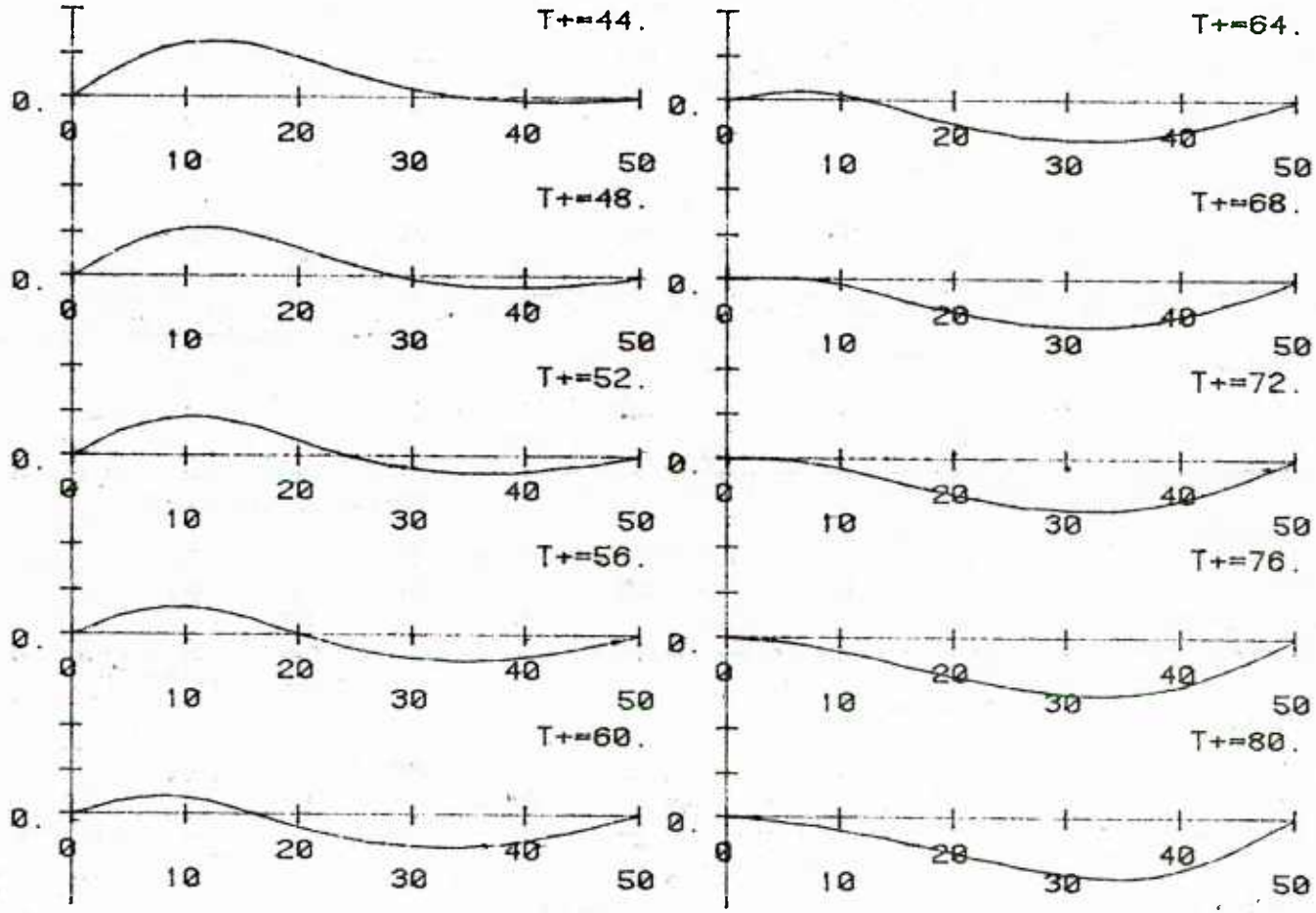

Figure 22b Plots of the spanwise velocity gradient at the wall versus z^+ from $t^+=44$ to $t^+=80$

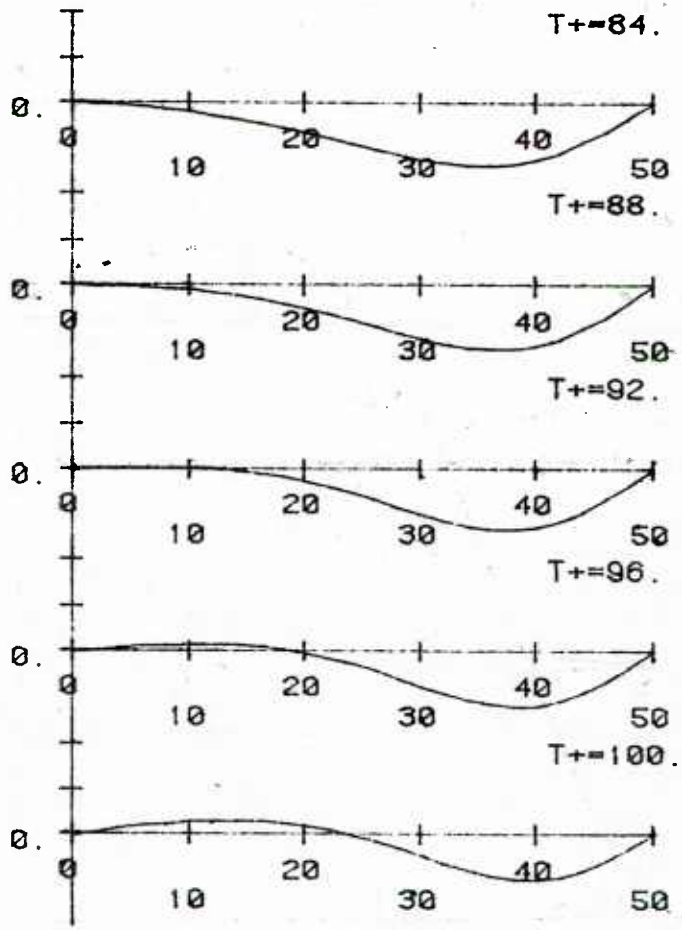

Figure 22c Plots of the spanwise velocity gradient at the wall versus z^+ from $t^+=84$ to $t^+=100$

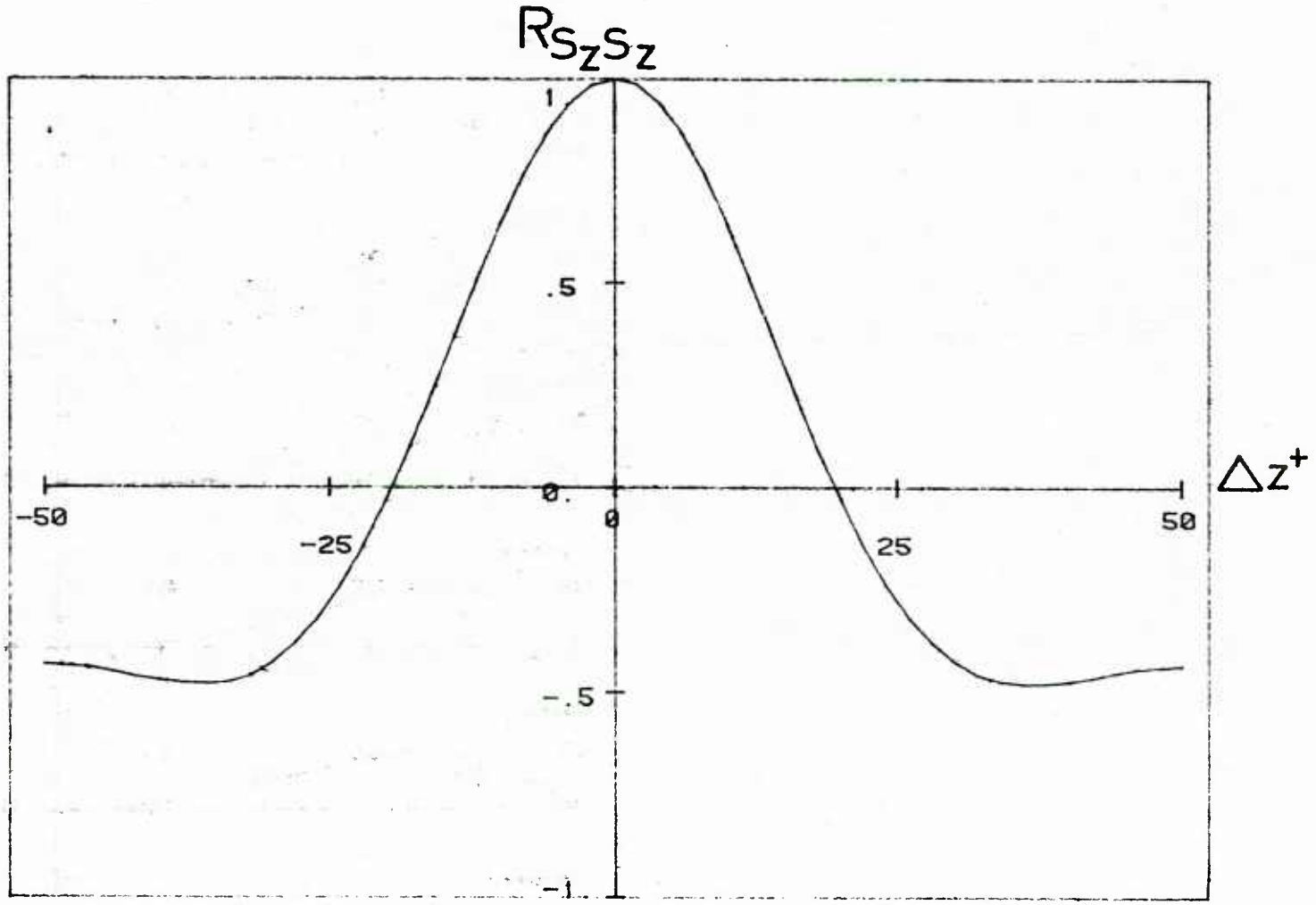

Figure 23 Plot of the $R_{s_z s_z}$ correlation versus Δz^+; single harmonic run.

$\Delta z^+ = 25$ and with a value of -1 at $\Delta z^+ = 50$. It is, however, seen that the computed $R_{\theta_z \theta_z}$ correlation gives a zero-crossing at $\Delta z^+ = 19.5$ and has a value of -0.435 at $\Delta z^+ = 50$.

Contour plots of the streamwise vorticity are presented in Figures 24 through 33. These plots have two main characteristics. The first one is that high values of the vorticity occur close to the upper boundary and close to the wall. The close spacing of the vorticity contours close to the outer boundary also reveals the existence of large gradients in the y-direction. The second feature of the vorticity contours is the location of the $\varsigma = 0$ curve. It can be seen that there are periods of time ($5 \leq t^+ \leq 20$, $60 \leq t^+ \leq 85$), in which there is an almost irrotational core, surrounded by the $\varsigma = 0$ line, that occupies a large portion of the cell. On the other hand there are time periods ($30 \leq t^+ \leq 55$, $90 \leq t^+ \leq 100$), in which the $\varsigma = 0$ line separates two regions of large values of vorticity and of opposite sign. These features will become more evident later, when plots of the streamwise vorticity versus the lateral coordinate, for a fixed spanwise location in the cell, will be presented.

Contour plots of the instantaneous streamwise velocity are presented in Figures 34 through 38. These plots are very illustrative of the dynamic sequence of inflows of high streamwise momemtum fluid and outflows of momentum deficient fluid, on the two sides of the cell, that are caused by the flow on the y–z plane. At $t^+ = 10$ an inflow occurs at $z^+ = 50$ and an outflow at $z^+ = 0$. As time goes on an inflow develops at $z^+ = 0$, and for $t^+ > 40$ there is an inflow at

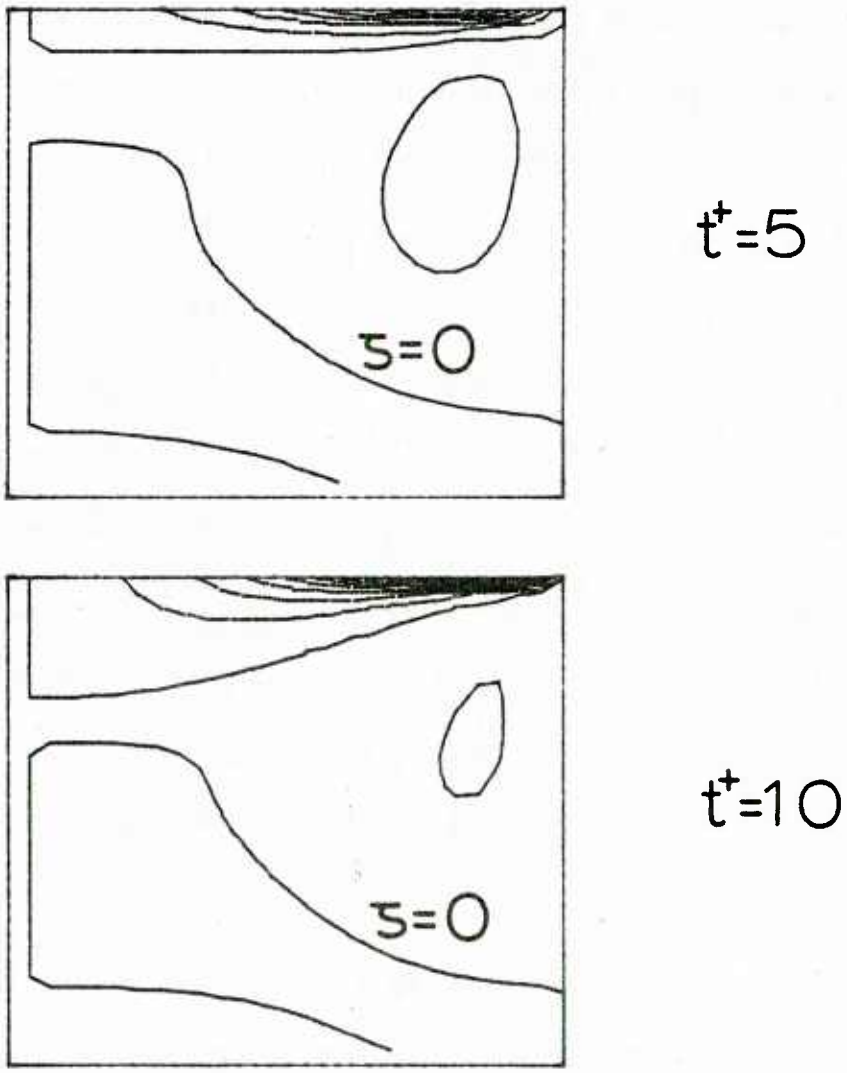

Figure 24 Streamwise vorticity contours for a single harmonic run at $t^+=5$ and 10; upper boundary at $y_o^+=40$

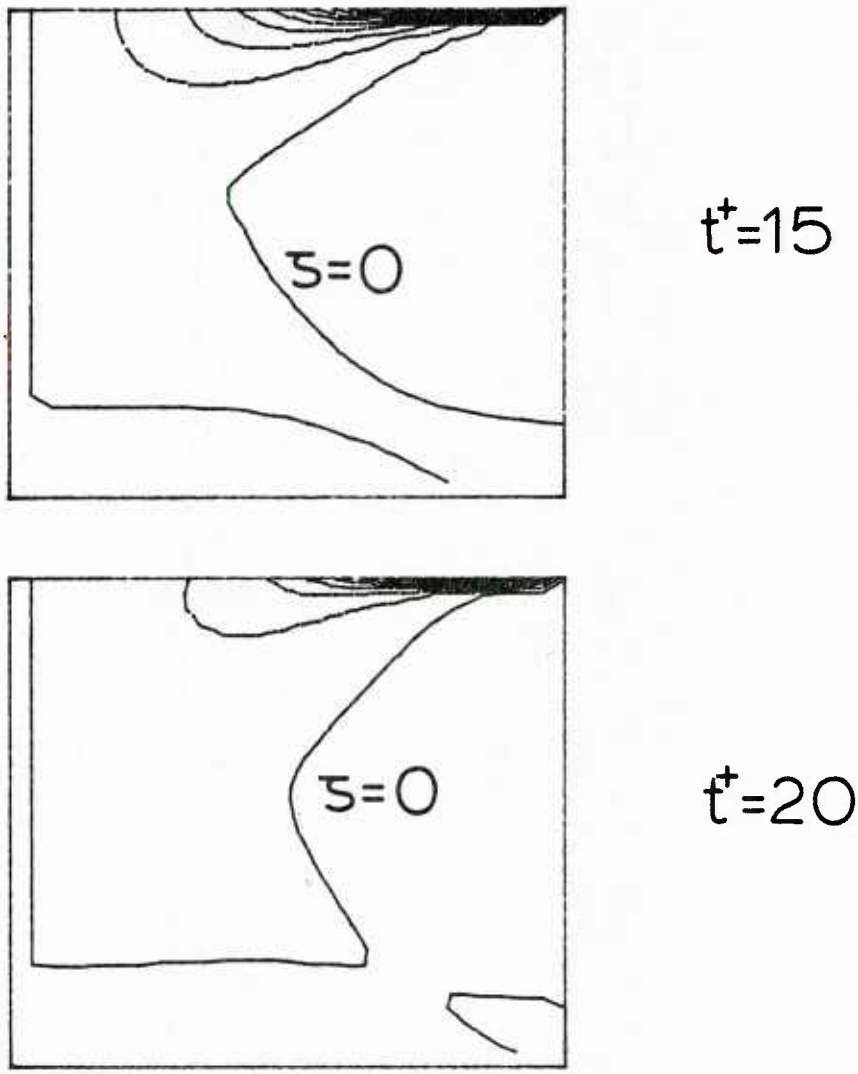

Figure 25 Streamwise vorticity contours for a single harmonic run at $t^+=15$ and 20; upper boundary at $y_o^+=40$

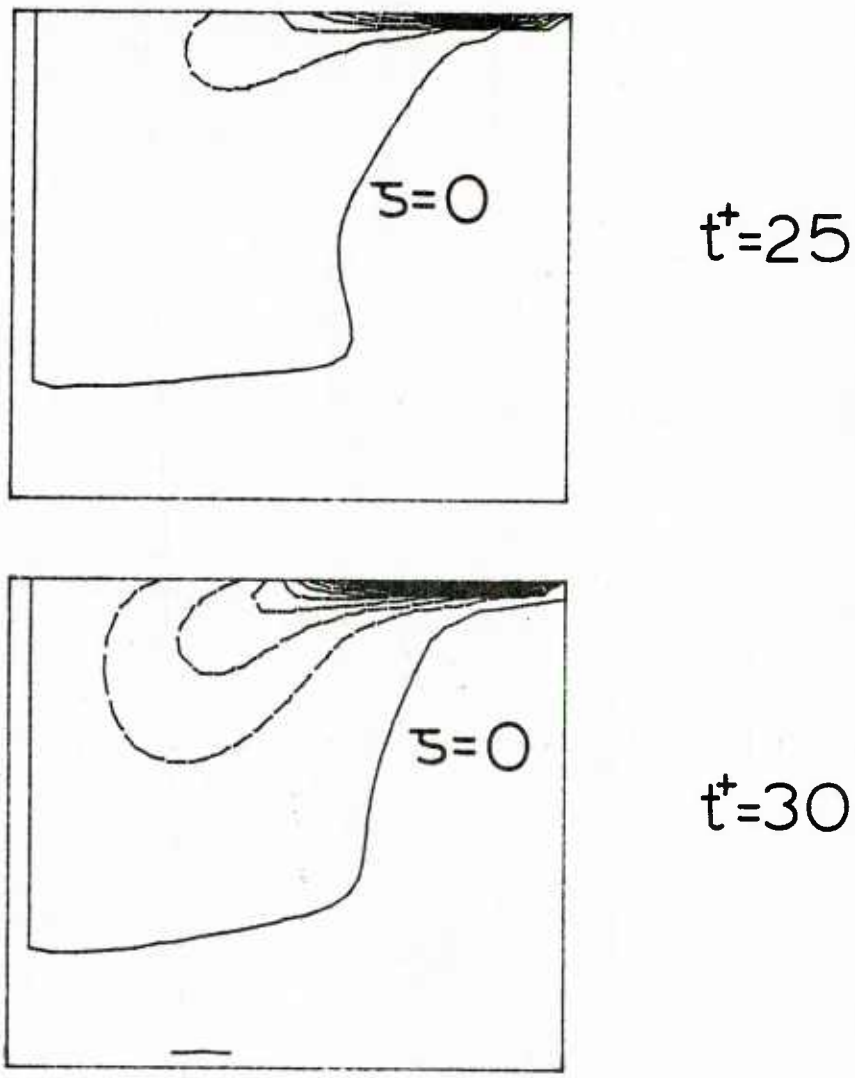

Figure 26 Streamwise vorticity contours for a single harmonic run at $t^+=25$ and 30; upper boundary at $y_o^+=40$

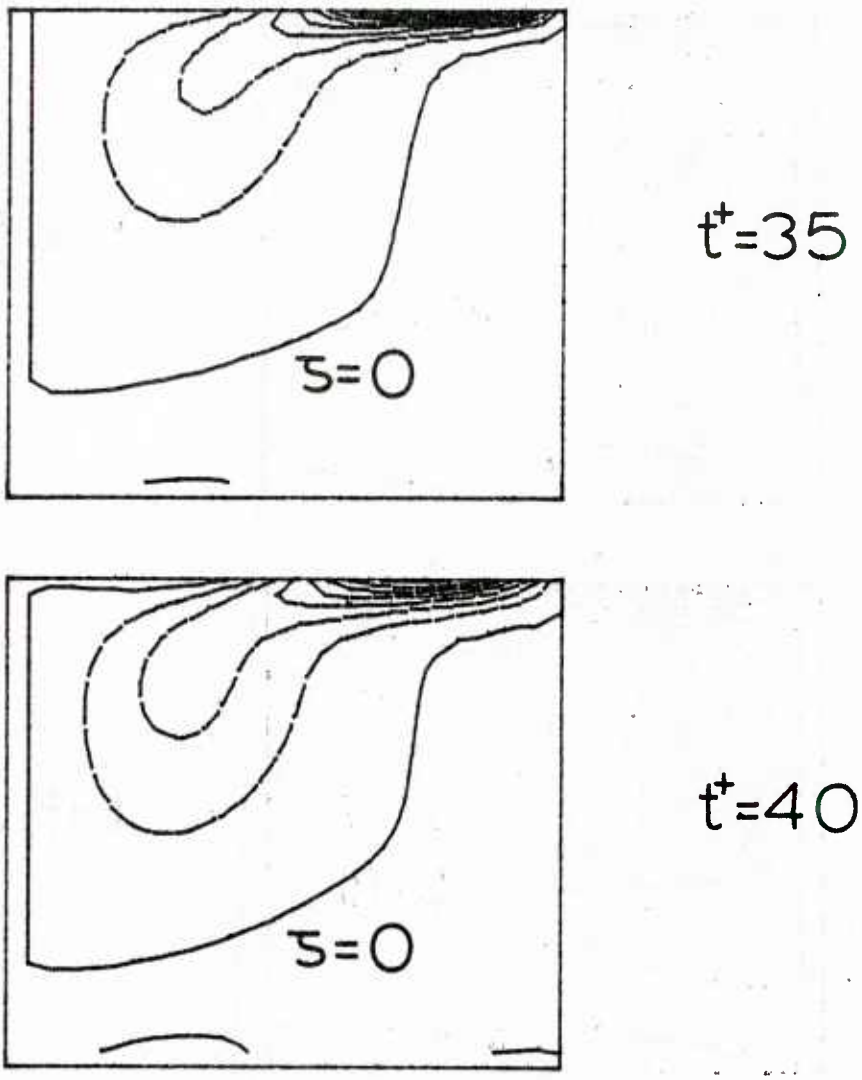

Figure 27 Streamwise vorticity contours for a single harmonic run at $t^+ = 35$ and 40; upper boundary at $y_o^+ = 40$

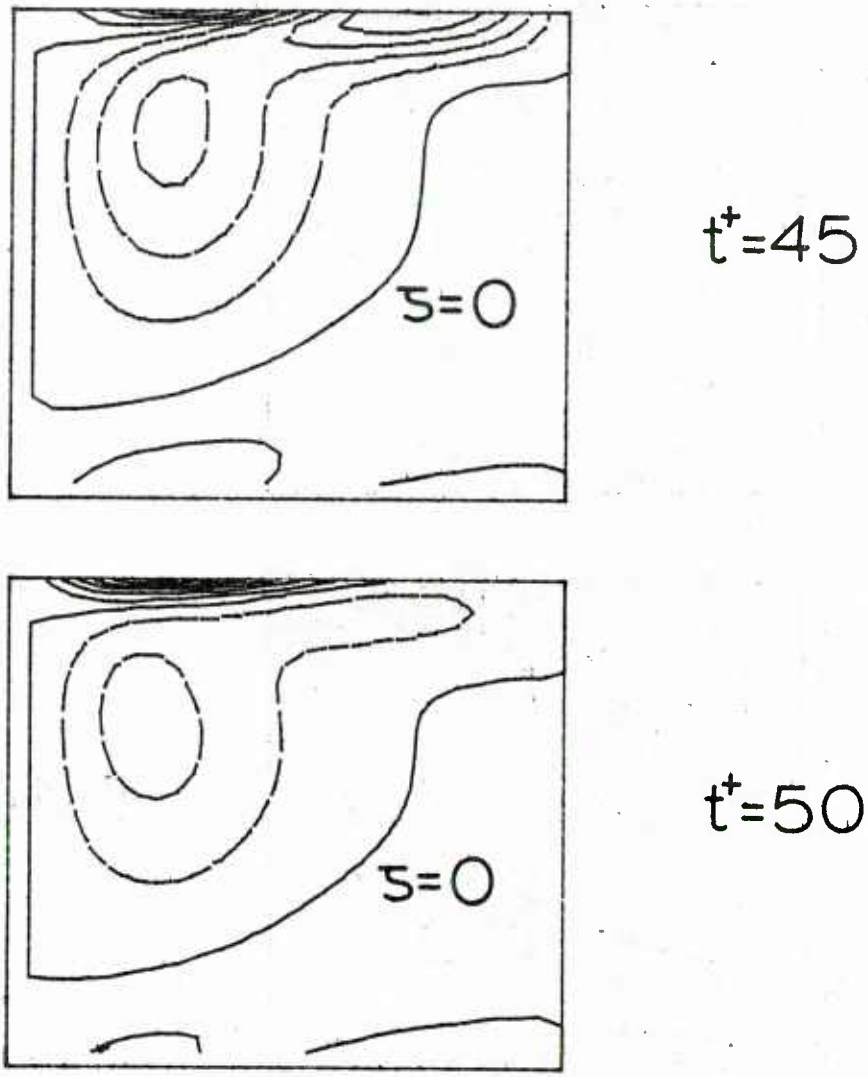

Figure 28 Streamwise vorticity contours for a single harmonic run at $t^+ = 45$ and 50; upper boundary at $y_o^+ = 40$

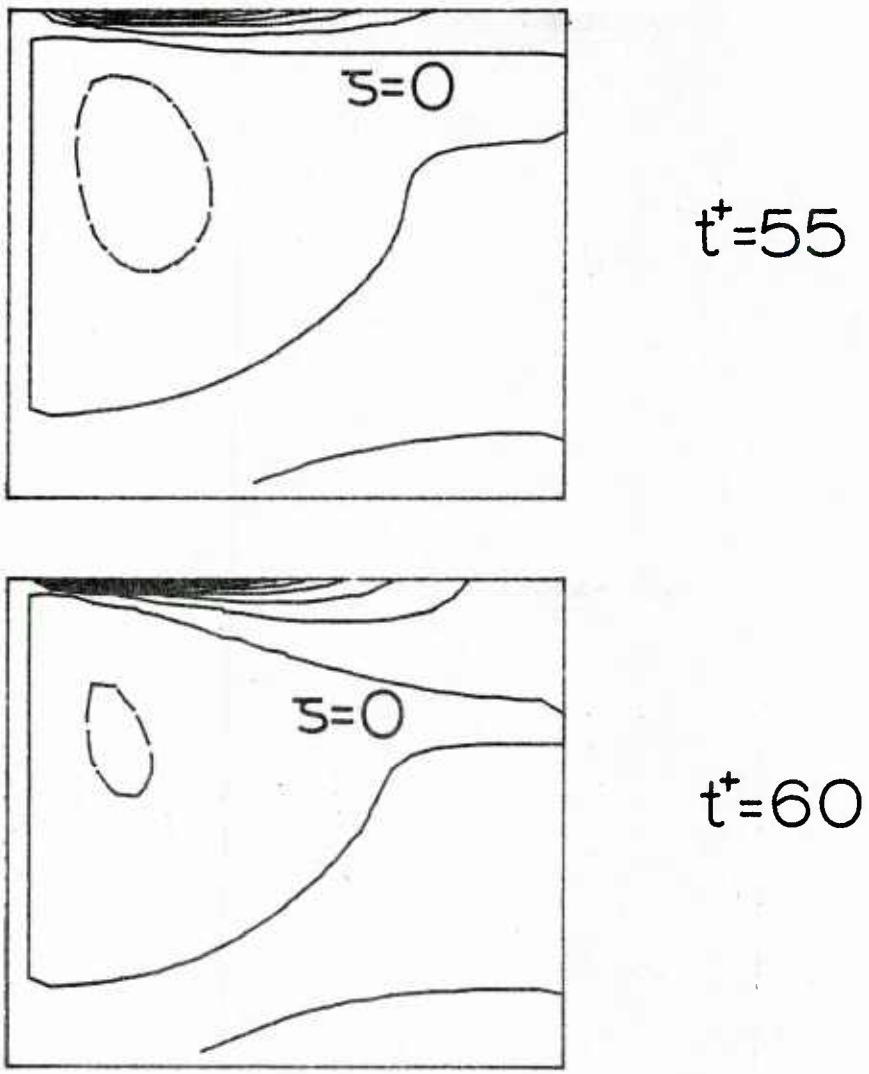

Figure 29 Streamwise vorticity contours for a single harmonic run at $t^+=55$ and 60; upper boundary at $y_o^+=40$

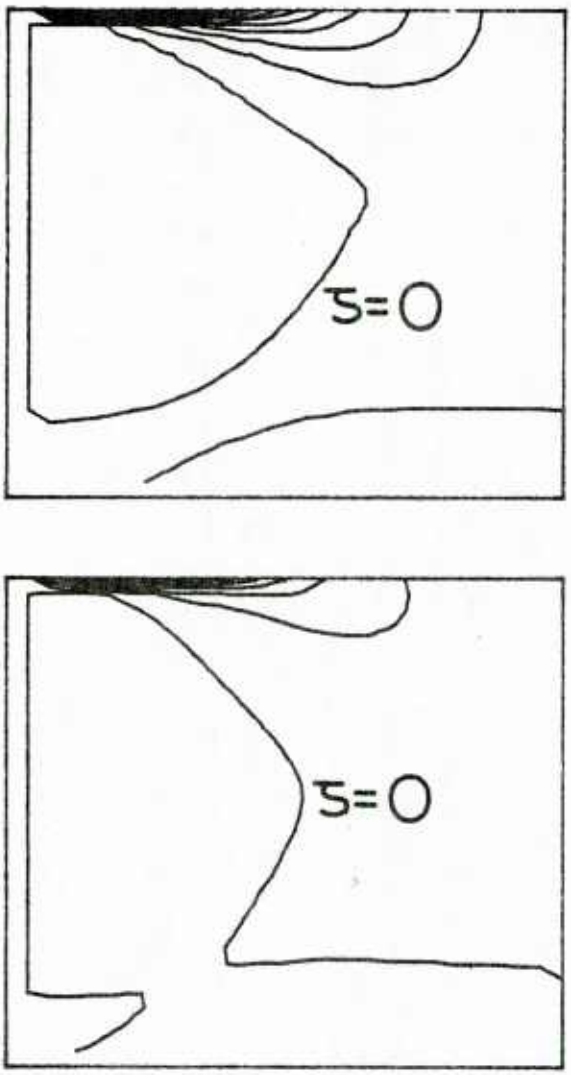

Figure 30 Streamwise vorticity contours for a single harmonic run at $t^+ = 65$ and 70; upper boundary at $y_o^+ = 40$

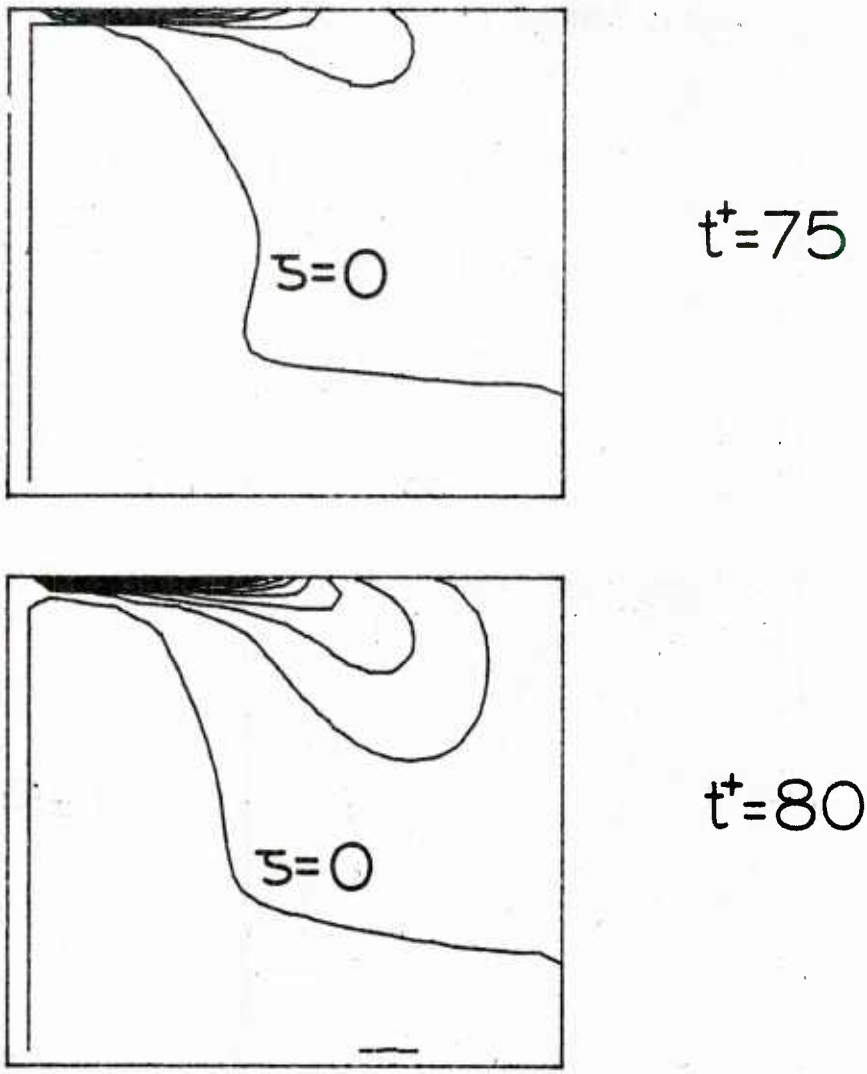

Figure 31 Streamwise vorticity contours for a single harmonic run at $t^+ = 75$ and 80; upper boundary at $y_o^+ = 40$

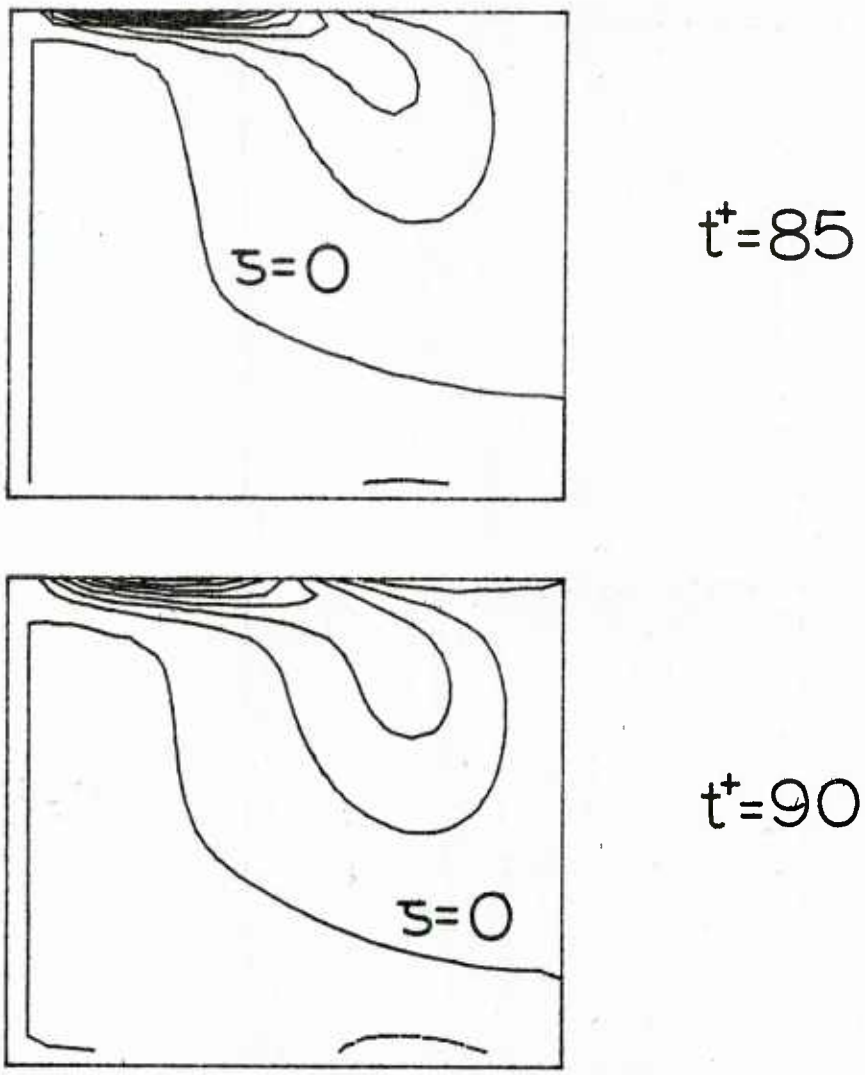

Figure 32 Streamwise vorticity contours for a single harmonic run at $t^+=85$ and 90; upper boundary at $y_o^+=40$

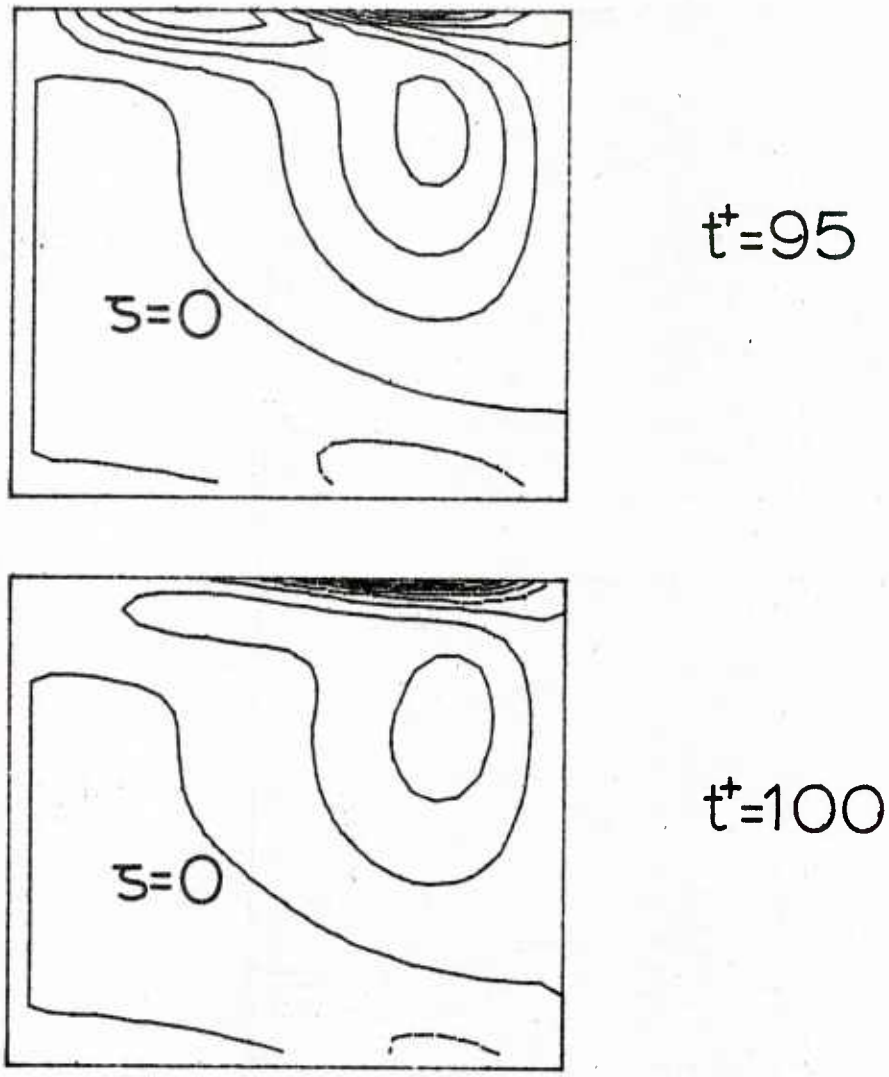

Figure 33 Streamwise vorticity contours for a single harmonic run at $t^+ = 95$ and 100; upper boundary at $y_o^+ = 40$

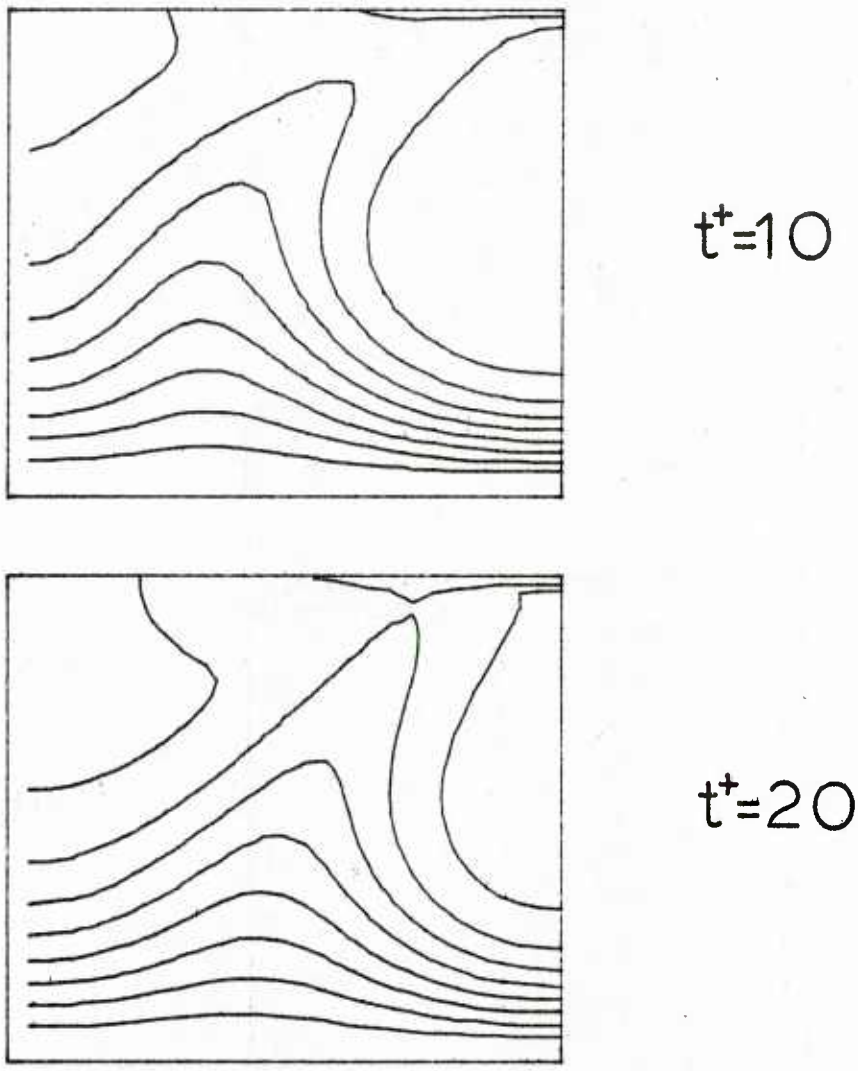

Figure 34 Instantaneous streamwise velocity contours for a single harmonic run at $t^+ = 10$ and 20; upper boundary at $y_o^+ = 40$

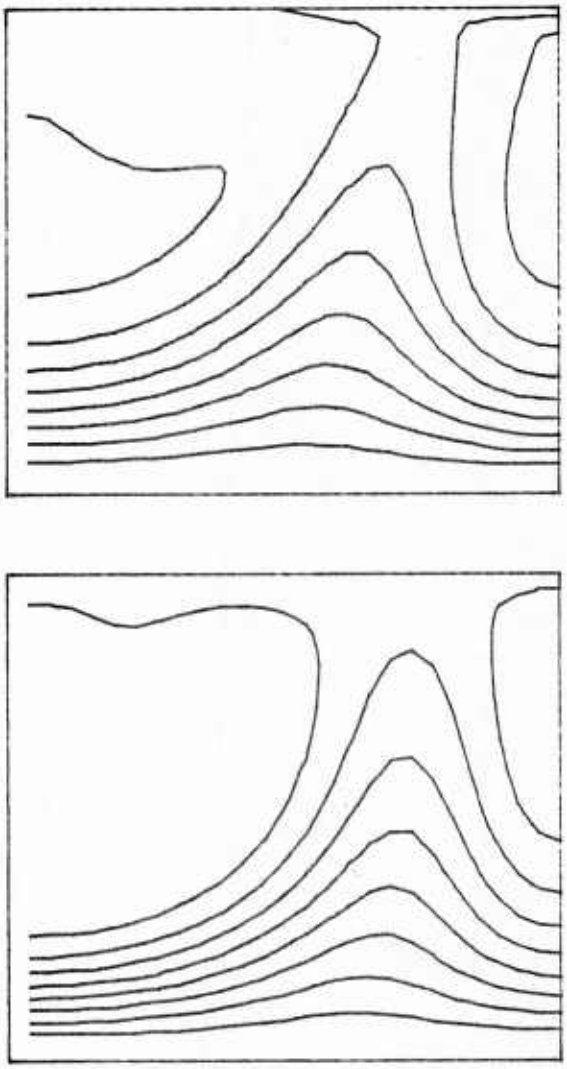

Figure 35 Instantaneous streamwise velocity contours for a single harmonic run at $t^+ = 30$ and 40; upper boundary at $y_o^+ = 40$

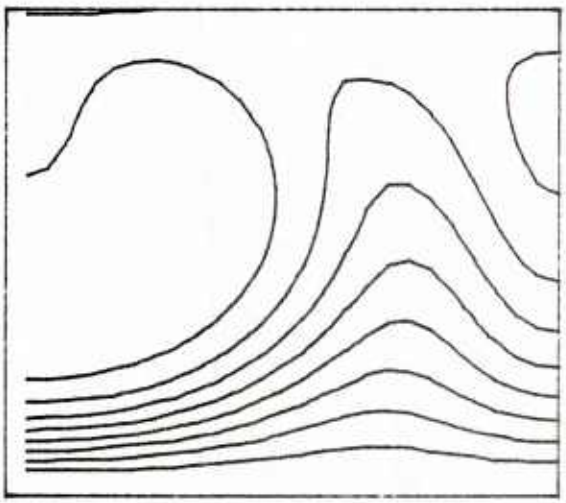

$t^+=50$

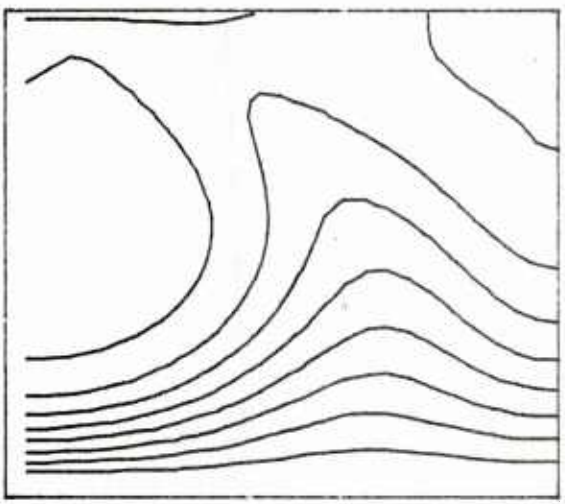

$t^+=60$

Figure 36 Instantaneous streamwise velocity contours for a single harmonic run at $t^+=50$ and 60; upper boundary at $y_o^+=40$

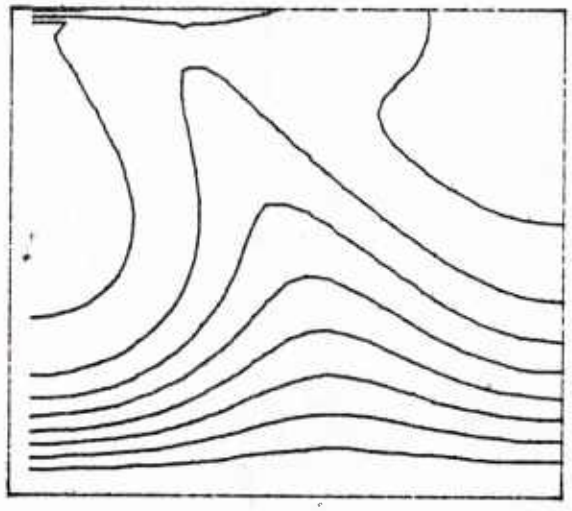

$t^+=70$

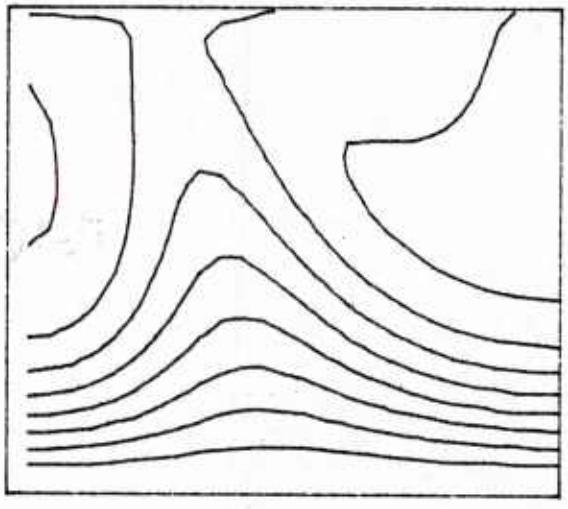

$t^+=80$

Figure 37 Instantaneous streamwise velocity contours for a single harmonic run at $t^+=70$ and 80; upper boundary at $y_o^+=40$

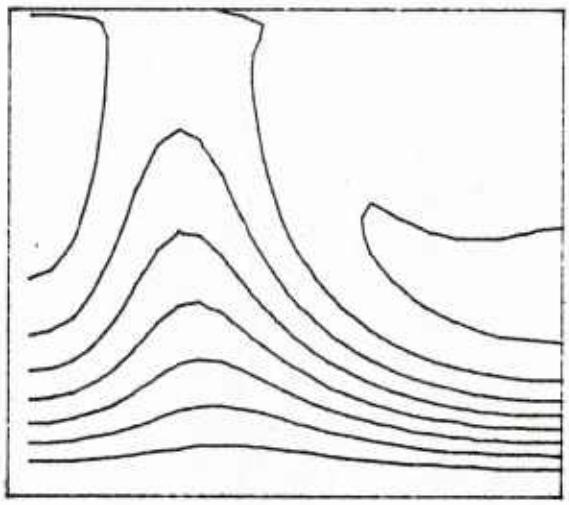

$t^+=90$

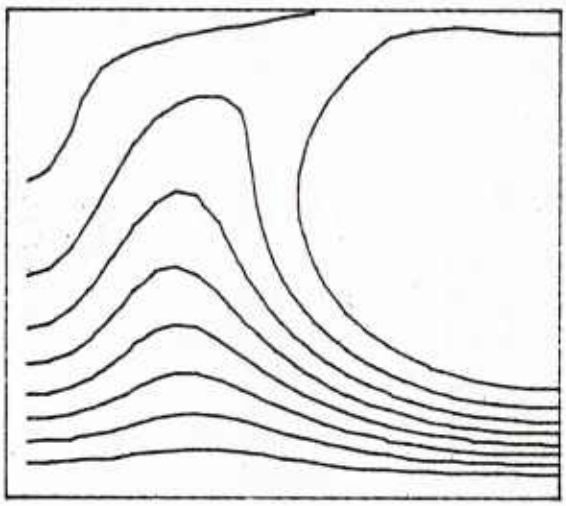

$t^+=100$

Figure 38 Instantaneous streamwise velocity contours for a single harmonic run at $t^+=90$ and 100; upper boundary at $y_o^+=40$

$z^+=0$ coupled with an outflow on the other side of the cell. For $t^+>80$ the same sequence occurs at $z^+=50$.

In order to get a picture of the relative temporal variation of the flow variables, plots of the three fluctuating components of the velocity and the streamwise vorticity are presented for a fixed spanwise or lateral location in the cell. Figures 39 through 42 show plots of u,v,w and ς versus time for fixed spanwise locations and various distances from the wall. The characteristic feature of the v and w plots is that the period of the fluctuations throughout the cell is equal to the period of the imposed fluctuations at the outer boundary ($T^+=100$). The amplitude of these fluctuations diminishes as the wall is approached and that of the normal component of the velocity goes to zero at a faster rate. At $y^+=40$ the period of the streamwise velocity fluctuations appears to be $T^+=400$. This is expected since most of the energy of these fluctuations at $y_o^+=40$ was attributed to infinite wavelength u-eddies of period $T_{u2}^+=400$. Nevertheless, periods of $T^+=100$ are still discernible and superimposed on the lower frequency $T^+=400$ fluctuations. As the wall is approached the picture is completely different. The dominant period is $T^+=100$ and there is no sign of lower frequency velocity fluctuations. The plots of the streamwise vorticity in Figure 42 present in another way the main features of the ς-contour plots that were shown before. It is easier to see from these plots that large values of the streamwise vorticity occur close to the upper boundary and close to the wall. At $y^+=10$ and $y^+=15$ there are hardly any fluctuations of the streamwise vorticity . This

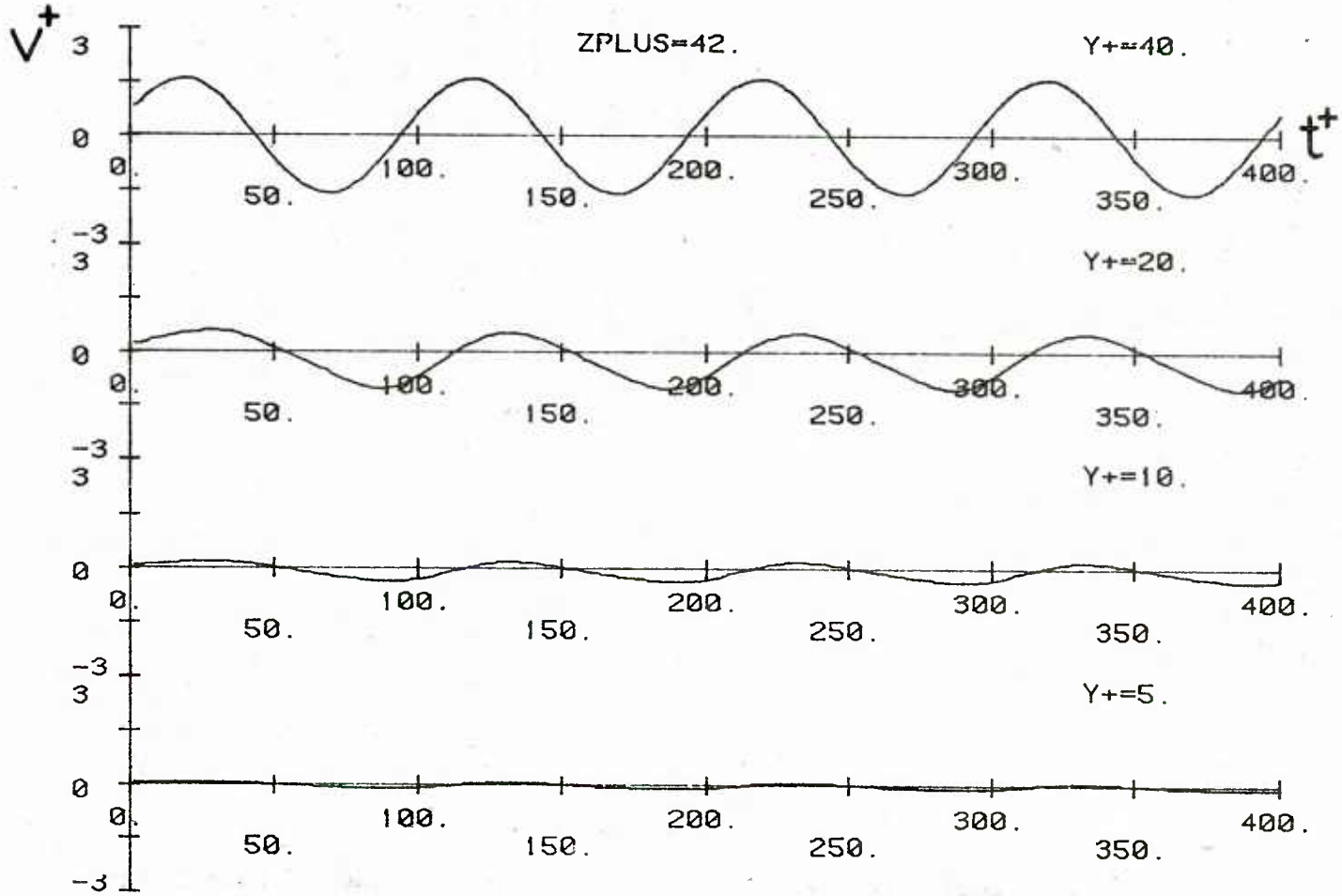

Figure 39 Plots of v^+ versus t^+ at $z^+ = 42$. Single harmonic run; upper boundary at $y_o^+ = 40$

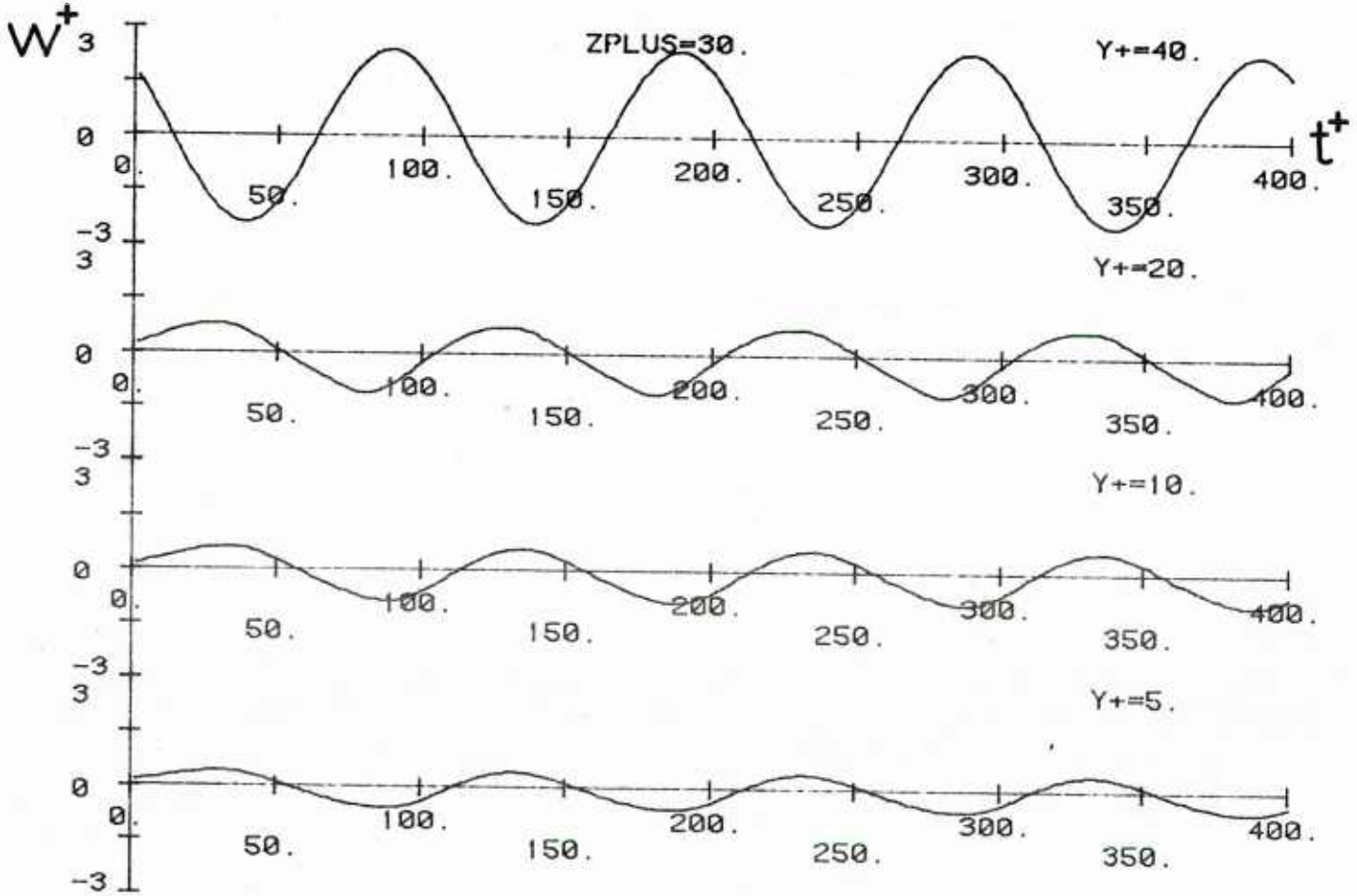

Figure 40 Plots of w^+ versus t^+ at $z^+ = 30$. Single harmonic run; upper boundary at $y_o^+ = 40$

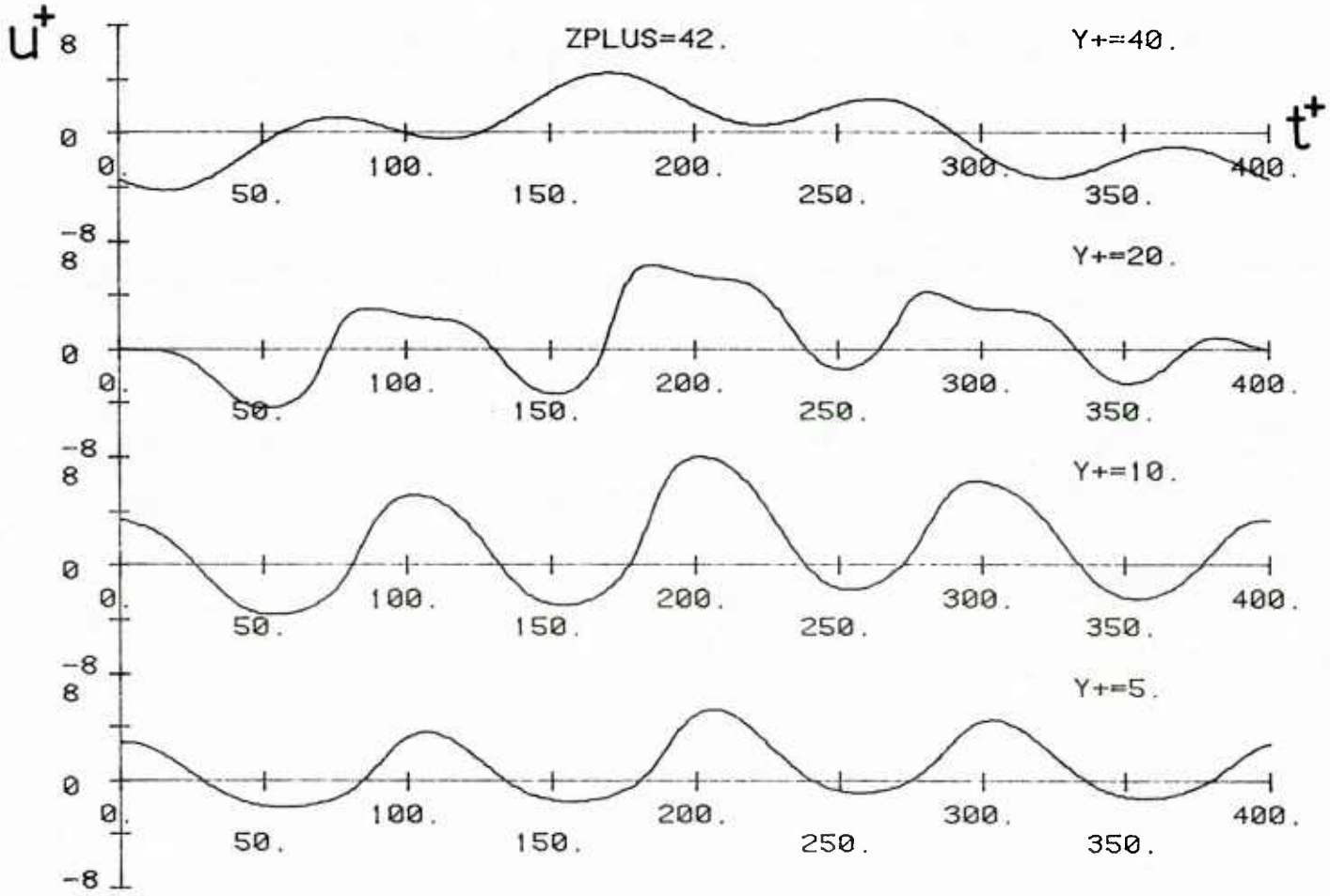

Figure 41 Plots of u^+ versus t^+ at $z^+ = 42$. Single harmonic run; upper boundary at $y_o^+ = 40$

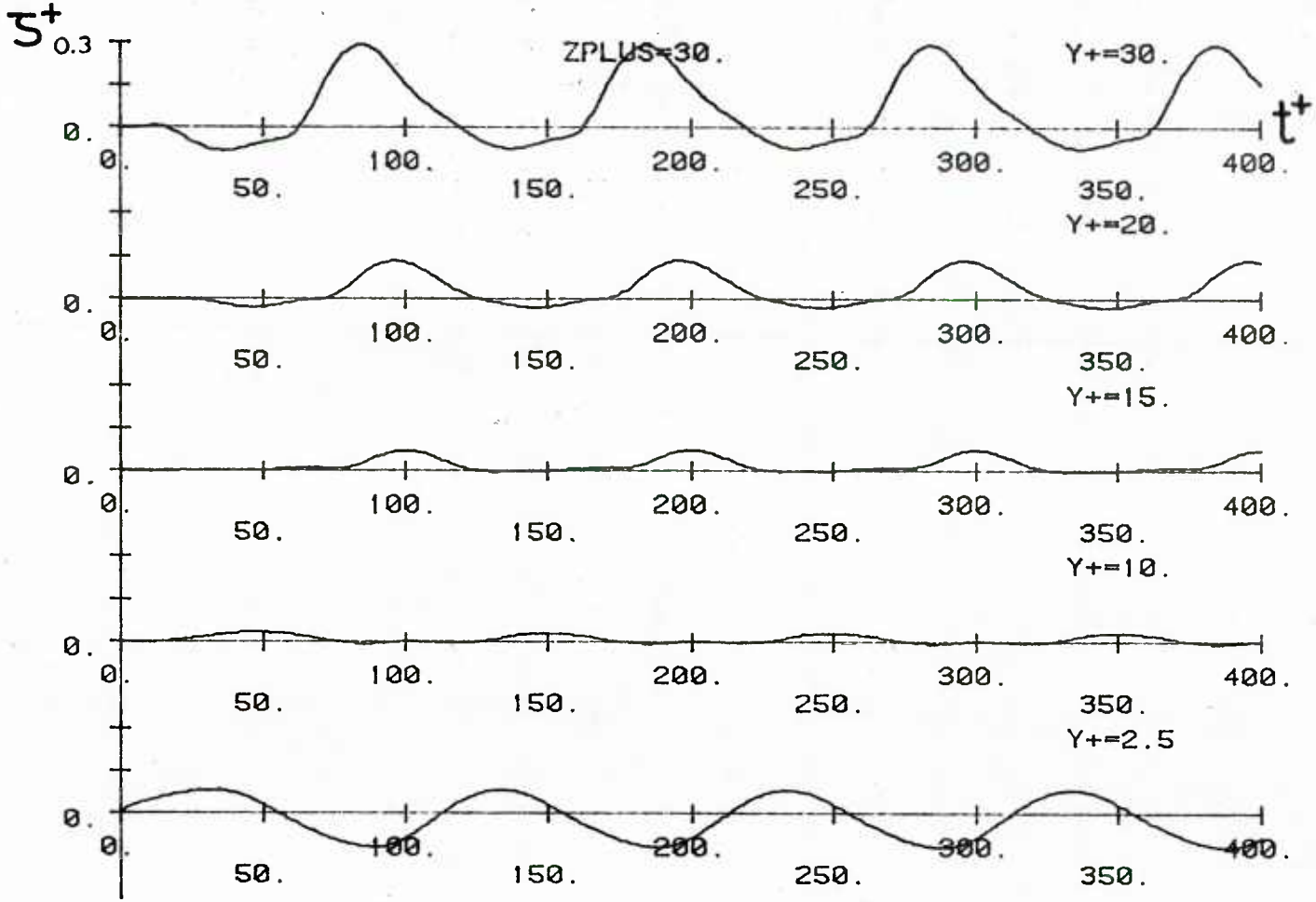

Figure 42 Plots of ζ^+ versus t^+ at $z^+=30$. Single harmonic run; upper boundary at $y_o^+=40$

is the region that the almost irrotational core, identified previously from the ς-contour plots, occupies for most of the time. These features of the streamwise vorticity were found to be characteristic of all the "fixed cell" calculations. In particular, the lateral profile of the streamwise vorticity which, will be shown later, constitutes the characteristic vorticity "signature" of the fixed cell.

Similar plots of u,v,w and ς are shown in Figures 43 through 46 but for a fixed distance from the wall and various spanwise locations in the cell. These plots also show the characteristic period of the fluctuating flow variables to be $T^+=100$. The plots of the normal component of the velocity are indicative of a slight degree of asymmetry in the v profiles with respect to the spanwise coordinate which is a consequence of the nonlinearity of the flow.

Figures 47 through 50 show plots of the three fluctuating velocity components and the streamwise vorticity versus the lateral coordinate for a fixed spanwise location in the cell and for various points in time. Figure 47 shows the lateral profiles of the streamwise vorticity for $z^+=18$, throughout a cycle of the $\lambda^+=100$ wall eddies. These plots confirm the observations made when the ς-contour plots were discussed. The existence of an almost irrotational region during $4\leq t^+\leq 20$ and $64\leq t^+\leq 84$ is verified. During the rest of the time the ς-profile attains an S-shaped form with a zero-crossing at $y^+\approx 10$. This is the characteristic signature of the streamwise vorticity that was observed in all the "fixed cell" computations. As will be discussed below the form of the lateral profile of the streamwise vorticity has a bearing on the distribution of the v and

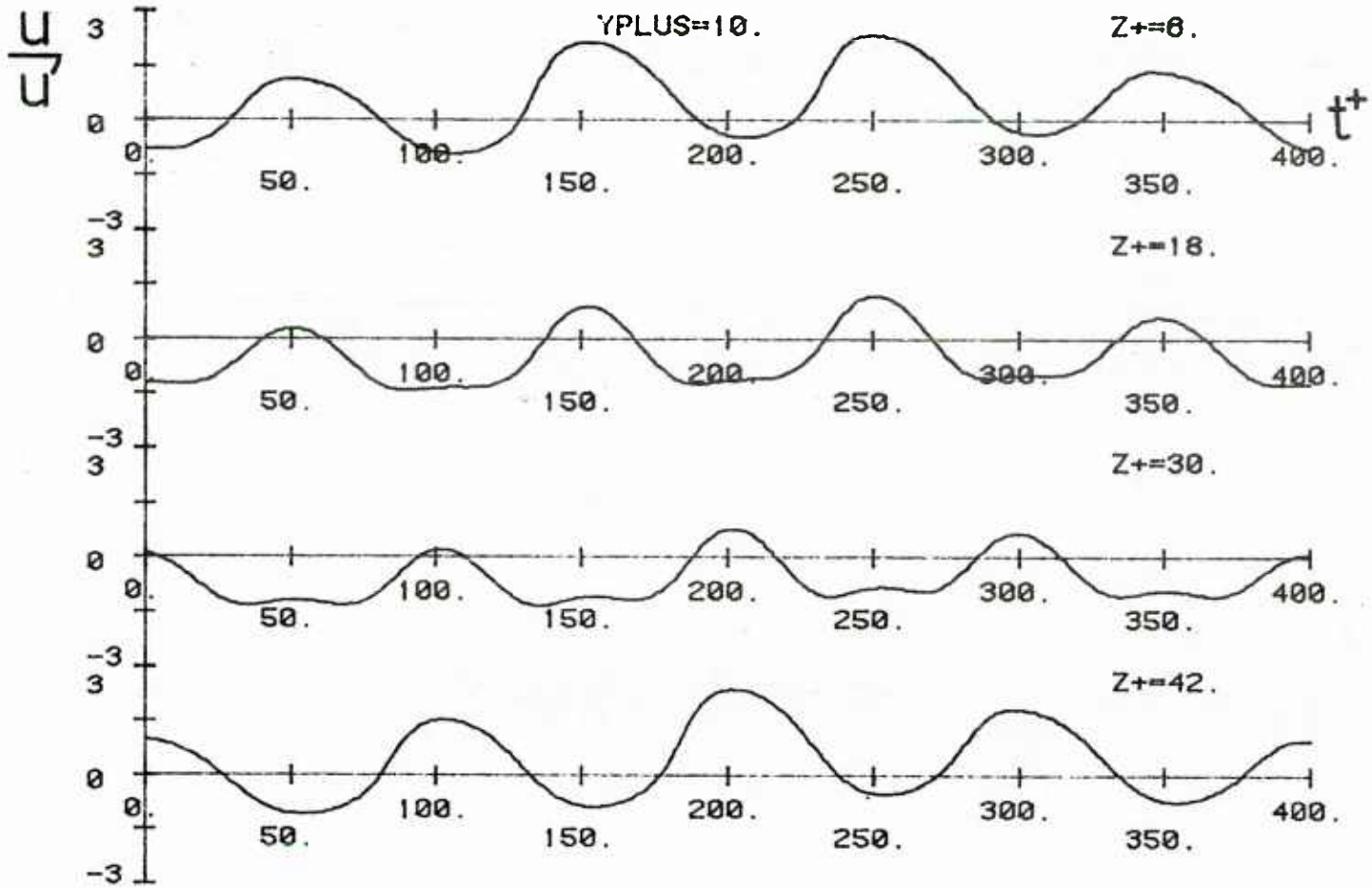

Figure 43 Plots of u/u' versus t^+ at $y^+ = 10$. Single harmonic run; upper boundary at $y_o^+ = 40$

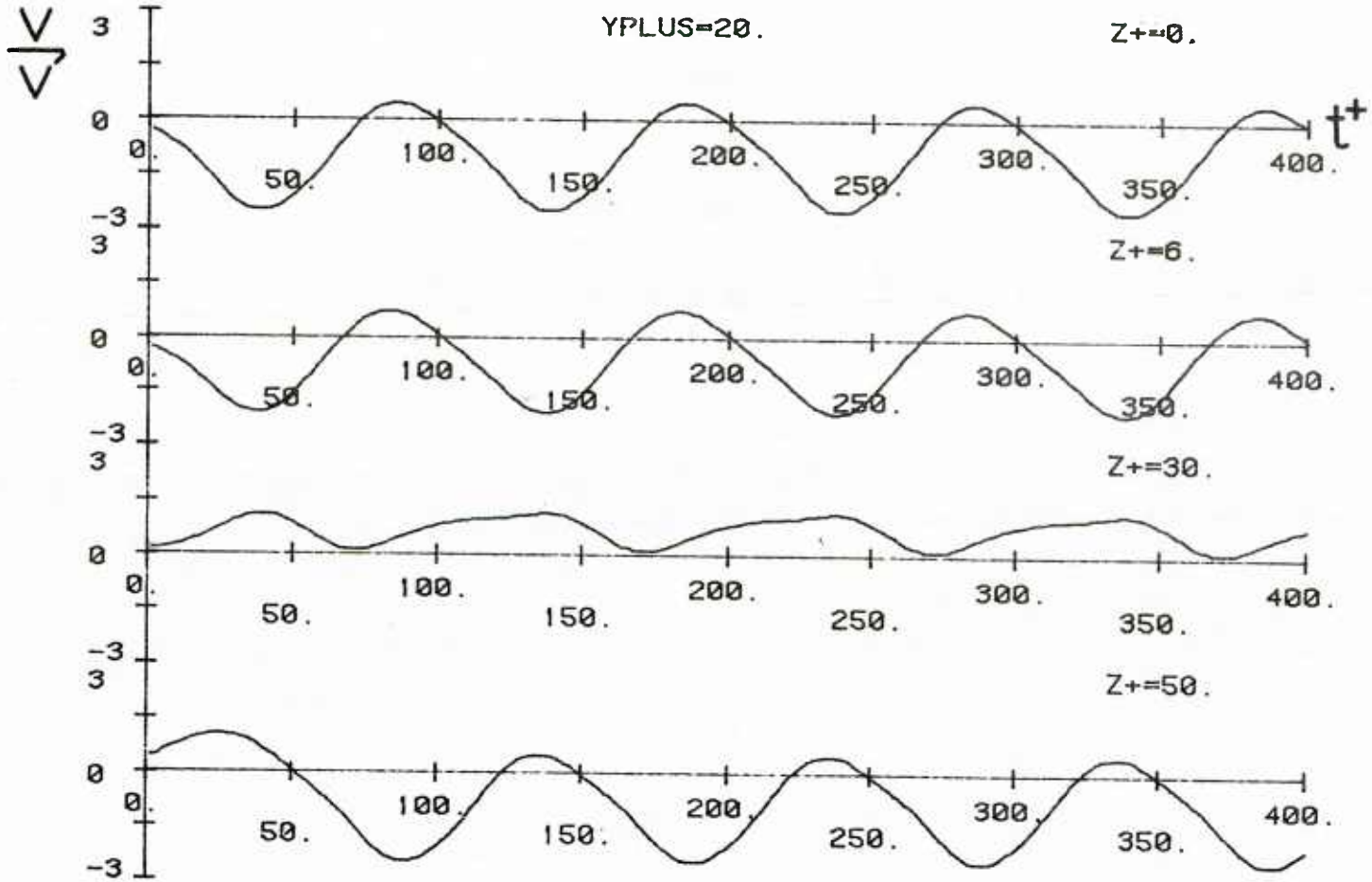

Figure 44 Plots of v/v' versus t^+ at $y^+ = 20$. Single harmonic run; upper boundary at $y_o^+ = 40$

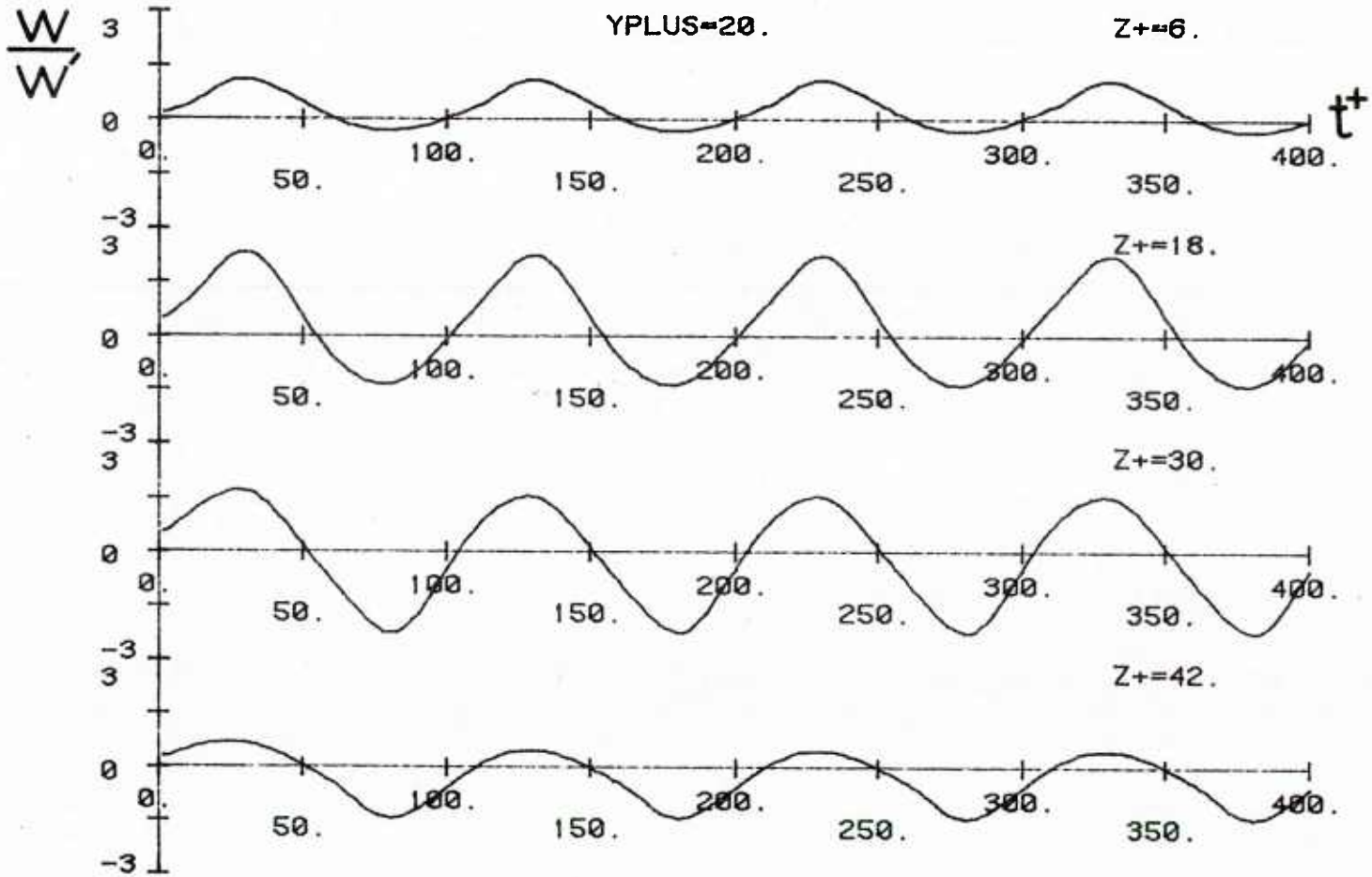

Figure 45 Plots of w/w' versus t^+ at $y^+ = 20$. Single harmonic run; upper boundary at $y_o^+ = 40$

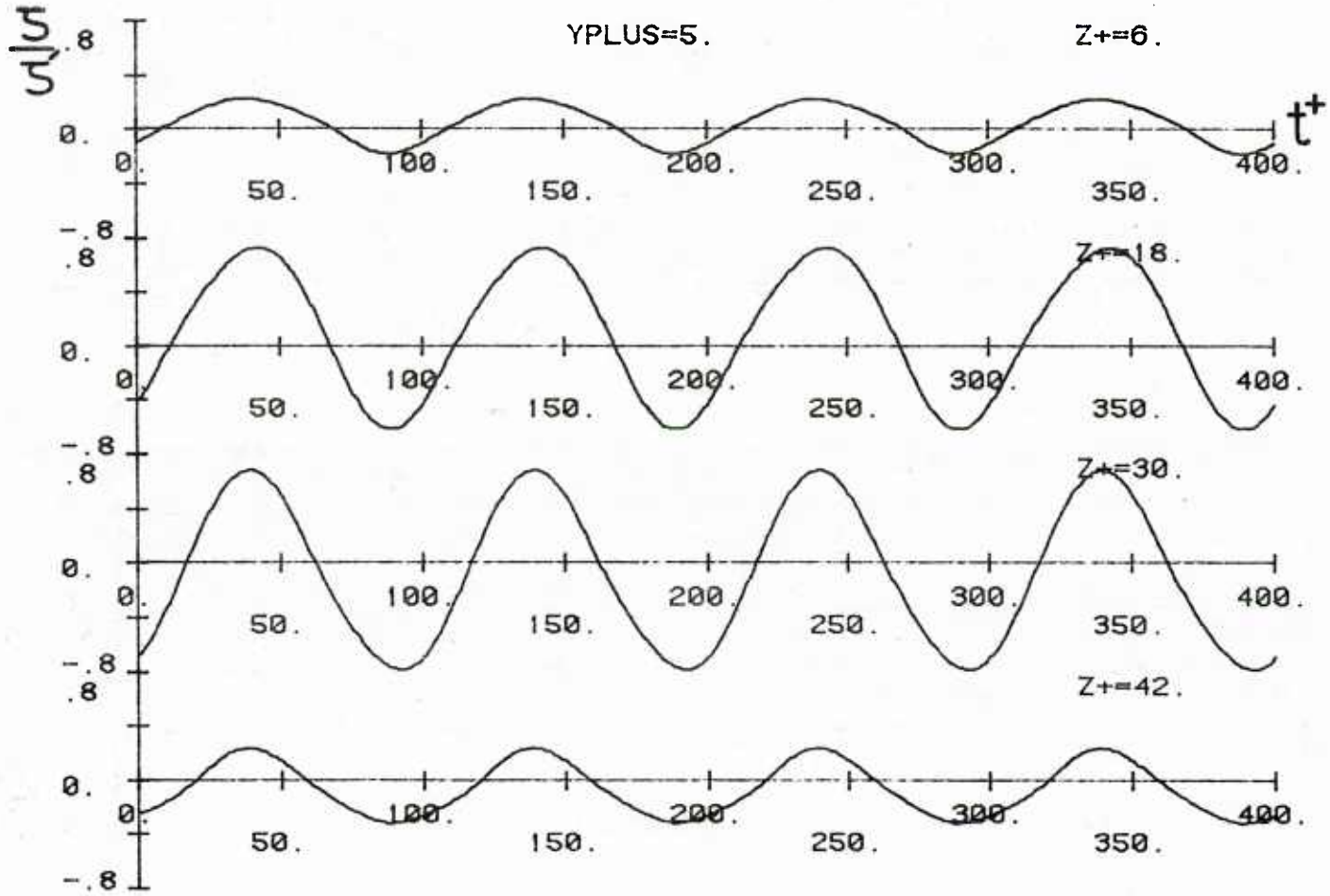

Figure 46 Plots of ς/ς' versus t^+ at $y^+=5$. Single harmonic run; upper boundary at $y_o^+=40$

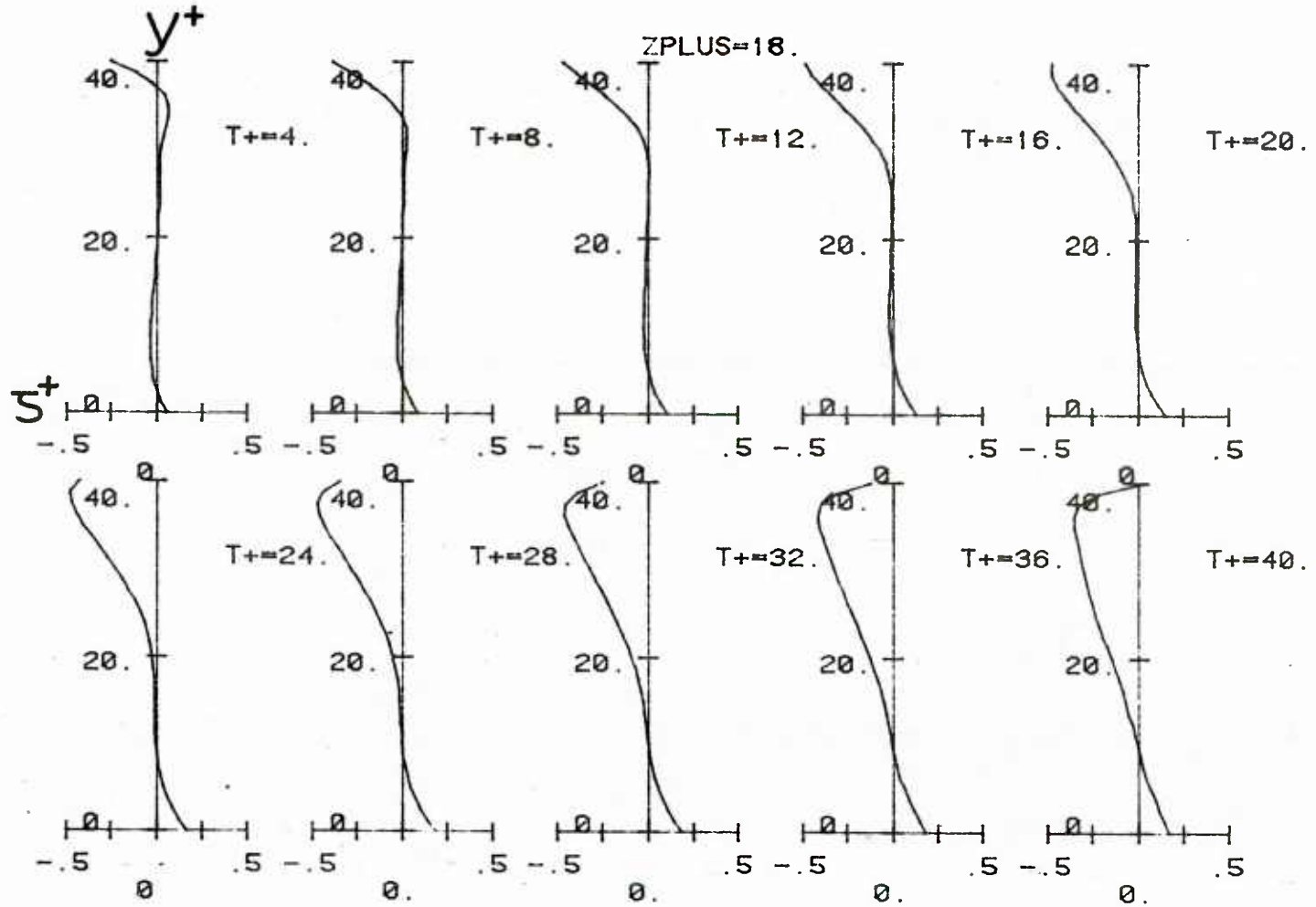

Figure 47a Plots of ς^+ versus y^+ at $z^+ = 18$ from $t^+ = 4$ to $t^+ = 40$. Single harmonic run; upper boundary at $y_o^+ = 40$

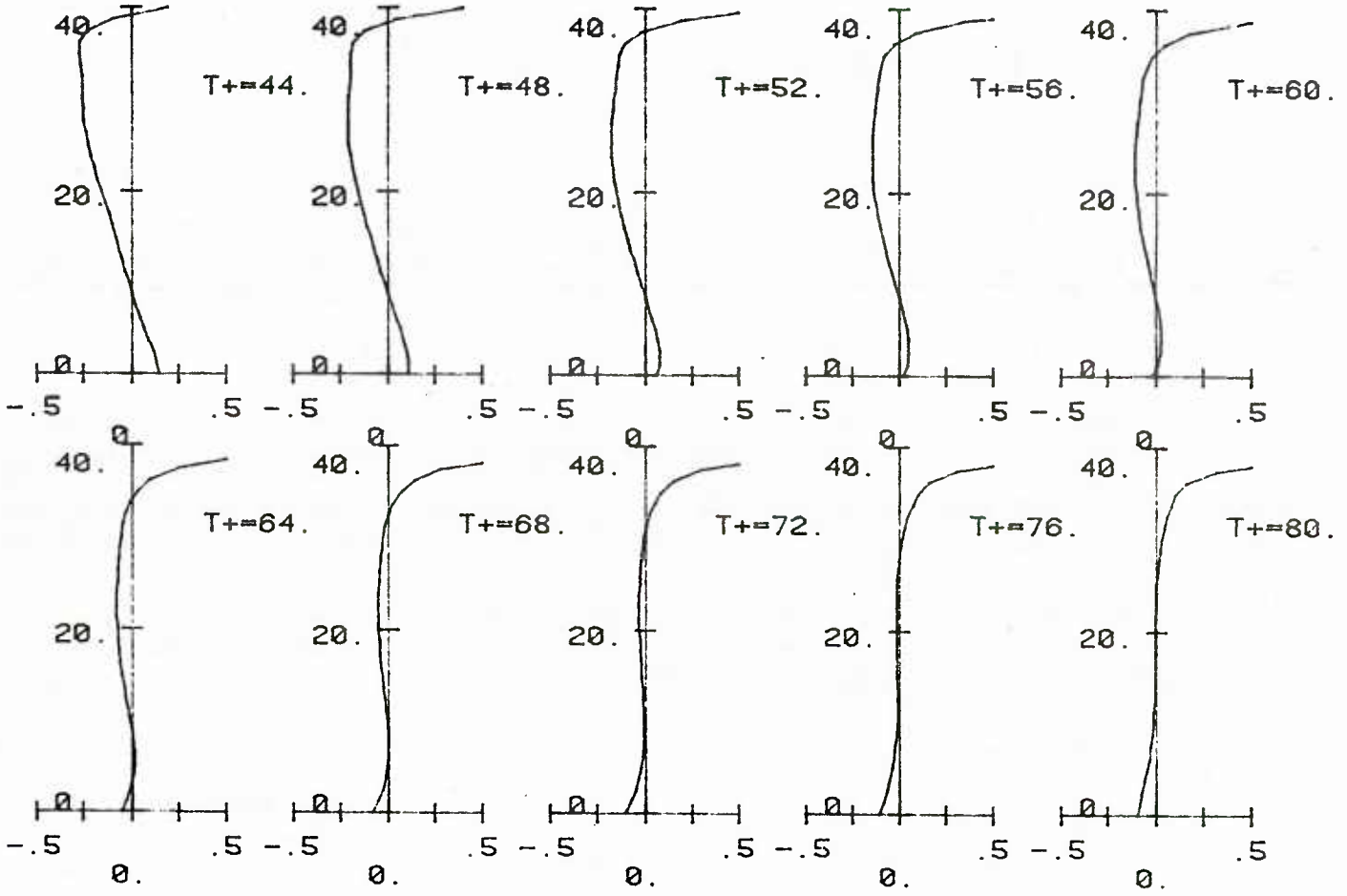

Figure 47b Plots of ς^+ versus y^+ at $z^+ = 18$ from $t^+ = 44$ to $t^+ = 80$. Single harmonic run; upper boundary at $y_o^+ = 40$

Figure 47c Plots of ζ^+ versus y^+ at $z^+=18$ from $t^+=84$ to $t^+=100$. Single harmonic run; upper boundary at $y_o^+=40$

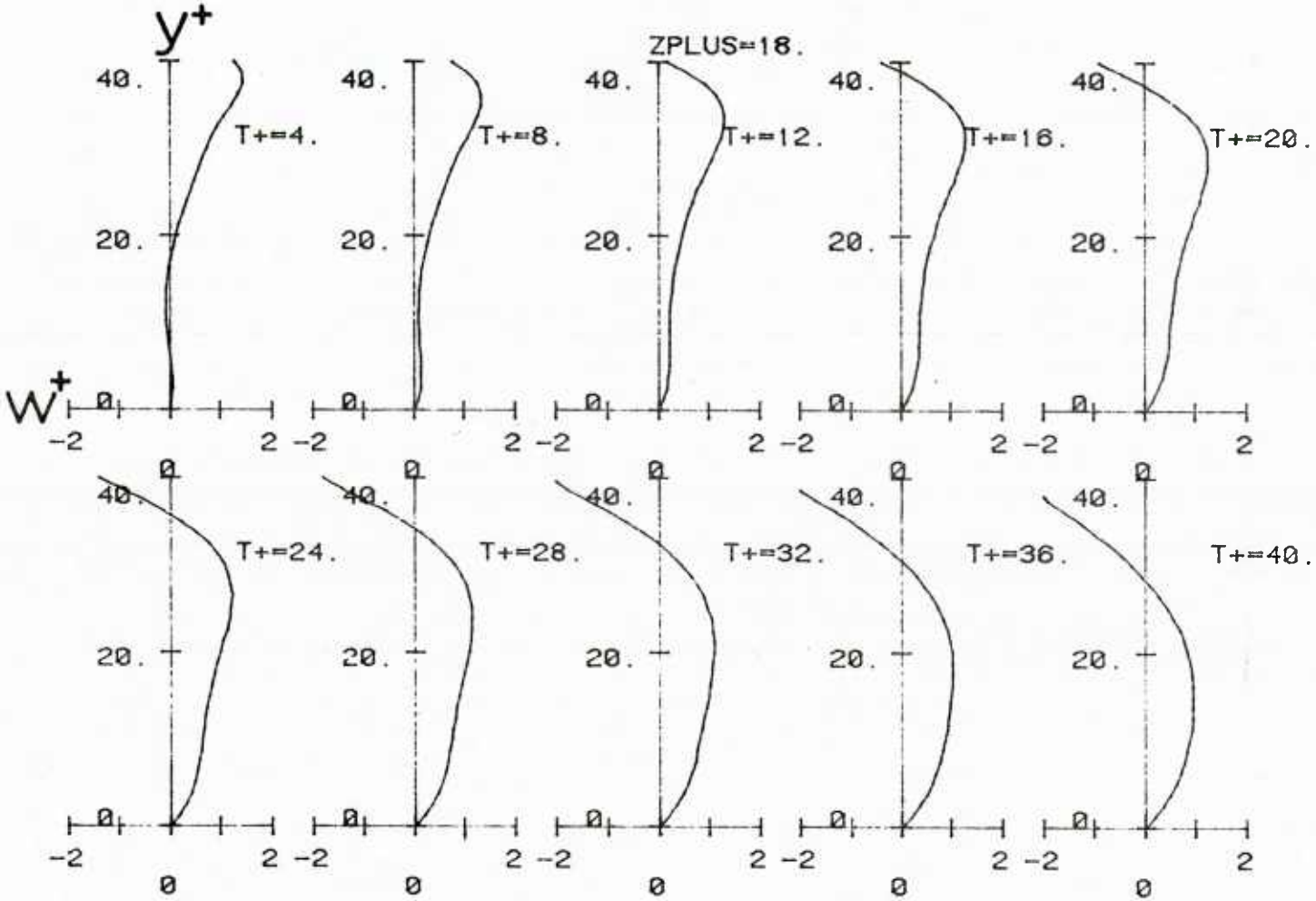

Figure 48a Plots of w^+ versus y^+ at $z^+ = 18$ from $t^+ = 4$ to $t^+ = 40$. Single harmonic run; upper boundary at $y_o^+ = 40$

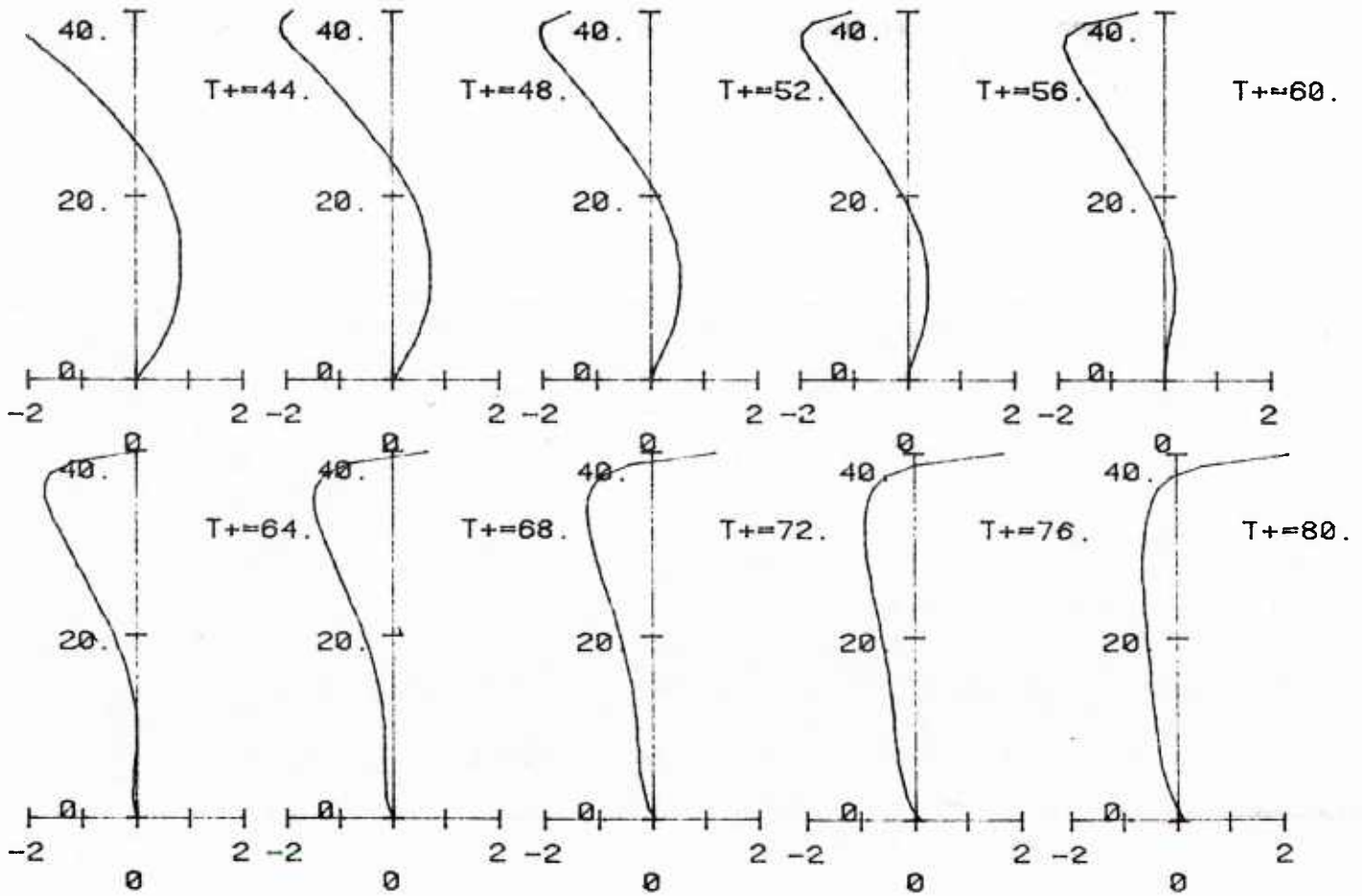

Figure 48b Plots of w^+ versus y^+ at $z^+ = 18$ from $t^+ = 44$ to $t^+ = 80$. Single harmonic run; upper boundary at $y_o^+ = 40$

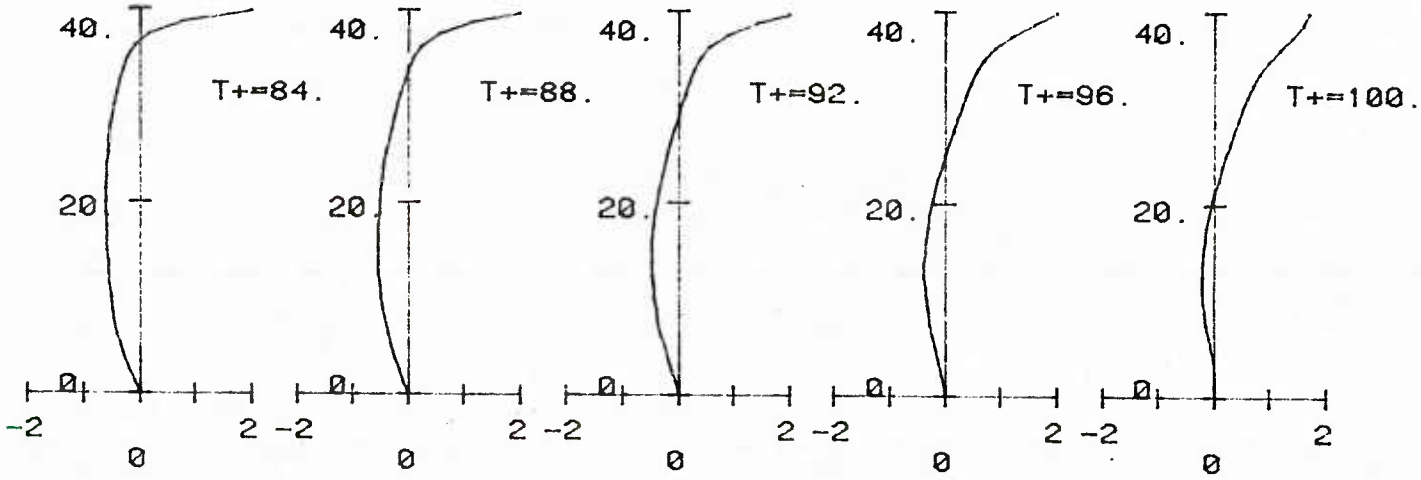

Figure 48c Plots of w^+ versus y^+ at $z^+=18$ from $t^+=84$ to $t^+=100$. Single harmonic run; upper boundary at $y_o^+=40$

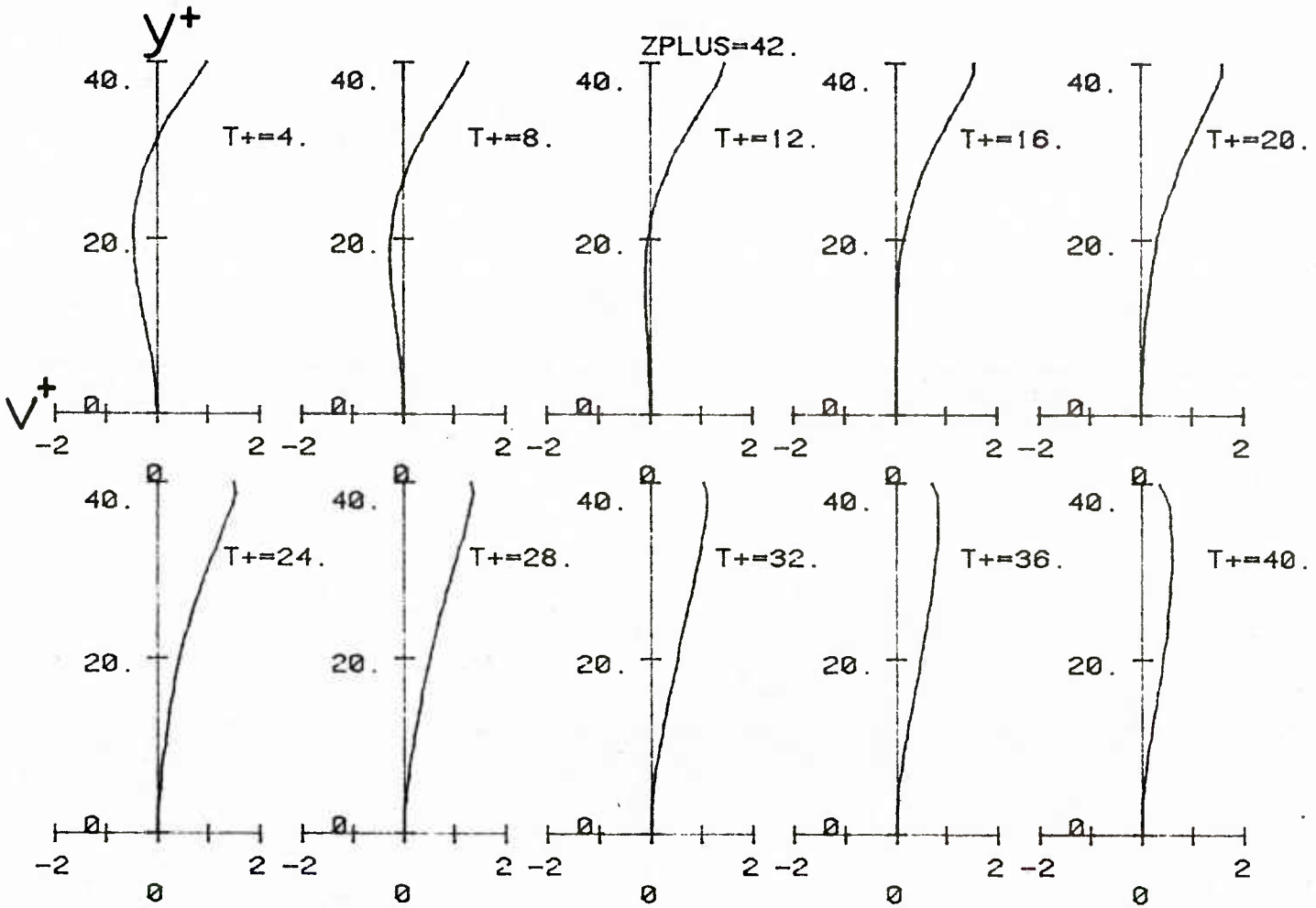

Figure 49a Plots of v^+ versus y^+ at $z^+ = 42$ from $t^+ = 4$ to $t^+ = 40$. Single harmonic run; upper boundary at $y_o^+ = 40$

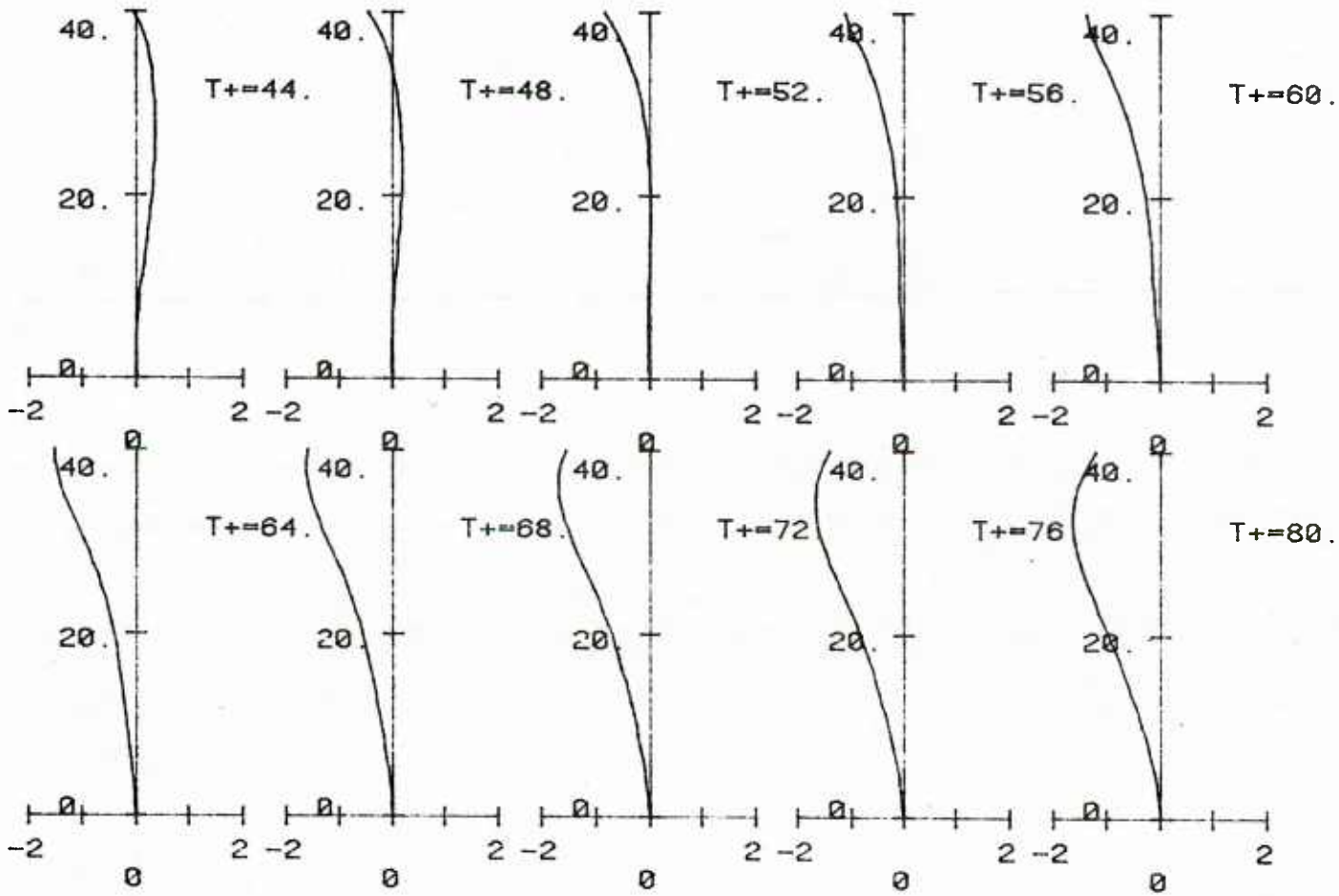

Figure 49b Plots of v^+ versus y^+ at $z^+ = 42$ from $t^+ = 44$ to $t^+ = 80$. Single harmonic run; upper boundary at $y_o^+ = 40$

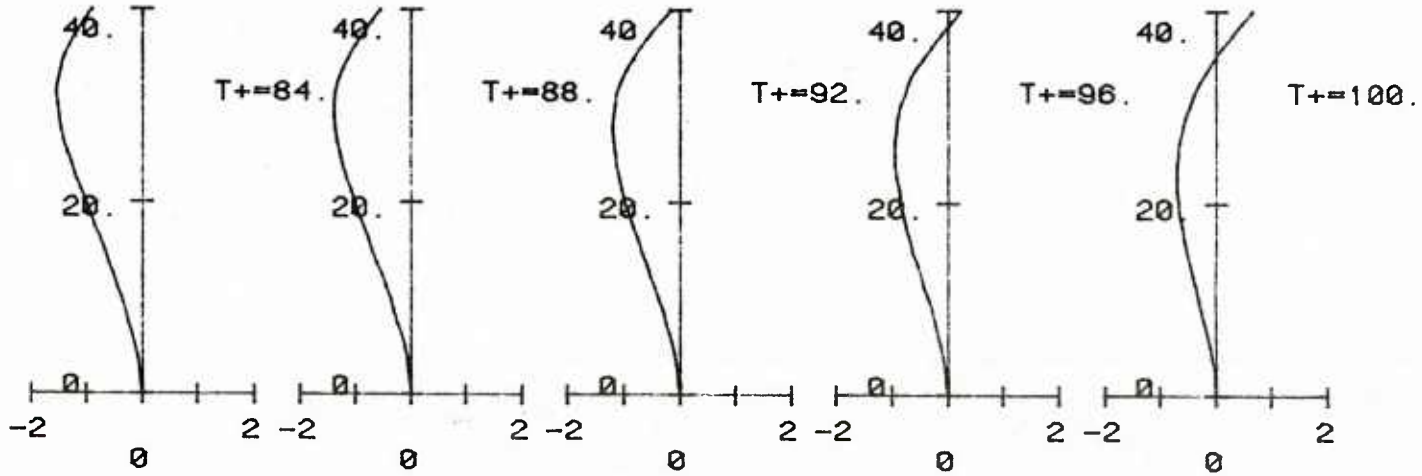

Figure 49c Plots of v^+ versus y^+ at $z^+=42$ from $t^+=84$ to $t^+=100$. Single harmonic run; upper boundary at $y_o^+=40$

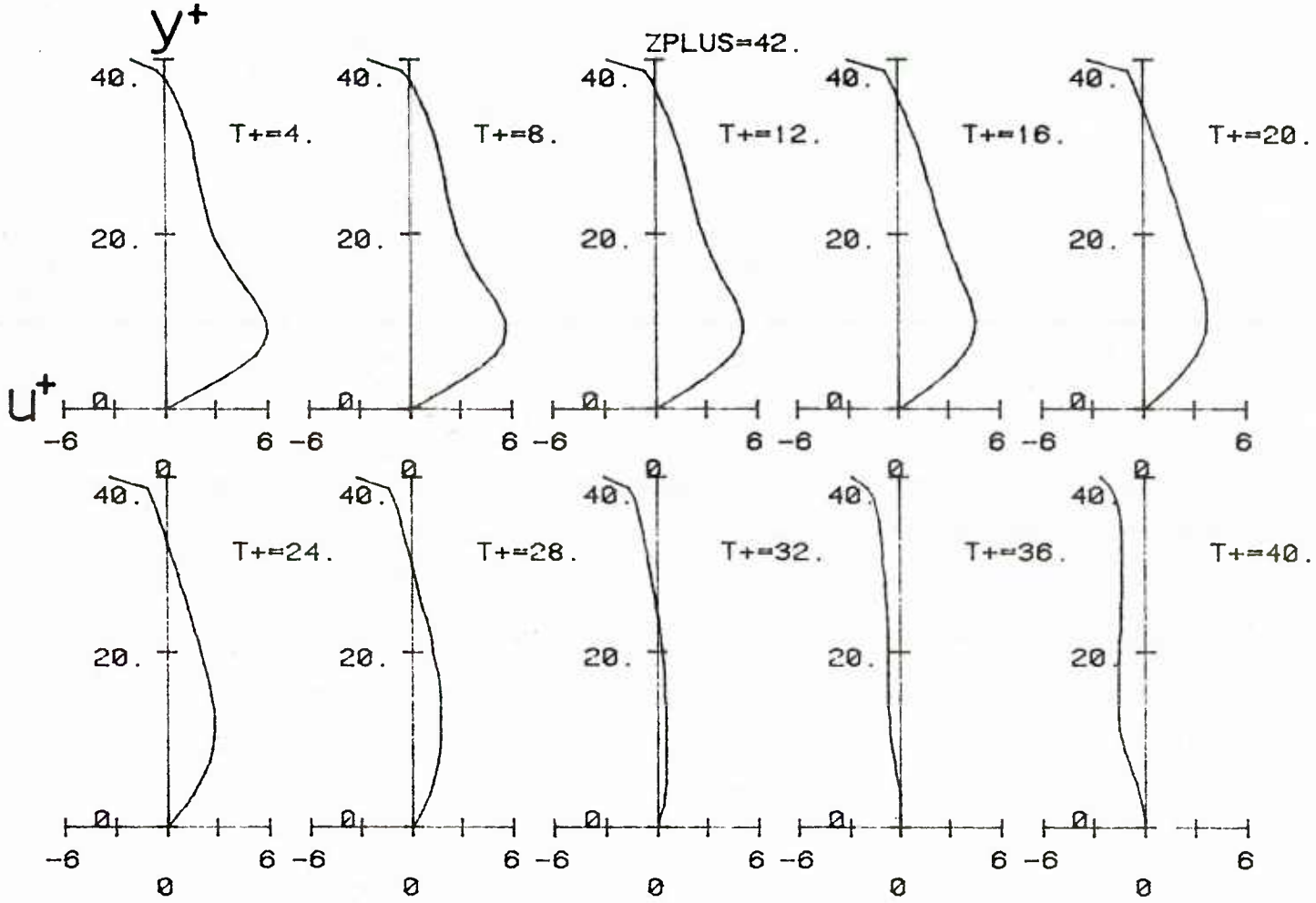

Figure 50a Plots of u^+ versus y^+ at $z^+ = 42$ from $t^+ = 4$ to $t^+ = 40$. Single harmonic run; upper boundary at $y_o^+ = 40$

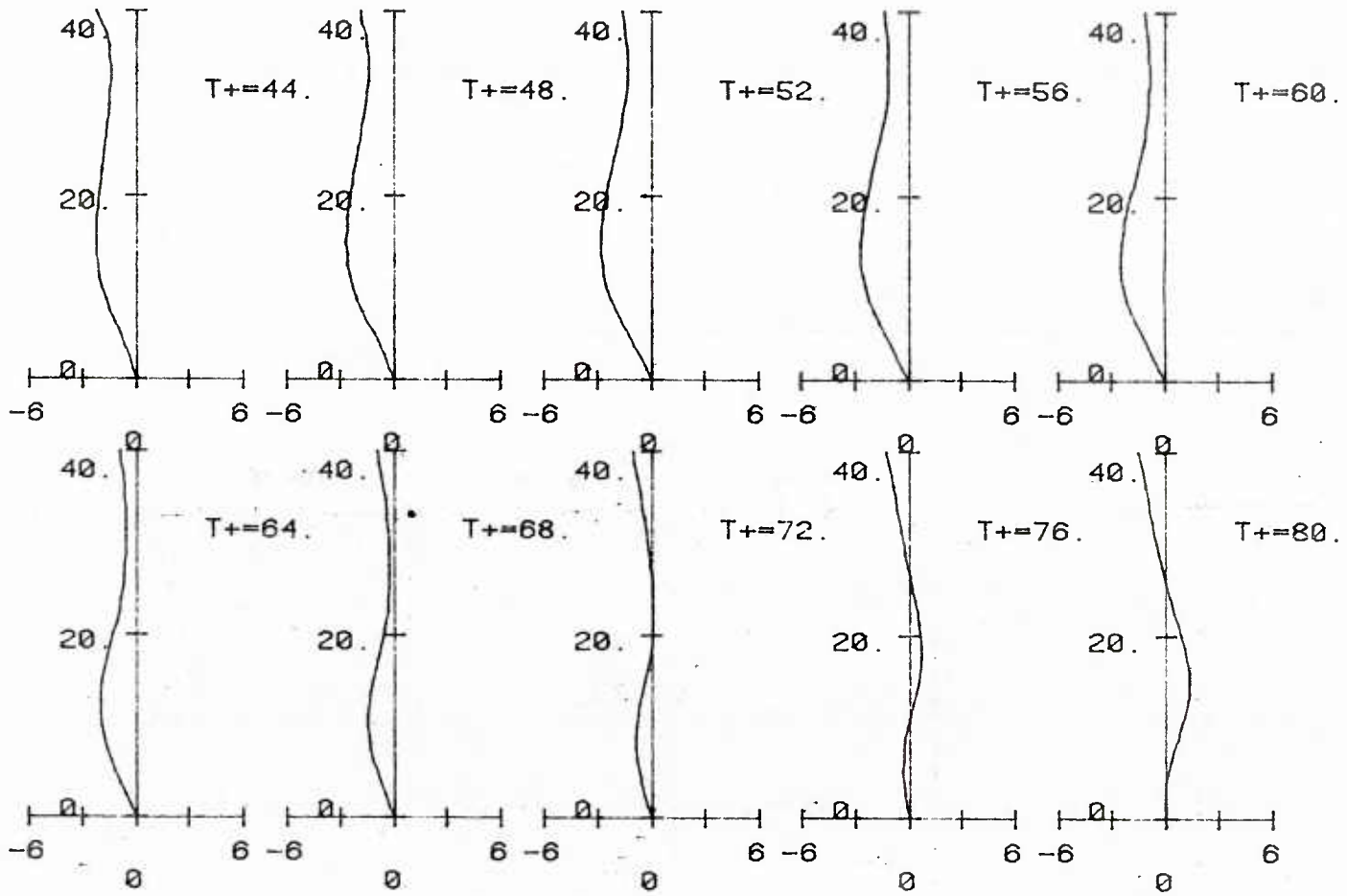

Figure 50b Plots of u^+ versus y^+ at $z^+ = 42$ from $t^+ = 44$ to $t^+ = 80$. Single harmonic run; upper boundary at $y_o^+ = 40$

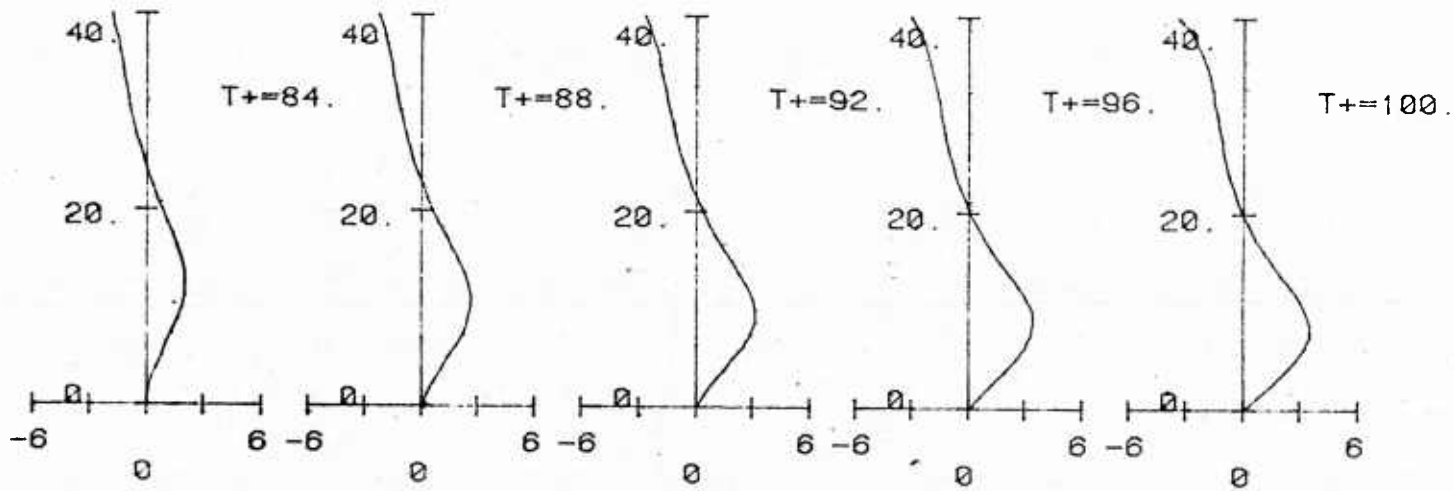

Figure 50c Plots of u^+ versus y^+ at $z^+=42$ from $t^+=84$ to $t^+=100$. Single harmonic run; upper boundary at $y_o^+=40$

w components of the velocity normal to the wall.

Figures 48 and 49 show the lateral profiles of v and w at $z^+=42$ and 18 respectively, where their amplitudes are expected to attain large values. It is interesting to note that during the time periods that the streamwise vorticity exhibits a region of very small values, the spanwise velocity profile shows a $\cosh y$ distribution in the same region. This behavior which is expected from inviscid-irrotational theory is evident during $8 \leq t^+ \leq 20$ and $64 \leq t^+ \leq 80$ for $10 \leq y^+ \leq 30$. During the same periods of time and for the same range of y^+'s, the v-profile exhibits a $\sinh y$ distribution, as can be seen from Figure 48. When the streamwise vorticity attains its characteristic "signature" with the zero crossing at $y^+ \approx 10$, a zero-crossing appears in the w-profiles which starts moving towards the wall. At the same time the spanwise velocity distribution normal to the wall attains a maximum ($\frac{\partial w}{\partial y}=0$), which lies in the region $10 \leq y^+ \leq 25$ and also moves towards the wall. During the same periods of time the normal velocity profiles bend over from the $\sinh y$ distribution and approach the upper boundary with either positive or negative slope.

The lateral profiles of the streamwise velocity distribution for $z^+=42$ are shown in Figure 50. An inflow of high streamwise momentum fluid can be identified during $4 \leq t^+ \leq 32$ and $80 \leq t^+ \leq 100$, and is associated with a sharp maximum at $y^+ \approx 10$. An outflow develops during $36 \leq t^+ \leq 72$ and is characterized by a milder maximum that gives almost a plug-flow character to the u-velocity profile.

In order to study the unsteady nature of the flow field on the y–z plane path-line calculations were carried out. The trajectories of two fluid particles along with the respective residence times in the cell are shown in Figure 51. The solid line corresponds to a particle whose initial position is at $y^+=1.25$ and the dash line is the trajectory of a particle that was located at $y^+=5$, at $t^+=0$. It can be seen that the fluid particle that originates at $y^+=1.25$ needs a much longer period of time, than the other particle, in order to escape from the cell. It can also be seen that this particle spends almost four cycles ($T^+=400$) in the region below $y^+=5$. This can be explained by the fact that the normal velocities in this region are very small and the weak spanwise flows cause the particle to travel back and forth in the spanwise direction.

The streakline calculations are presented in Figure 52. The shape of a calculated streakline is representative of a dye-streak that would originate from a pointwise injection in a dye-visualization experiment. The streaklines are plotted every $\Delta t^+=40$ and cover a period of time equal to $T^+=400$. The characteristic of this plot is the initial spreading of the dye in the spanwise direction followed by a gradual lifting and an ejection towards the upper boundary.

In order to be able to compare the average properties of the computed field with experimental data, space and time averages of the flow variables are calculated and plotted versus the distance from the wall. These kinds of averages are needed in order to compare the results from the "fixed cell" calculations with what a fixed probe would measure in a real turbulent field. Figures 53 through

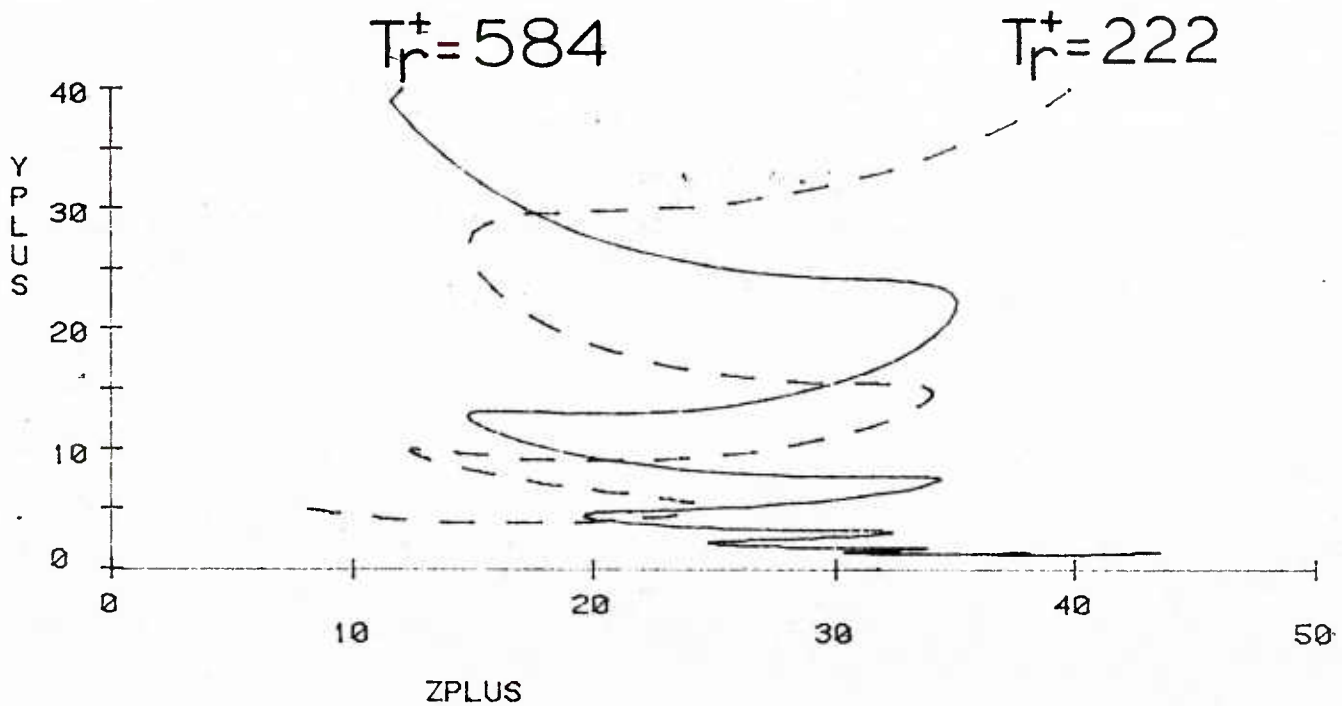

Figure 51 Trajectories of fluid particles in the cell. Single harmonic run.

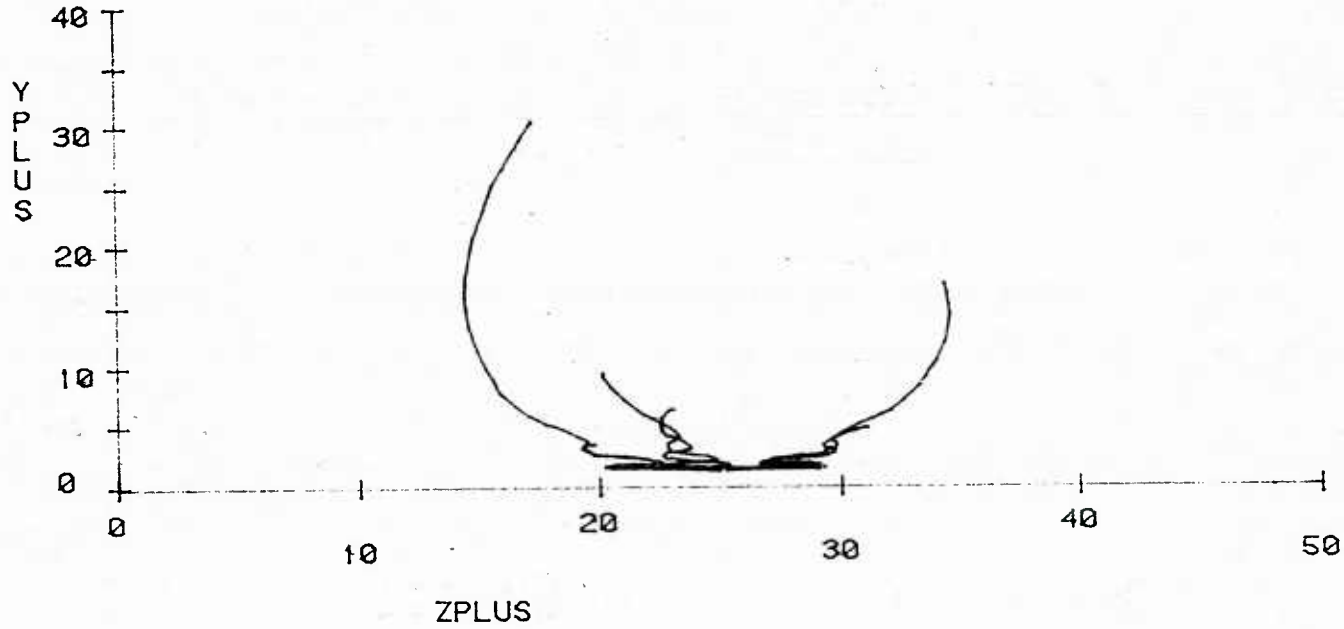

Figure 52 Streaklines for a single harmonic run. Injection point at $z_i^+ = 25$, $y_i^+ = 1.25$

57 present the average mean velocity profile, the Reynolds stress, the intensities of the three fluctuating components of the velocity and the skewness and flatness of the streamwise velocity component. It can be seen that, overall, the agreement with the experimental data is satisfactory, except the calculated intensity of the spanwise component of the velocity. In particular the calculated Reynolds stress, both in wall variables and as a correlation coefficient, shows a very good agreement with experiments for $0 \leq y^+ \leq 40$. The calculated v-intensity profile attains somewhat lower values than what the experiments indicate close to the wall, but agrees with the experimental data quite well in the region $y^+ \geq 25$. The w-intensity profile agrees with experiments close to the wall ($0 \leq y^+ \leq 5$) but exhibits a plateau region for $10 \leq y^+ \leq 25$ and then rises up in order to satisfy the imposed boundary condition. It was found throughout the computations, that such a profile of the w-intensity is characteristic of all the $\lambda^+ = 100$ single harmonic "fixed cell" runs.

The skewness of the streamwise velocity component shows satisfactory agreement with experiments up to $y^+ = 20$ but assumes larger values in the region $20 \leq y^+ \leq 40$. As it will be seen later, this is caused by the fact that there is no energy in scales longer than $\lambda^+ = 100$ on the y–z plane and especially in the spanwise component of the velocity for the single harmonic runs. The flatness of the u-component of the velocity is seen to agree with experiments throughout the viscous wall region.

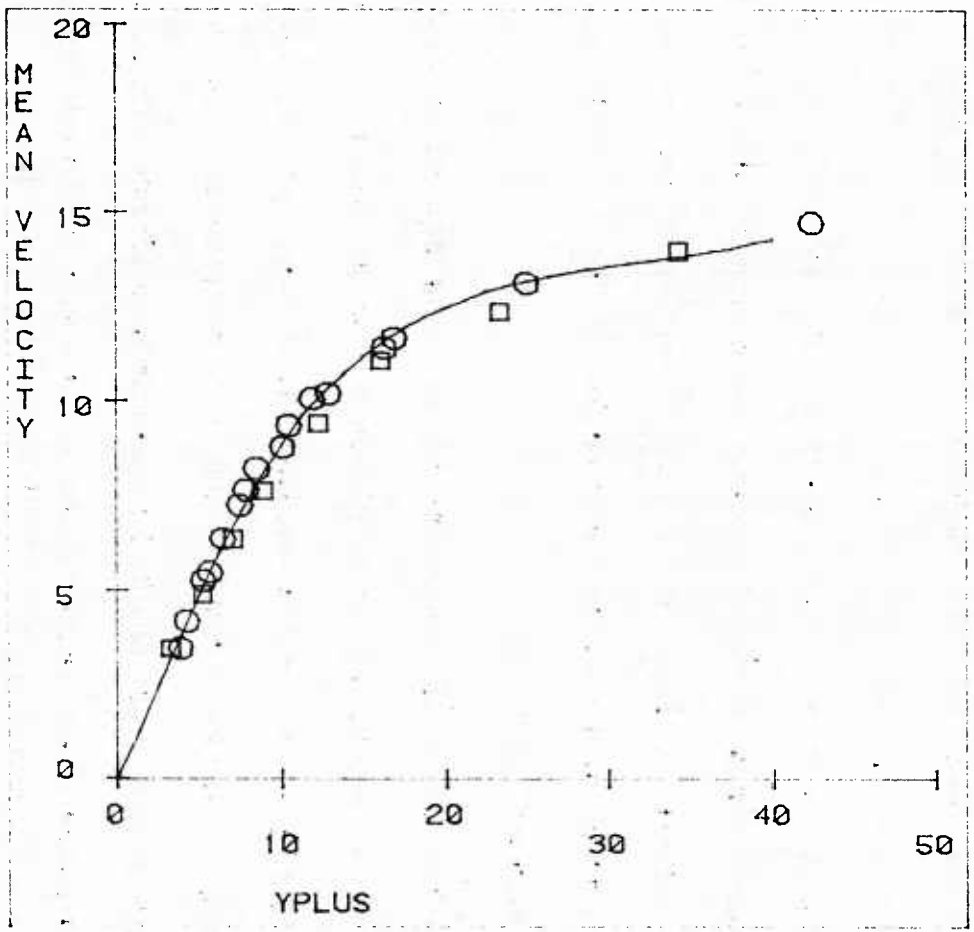

Figure 53 Mean streamwise velocity for a single harmonic run; upper boundary at $y_o^+ = 40$

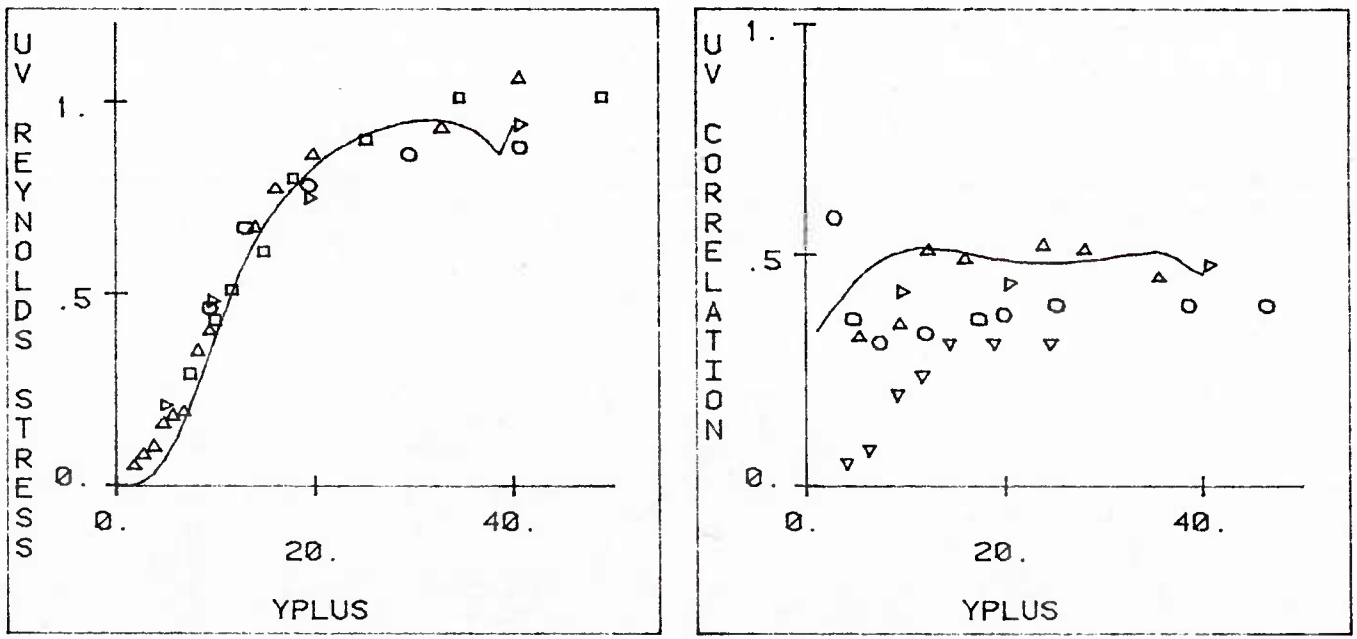

Figure 54 Reynolds stress and $-\overline{uv}/u'v'$ correlation for a single harmonic run; upper boundary at $y_o^+ = 40$

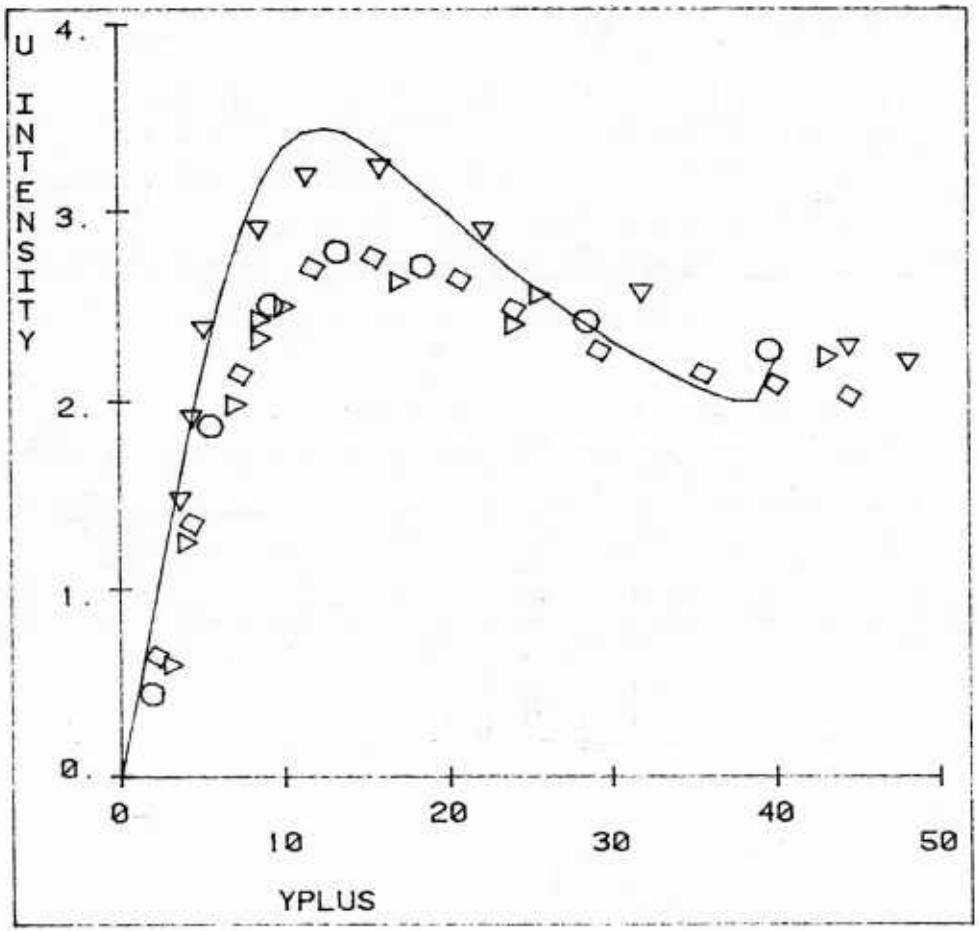

Figure 55 Intensity of streamwise velocity fluctuations for a single harmonic run; upper boundary at $y_o^+ = 40$

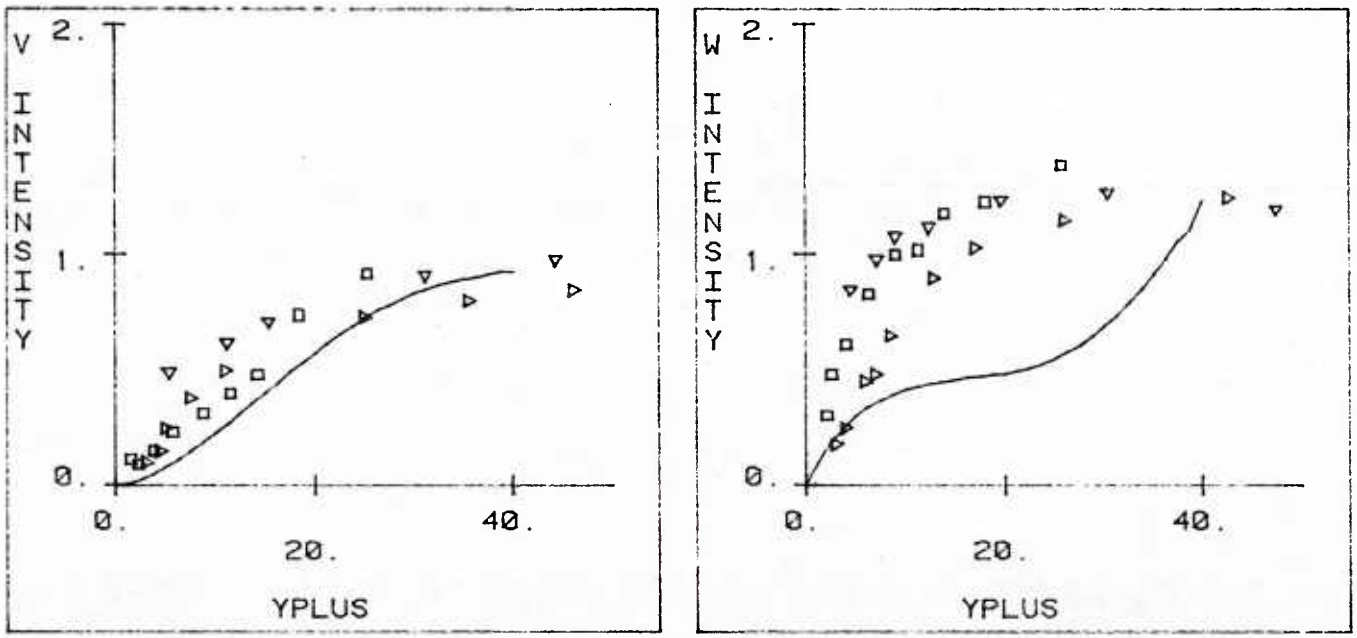

Figure 56 Intensities of the normal and spanwise velocity fluctuations for a single harmonic run; upper boundary at $y_o^+ = 40$

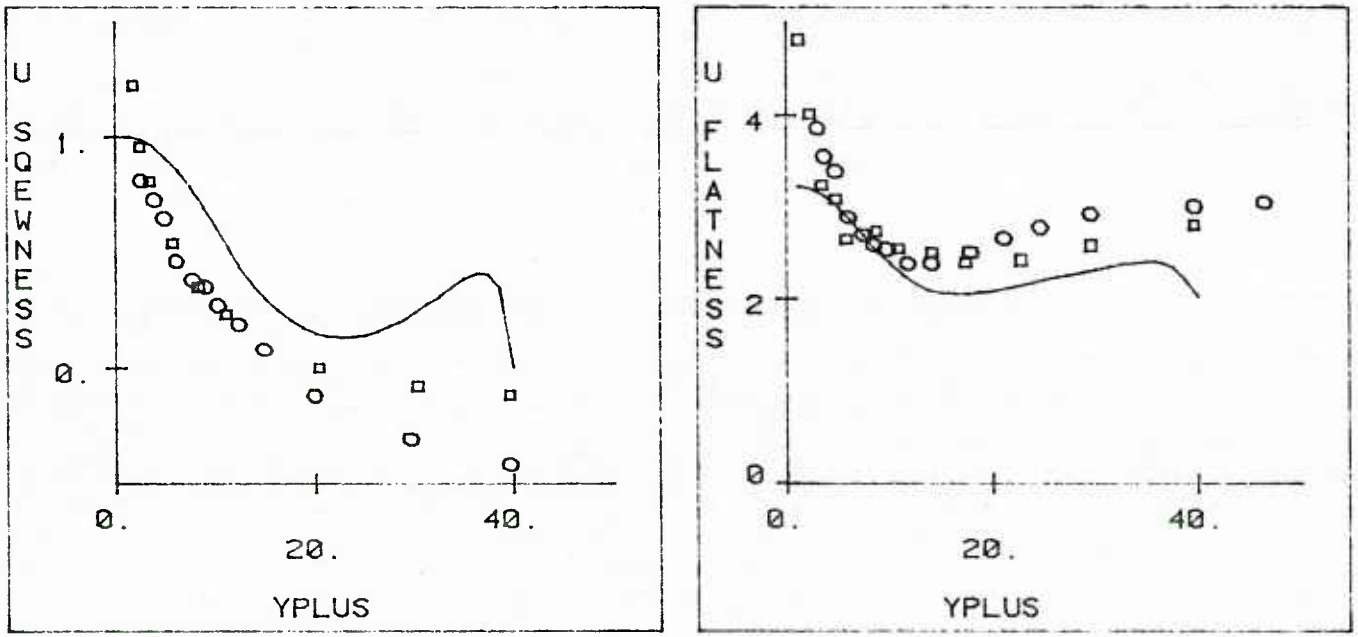

Figure 57 Skewness and flatness of streamwise velocity fluctuations for a single harmonic run; upper boundary at $y_o^+ = 40$

In all the above calculations the temporal variation of the $\lambda^+=100$ eddies at $y_o^+=40$ was approximated by a single harmonic with a period of $T^+=100$. In what follows, we will present some results of calculations in which experimental data were used in order to prescribe the time signature of the three components of the velocity at $y_o^+=40$. The statistically averaged results of these calculations were similar to the ones presented above. The most interesting feature of the computed time signals is a filtering mechanism, according to which the streamwise velocity appears to contain much lower frequencies than the velocity fluctuations on the $y-z$ plane. This is evident in the plots of v and u presented in Figures 58 and 59. The low frequency streamwise velocity fluctuations contrast the normal velocity fluctuations which clearly contain higher frequencies. The spanwise velocity fluctuations, which are not shown here, were found to have a similar behavior to the fluctuations of the normal component of the velocity. The filtering effect that appears on the streamwise velocity component can be elucidated, if one observes the path-lines of fluid particles in the cell. Such path-line calculations are shown in Figure 60. It can be seen that for a fluid particle starting very close to the wall ($y^+=1.25$) the trajectory is almost a straight line parallel to the wall. The residence time for this particle in the cell is longer than $t^+=700$ which is the total duration of the run. If such a particle carried high streamwise momentum as a result of an inflow at $z^+=0$ then it will take a very long time for the particle to travel along the wall, exchange its momentum and emerge as a momentum deficient particle. It is this fact, then,

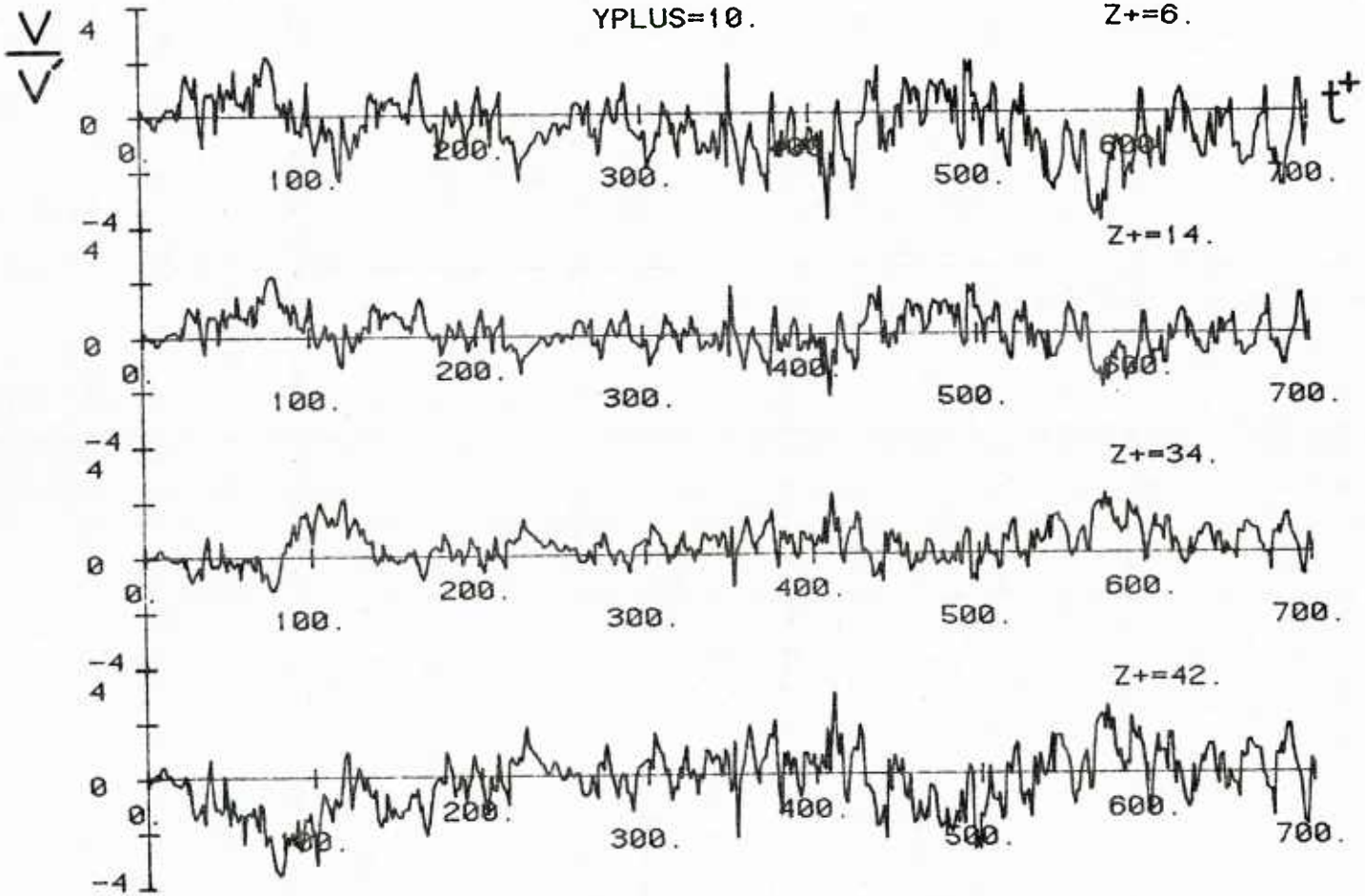

Figure 58 Plots of v/v' versus t^+ at $y^+=10$. Signals at $y_o^+=40$ contain a wide range of frequencies.

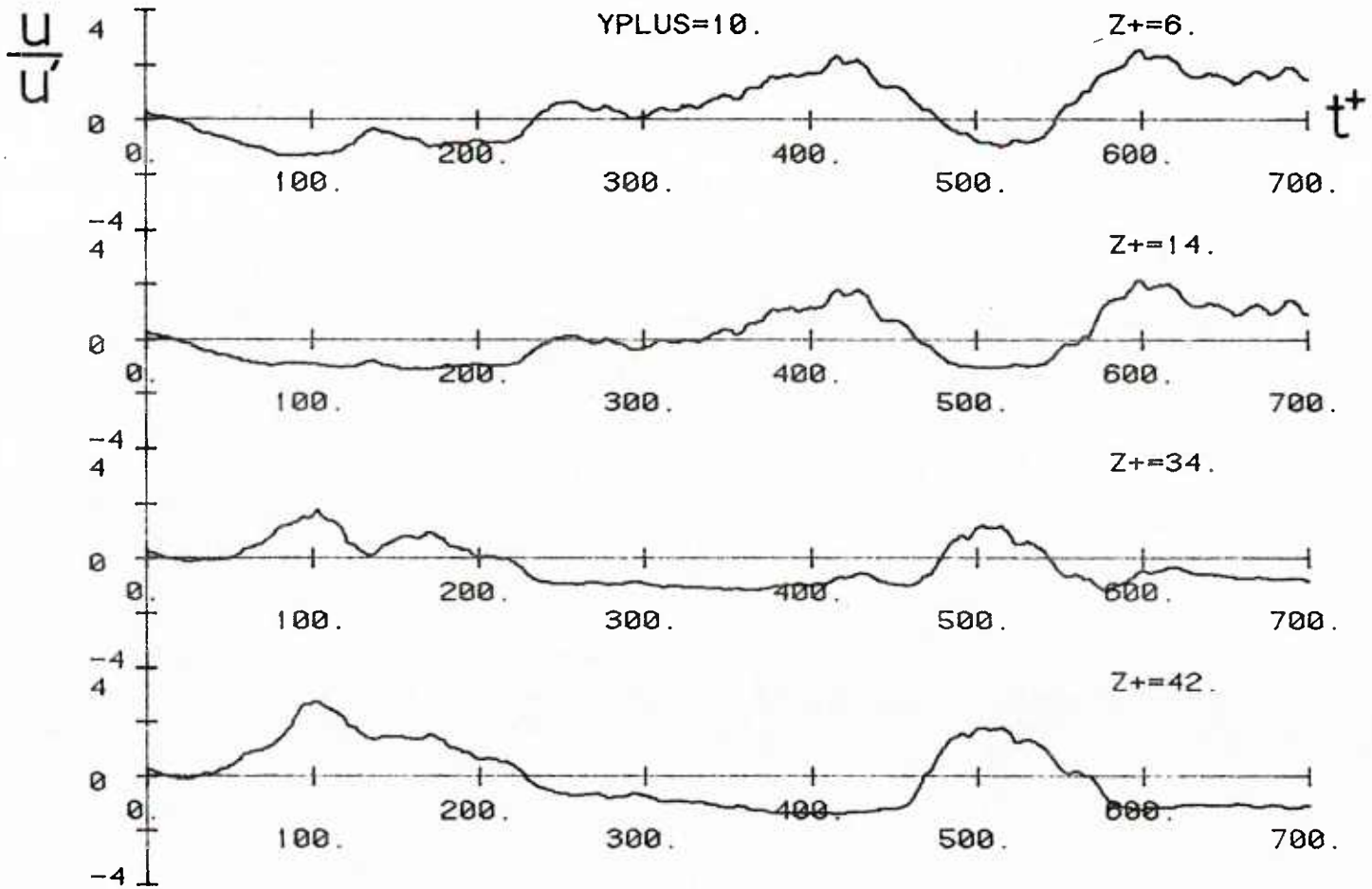

Figure 59 Plots of u/u' versus t^+ at $y^+=10$. Signals at $y_o^+=40$ contain a wide range of frequencies.

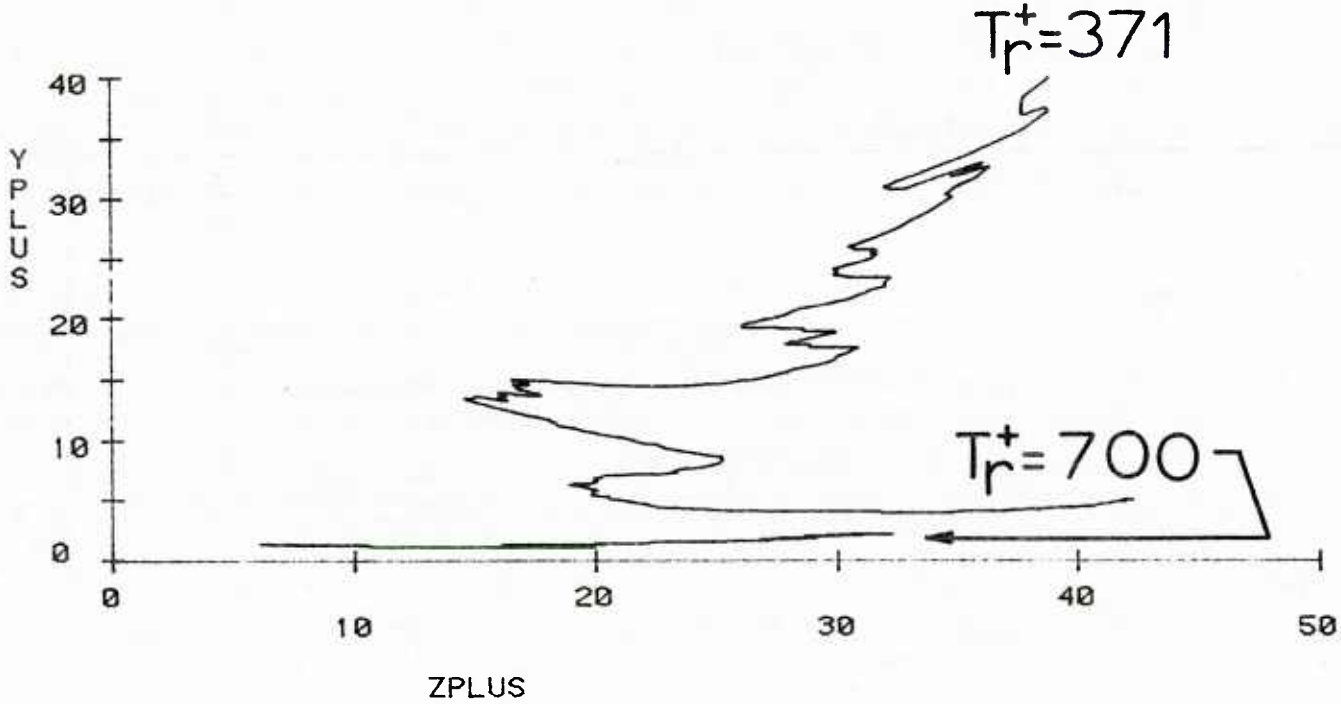

Figure 60 Trajectories of fluid particles in the cell. Signals at $y_o^+ = 40$ contain a wide range of frequencies.

that causes the streamwise velocity component to contain much lower frequencies than the velocities on the y–z plane. For another particle starting at $y^+=5$ the residence time is $t^+=371$ which is much shorter than the one for the particle close to the wall.

Before closing the presentation of the results for the single harmonic case we will discuss the effects of different boundary conditions at $y_o^+=40$, for the $\lambda^+=100$ eddies, on the computed dynamics. Two boundary conditions that were nondescript in the normal velocity component at $y_o^+=40$ were explored. These were the specification of zero vorticity or zero normal flux of vorticity along with the spanwise component of the velocity at the upper boundary of the computational domain. These boundary conditions were found to affect greatly the calculated lateral profiles of the streamwise vorticity. In particular, it was found that the vorticity stayed close to zero in a region extending from the outer boundary down to $y^+\approx 10$. These profiles were, thus, very different from the characteristic signature of the streamwise vorticity, presented earlier, when both v and w are specified at $y_o^+=40$.

2. Two harmonics in the spanwise direction

In these calculations a certain fraction of the energy on the y–z plane was associated with the $\lambda^+=400$ outer flow eddies according to arguments presented in Chapter 4. The results of the calculations are presented in the series of Figures 61 through 87. Figures 61 through 70 show the streamline contours for a calculation with $N_1=80\%$ and $E_{w1}=40\%$. The streamlines are plotted for a period

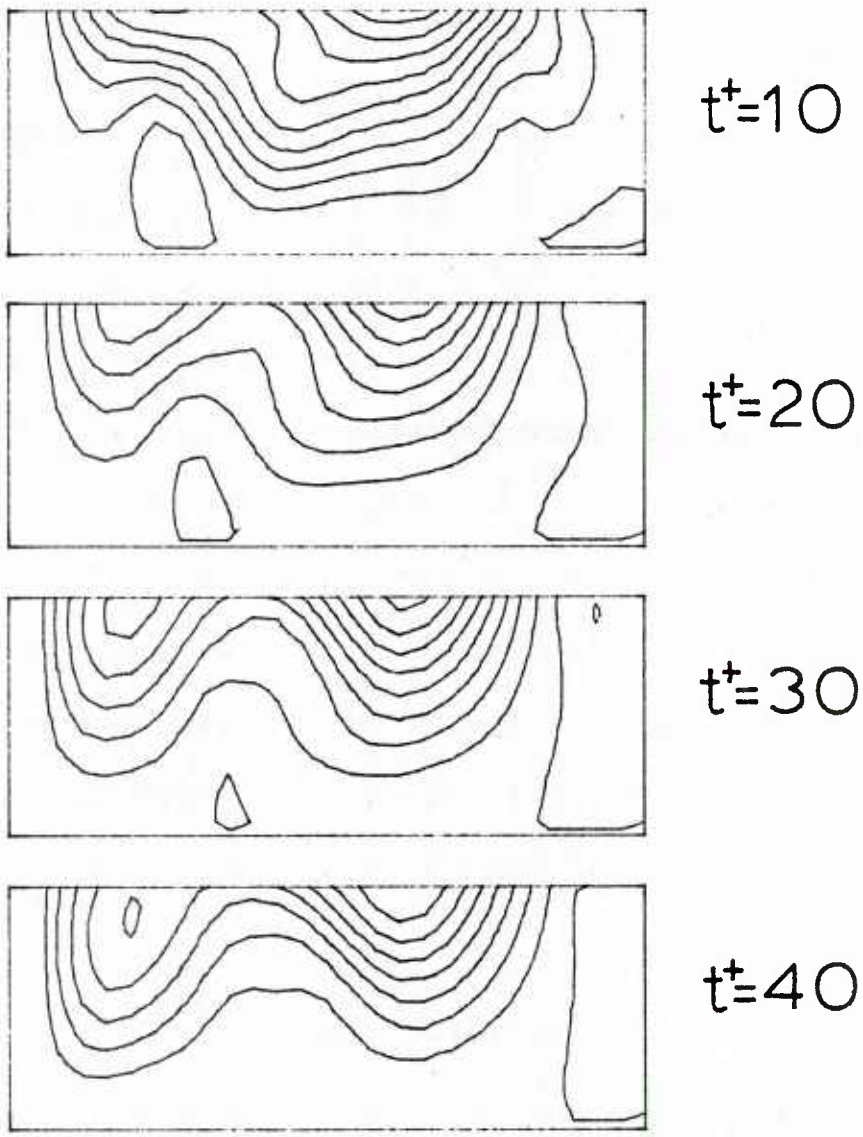

Figure 61 Streamline contours for a double harmonic run at $t^+=10$, 20, 30 and 40; upper boundary at $y_o^+=40$

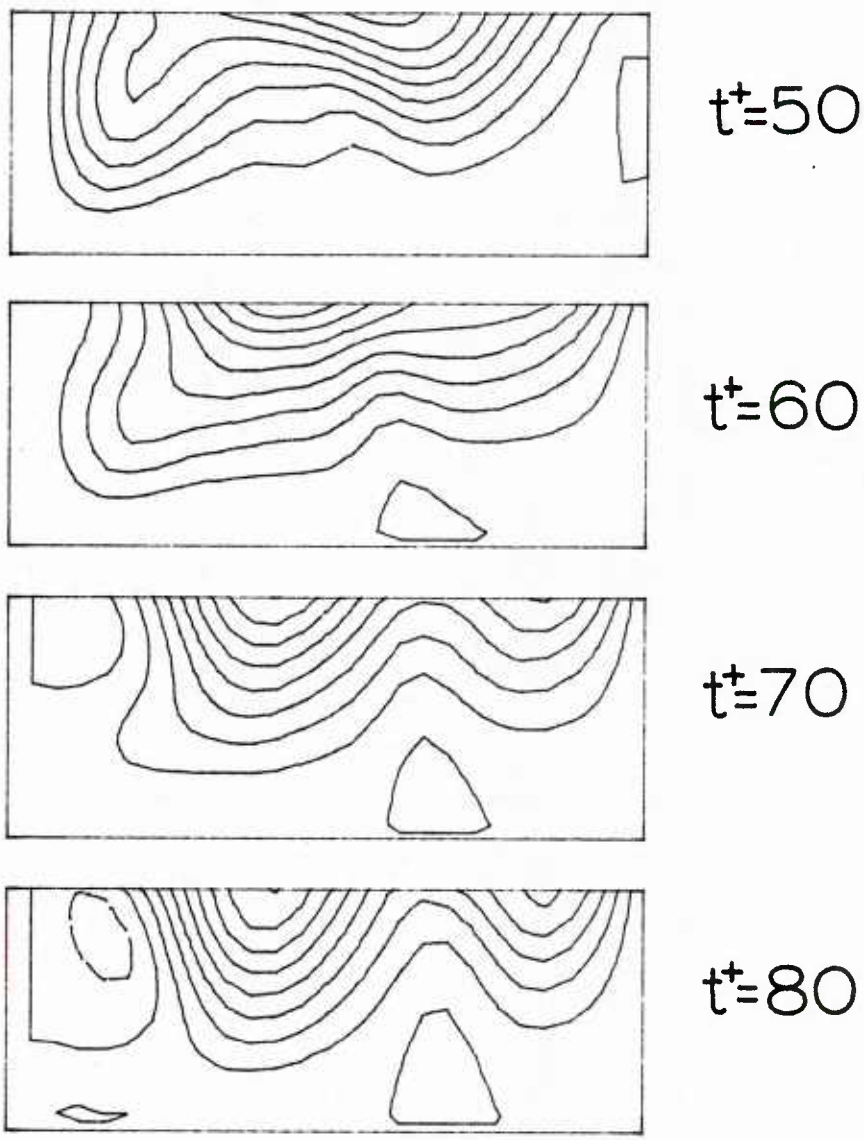

Figure 62 Streamline contours for a double harmonic run at $t^+ = 50, 60, 70$ and 80; upper boundary at $y_o^+ = 40$

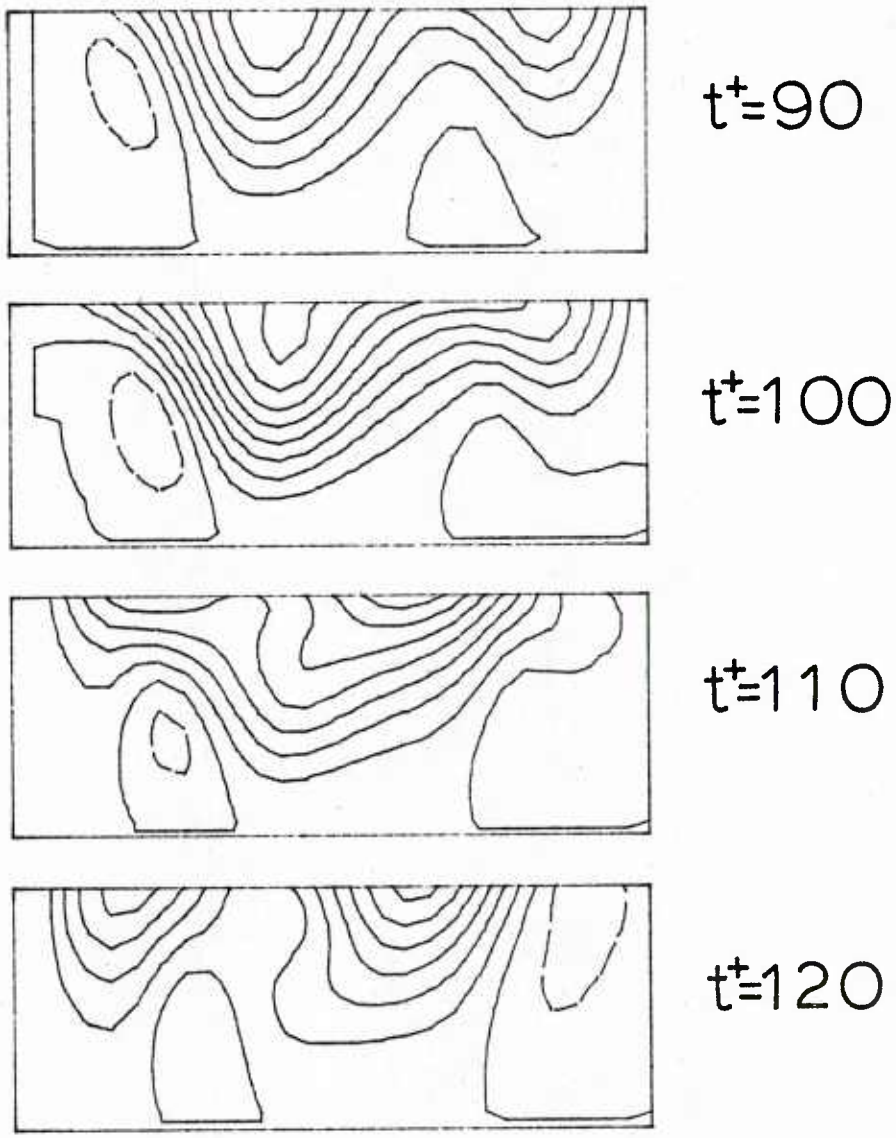

Figure 63 Streamline contours for a double harmonic run at $t^+=90$, 100, 110 and 120; upper boundary at $y_o^+=40$

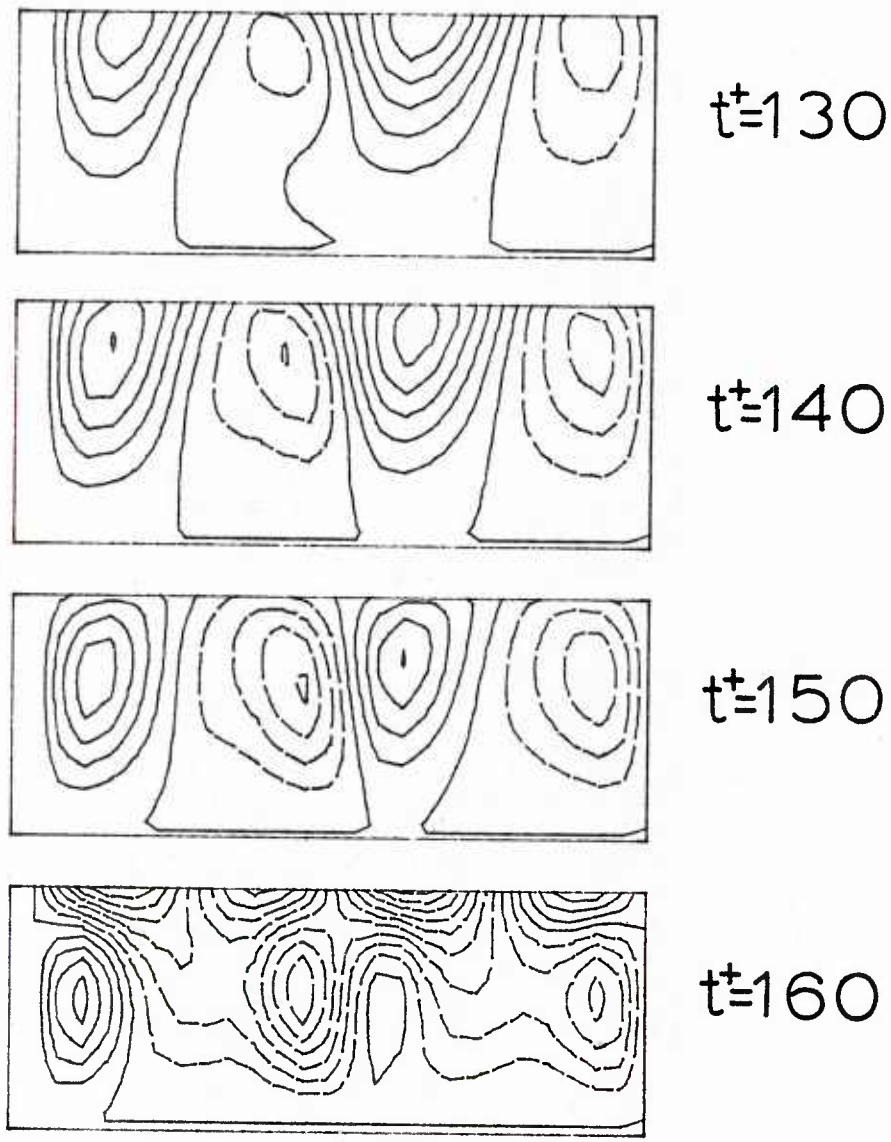

Figure 64 Streamline contours for a double harmonic run at $t^+ = 130,140,150$ and 160; upper boundary at $y_o^+ = 40$

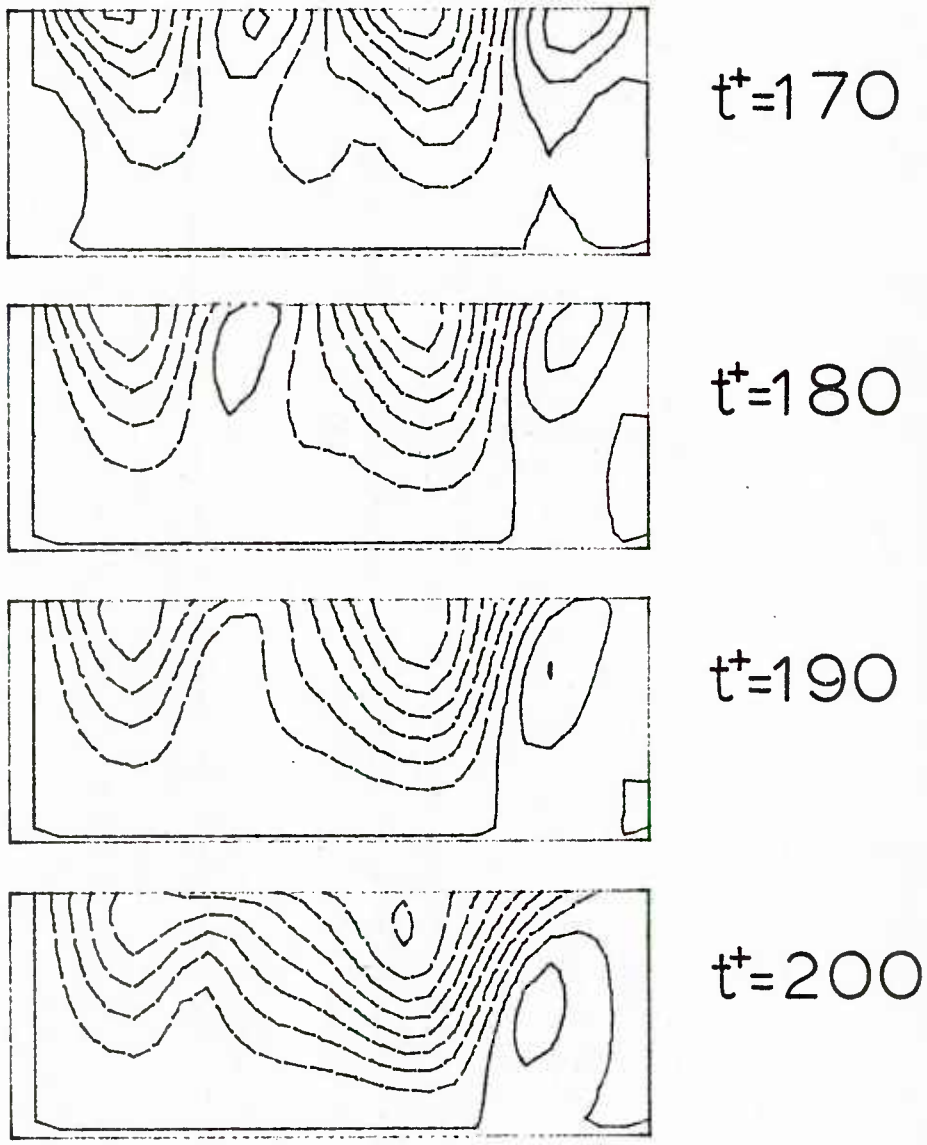

Figure 65 Streamline contours for a double harmonic run at $t^+ = 170,180,190$ and 200; upper boundary at $y_o^+ = 40$

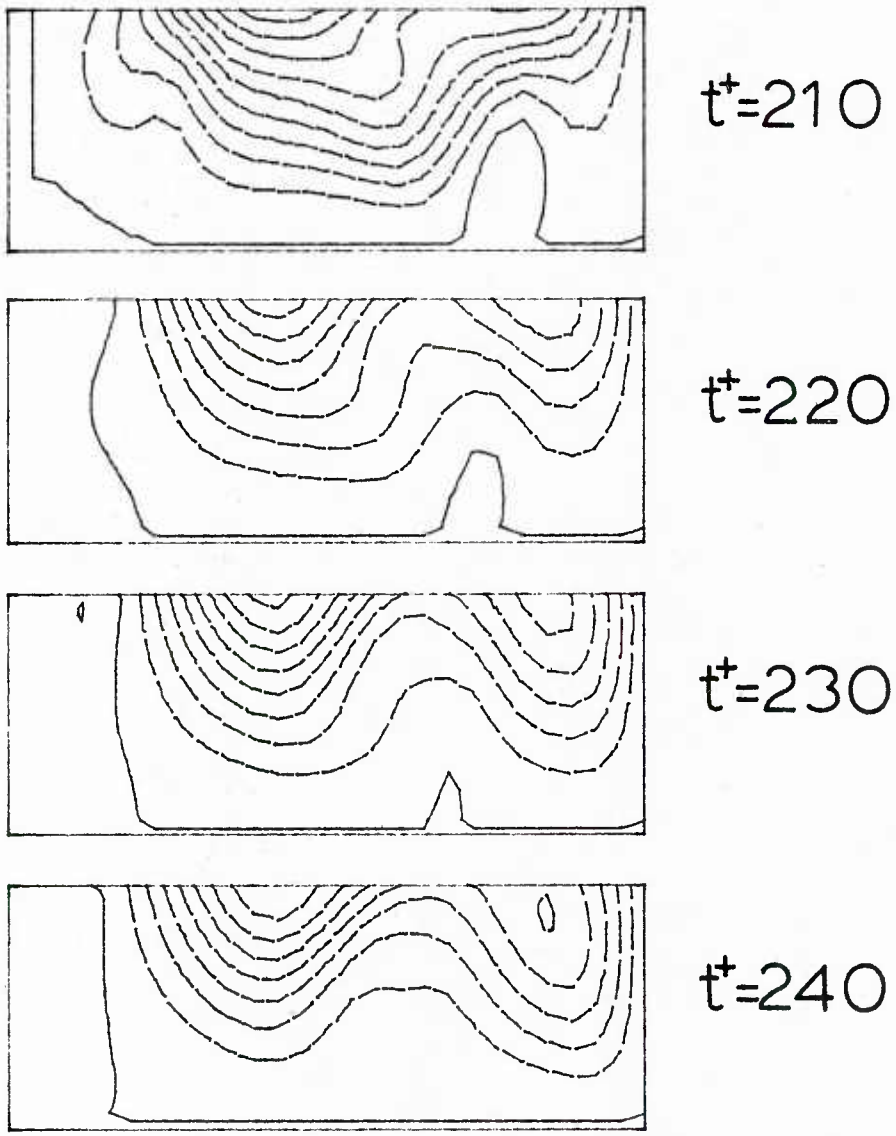

Figure 66 Streamline contours for a double harmonic run at $t^+ = 210,220,230$ and 240; upper boundary at $y_o^+ = 40$

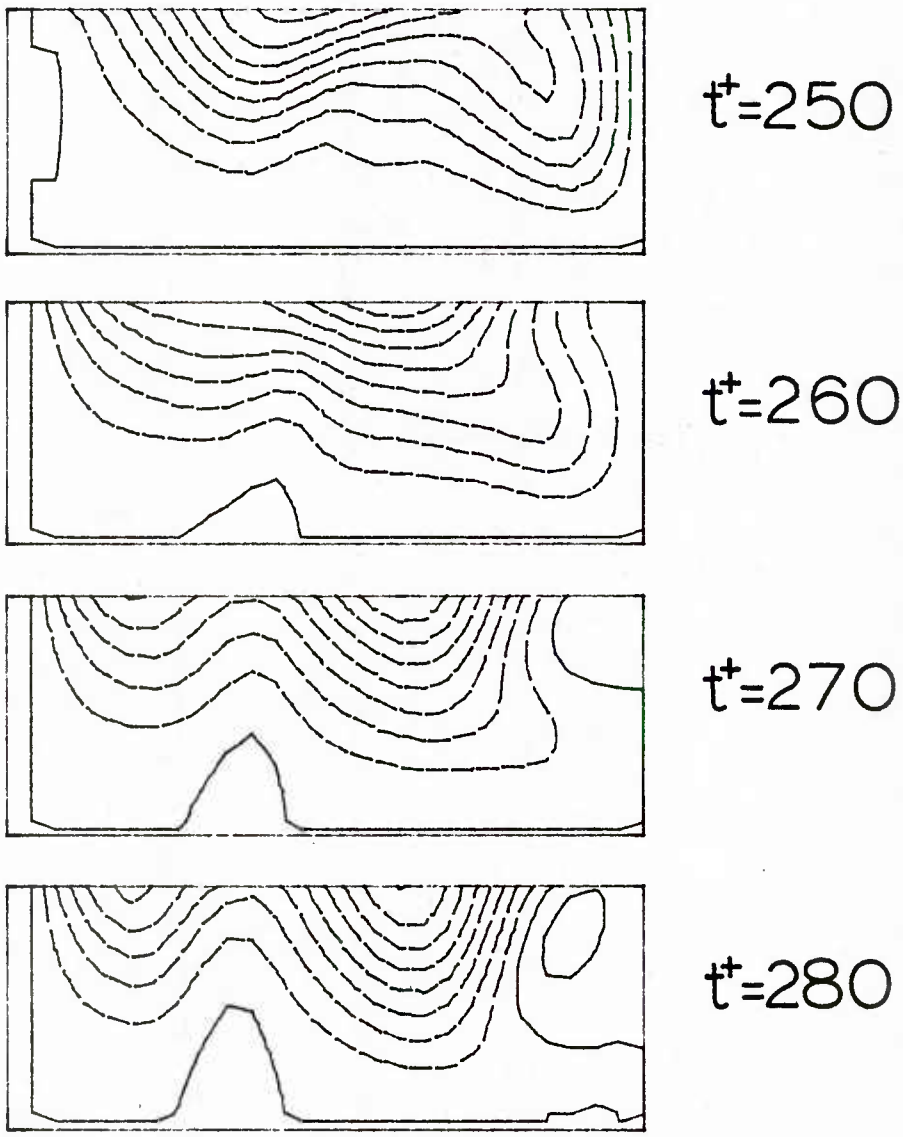

Figure 67 Streamline contours for a double harmonic run at $t^+ = 250,260,270$ and 280; upper boundary at $y_o^+ = 40$

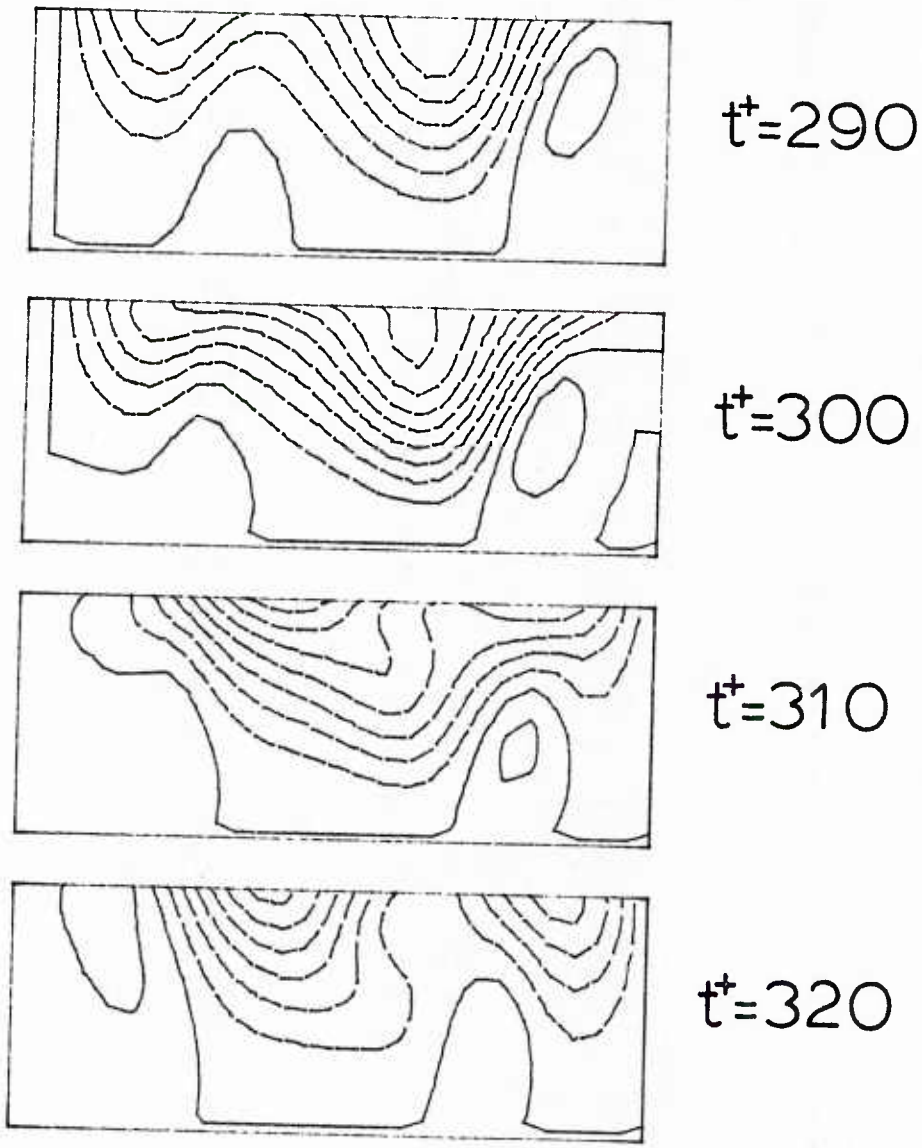

Figure 68 Streamline contours for a double harmonic run at $t^+ = 290,300,310$ and 320; upper boundary at $y_o^+ = 40$

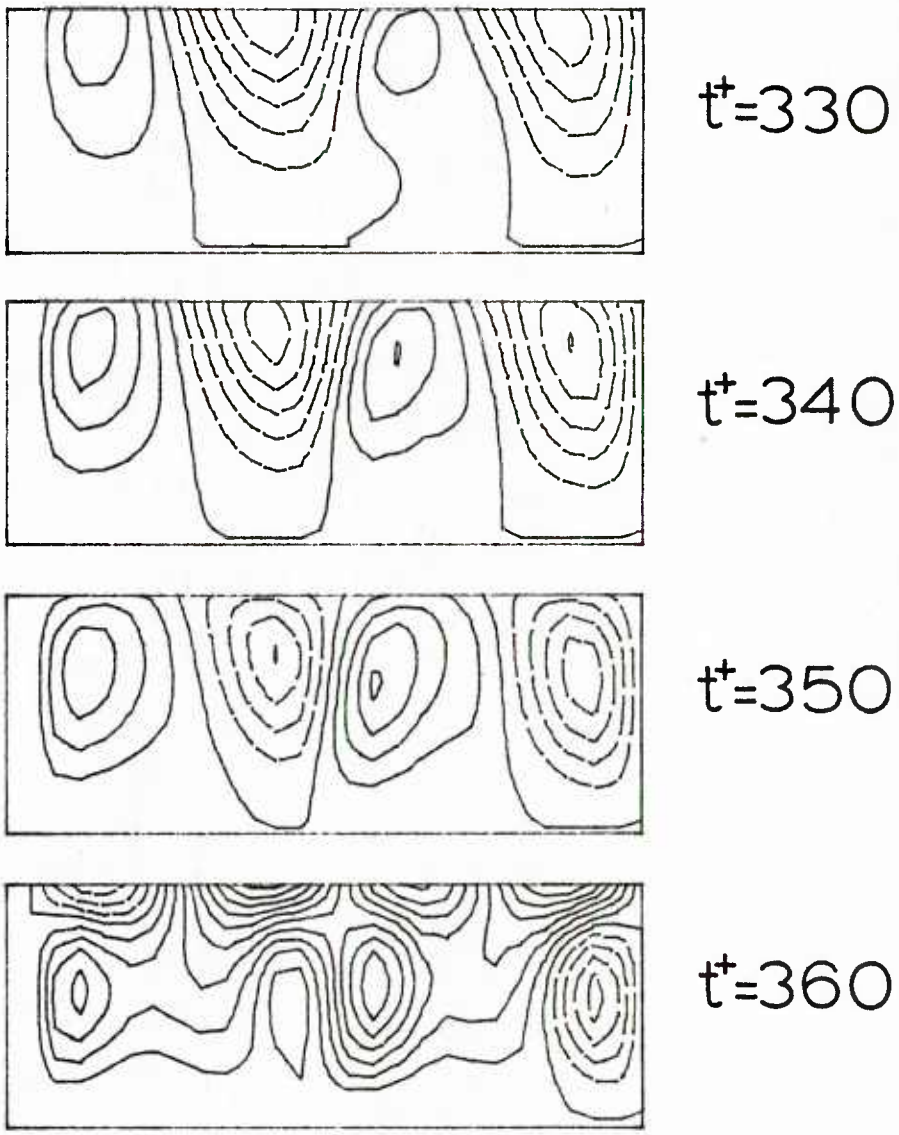

Figure 69 Streamline contours for a double harmonic run at $t^+ = 330,340,350$ and 360; upper boundary at $y_o^+ = 40$

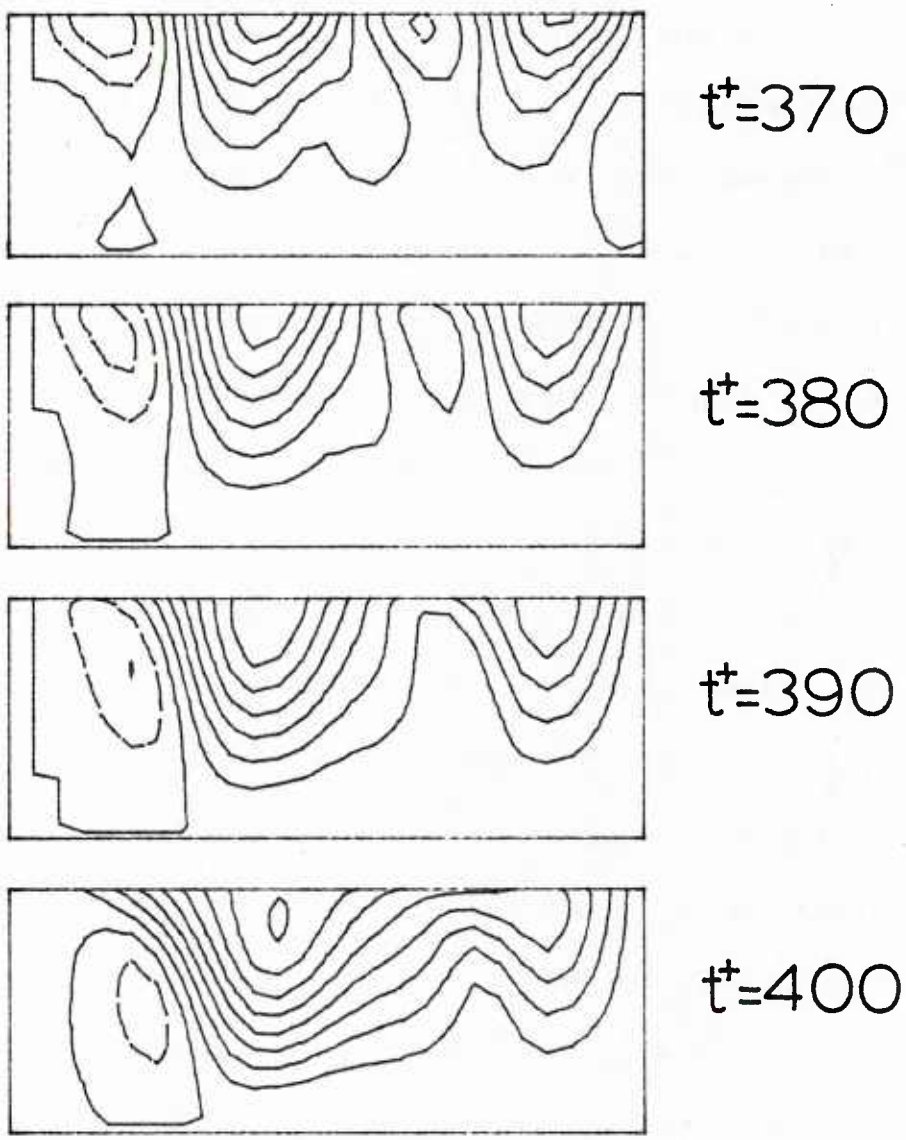

Figure 70 Streamline contours for a double harmonic run at $t^+ = 370,380,390$ and 400; upper boundary at $y_o^+ = 40$

of time that is equal to one cycle of the outer flow eddies ($T^+=400$). The most interesting characteristic of these plots is the alteration of small scale and large scale velocity fluctuations in the viscous wall region. It is seen that at $t^+=30$ large scale spanwise flows start to develop in the cell and last until $t^+=80$. These flows have a wavelength of $\lambda^+=400$, which is the longest wavelength that can be handled by the computational domain. At $t^+=90$ smaller scale flows start to appear and these are associated with eddies of $\lambda^+=100$. These eddies last until $t^+=200$ and from then on the same sequence is repeated until a full cycle is completed. The streamline patterns presented above were found to be characteristic of the two harmonic "fixed cell" computations and are consistent with the prescribed boundary conditions at $y^+=40$. These boundary conditions view the flow in the viscous wall region to result from the dynamic interaction of the $\lambda^+=100$ wall eddies and the outer flow eddies that are of longer wavelength. The calculated ς- and U- contours were found to have the same characteristics as for the single harmonic runs. These characteristics will be presented later in plots of the vorticity and the streamwise velocity versus time at various distances from the wall. As mentioned in Chapter 4, an important concern of this work is the agreement of calculated wall patterns with experimental results. This would then reflect the degree to which the $\lambda^+=100$ eddies or the longer wavelength outer flow eddies are important in the immediate vicinity of the wall. A measure of the dominant scale of the velocity fluctuations very close to the wall can be provided by the correlation of the spanwise velocity gradient at the wall in the

spanwise direction ($R_{\theta_z\theta_z}(\Delta z)$). The computed correlation is shown in Figure 71. This correlation has a zero crossing at $\Delta z^+ = 35$ and attains small values for longer separations. The general shape of the curve for $0 \leq \Delta z^+ \leq 100$ is in good agreement with experimental results (Lau 1980). If the $\lambda^+ = 400$ eddies were important at the wall then the zero crossing would be expected to be close to $\Delta z^+ \approx 100$. So the calculated $R_{\theta_z\theta_z}$ correlation shows that the $\lambda^+ = 100$ eddies are the important eddies close to the wall, in agreement with experiments.

Figure 72 through 75 show the three components of the velocity and the vorticity at a fixed spanwise location plotted versus time for various distances from the wall. The main features of these plots are similar to the ones presented for the single harmonic runs. The dominant period is $T^+ = 100$ and the streamwise vorticity exhibits again very low fluctuations at $y^+ = 10$ and 15.

Similar plots, but for a fixed lateral location in the cell are presented in Figures 76 through 79. Again the dominant period of $T^+ = 100$ is identified in these plots.

The spanwise velocity component is plotted in Figure 80 for a fixed spanwise location versus the distance from the wall and for various points in time. It is seen that the zero-crossing of the spanwise velocity profile is not the sole feature of these plots since there are periods of time that w attains large values throughout the viscous wall region. These periods of time are associated with the predominance of the $\lambda^+ = 400$ outer flow eddies. Since these eddies have their eye above $y_o^+ = 40$ for 100% of the time they induce spanwise velocity profiles of

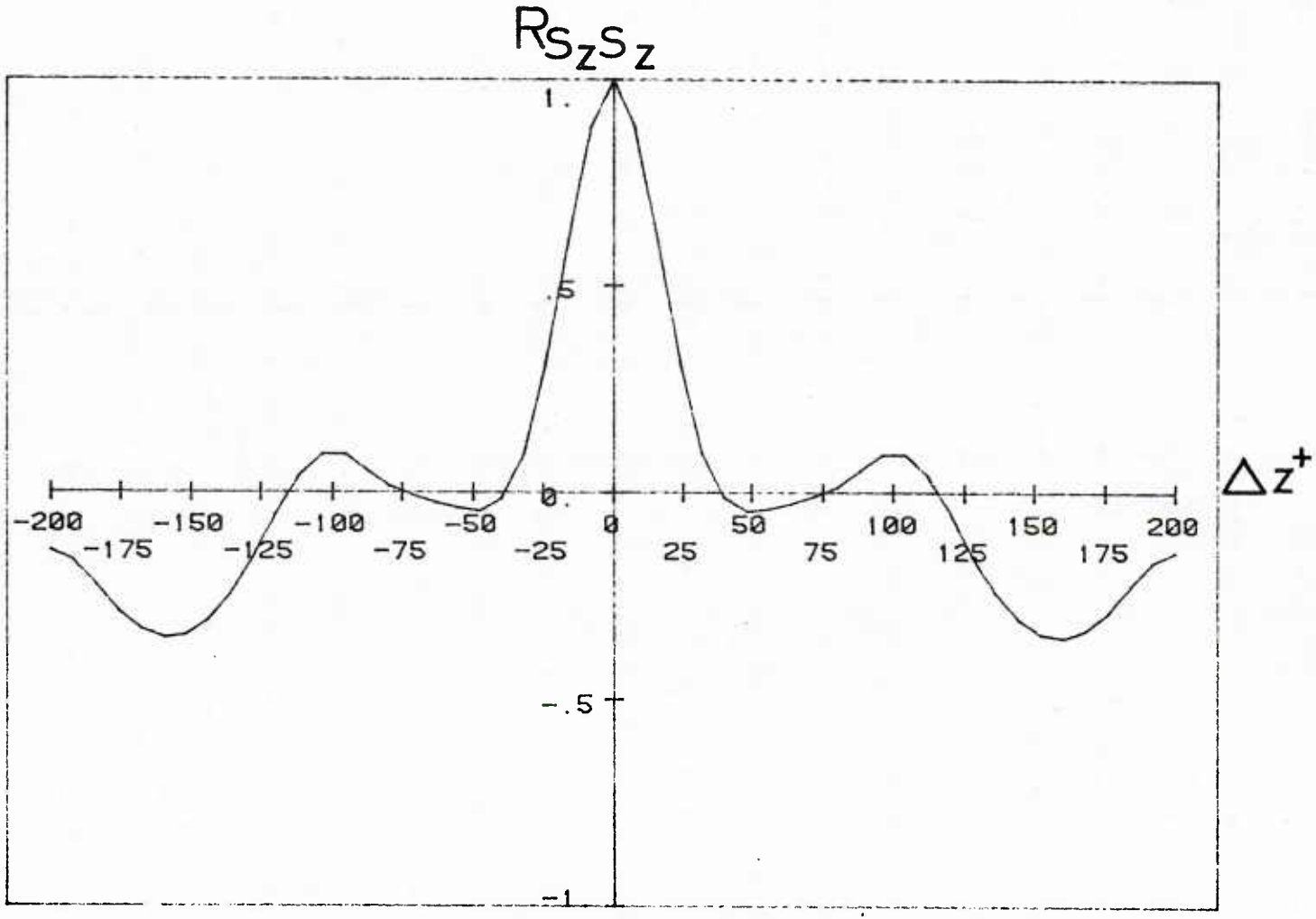

Figure 71 Plot of the $R_{s_z s_z}$ correlation versus Δz^+; double harmonic run.

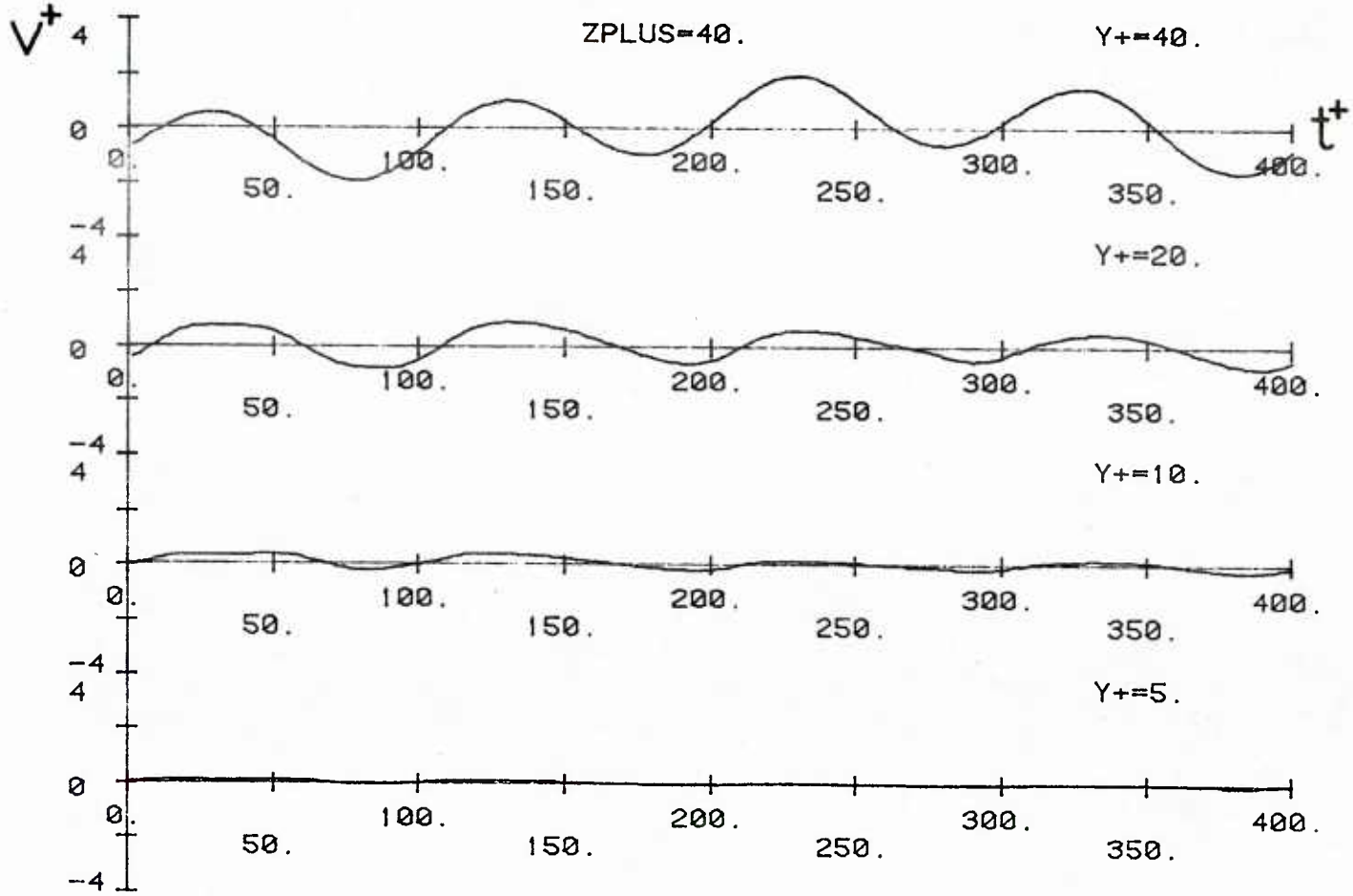

Figure 72 Plots of v^+ versus t^+ at $z^+ = 40$. Double harmonic run; upper boundary at $y_o^+ = 40$

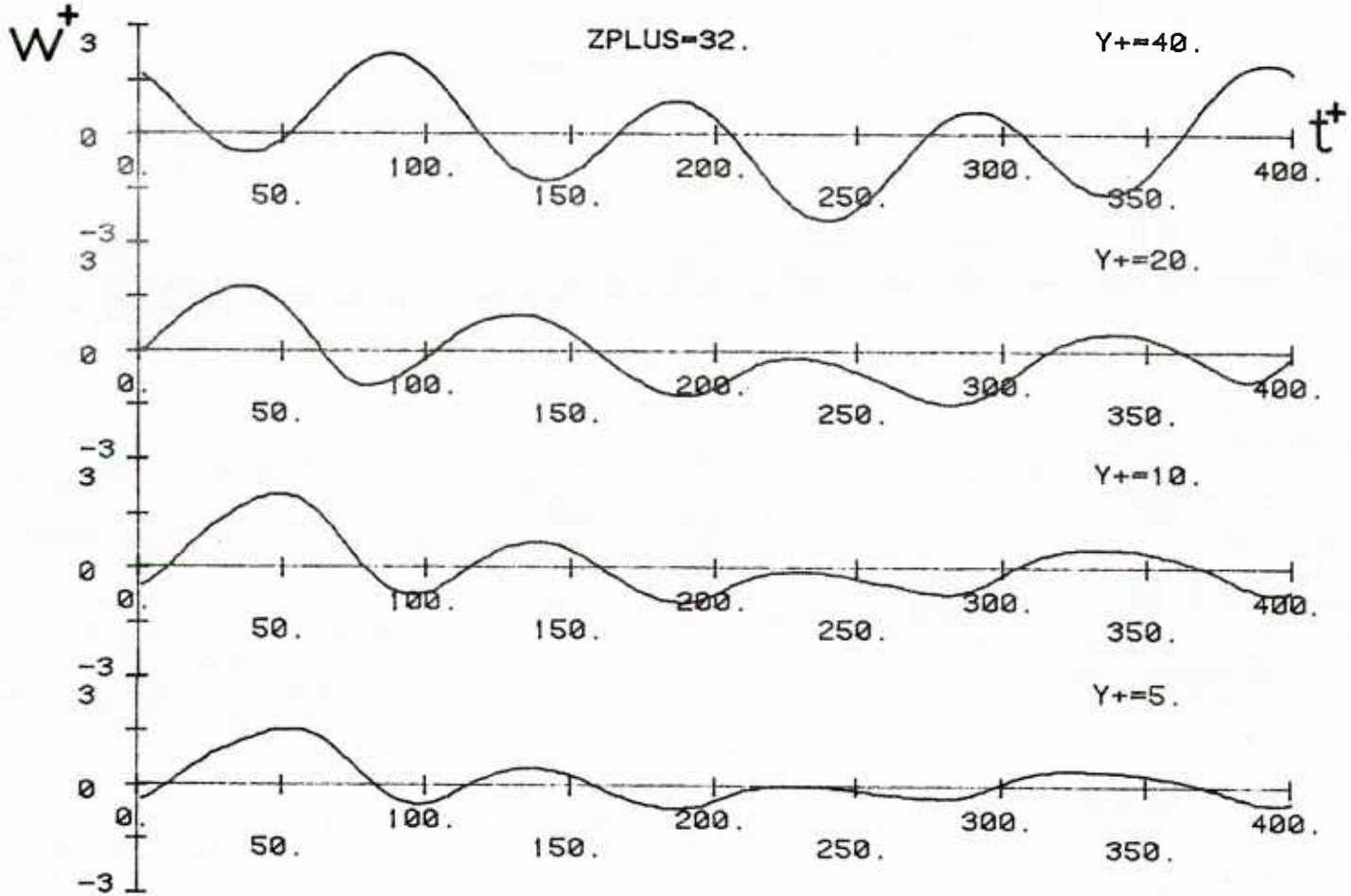

Figure 73 Plots of w^+ versus t^+ at $z^+ = 32$. Double harmonic run; upper boundary at $y_o^+ = 40$

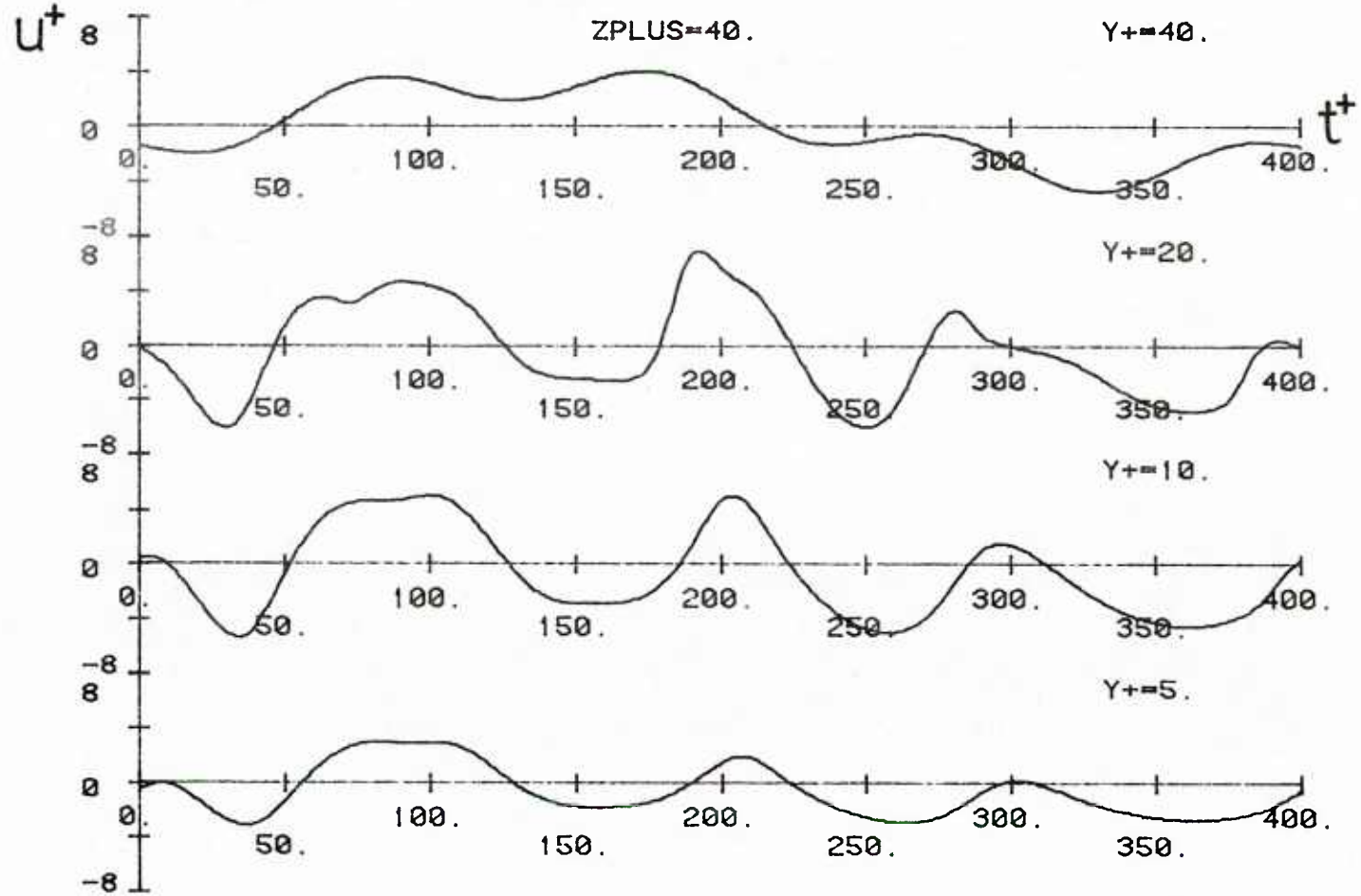

Figure 74 Plots of u^+ versus t^+ at $z^+ = 40$. Double harmonic run; upper boundary at $y_o^+ = 40$

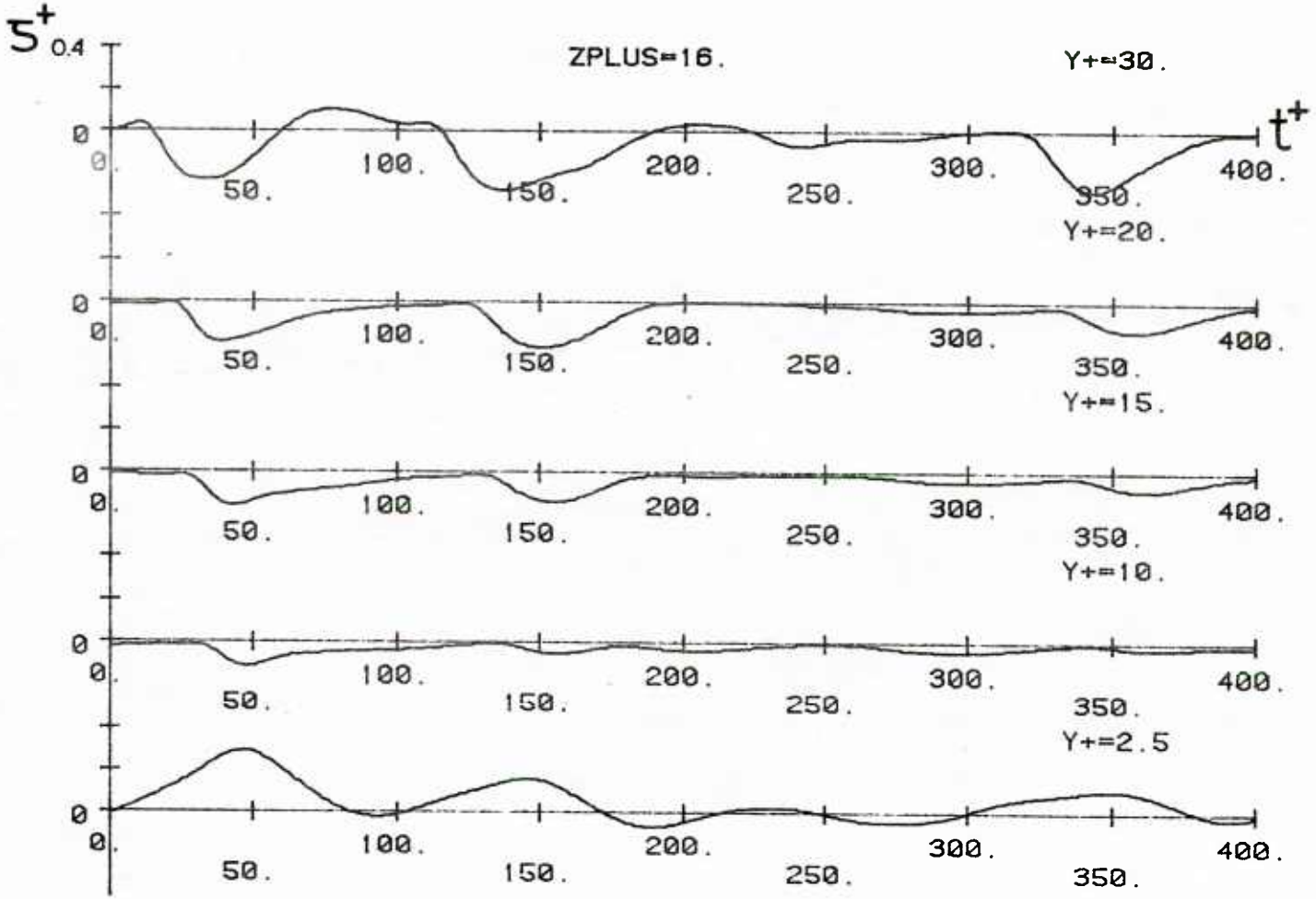

Figure 75 Plots of ζ^+ versus t^+ at $z^+ = 16$. Double harmonic run; upper boundary at $y_o^+ = 40$

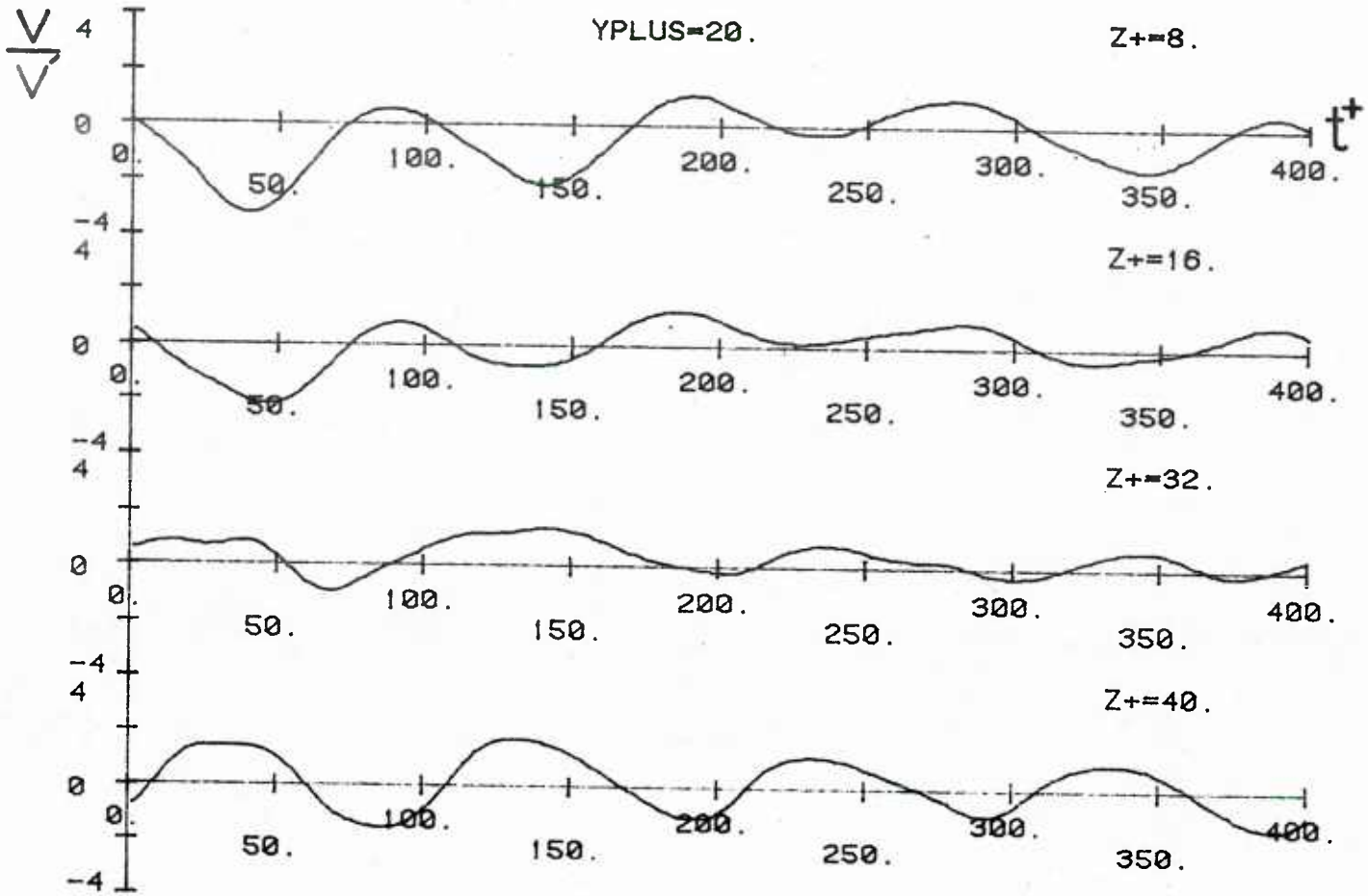

Figure 76 Plots of v/v' versus t^+ at $y^+ = 20$. Double harmonic run; upper boundary at $y_o^+ = 40$

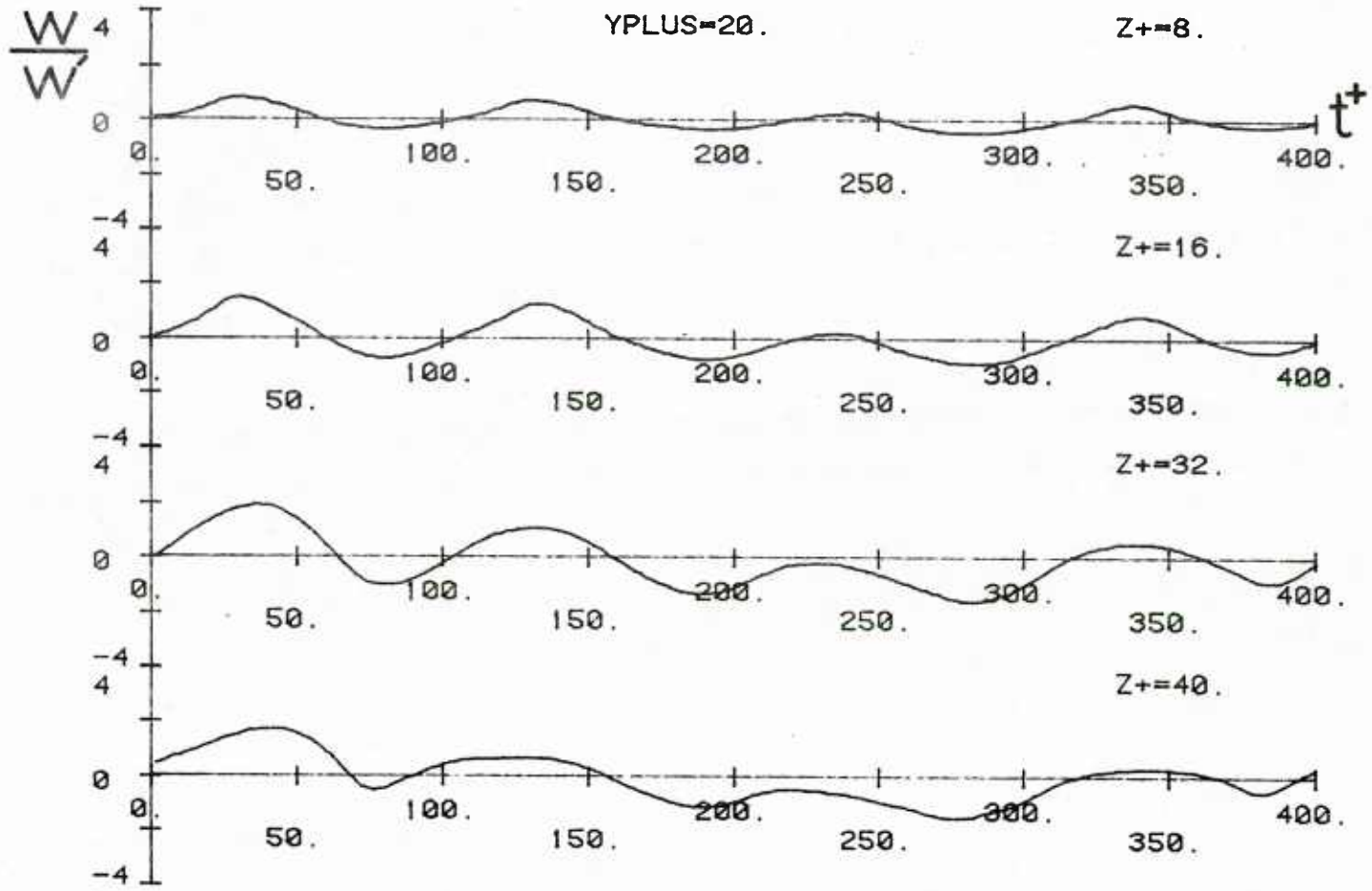

Figure 77 Plots of w/w' versus t^+ at $y^+ = 20$. Double harmonic run; upper boundary at $y_o^+ = 40$

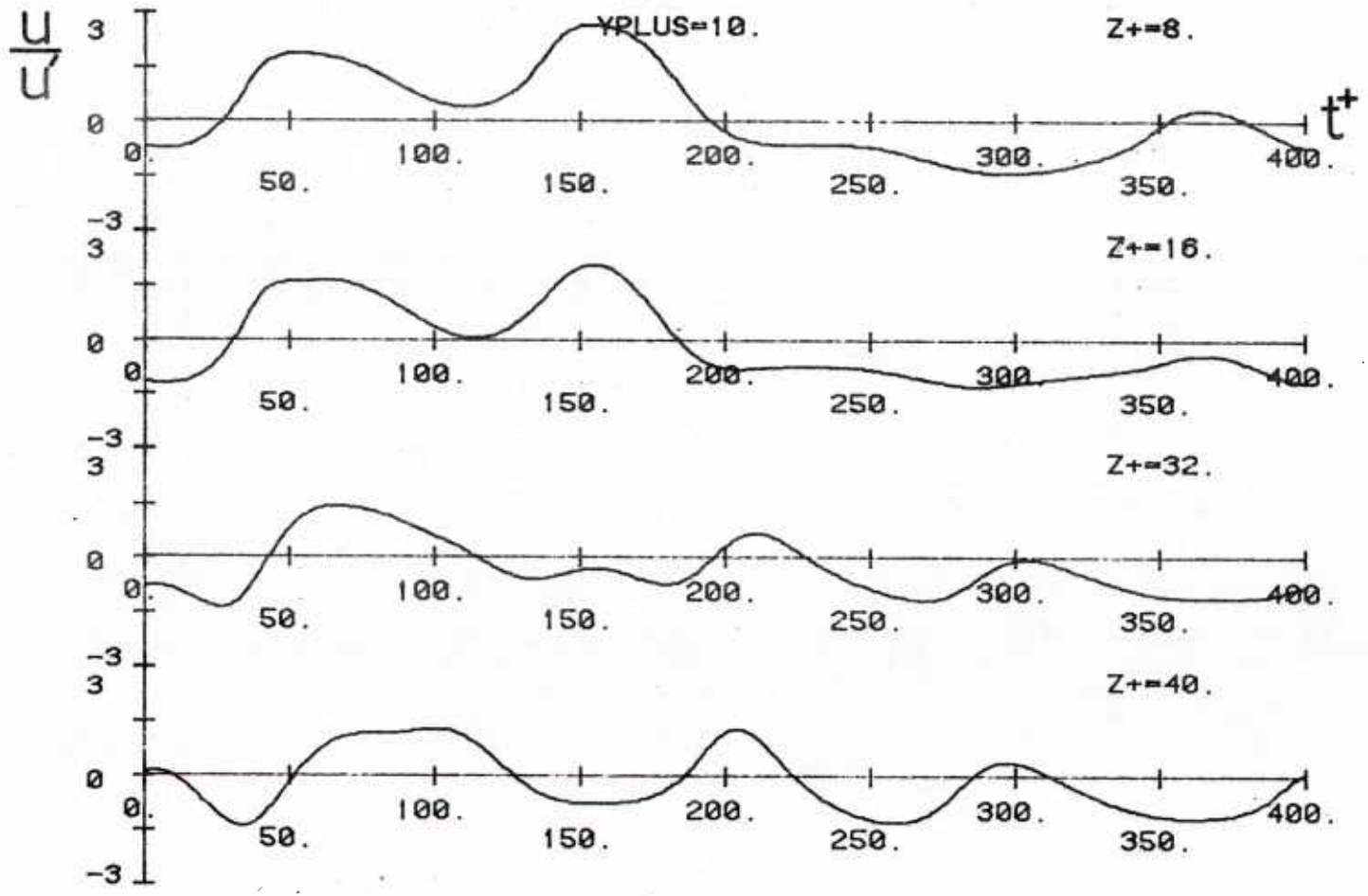

Figure 78 Plots of u/u' versus t^+ at $y^+ = 10$. Double harmonic run; upper boundary at $y_o^+ = 40$

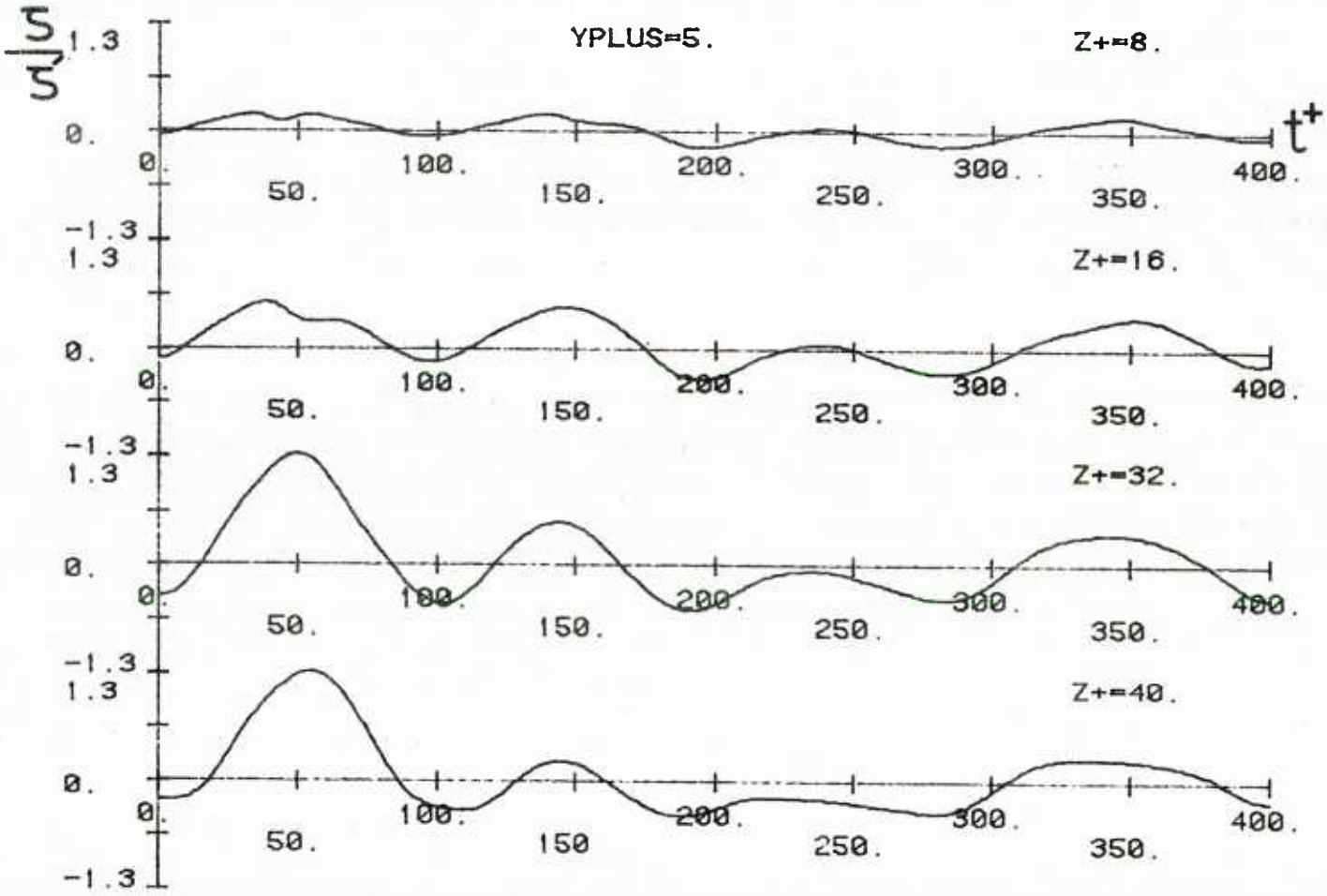

Figure 79 Plots of ς/ς' versus t^+ at $y^+ = 5$. Double harmonic run; upper boundary at $y_o^+ = 40$

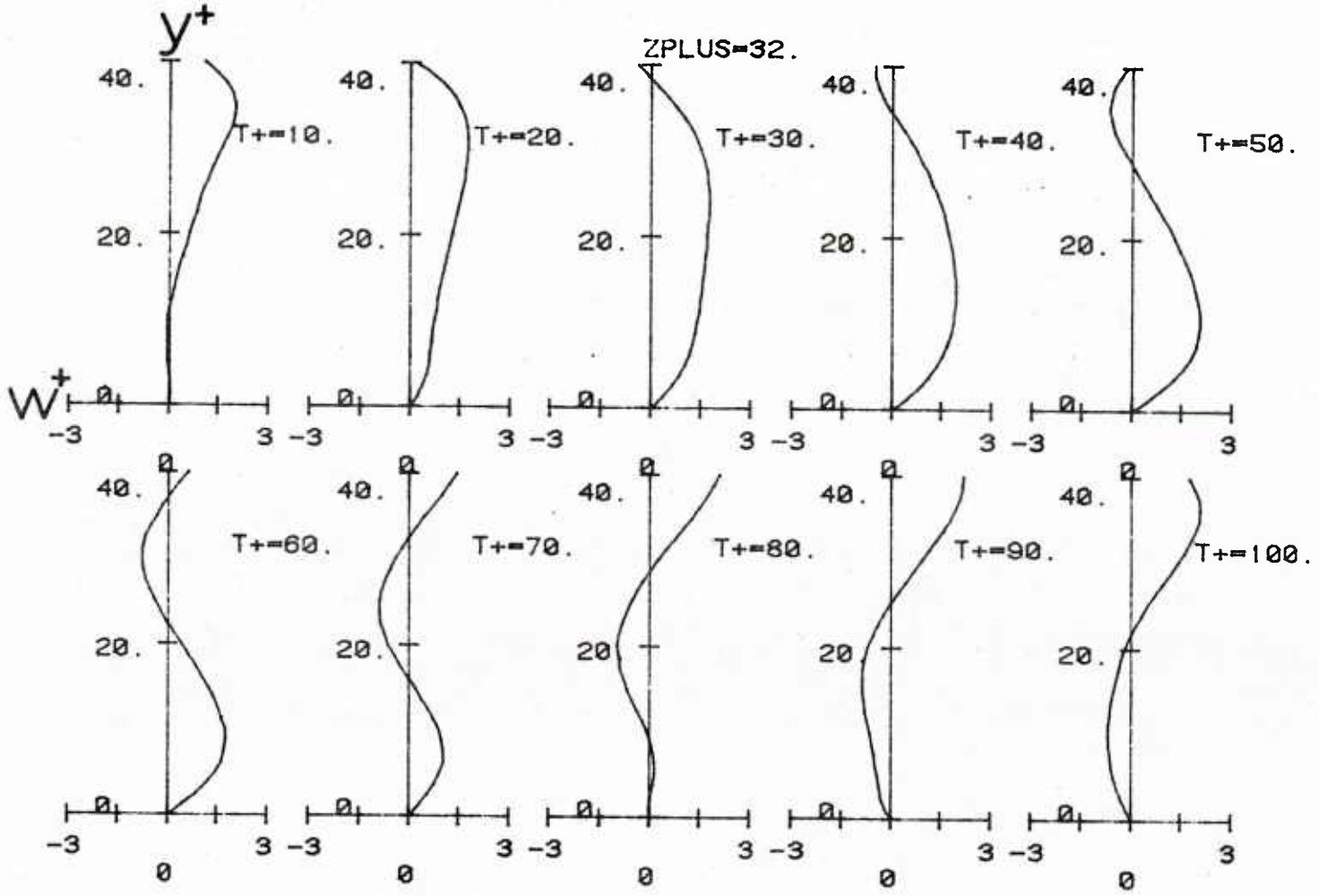

Figure 80a Plots of w^+ versus y^+ at $z^+=32$ from $t^+=10$ to $t^+=100$. Double harmonic run; upper boundary at $y_o^+=40$

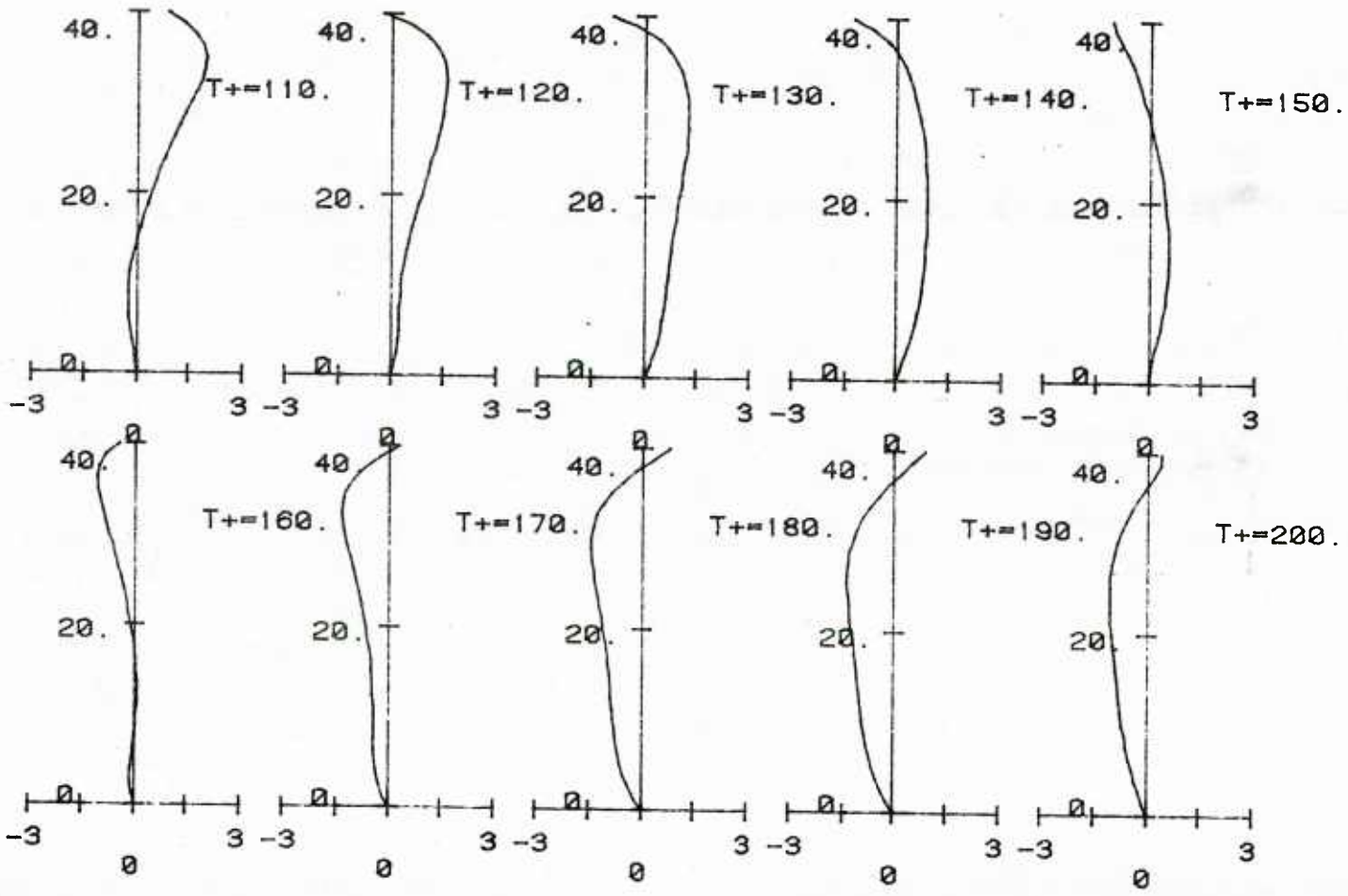

Figure 80b Plots of w^+ versus y^+ at $z^+=32$ from $t^+=110$ to $t^+=200$. Double harmonic run; upper boundary at $y_o^+=40$

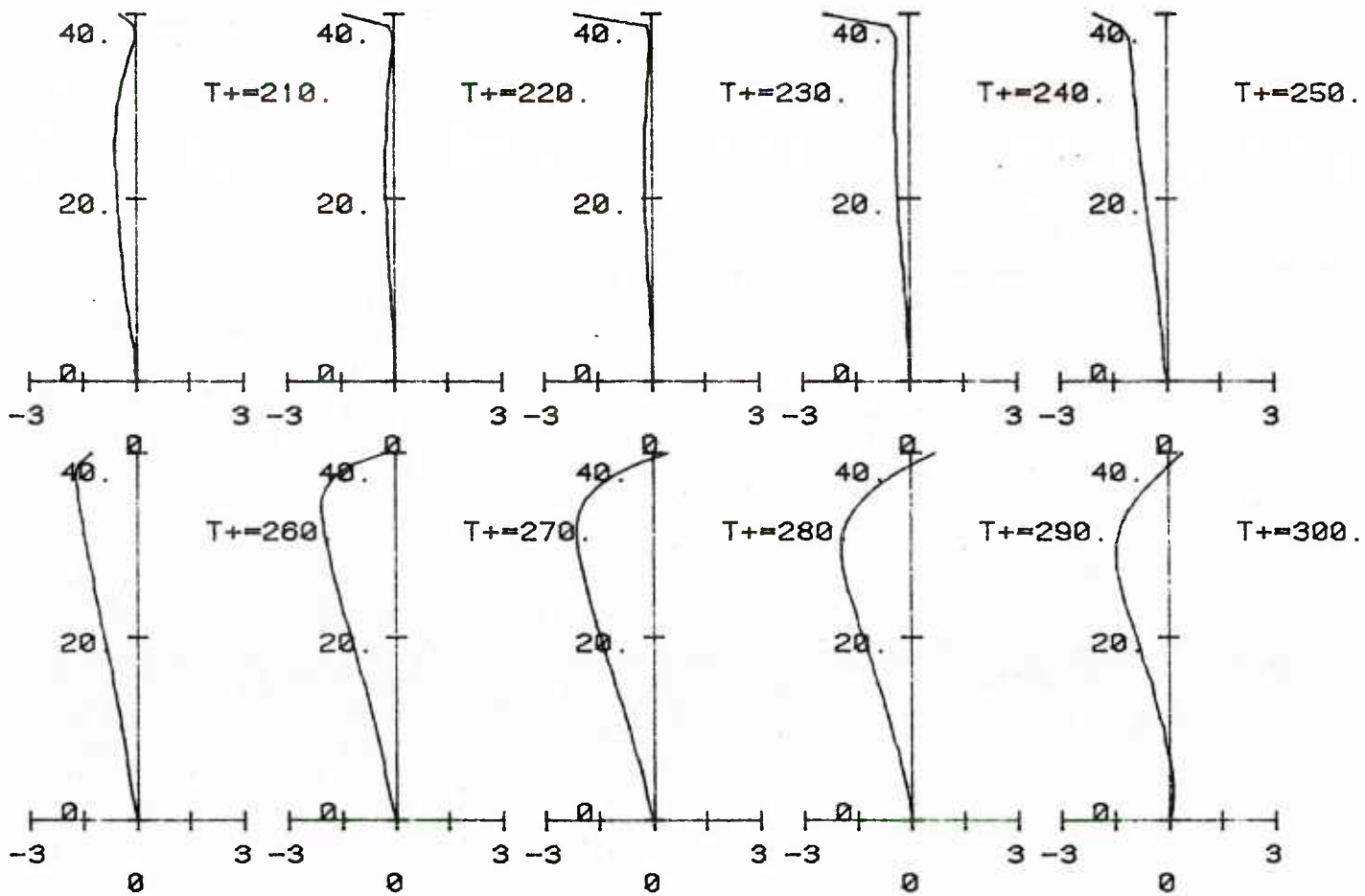

Figure 80c Plots of w^+ versus y^+ at $z^+=32$ from $t^+=210$ to $t^+=300$. Double harmonic run; upper boundary at $y_o^+=40$

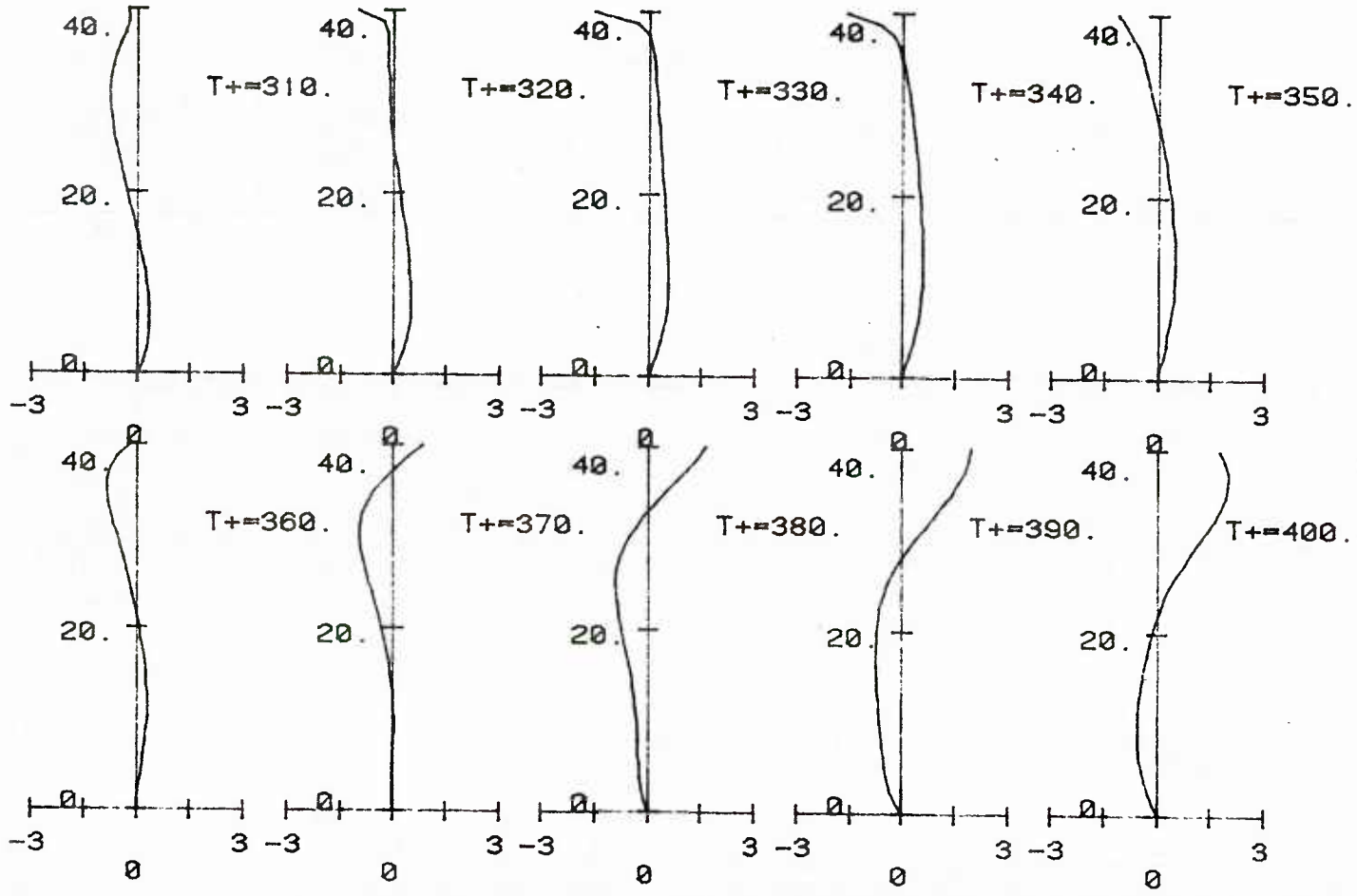

Figure 80d Plots of w^+ versus y^+ at $z^+=32$ from $t^+=310$ to $t^+=400$. Double harmonic run; upper boundary at $y_o^+=40$

the same direction from the wall up to the outer boundary.

The path-line and streakline calculations are presented in Figures 81 and 82. The same observations that were made for the single harmonic runs apply in this case too.

The statistically averaged flow variables are presented in Figures 83 through 87. The most important result is the much better agreement of the spanwise intensity profile with experimental data. The v-intensity profile shows the same behavior as in the single harmonic runs. The skewness of the u-velocity profile is very much improved compared to the runs with one harmonic in the spanwise direction. Both skewness and flatness show very good agreement with experimental data. The Reynolds stress, again, agrees with the experiments very well and the same applies for the average streamwise velocity profile. The calculated u-intensity profile shows a somewhat large peak compared to the runs with a single harmonic .

B. Upper boundary at $y_o^+ = 15$

In these calculations all the energy in the three components of the velocity was associated with the $\lambda^+ = 100$ eddies. The results of the computations are shown in Figures 88 through 105.

The streamline contours are shown in Figures 88 through 92 for a calculation with $N_1 = 15\%$. The flow at $y_o^+ = 15$ is thus, seen to be open for 85% of the time. A streamwise vortical motion is only evident at $t^+ = 20$ and 70 and disappears quickly from the computational domain.

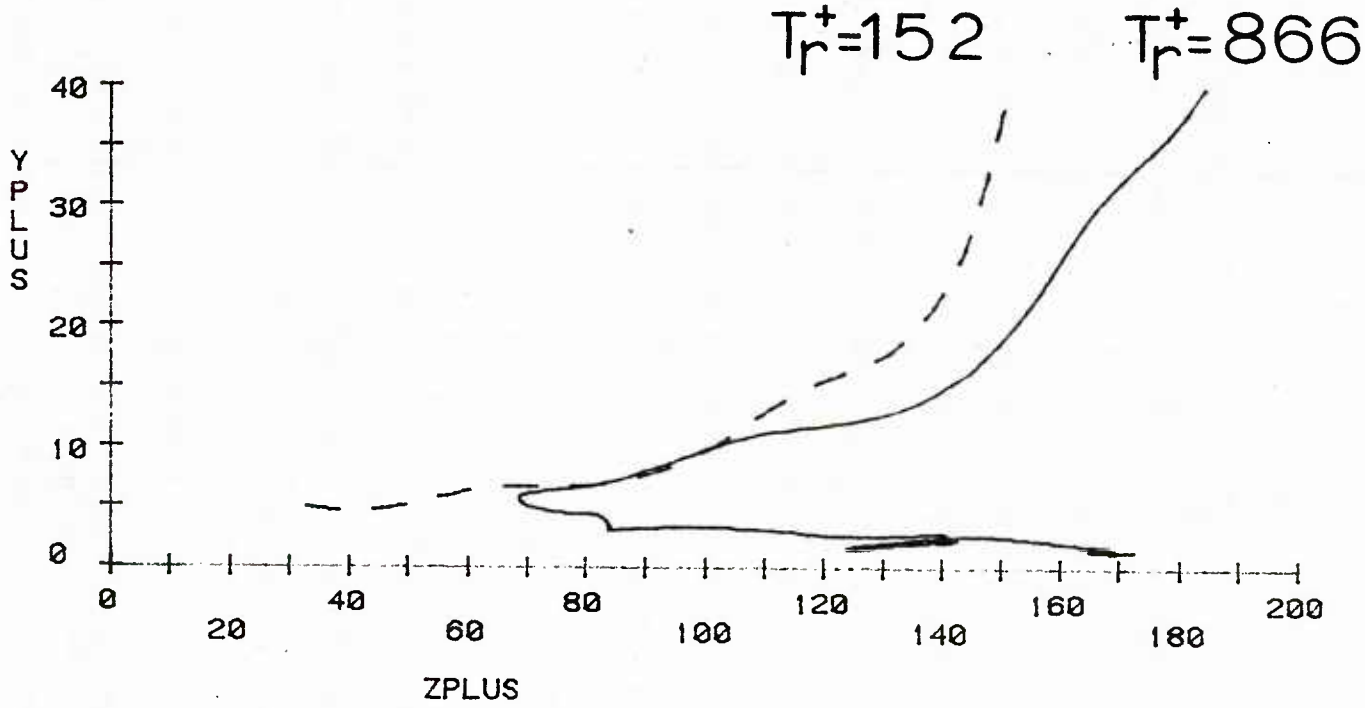

Figure 81 Trajectories of fluid particles in the cell. Double harmonic run.

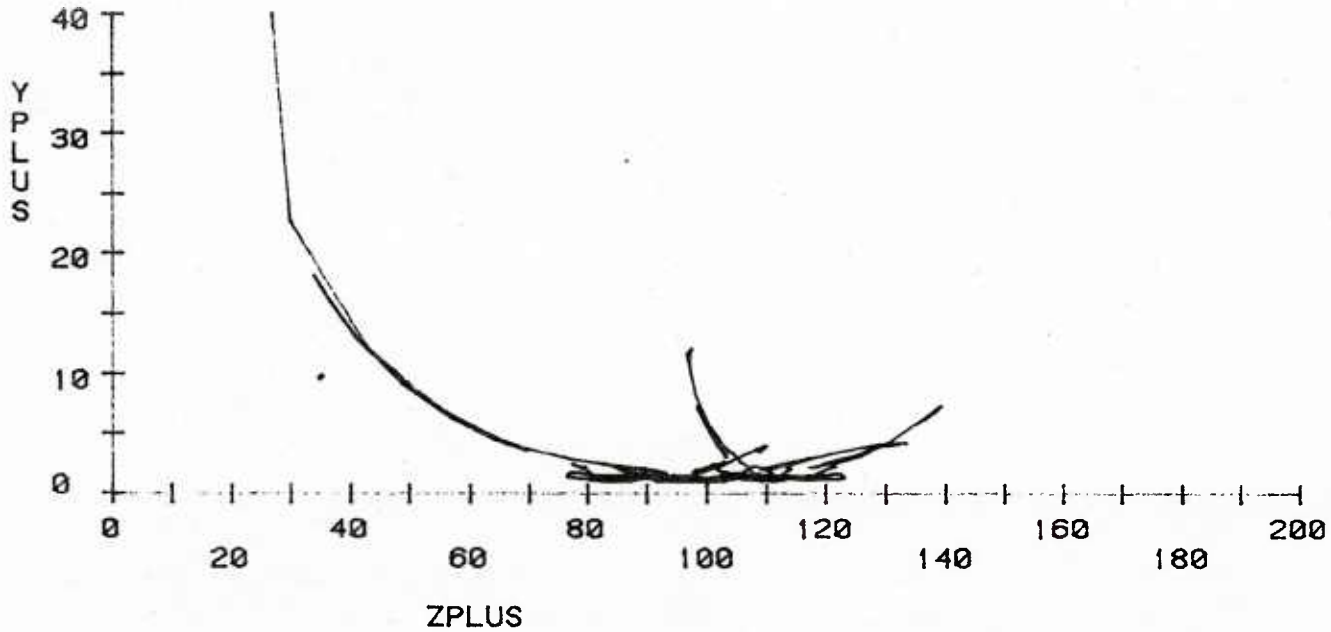

Figure 82 Streaklines for a double harmonic run. Injection point at $z_i^+ = 100$, $y_i^+ = 1.25$

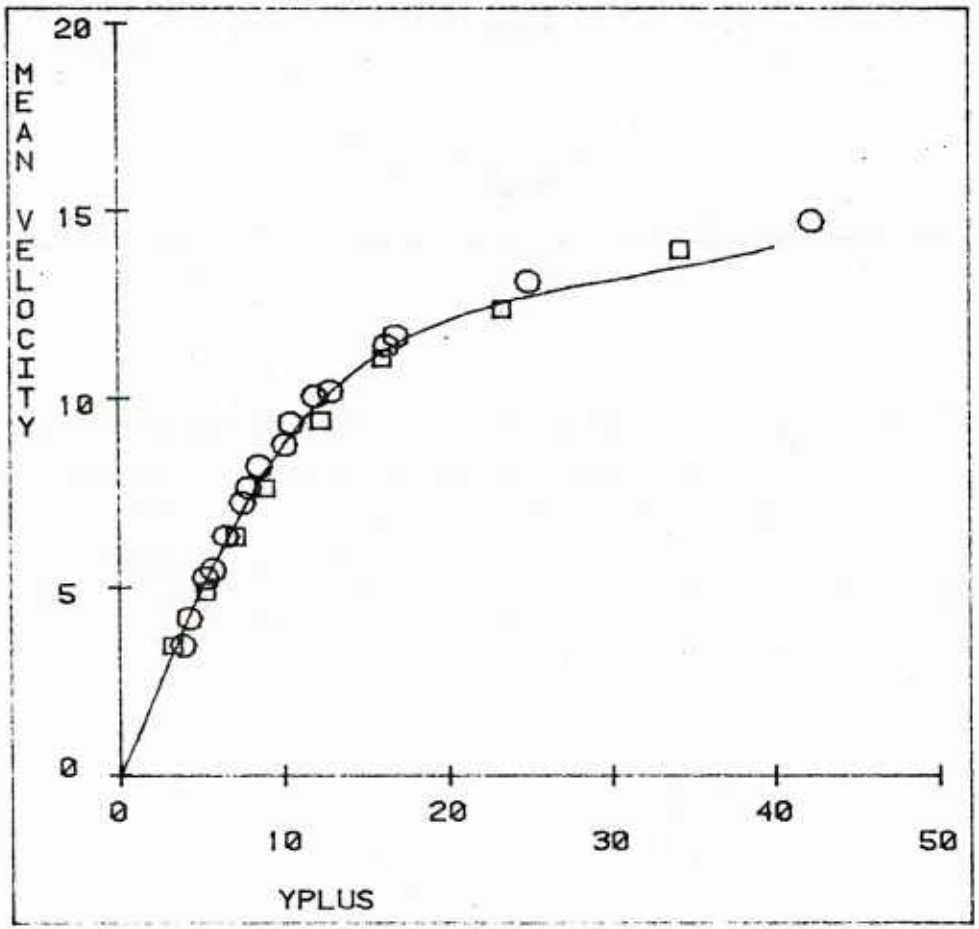

Figure 83 Mean streamwise velocity for a double harmonic run; upper boundary at $y_o^+ = 40$

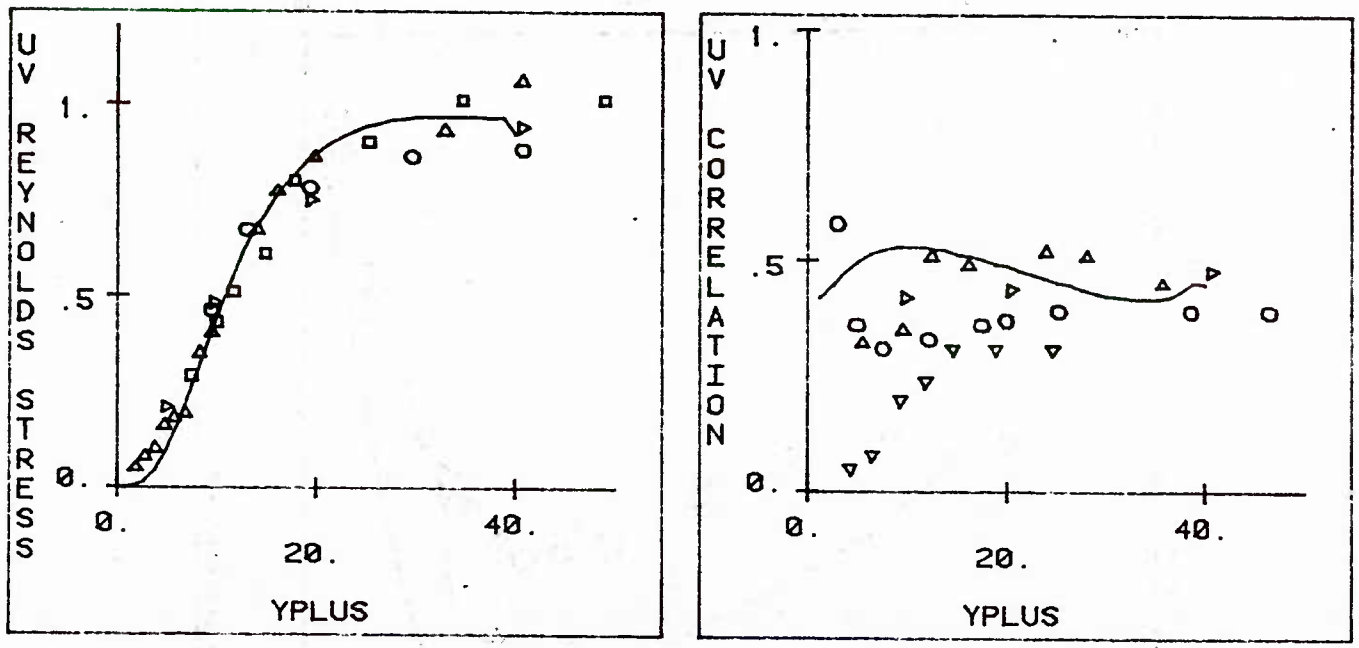

Figure 84 Reynolds stress and $-\overline{uv}/u'v'$ correlation for a double harmonic run; upper boundary at $y_o^+ = 40$

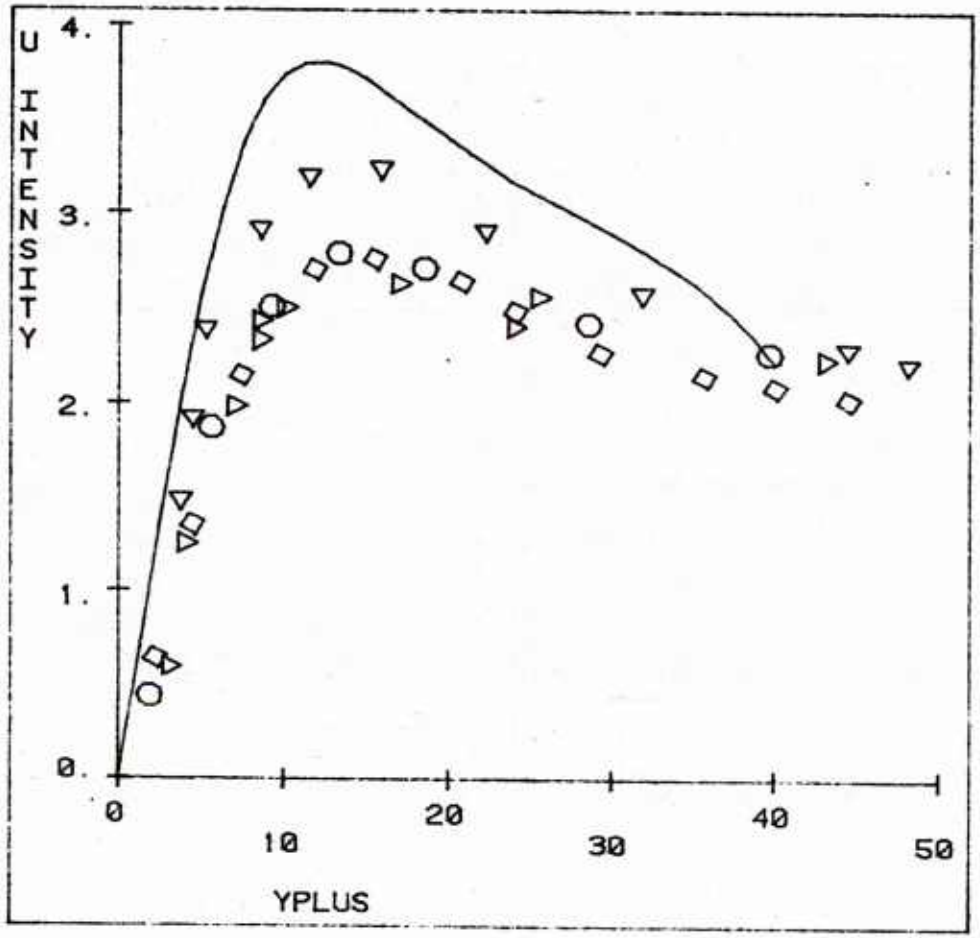

Figure 85 Intensity of streamwise velocity fluctuations for a double harmonic run; upper boundary at $y_o^+ = 40$

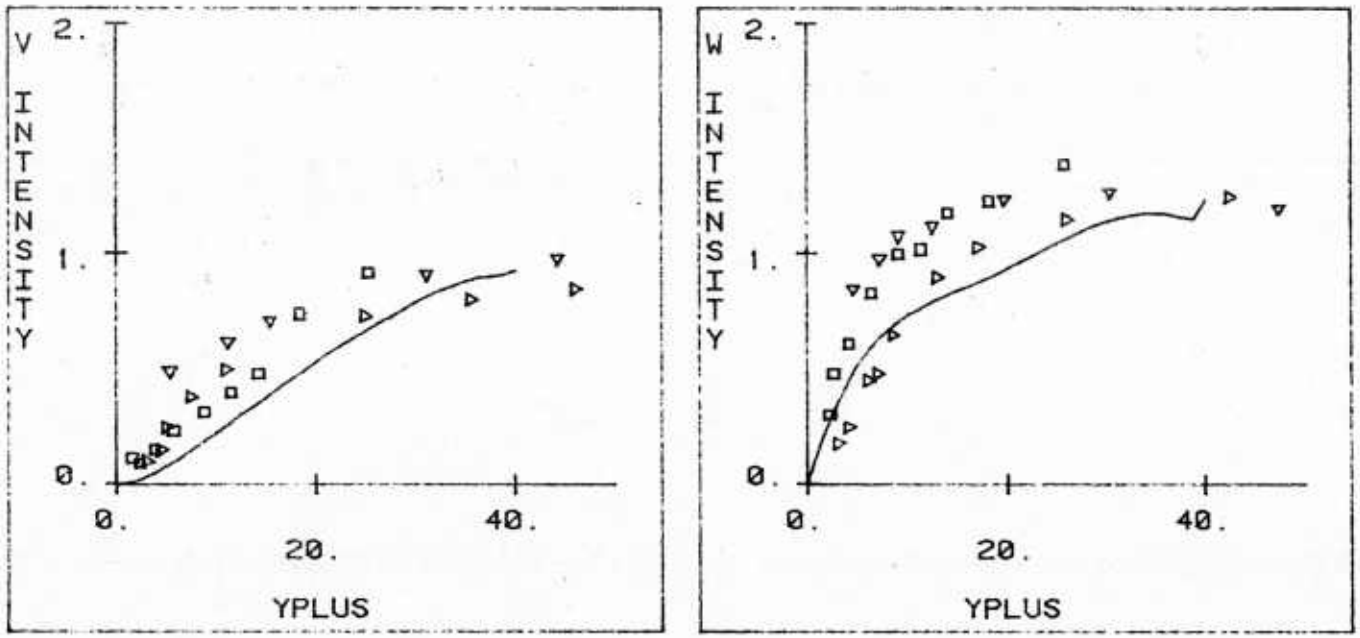

Figure 86 Intensitites of the normal and spanwise velocity fluctuations for a double harmonic run; upper boundary at $y_o^+ = 40$

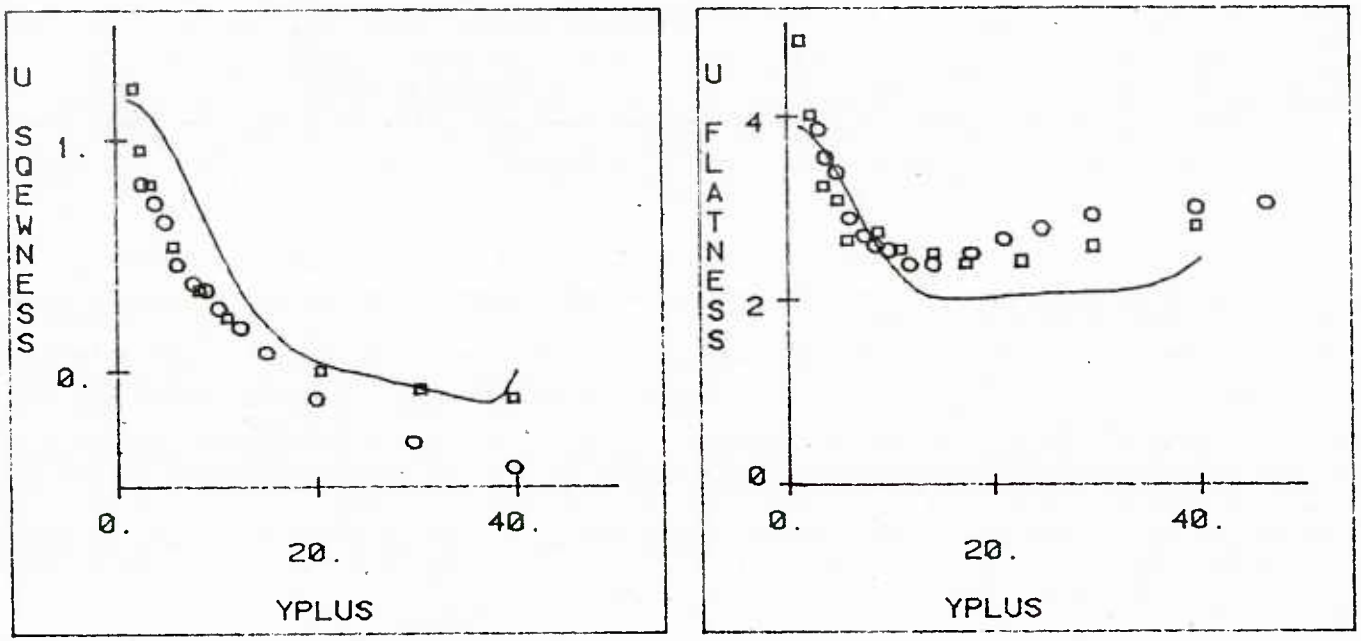

Figure 87 Skewness and flatness of streamwise velocity fluctuations for a double harmonic run; upper boundary at $y_o^+ = 40$

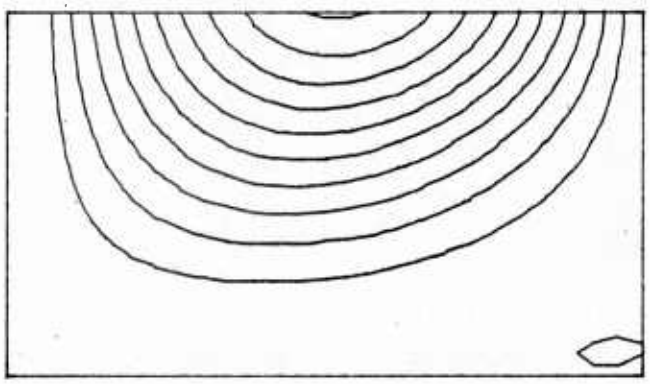

$t^+=10$

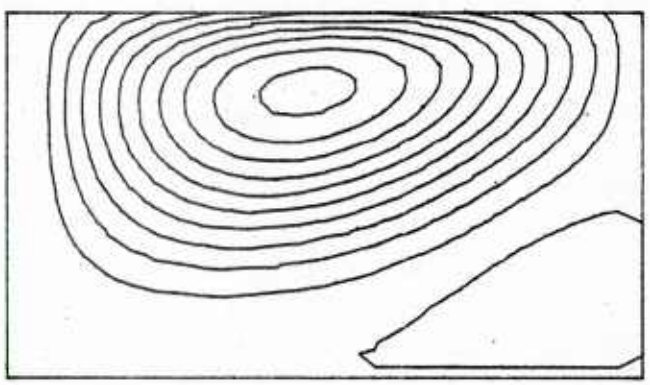

$t^+=20$

Figure 88 Streamline contours for a single harmonic run at $t^+=10$ and 20; upper boundary at $y_o^+=15$

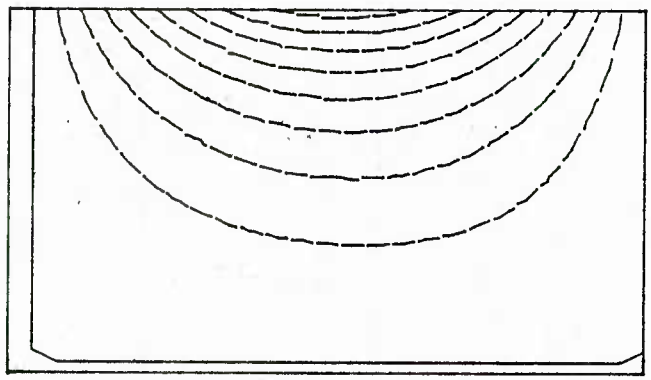

$t^+=30$

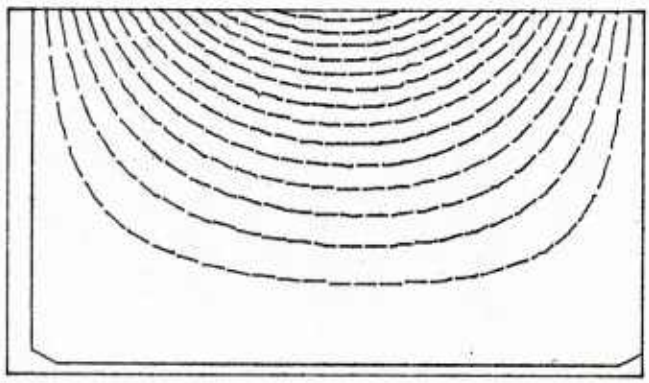

$t^+=40$

Figure 89 Streamline contours for a single harmonic run at $t^+=30$ and 40; upper boundary at $y_o^+=15$

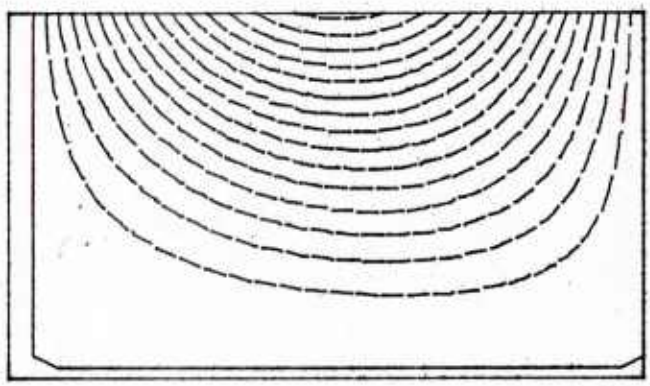

$t^+=50$

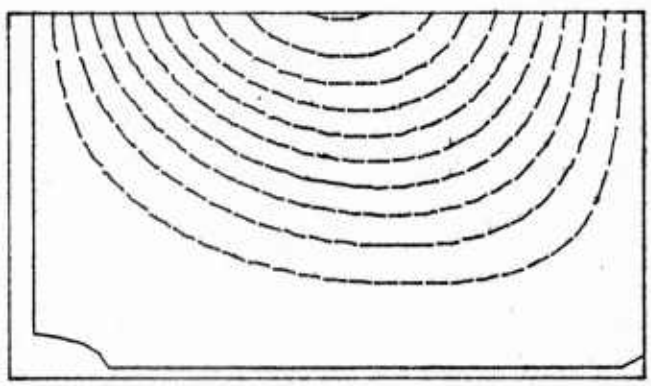

$t^+=60$

Figure 90 Streamline contours for a single harmonic run at $t^+=50$ and 60; upper boundary at $y_o^+=15$

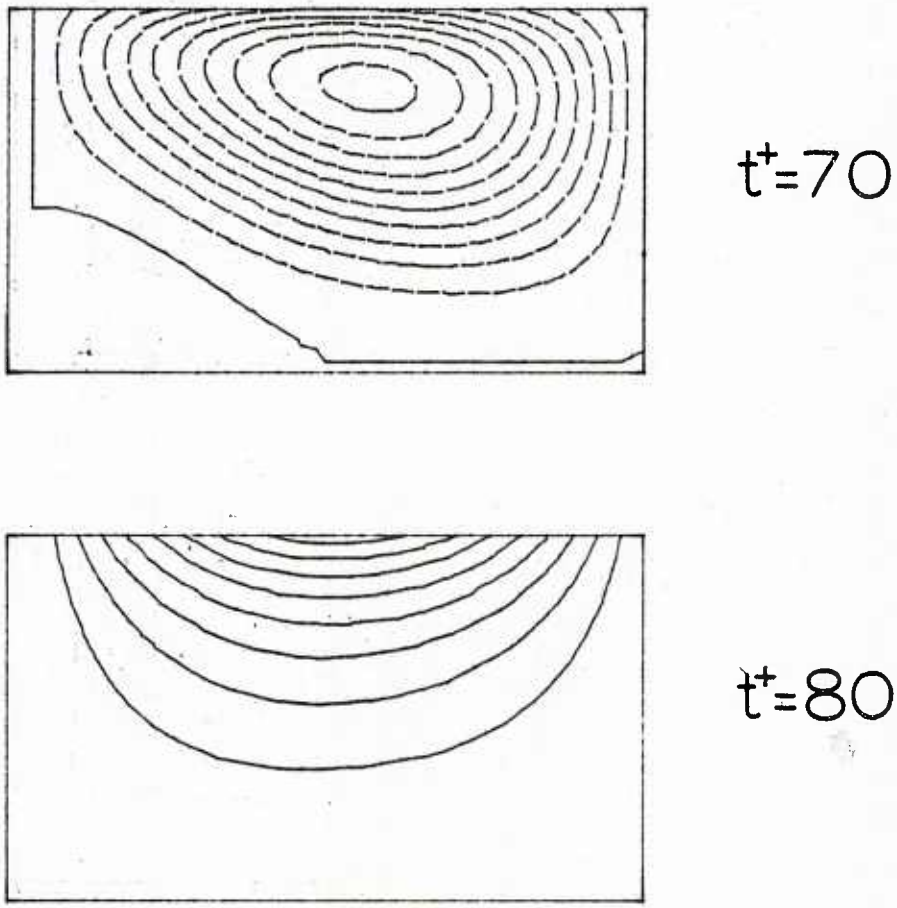

Figure 91 Streamline contours for a single harmonic run at $t^+=70$ and 80; upper boundary at $y_o^+=15$

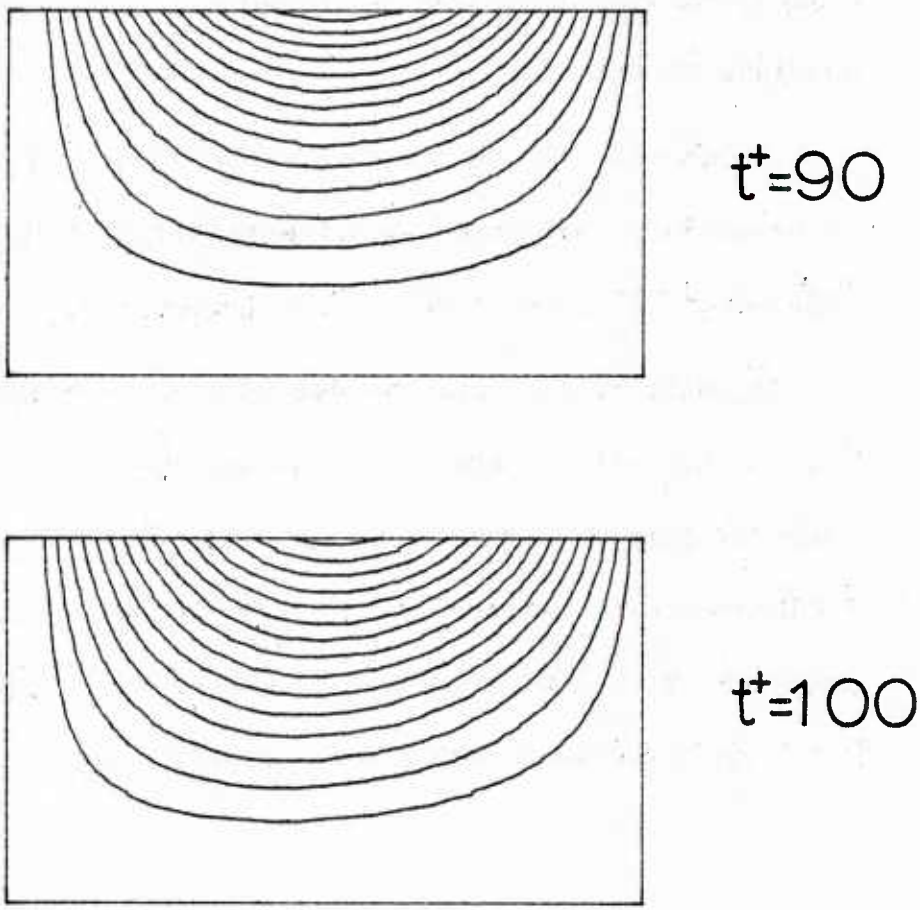

Figure 92 Streamline contours for a single harmonic run at $t^+=90$ and 100; upper boundary at $y_o^+=15$

The ς-contour plots shown in Figures 93 through 97 are different from the single harmonic runs with $y_o^+ = 40$, in that they show large values of the vorticity for most of the time. There is no identifiable "irrotational" core and the $\varsigma = 0$ line lies close to the upper boundary or disappears completely from the computational domain causing values of the streamwise vorticity to have the same sign throughout the cell.

Characteristic time signatures of the three components of the velocity and the streamwise vorticity are shown in Figures 98 through 101. The main feature is the period of $T^+ = 100$ for all the above flow quantities.

The statistically averaged variables are shown in Figures 102 through 105. It is seen that very good agreement with experimental data is obtained. In particular the w-intensity profile agrees very well with experiments in this region. The Reynolds stress correlation appears to be low close to the wall. It was found during other runs that higher values can be obtained if a slightly longer period ($T^+ = 120$) for the velocity fluctuations at $y_o^+ = 15$ is used.

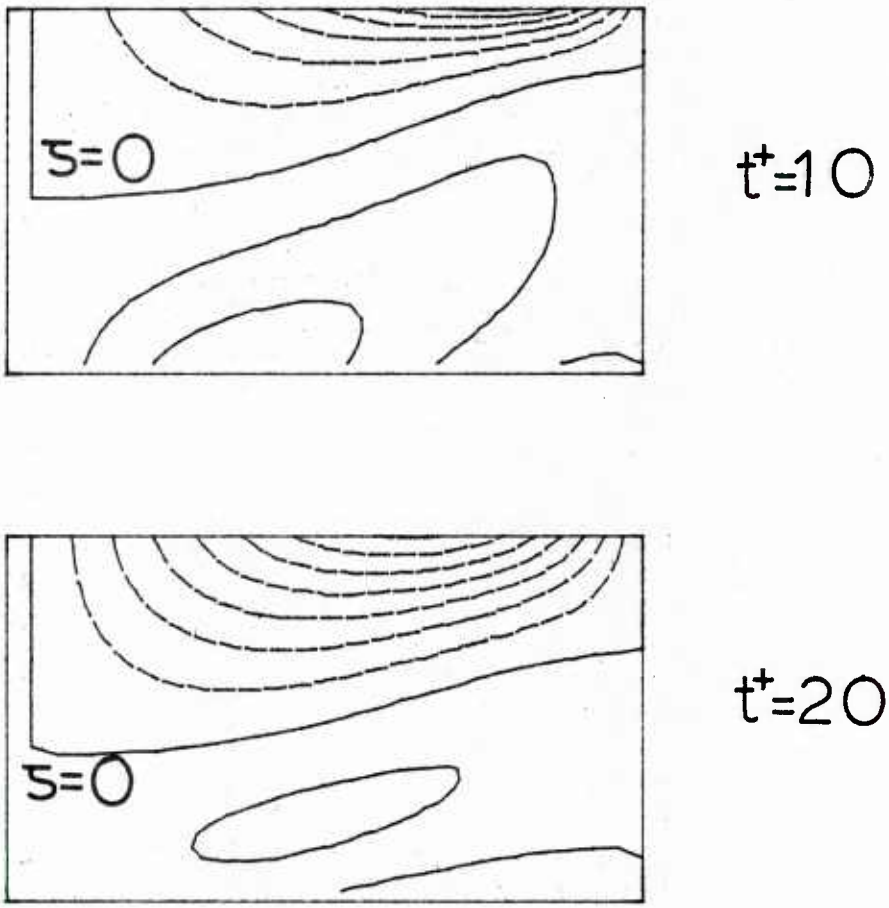

Figure 93 Streamwise vorticity contours for a single harmonic run at $t^+ = 10$ and 20; upper boundary at $y_o^+ = 15$

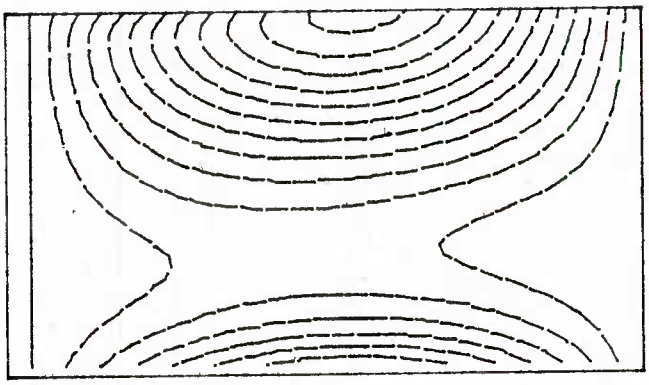

$t^+=30$

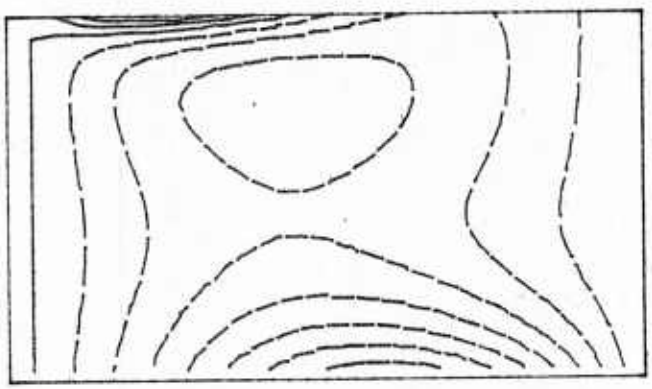

$t^+=40$

Figure 94 Streamwise vorticity contours for a single harmonic run at $t^+=30$ and 40; upper boundary at $y_o^+=15$

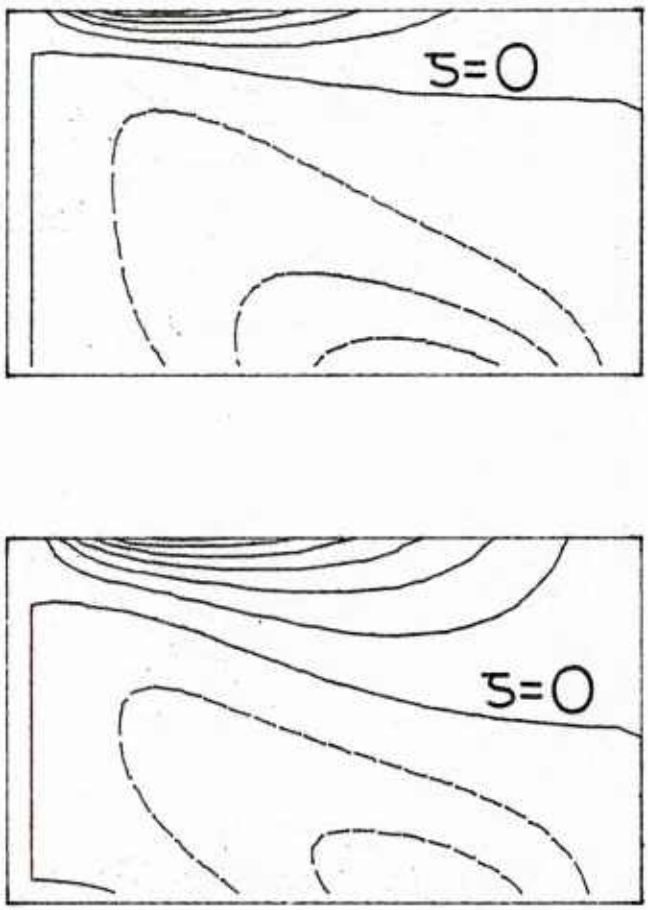

Figure 95 Streamwise vorticity contours for a single harmonic run at $t^+=50$ and 60; upper boundary at $y_o^+=15$

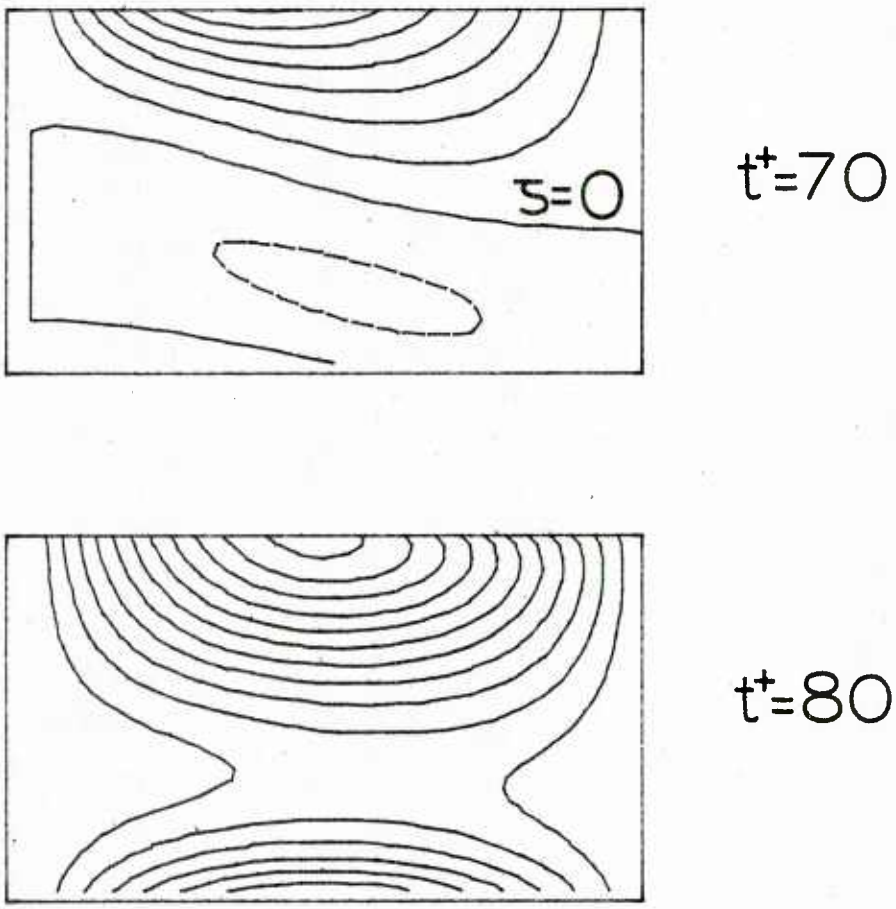

Figure 96 Streamwise vorticity contours for a single harmonic run at $t^+ = 70$ and 80; upper boundary at $y_o^+ = 15$

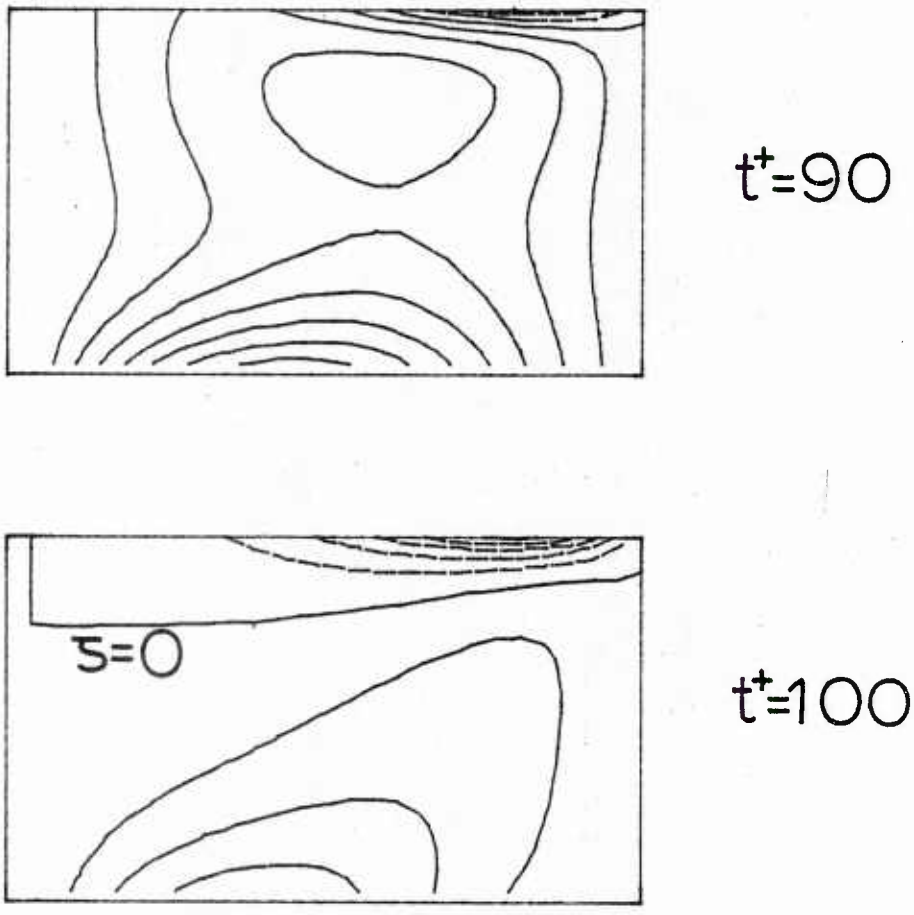

Figure 97 Streamwise vorticity contours for a single harmonic run at $t^+ = 90$ and 100; upper boundary at $y_o^+ = 15$

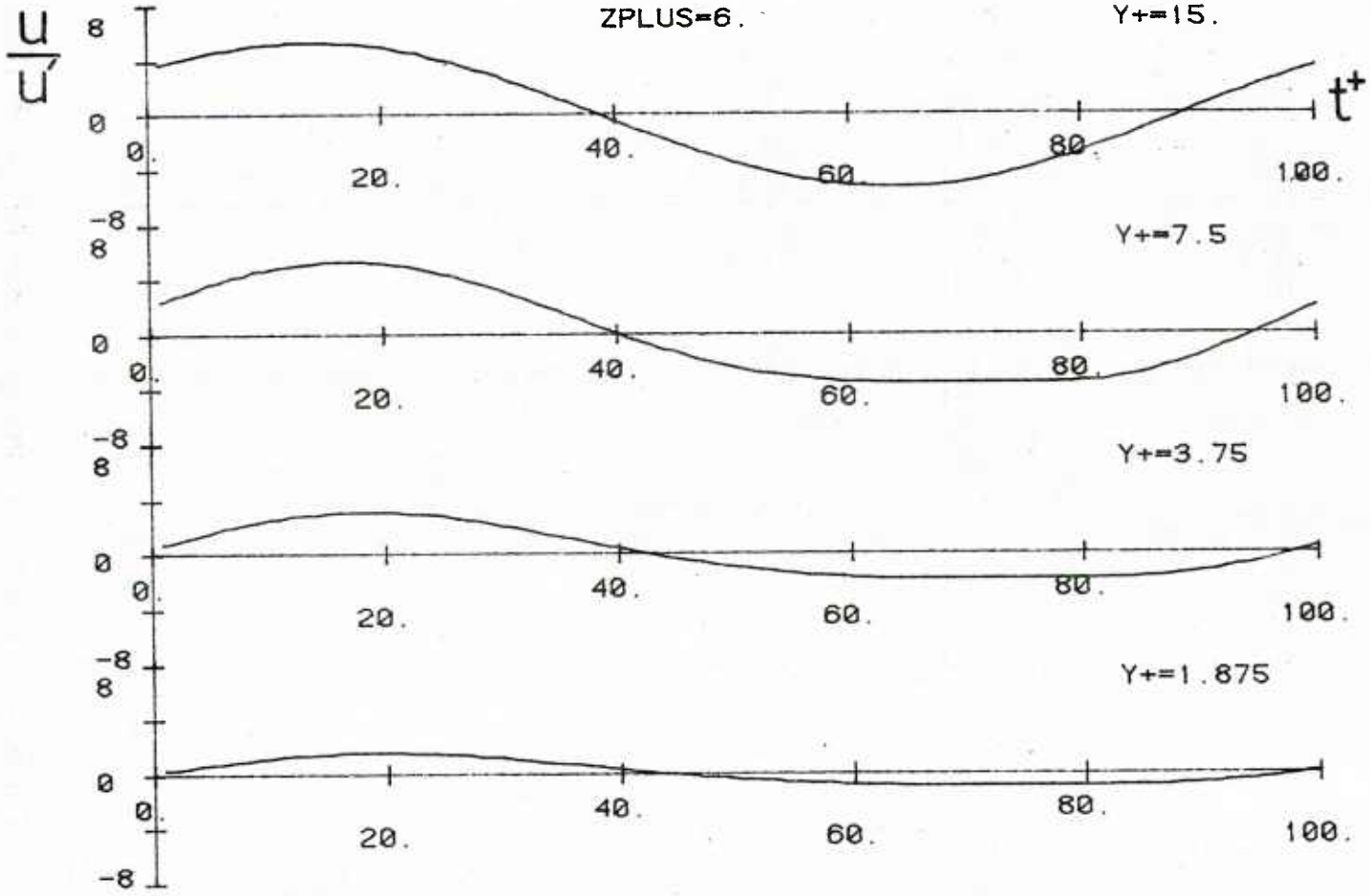

Figure 98 Plots of u/u' versus t^+ at $z^+ = 6$. Single harmonic run; upper boundary at $y_o^+ = 15$

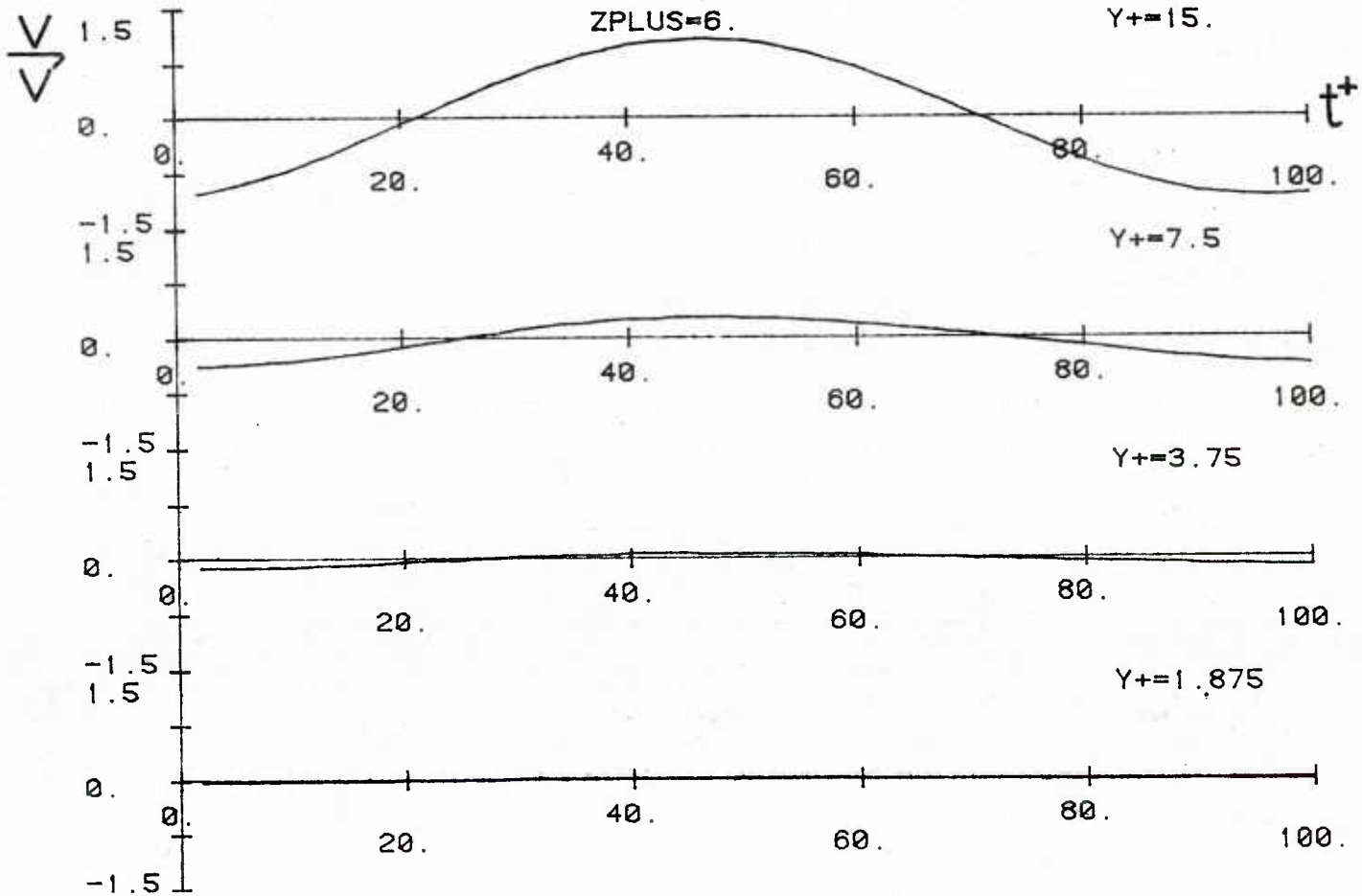

Figure 99 Plots of v/v' versus t^+ at $z^+ = 6$. Single harmonic run; upper boundary at $y_o^+ = 15$

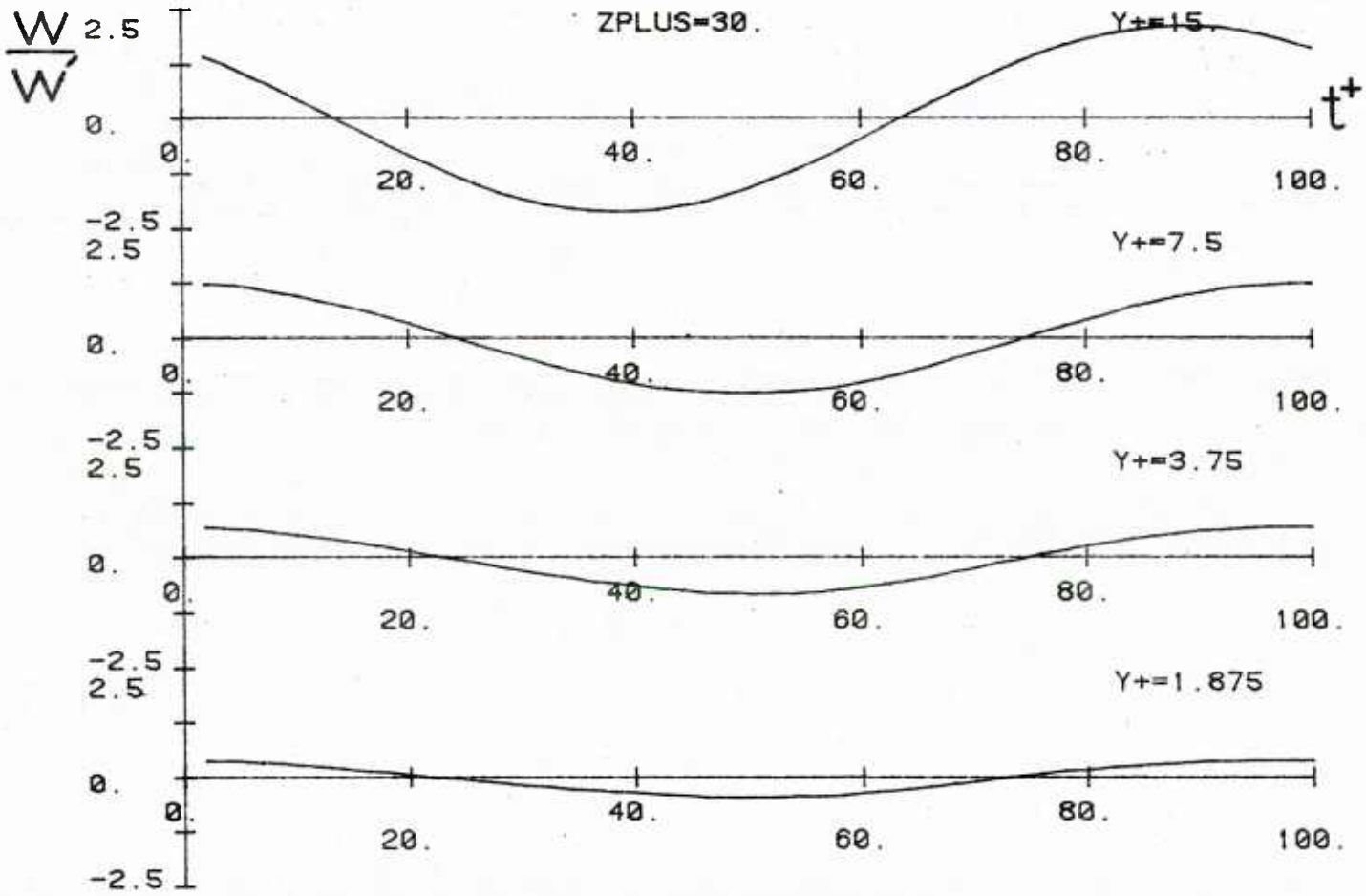

Figure 100 Plots of w/w' versus t^+ at $z^+ = 30$. Single harmonic run; upper boundary at $y_o^+ = 15$

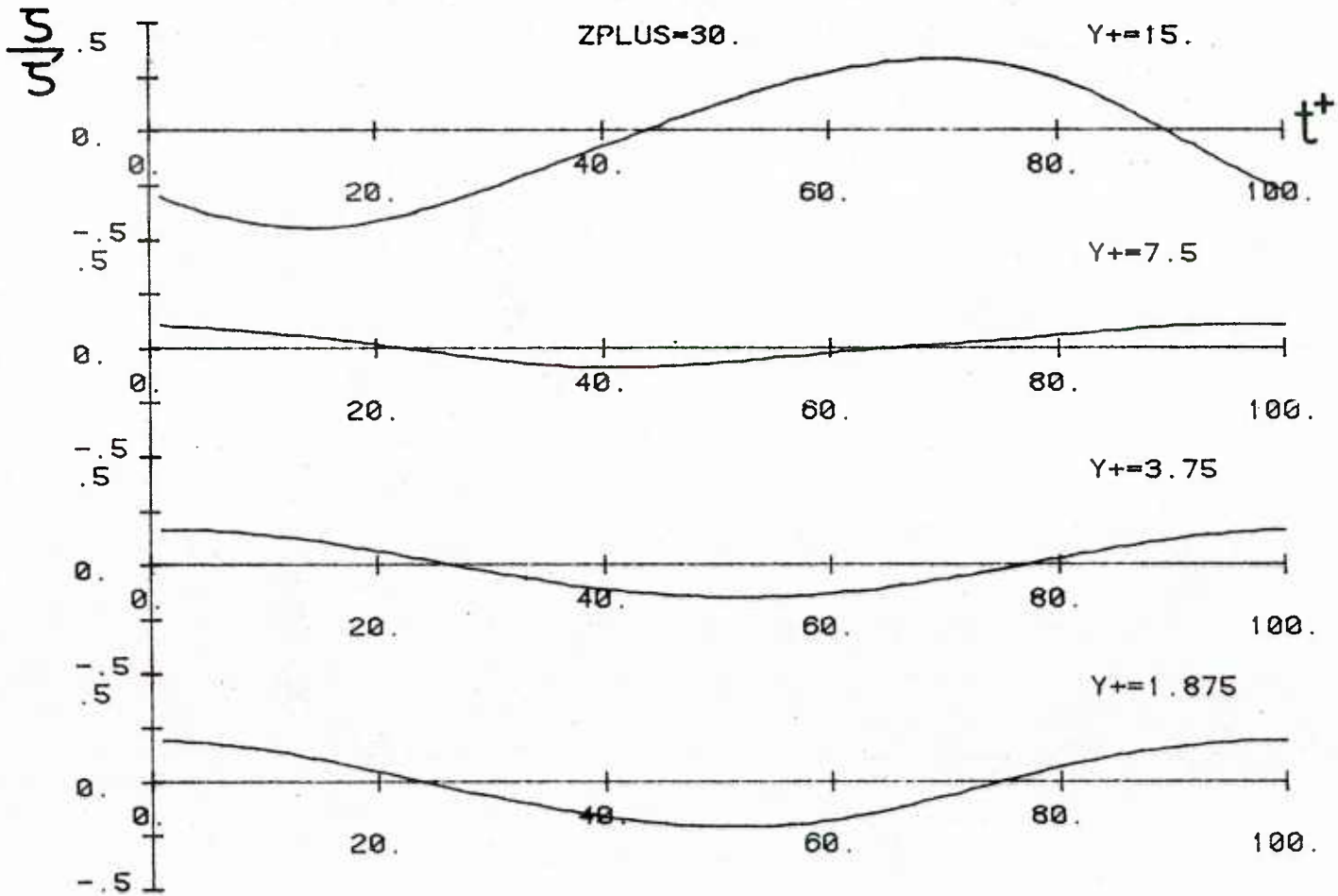

Figure 101 Plots of ς/ς' versus t^+ at $z^+ = 30$. Single harmonic run; upper boundary at $y_o^+ = 15$

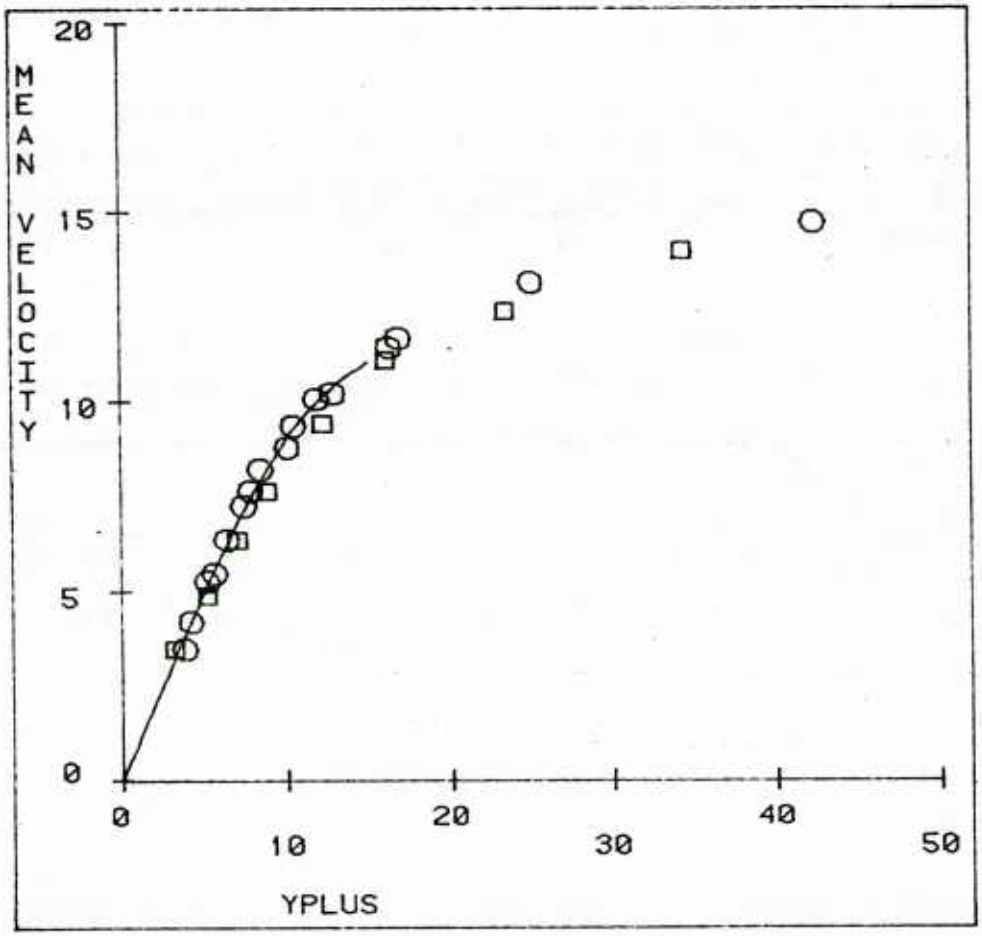

Figure 102 Mean streamwise velocity for a single harmonic run; upper boundary at $y_o^+ = 15$

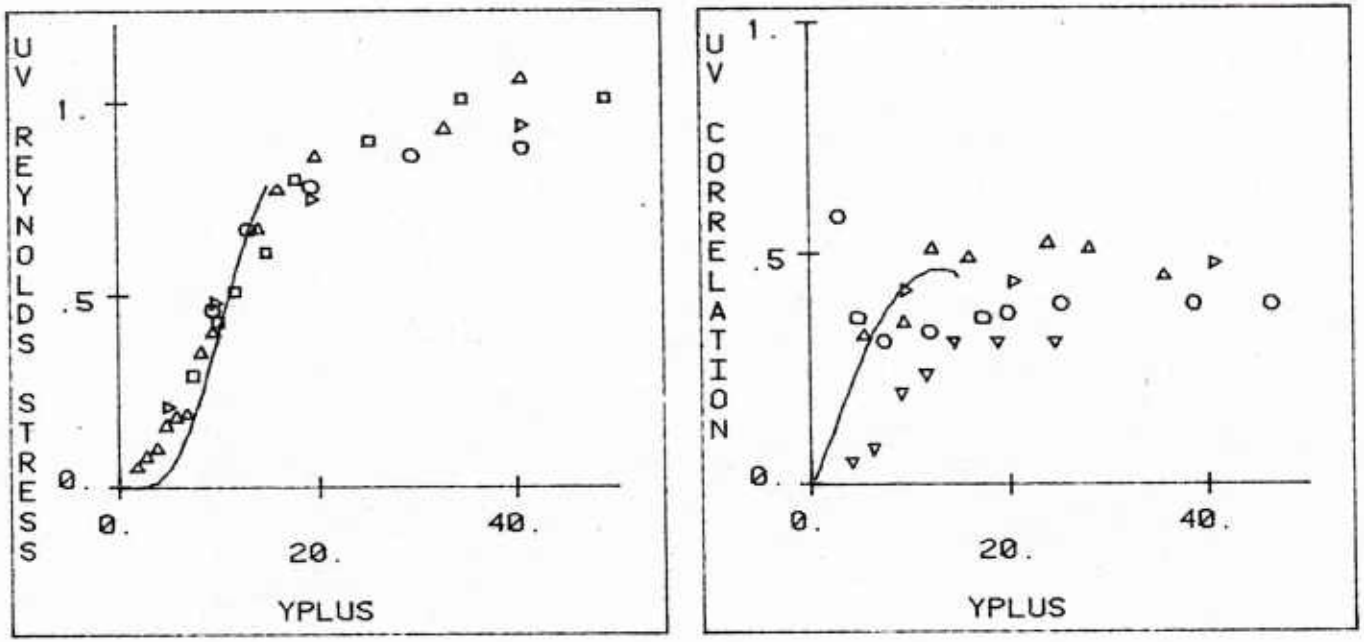

Figure 103 Reynolds stress and $-\overline{uv}/u'v'$ correlation for a single harmonic run; upper boundary at $y_o^+ = 15$

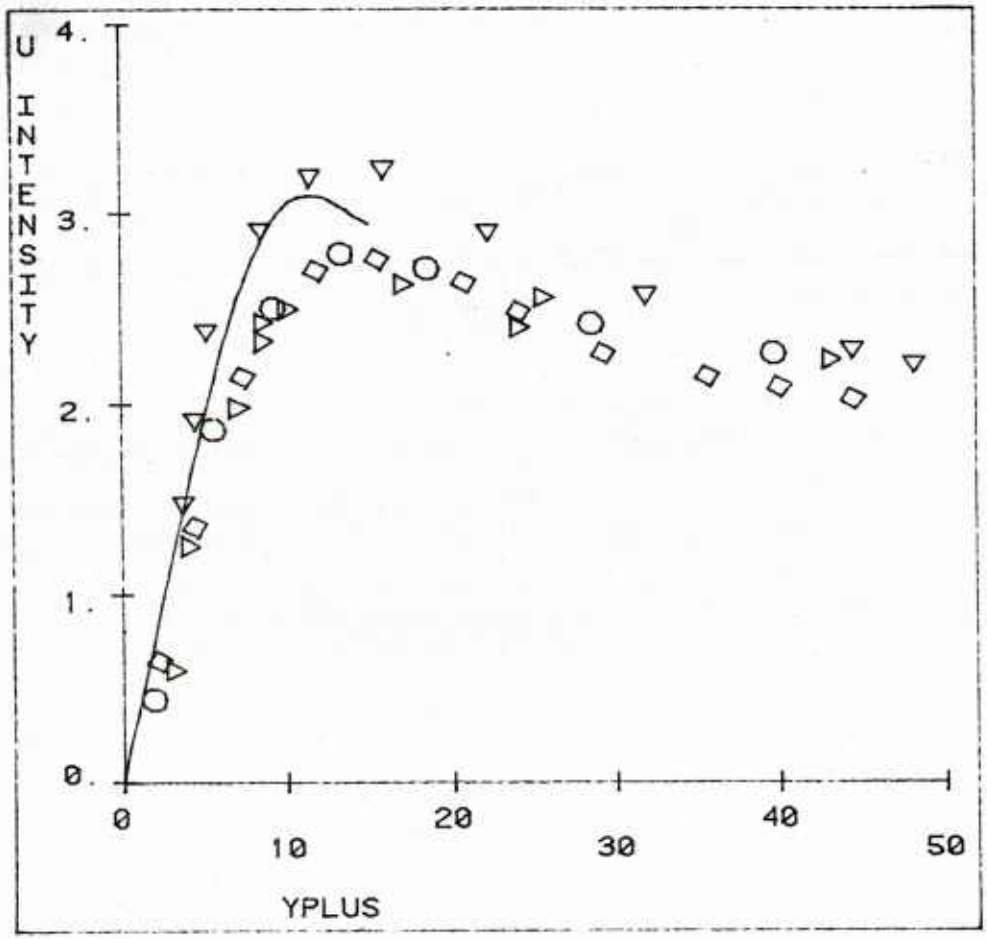

Figure 104 Intensity of streamwise velocity fluctuations for a single harmonic run; upper boundary at $y_o^+ = 15$

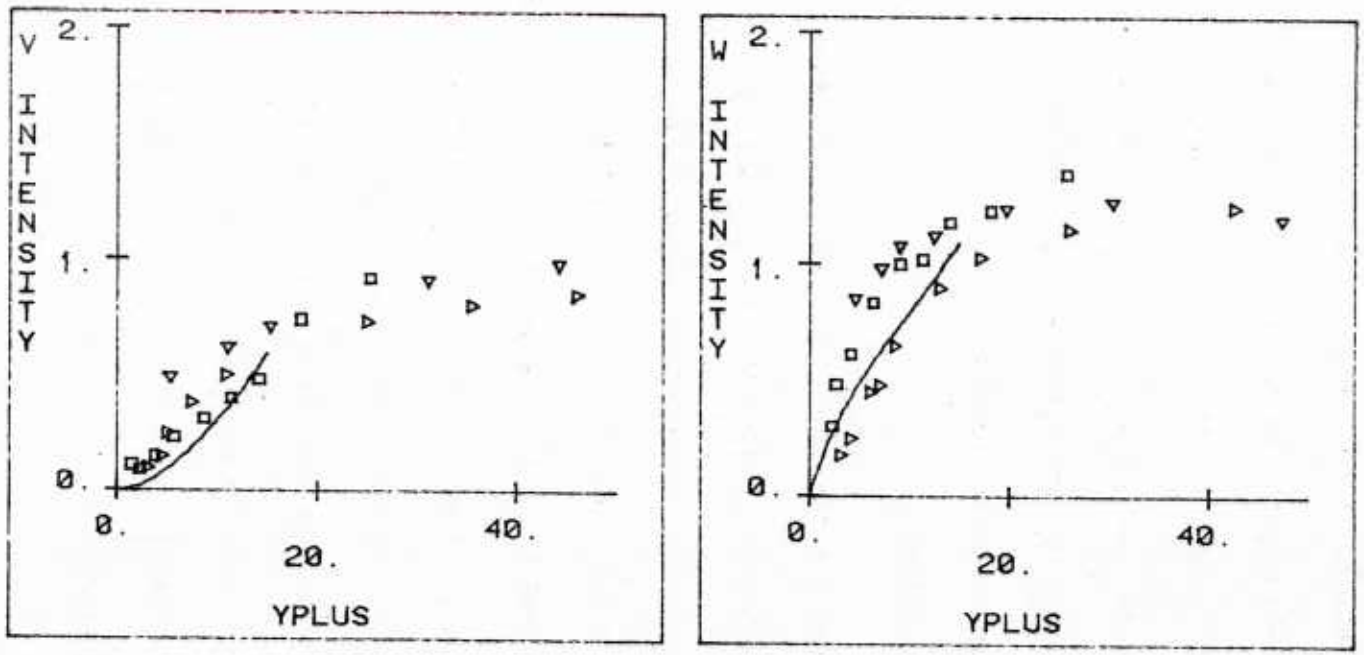

Figure 105 Intensities of the normal and spanwise components of the velocity for a single harmonic run; upper boundary at $y_o^+ = 15$

CHAPTER 6

ENERGY CALCULATIONS FOR THE MODEL FLOW

The results of the numerical computations for the terms appearing in the energy balance equations (4.50), (4.51), (4.52) and (4.53) will be presented in this chapter. The terms that were calculated are the ones appearing in the "isotropic" formulation of these equations because of the most straightforward physical interpretation of the viscous terms. On the other hand, the difference between the true and the "isotropic" dissipation in the turbulent kinetic energy balance was found to be negligible.

The results for the single and double harmonic runs were found to show no significant differences. Figures 106 through 110 present the energy calculations for the single harmonic run described in the previous chapter. All the terms are expressed in wall variables and the explanation of the various symbols used appear in Figure 106. Figure 106 shows the calculated term for the balance of $\overline{u^2}$. As mentioned in Chapter 4, the production of $\overline{u^2}$ is large throughout the viscous wall region. The production curve reaches a maximum of 0.25 at $y^+ = 12$. This is expected because the production is the product of the turbulent and viscous stresses, whose sum is equal to 1 in wall variables. This means that the product is maximized when the two stresses are equal to each other and attain the value of 0.5 in wall units. At the wall the dissipation is equal to the viscous diffusion of $\overline{u^2}$

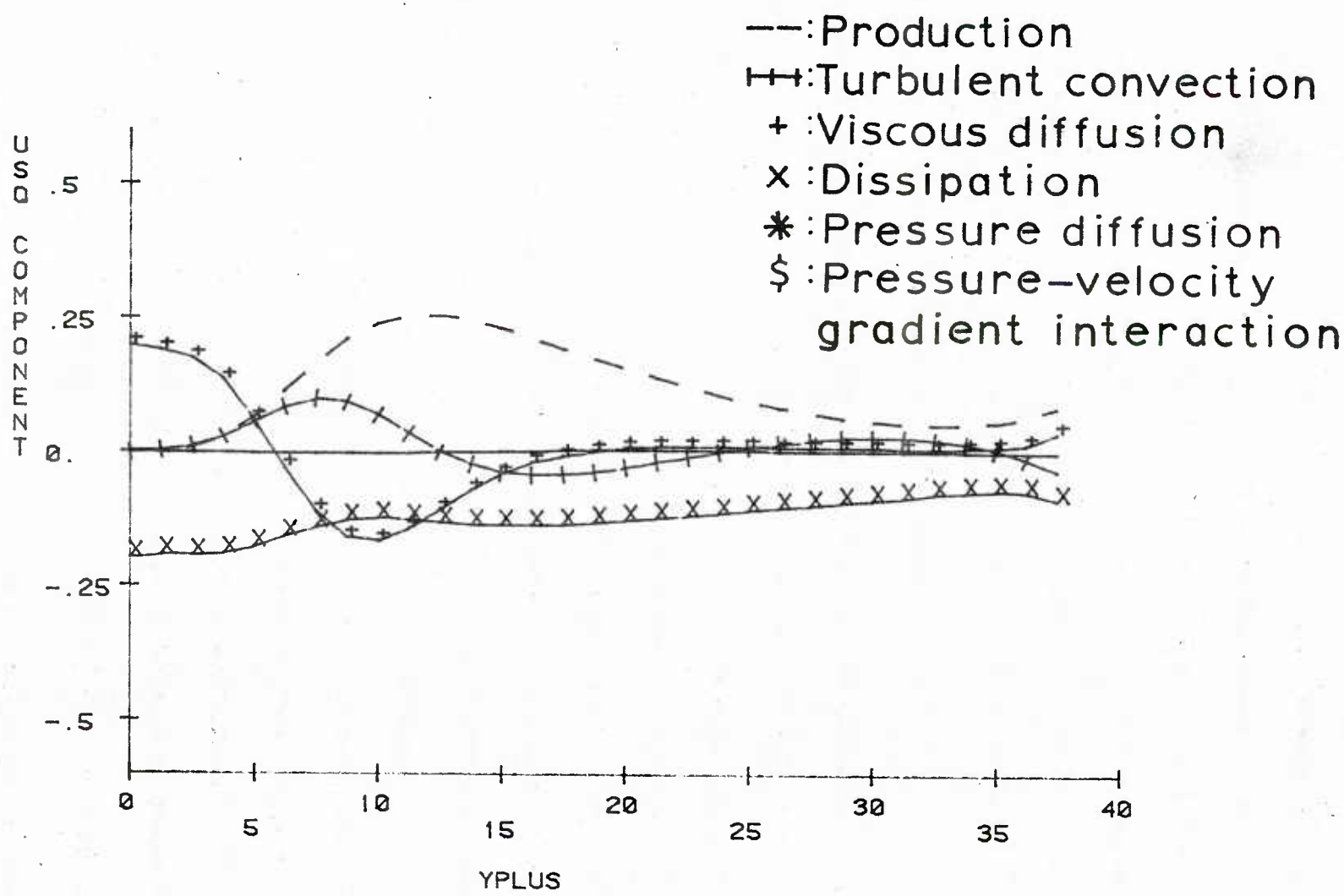

Figure 106 Balance of the streamwise component of the turbulent kinetic energy.

energy. The viscous diffusion is positive for $0 \leq y^+ \leq 6$ and becomes negative for the rest of the viscous wall region showing a (negative) maximum at $y^+ \approx 10$. The dissipation has fairly large values throughout the wall layer and the turbulent convection term is positive for $0 \leq y^+ \leq 12$ and attains small negative values for the rest of the field. Figures 107 and 108 show the calculated balances of $\overline{v^2}$ and $\overline{w^2}$. It can be seen that for $\overline{v^2}$ the turbulent convective term is positive for $0 \leq y^+ \leq 32$ and that the pressure-velocity gradient interaction term $(\overline{p\frac{\partial v}{\partial y}})$ is negative throughout the viscous wall region attaining higher values close to the upper boundary. The dissipation is very small and the pressure-diffusion term assumes large values close to the upper boundary. The picture for $\overline{w^2}$ is different. The turbulent convective term is negative for $0 \leq y^+ \leq 35$ and the pressure- velocity gradient interaction term is positive throughout the viscous wall region. The dissipation term, while negligible close to the wall, attains large values close to the upper boundary. For both $\overline{v^2}$ and $\overline{w^2}$ the viscous diffusion term is very small throughout the wall layer. As mentioned in Chapter 4 the pressure-velocity gradient interaction terms represent transfer of kinetic energy between the two components of the velocity on the y–z plane. The calculations show that the direction of this energy transfer is from the v to the w component of the velocity. In order to remove the effect of the amplitude of the pressure fluctuations the correlation coefficient $\overline{p\frac{\partial v}{\partial y}}/p'(\frac{\partial v}{\partial y})'$ is shown plotted in Figure 109 and the primed variables are the respective r.m.s. values of the quantities in the numerator. It is

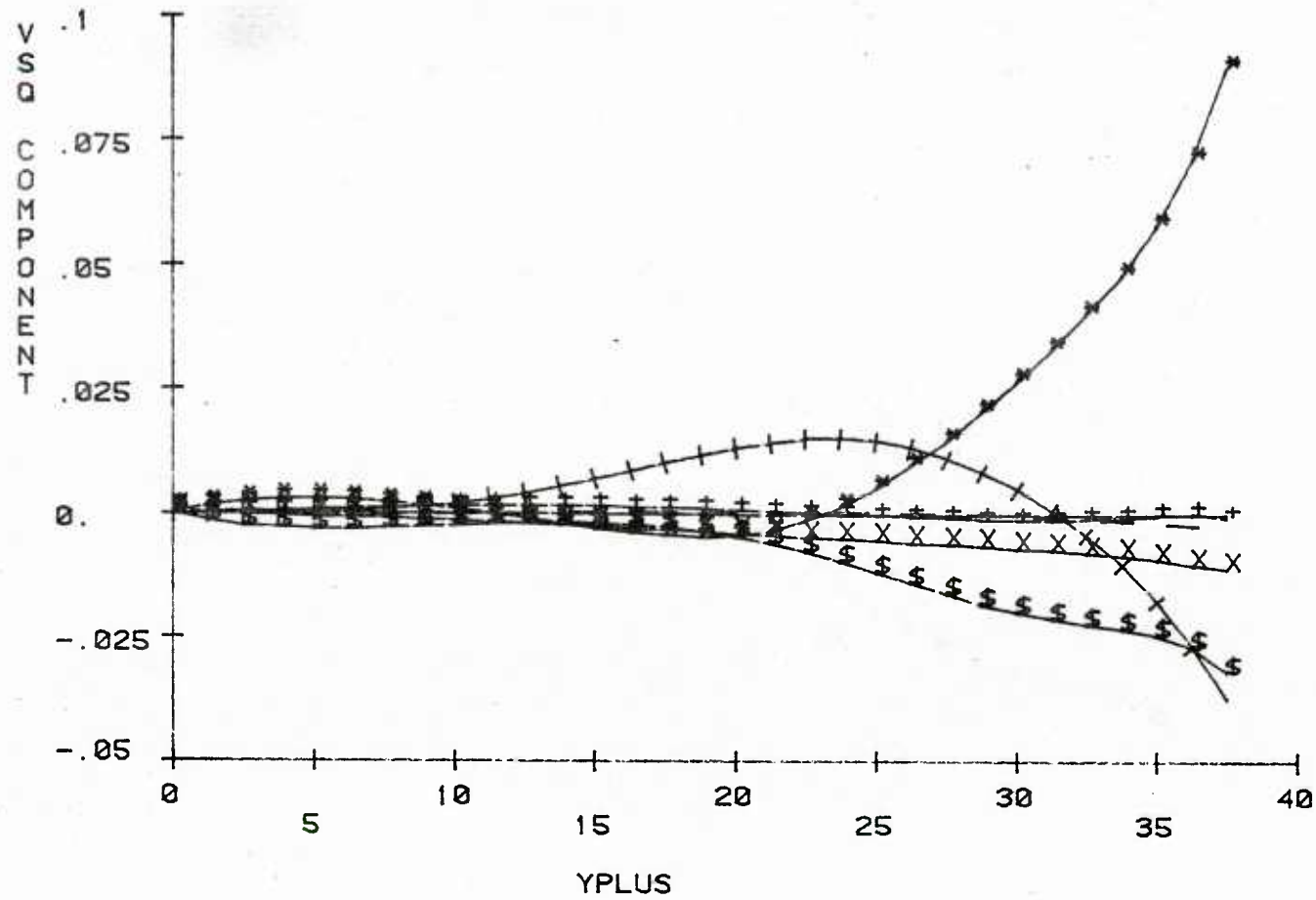

Figure 107 Balance of the normal component of the turbulent kinetic energy.

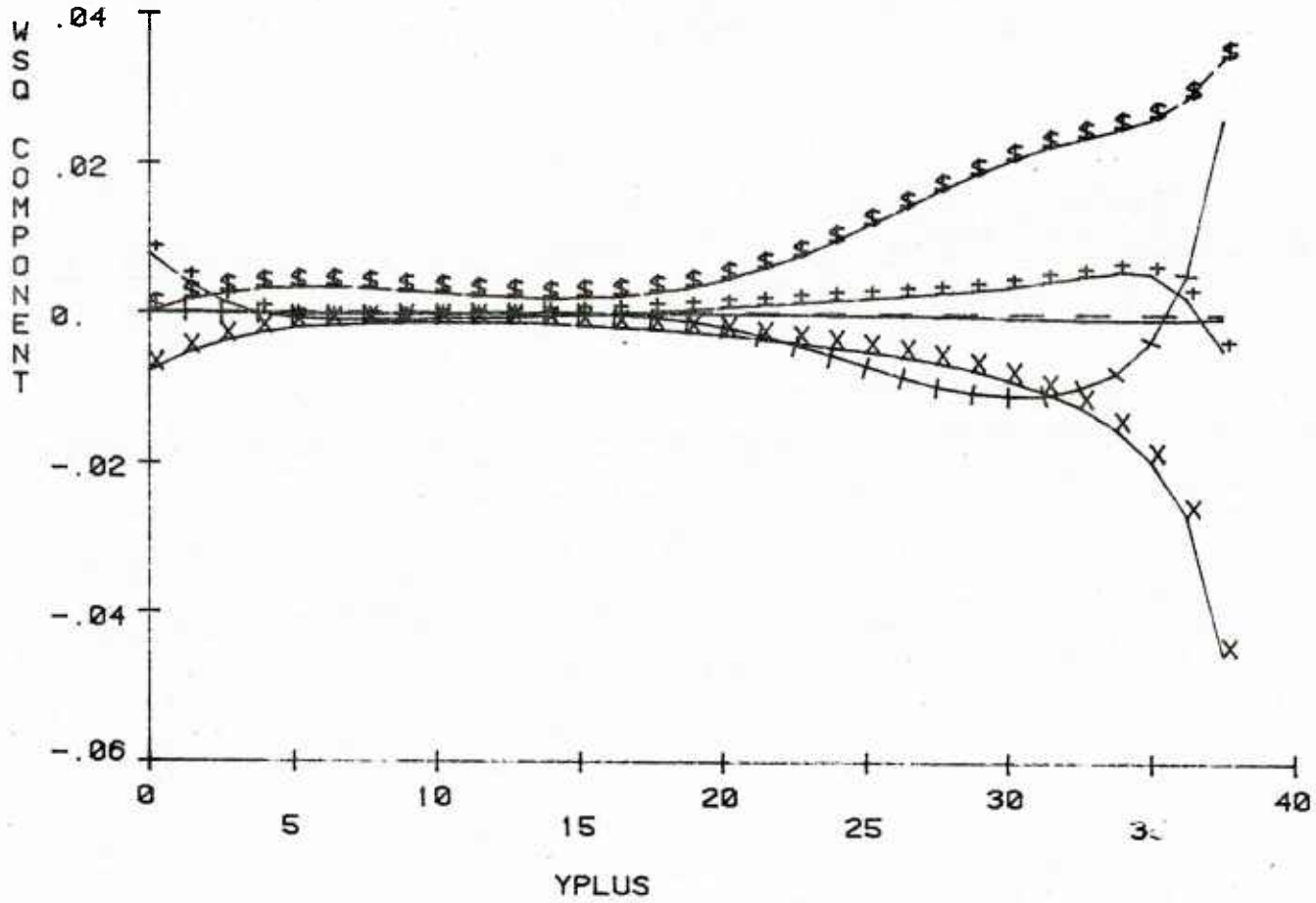

Figure 108 Balance of the spanwise component of the turbulent kinetic energy.

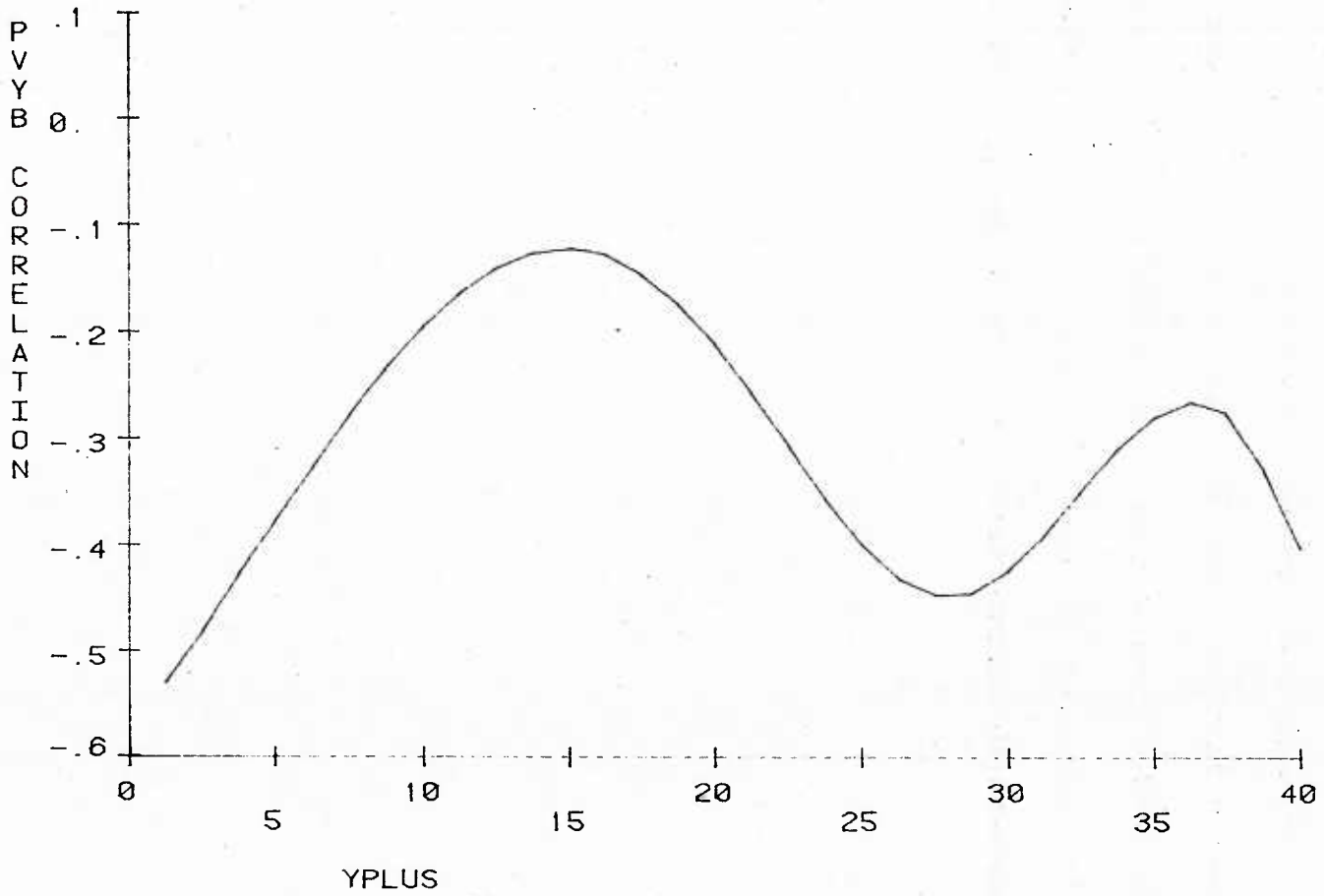

Figure 109 Pressure-velocity gradient correlation coefficient.

seen that large values of the correlation are obtained close to the wall and close to the upper boundary. For comparison purposes we mention that the $-\overline{uv}/u'v'$ correlation has a value of 0.45 throughout the viscous wall region.

Figure 110 shows the balance for the turbulent kinetic energy. It can be seen from a comparison with Figure 106 that almost all the terms are the same with the ones appearing in the balance equation for $\overline{u^2}$. The pressure-diffusion term is seen to have very small values in relation to the rest of the terms. The same comments that were made about Figure 106 apply in this case too.

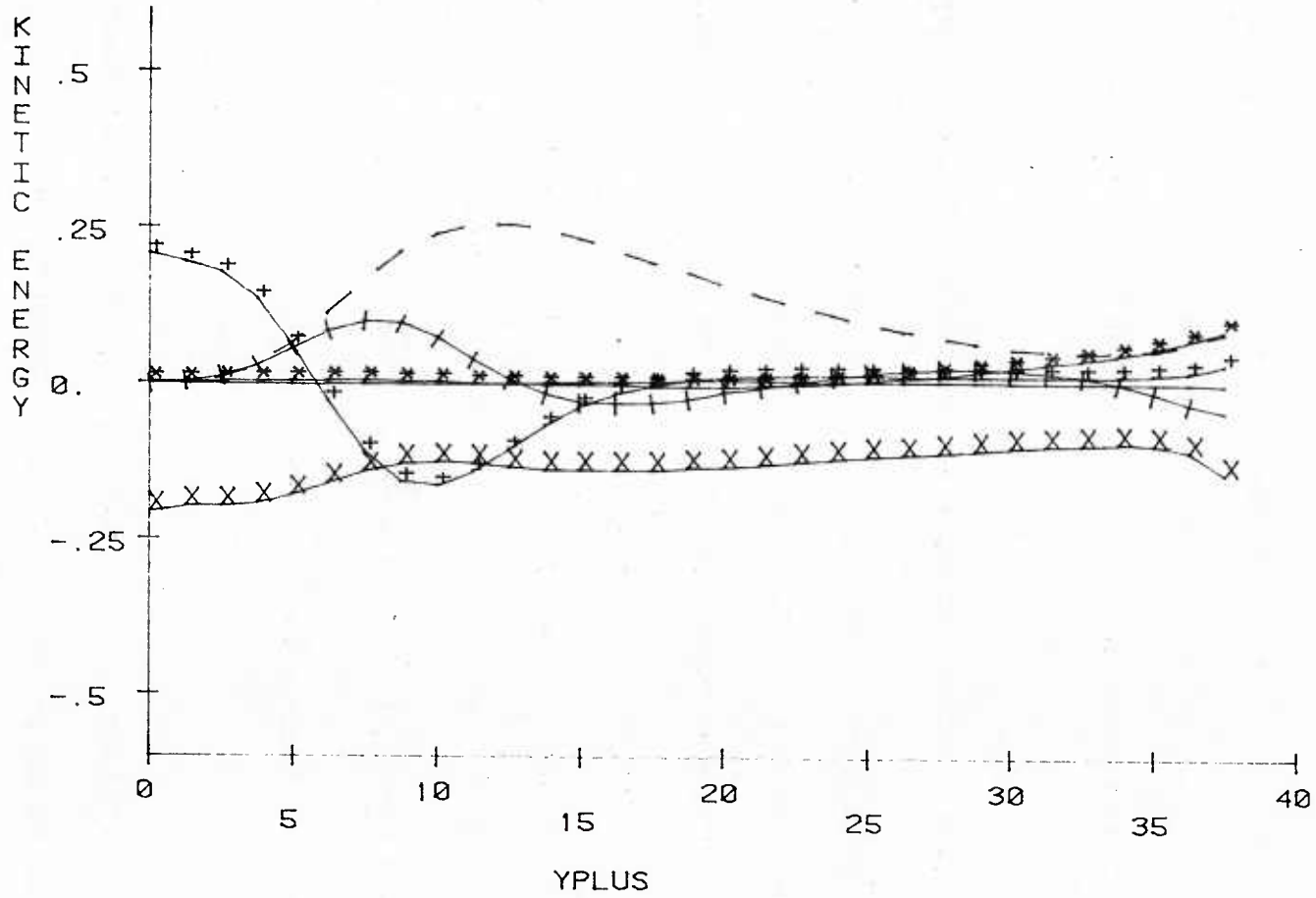

Figure 110 Balance of the turbulent kinetic energy.

CHAPTER 7

SCALING FOR THE MODEL FLOW

In this chapter we will attempt to relate the various parameters that are important in defining the structure of the wall layer and to construct guidelines for an optimization scheme in order to predict the characteristics of the optimal eddies.

For a Gaussian signal the zero-crossing scale defined as $\Lambda \equiv \frac{1}{2\pi N_o}$ (where N_o is the frequency with which the signal crosses zero) is equal to the Taylor microscale λ_T (Rice, 1954). Measurements of the ratio Λ/λ_T by Antonia et al (1976) and Sreenivasan et al (1977), in several turbulent shear flows, suggest that $\Lambda/\lambda_T \approx 1$ (the value for a Gaussian signal)

We will now assume that the wall eddies, calculated in Chapter 5, are related to the Taylor microscale λ_T as follows: Since there are two zero-crossings over a wavelength of λ^+, $N_o = \frac{2}{\lambda^+}$ and $\Lambda^+ = \frac{\lambda^+}{4\pi}$. So for the dominant eddies in the viscous wall region of a turbulent shear flow we obtain the following relation:

$$\lambda_T^+ = \frac{\lambda^+}{4\pi} \tag{7.1}$$

At the edge of the viscous wall region, which lies in the logarithmic portion of the velocity profile, the production of turbulent kinetic energy is equal to the dissipation ($P = \epsilon$). If we use the inviscid estimate $\epsilon = c_1 \frac{q^3}{l}$ for the dissipation

(Tennekes and Lumley, 1977) the equality of production and dissipation gives us the following relation: $-\overline{uv}\frac{d\overline{U}}{dy}=c_1\frac{q^3}{l}$ where q is the r.m.s. turbulent kinetic energy and l is the characteristic size of the large eddies. In the above equation we notice that for the log-region $\overline{uv}=c_2u_*^2$ and $\frac{d\overline{U}}{dy}=\frac{u_*}{Ky}$ where K is the von-Karman constant. If we also assume that $l=Ky$ (from mixing length arguments) we obtain that $q=c_3u_*$ or that q^+ is constant at the edge of the viscous wall layer. We now assume that the dissipation at the same location is given by the isotropic relation $\epsilon=15\nu\frac{q^2}{\lambda_T^2}$. By equating this form of the dissipation with the one used above we obtain

$$15\nu\frac{q^2}{\lambda_T^2}=c_1\frac{q^3}{l} \quad \text{or} \quad \frac{\lambda_T^2q^2}{\nu^2}=(\frac{15}{c_1})\cdot\frac{lq}{\nu}$$

Since we found previously that $q=c_3u_*$, the above relation becomes $\lambda_T^{+2}=\frac{15}{c_1c_3}l^+$ and if assume again that $l=Ky$ we obtain for the edge of the viscous wall region ($y=y_o$) the following relation :

$$\lambda_T^{+2}=\frac{15K}{c_1c_3}y_o^+ \tag{7.2}$$

The constants appearing in equation (7.2) are $K=0.4$, $c_1=0.8$ (Tennekes and Lumley, 1977) and $c_3=2.72$ (Laufer, 1954). Substituting in equation (7.2) we obtain $\lambda_T^{+2}=2.76y_o^+$ and using equation (7.1) we get

$$\lambda^{+2}=435.8y_o^+ \tag{7.3}$$

If we now take $y_o^+=40$ the above equation gives $\lambda^+=130$ a value which is very

close to the value measured experimentally ($\lambda^+ \approx 100$).

It thus appears that the dominant eddies in the viscous wall region are indeed characterized by the Taylor microscale. It is to be noted that the Taylor microscale is not a dissipative scale but that the ratio $\frac{\lambda_T}{q}$ is a dissipative time scale. Therefore the wall eddies are not necessarily dissipative but they are related to the Taylor microscale through the zero crossing scale Λ. The relation obtained above i.e. $\lambda^{+2} = cy_o^+$, where c is a constant, implies that if y_o^+ is constant, independent of Reynolds number, then λ^+ will also not vary with the Reynolds number. For fully developed flows in pipes or channels and for zero-pressure gradient boundary layers y_o^+ is indeed independent of Reynolds number. There are indications in the literature though that it may vary with non-zero pressure gradients (Kline et al 1967).

A major goal of a theory of the wall eddies would be to predict λ^+ without specifying a priori a value for y_o^+. In such a case, then, we would need to find an optimization criterion that would allow us to select the optimum value of λ^+. The optimization process could make use of the computational model described in Chapter 4 in the following way: A value of λ^+ can be selected and y_o^+ is subsequently picked so that equation (7.3) is satisfied. The period of the wall eddies is selected so that $T^+ = \lambda^+$ from arguments presented in Chapter 4. In order to implement the calculations we need to know the energy of the $v-w$ motion at $y^+ = y_o^+$. If this were known then we could calculate the average streamwise

velocity $\overline{U}_L^+$ at $y^+ = y_o^+$, at the end of the computation, by enforcing Newton's law of viscosity at the wall. By repeating, then, the same calculation we could obtain pairs of $\lambda^+, \overline{U}_L^+$ and the optimum λ^+ would have to satisfy a certain criterion. For the above described optimization process such a criterion could be the maximization of $\overline{U}_L^+$. This would then mean that the optimal eddies are the ones that are the most effective in transporting streamwise momentum to and from the wall. Similar optimization processes could be constructed using different criteria (e.g. maximization of the production of turbulent kinetic energy etc.) but the details for such calculations are not known at the present time. We, nevertheless, can conclude that the dominant wall eddies are associated with the Taylor microscale λ_T and that equation (7.3) is an important relation for the spatial structure of these eddies.

CHAPTER 8

DISCUSSION

In this chapter we will discuss the results of conditional averaging on the experimental data of Lau (1980) and we will elaborate on the calculated turbulent characteristics of the viscous wall region. On the basis of this discussion we will propose a physical picture of the flow field that we believe is capable of describing the energy and vorticity dynamics of the viscous wall region and its interaction with the outer flow.

I. Conditional averaging

The use of conditional averaging techniques revealed that strong spanwise flows at the wall are closely associated with strong spanwise flows at $y^+=40$ and 20 that have the same direction and occur at an earlier instant in time. A characteristic feature of the flow field was found to be the reversal of the spanwise flow at $y^+=40$ during the time that a strong spanwise flow occurs at the wall. At $y^+=20$ the conditionally averaged spanwise velocity, leads but always has the same phase, as the flow at the wall.

The measurements of the conventional correlation coefficients as a function of the three spatial coordinates and time are consistent with the above observations. In addition they provide support for the notion that the flow is coherent from the wall out to $y_o^+=40$.

Various other models, that attempt to account for the kinematics of the viscous wall region, have been proposed in the literature. Prominent among these is the suggestion that the flow is dominated by counterrotating vortices, whose length in the flow direction is of the order of $\Delta x^+ \approx 1200$. Their extent in the direction normal to the wall doesn't seem to be well defined but conventional correlation measurements and conditionally averaged measurements suggest that the eye of such vortices would not move, on average, below $y^+ \approx 20$–30. Such vortices are visualized to be "pumping" low momentum fluid away from the wall and thus influencing the streamwise velocity field.

The results of the present work agree with this model in that they support the notion that the wall structures transfer negative momentum fluid away from the wall and thus influence the dynamics of the flow in the streamwise direction. However, the conditionally averaged results at $y^+ = 40$ indicate that the spanwise flow patterns at the wall are caused by flow deviations outside the viscous wall region that are in the same direction. The appearance of streamwise vortical structures is, therefore, considered to be a consequence of the lag time for a spanwise disturbance to travel from $y^+ = 40$ to the wall.

According to the flow model used in this paper the streamwise extent of this "vortical" structure should be $\Delta x^+ \approx -300$: If it is assumed that a spanwise disturbance originates at $y^+ = 40, x^+ \approx -300$ and $T^+ = 0$ and travels both downstream and towards the wall, then it reaches $x^+ \approx 0, y^+ = 40$ and $x^+ \approx -300, y^+ = 0$ at about the same time ($T^+ \approx 20$). The flow at the wall at

$x^+ \approx 0, T^+ \approx 20$ will, on average, be in the opposite direction, having been caused by a spanwise flow that occurred earlier in time. So when the flow changes direction at $x^+ = 0, y^+ = 40$ and $T^+ \approx 20$, the flow at the wall is expected to be in the opposite direction for $-150 \leq x \leq 150$, which is consistent with the results of Figure 7. Similar conclusions were reached, lately, by Kim (1983) from an analysis of a large-eddy simulation of turbulent channel flow. This work will be discussed later in more detail in connection with the structure of vorticity in the viscous wall region.

Blackwelder and Eckelmann (1979) used a conditional averaging scheme that is triggered by a sharp acceleration of the flow in the streamwise direction following a streamwise momentum deficient flow at $y^+ = 15$. Their results differ from the results presented in this work in a number of ways and this could partially account for their different viewpoint on the wall eddies. The wavelength of their wall patterns is not very well defined and there is a loss of correlation at $z^+ = 34$, especially with the $<u>$ velocity profile. Their measurements of $<w>$ at $y^+ = 40$ don't show the characteristic signature of the spanwise component of the velocity that our measurements revealed; that is, a flow reversal, with the return flow having the same magnitude as the flow that preceded it in time.

Their measurements, especially at $z^+ = 34$, would also imply that a vortical structure appears as a suddenly spinning mass of fluid and not because of the lag time between flow changes at $y^+ = 40$ and $y^+ = 0$. We believe that these

differences arise because the detection scheme used by Blackwelder and Eckelmann has the disadvantage, that a single fixed detection probe does not use information regarding the spatial development of the patterns under investigation.

It is also our contention that the event that triggered the conditional averaging scheme used by Blackwelder and Eckelmann is just one aspect of the evolution of the coherent structures in the wall region. Consequently, they were not able to focus sharply on the spanwise variations in w or s_z that give evidence of flow flow oriented wall eddies.

II. Numerical computations

The purpose of the numerical computations, described in Chapter 5, was to calculate the turbulent characteristics of the viscous wall region by specifying realistic boundary conditions at the edge of the wall layer. The primary objective was to obtain the best agreement between the calculated statistically averaged flow variables and experimental measurements in the viscous wall region.

When the upper boundary of the computational domain was set at $y_o^+ = 15$ a single harmonic, of $\lambda^+ = 100$, was used in order to describe the spanwise variation of the velocity fluctuations. The calculated streamwise contours show that the flow at $y_o^+ = 15$ is open for most of the time and is, therefore, in phase with the flow very close to the wall. This is an agreement with the conditionally averaged results at $y^+ = 20$ where the $< w >$ signal was found to be in phase with the

$<s_z>$ patterns at the wall. The very good agreement of the calculated average streamwise velocity, Reynolds stress and turbulent intensities with experimental data indicates that the $\lambda^+=100$ eddies are, indeed, the dominant eddies from the wall up to $y_o^+=15$. In this region, therefore, these eddies create a turbulent flow field which can account for momentum transport and for the production of Reynolds stress, and whose intensity, in all three directions, agrees very well with experiments.

When the upper boundary of the computational domain is set at $y_o^+=40$ the situation is different. The results of the single harmonic, $\lambda^+=100$, calculations show that the computed average properties of the flow have good agreement with experiments, except the intensity of the spanwise component of the velocity. As mentioned in Chapter 5, the main feature of the lateral profiles of w is a zero-crossing which moves, as time progresses, towards the wall. This behavior causes the development of large stresses $(\partial w/\partial y)$ close to the upper boundary and the appearance of a local maximum $(\partial w/\partial y=0)$ in the region $10\leq y^+\leq 25$, which also moves towards the wall. The low values of the spanwise intensity profile in the region $10\leq y^+\leq 25$ are a consequence of the zero-crossing in the w profiles. This in turn is related to the streamwise vortical structures that were found to be the main feature of the flow in the viscous wall region. These structures are associated with strong spanwise flows at $y_o^+=40$ which are of opposite sign to the spanwise flows at the wall, in accordance with the conditionally averaged results. The "eye" of the streamwise vortices spends most of the time below

$y_o^+ = 40$ in the central region of the cell, where the spanwise distribution of w is expected to show a maximum. This does not prevent the normal component of the velocity from attaining high values, since v is expected to reach a maximum close to the sides of the cell. Therefore, the presence of the "eye" of the streamwise vortical structures below $y_o^+ = 40$, for most of the time, affects only he amplitude of the calculated spanwise flows. The implication of these results is that the $\lambda^+ = 100$ wall eddies can not account for the large amplitude spanwise flows in the region $15 \leq y^+ \leq 40$, that have been observed experimentally. They can, however account for the momentum transport and the Reynolds stress production throughout the viscous wall region. Moreover, the calculated $u-$ and $v-$ intensity profiles agree well with experiments and this is reflected by the good agreement of the computed $-\overline{uv}/u'v'$ correlation with measurements.

The characteristic signature of the streamwise vorticity in the y-direction was found to be associated with large values of the vorticity close to the upper boundary and at the wall that are of opposite sign. Kim (1983) calculated, recently, conditional averages of the streamwise vorticity in the viscous wall region by applying the V.I.T.A. technique to data obtained from a large eddy simulation of turbulent channel flow. Based on his results, he proposed a characteristic profile for the streamwise vorticity which is in good agreement with the one calculated in the present work. He found that there are two distinct groups of vortical structures that contain opposite signs of streamwise vorticity: one near the wall and the other slightly away from the wall. These findings are in agree-

ment with the results shown in Figure 42, where these two groups can be observed around $y^+ = 30$ and close to the wall.

The dynamic picture of the streamwise velocity field agrees with the measurements of Hogenes (1979) in regard to the dynamic sequence of inflows and outflows. Figure 50 shows the temporal succession of inflows and outflows for a fixed spanwise location in the cell. Both the temporal and spatial coupling of inflows and outflows is evident from the contour plots in Figures 34 through 38. The results agree with the findings of Hogenes and Hanratty (1982), in that they show that the v–w motion affects the dynamics of the flow in the axial direction by creating large fluctuations of the streamwise velocity component.

The calculated s_z-profiles at the wall and the correlation $R_{s_z s_z}(\Delta z)$ indicate that the separation of the flow in the spanwise direction from the wall is responsible for the creation of smaller scale velocity fluctuations close to the wall and for the shifting of the s_z-patterns. The separation of the flow also appears to be a precursor for the shrinking of the streamwise vortical structures and the movement of their centre towards the wall.

The path-line and streakline calculations are important because they emphasize the unsteady nature of the flow field. It can be seen from Figure 51 that the fluid particles that are close to the wall stay there for a long time compared to the period of the imposed velocity fluctuations at the upper boundary. This then implies that dye injected close to the wall would tend to stay in the same region for a long period of time. This observation is made more clear by the

streaklines shown in Figure 52. It is seen that the dye initially tends to remain close to the wall. Because of the very small normal velocities in this region, the changes of the v–w field result in only a spanwise spreading of the dye-particles. As time goes on the dye lifts up gradually away from the wall and is finally ejected outward, towards the upper boundary. This picture of the flow agrees very well with the flow visualization experiments of Kim et al (1971) in which they injected dye through a slot at the wall of a turbulent boundary layer. The dye was observed to be pushed in the spanwise direction, thus forming the well known "wall streaks". As the streaks migrated downstream they lifted up away from the wall and created turbulent "bursts" of low-streamwise velocity fluid. The streakline calculations of the present work represent a two-dimensional picture of the flow field. If the streamwise motion were taken into account, the dye-streaks at the wall would look like elongated filaments meandering in the spanwise direction and ejecting low-streamwise velocity fluid from the wall towards the upper boundary.

The implications of the above observations can be appreciated more in the case where a wide range of frequencies is used for the signals at $y_o^+ = 40$. It can be seen from Figures 58 through 60 that even though the v–w field changes direction with high frequency, much lower frequencies are obtained in the streamwise velocity component. Since the period of the streamwise velocity fluctuations is related to the bursting frequency, it can be seen that bursting arguments may fail to specify the period of the velocity fluctuations on the y–z plane. It is not

clear, however, whether the higher frequency v and w fluctuations should be associated with the $\lambda^+=100$ eddies or with eddies of much smaller scales that are probably not so important in transferring momentum to and from the wall.

Similar calculations to the ones described above have been carried out by Hatziavramidis (1978). In these calculations the outer flow was visualized to be well mixed and the boundary conditions at $y_o^+=40$ specified the spanwise velocity component of the $\lambda^+=100$ eddies and a zero stress ($\frac{\partial w}{\partial y}=0$). The calculated streamline patterns showed that the flow at the upper boundary is open for most of the time. Therefore, the streamwise vortical structures, that were found in this work to be the main feature of the flow field, lasted for a shorter time. The advantage of prescribing both v and w at $y_o^+=40$ is that the percentage of the closed flow can be defined a priori, in accordance with the results of conditional averaging.

The spanwise intensity profile, in the calculations of Hatziavramidis, was found to have fair agreement with experiments, exhibiting low values in the region $15\leq y^+\leq 30$. The intensity of the normal component of the velocity assumed high values especially in the region $30\leq y^+\leq 40$. In the present work the v-intensity profile shows good agreement with experiments in the same region. There is an indication that the slightly lower values (when compared to experiments) of the v-intensity close to the wall, that were calculated in this work, could be improved by the introduction of smaller scales. It is not clear, however, what fraction of the $\overline{v^2}$ energy these eddies should contribute to the

flow. As mentioned earlier, the "eye" of the vortical structures affects only the spanwise intensity profile giving rise to a plateau region from $y^+=10$ to $y^+=25$. This was found to be the characteristic profile of all the fixed cell single harmonic runs.

The most important achievement of the computational work is the use of two spatial harmonics in order to represent the velocity field at $y_o^+=40$. The limited amount of experimental data indicates that the scale of the important eddies in the viscous wall region increases with distance from the wall. The specification of two length scales at $y_o^+=40$ actually defines the interaction of the viscous wall region with the outer flow. As will be discussed later, it is this interaction that controls the energy and vorticity dynamics of the flow and provides the ground for the creation and maintenance of wall turbulence.

The difference between these calculations and the single harmonic runs is that a fraction of the $\overline{v^2}$ and $\overline{w^2}$ energy at $y_o^+=40$ is attributed to scales of $\lambda^+=400$. Most of the $\overline{u^2}$ energy at the upper boundary is also associated with eddies of $\lambda^+=400$. These eddies are visualized to have their effective centres above $y_o^+=40$ for 100% of the time and, as a result, the induced flow field is 100% open.

The results presented in Chapter 5 show that the average properties of the calculated flow field are in good agreement with experimental measurements. The most noticeable result is that the spanwise intensity profile has good agreement with experimental data throughout the viscous wall region. It is thus seen

that the introduction of longer scales at $y_o^+ = 40$ induces the necessary flow conditions for the creation of large spanwise flows, whose magnitude agrees with measured values of the spanwise intensity. That leads us to the conclusion that the experimentally measured spanwise intensity profiles are not associated with the $\lambda^+ = 100$ wall eddies. If this were the case, then the experiments should give us a profile similar to the one obtained from the single harmonic, $\lambda^+ = 100$, fixed cell runs.

The rest of the statistically averaged flow quantities show the same behavior as in the single harmonic runs. The only difference is that the values of the skewness of the streamwise velocity component are greatly improved close to the upper boundary. This is believed to be caused by the large scale spanwise flows which were absent in the single harmonic runs. These flows provide spanwise mixing on the same range of scales that are characteristic of the large scale u-eddies.

As mentioned above the spanwise intensity signature of the $\lambda^+ = 100$ wall eddies is completely masked by the larger scale spanwise flows. One then might wonder whether this is also true right at the wall, where it has unambiguously been established experimentally that the $\lambda^+ = 100$ eddies define the scale of the velocity fluctuations (Kim et al 1971, Lee et al 1974). The calculated $R_{\theta_i \theta_i}(\Delta z)$ correlation in Figure 71 shows that, indeed, the $\lambda^+ = 100$ eddies are the dominant eddies close to the wall. It is thus seen that even though the outer flow eddies are important in defining the level of spanwise mixing in the viscous wall region,

their importance close to the wall is negligible. It is the $\lambda^+ = 100$ eddies that contain most of the energy of the velocity fluctuations close to the wall and control the momentum transport to and from the solid boundary.

In order to compare the results of the single and double harmonic calculations, the statistically averaged flow variables are reproduced in the series of Figures 111 through 115. The solid lines represent the results of the double harmonic runs and the dashed lines are the results of the single harmonic computations. These plots emphasize the similarities and differences in the results of the two calculations. It can be seen that there is no essential difference in the prediction of the average velocity profile, the Reynolds stress, the u- and v- intensity profiles and the flatness of the streamwise velocity fluctuations. As discussed previously, the spanwise intensity profile from the double harmonic calculations shows good agreement with experiments. It can now be seen that the small "wiggle" at $y_o^+ = 40$ is not computational but is a "remnant" of the characteristic spanwise intensity profile of the single harmonic runs, where large stresses $(\partial w/\partial y)$ are developed at the upper boundary. The improved values for the u-skewness in the region $20 \leq y^+ \leq 40$ are also made clear in Figure 115.

Similar calculations with the double harmonic runs described above have been carried out by Chapman and Kuhn (1981). The main difference is that the outer flow eddies were visualized to be associated with a "pulsating" type of flow at $y_o^+ = 40$ on a plane parallel to the wall with negligible amount of energy in the normal component of the velocity. These calculations, with different model

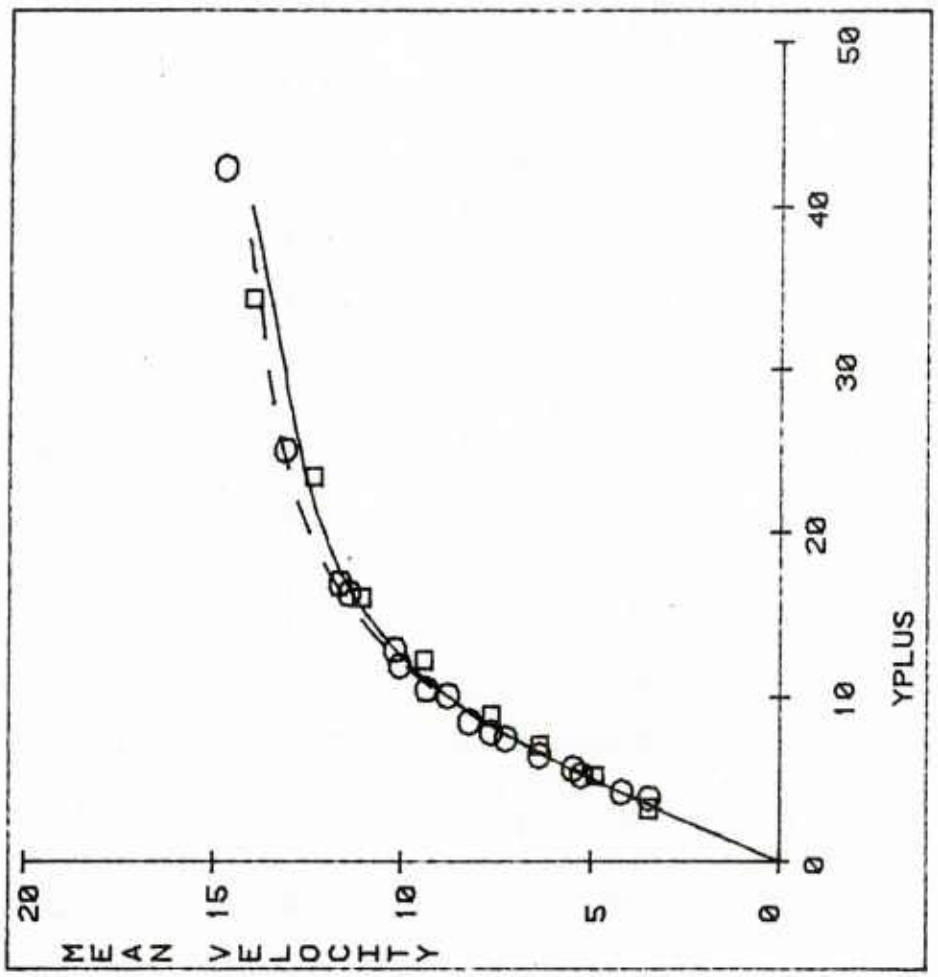

Figure 111 Mean streamwise velocity profiles for single and double harmonic runs; upper boundary at $y_o^+ = 40$

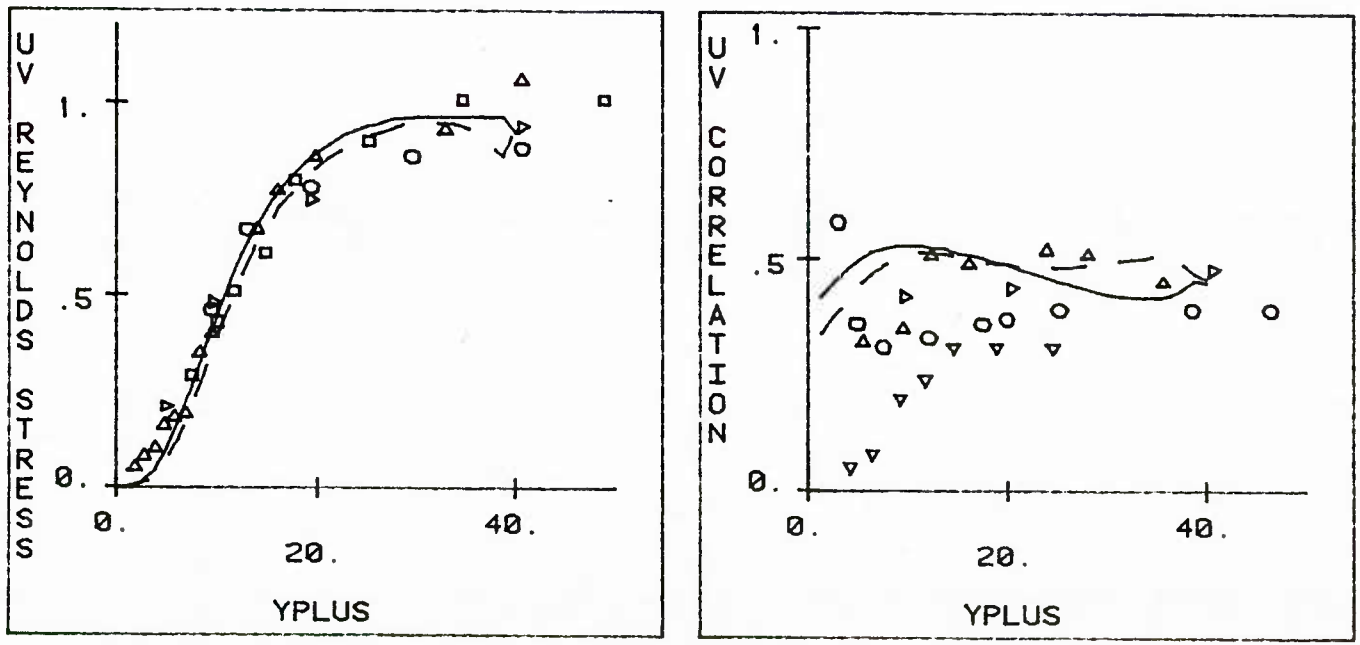

Figure 112 Reynolds stress and $-\overline{uv}/u'v'$ correlation for single and double harmonic runs; upper boundary at $y_o^+ = 40$

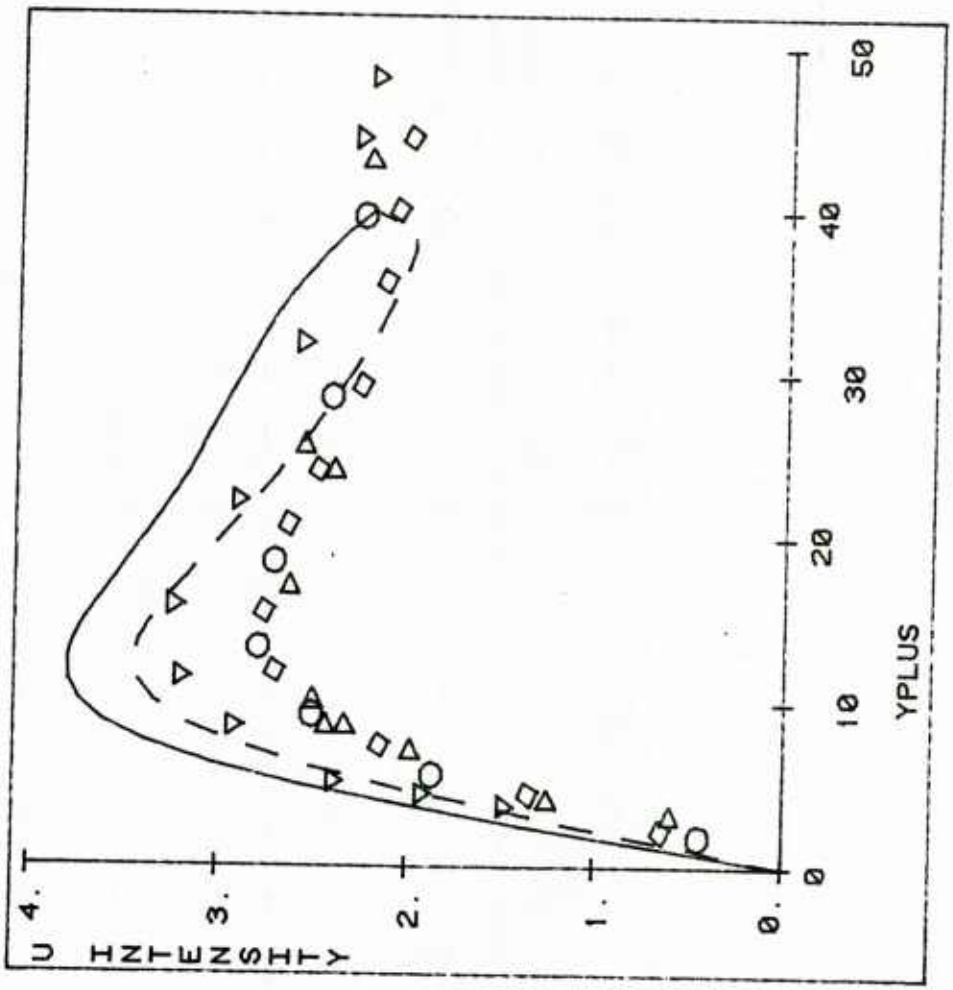

Figure 113 Intensity of streamwise velocity fluctuations for single and double harmonic runs; upper boundary at $y_o^+ = 40$

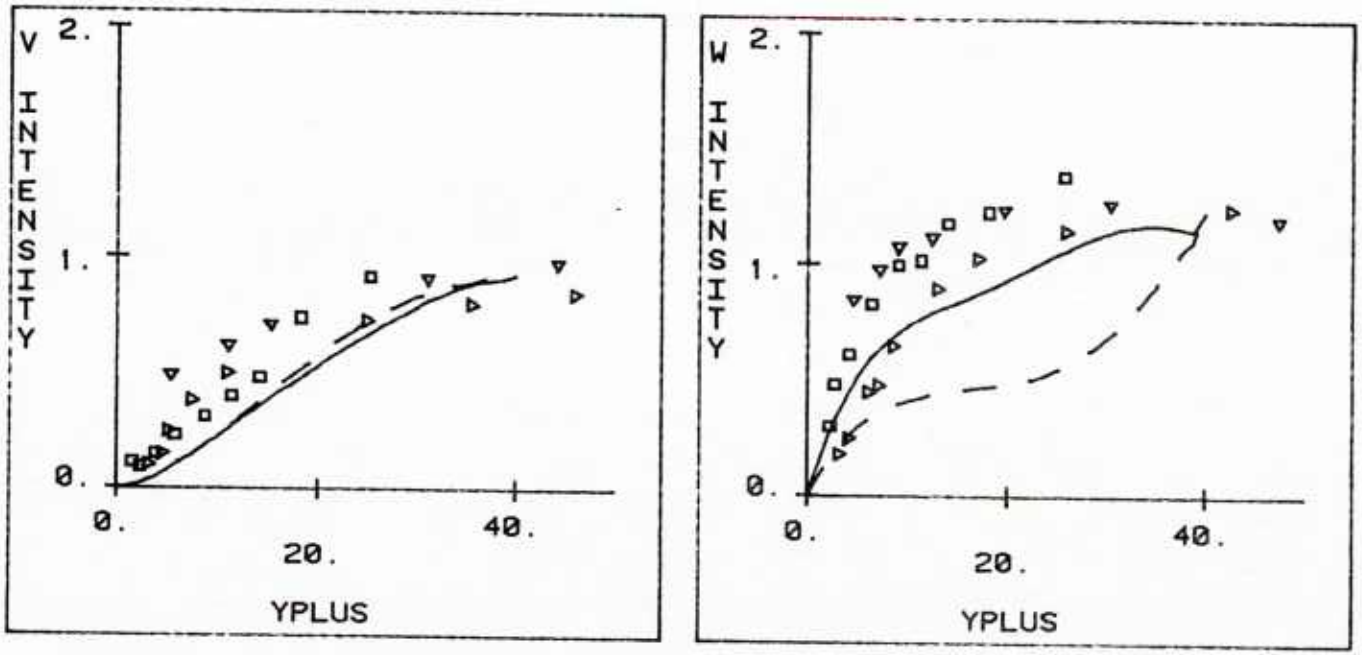

Figure 114 Intensities of the normal and spanwise components of the velocity for single and double harmonic runs; upper boundary at $y_o^+ = 40$

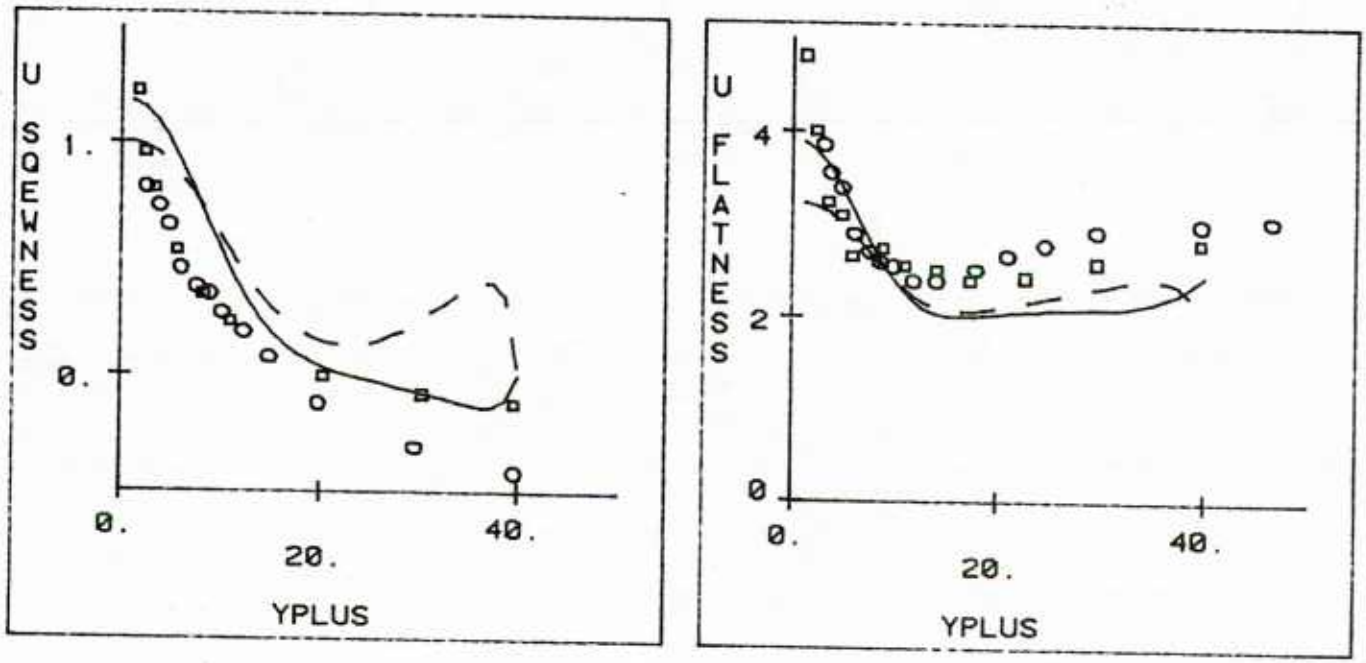

Figure 115 Skewness and flatness of streamwise velocity fluctuations for single and double harmonic runs; upper boundary at $y_o^+ = 40$

parameters, were reproduced during the course of this work and are presented in Appendix B. Even though good agreement is obtained with experiments, wall correlations show that the wall s_z- patterns are greatly affected by the pulsating spanwise flows at the upper boundary. If is thus concluded that the outer flow eddies have to be modelled as eddies with finite wavelengths contributing a fraction of the $\overline{v^2}$ energy at $y_o^+ = 40$.

The calculated energy balances for the model flow show a number of interesting characteristics. The turbulent convective transport of $\overline{u^2}$ energy is positive close to the wall and attains small negative values for the rest of the viscous wall region. The same term for the $\overline{v^2}$ energy is positive up to $y^+ \approx 32$ and for the $\overline{w^2}$ energy it is negative up to $y^+ \approx 35$. This, then, means that $\overline{v^2}$ energy is convected into the region $0 \leq y^+ \leq 32$ and $\overline{w^2}$ energy is convected outside the region $0 \leq y^+ \leq 35$ by the fluctuating normal component of the velocity. On the other hand there is convective transport of $\overline{u^2}$ energy in the region $0 \leq y^+ \leq 12$ and outside the region $12 \leq y^+ \leq 40$. The calculated pressure-velocity gradient interaction correlation coefficient shown in Figure 109 indicates that there is significant transfer of energy from the v to the w component of the velocity. It is to be noted that the same behavior was observed in the large-eddy simulation calculations of Kim and Moin (1979) and Moin and Kim (1981). They, also, found that there is considerable transfer of energy from the normal to the spanwise component of the velocity by what they called "splatting effect".

The calculations presented in Chapter 5 have established the notion that the $v-w$ motion creates large amplitude streamwise velocity fluctuations. Figures 106, 107 and 108 show that there is production of turbulent kinetic energy only in the streamwise component of the velocity. The fact that this energy is produced by the flow field on the $y-z$ plane is supported by the calculations of Hatziavramidis (1978). In these calculations zero-energy was prescribed to the u-component of the velocity at $y_o^+ = 40$. The results of the computations showed that the calculated u-intensity profile had good agreement with experiments for $0 \leq y^+ \leq 25$.

The results of the calculations discussed earlier and the computed energy balances for the model flow can now help us to construct a physical model that describes the interaction of the viscous wall region with the outer flow. A schematic of this interaction is shown in Figure 116. The dominant eddies at the wall are the $\lambda^+ = 100$ eddies. It was shown before that these eddies can account for momentum transport, Reynolds stress production and the creation of u and v velocity fluctuations whose intensity agrees with experiments. Since there is no production of $\overline{v^2}$ energy in the viscous wall region, this energy should come from the outer flow. The positiveness of the turbulent transport term for $0 \leq y^+ \leq 32$ shows that indeed $\overline{v^2}$ energy is transferred into this region from the outer flow. Part of the $\overline{v^2}$ energy transferred into the wall region is converted to $\overline{w^2}$ energy through pressure-velocity gradient interactions. The positiveness of the turbulent convective transport term, in the $\overline{w^2}$ energy balance, for $y^+ > 35$ shows that there

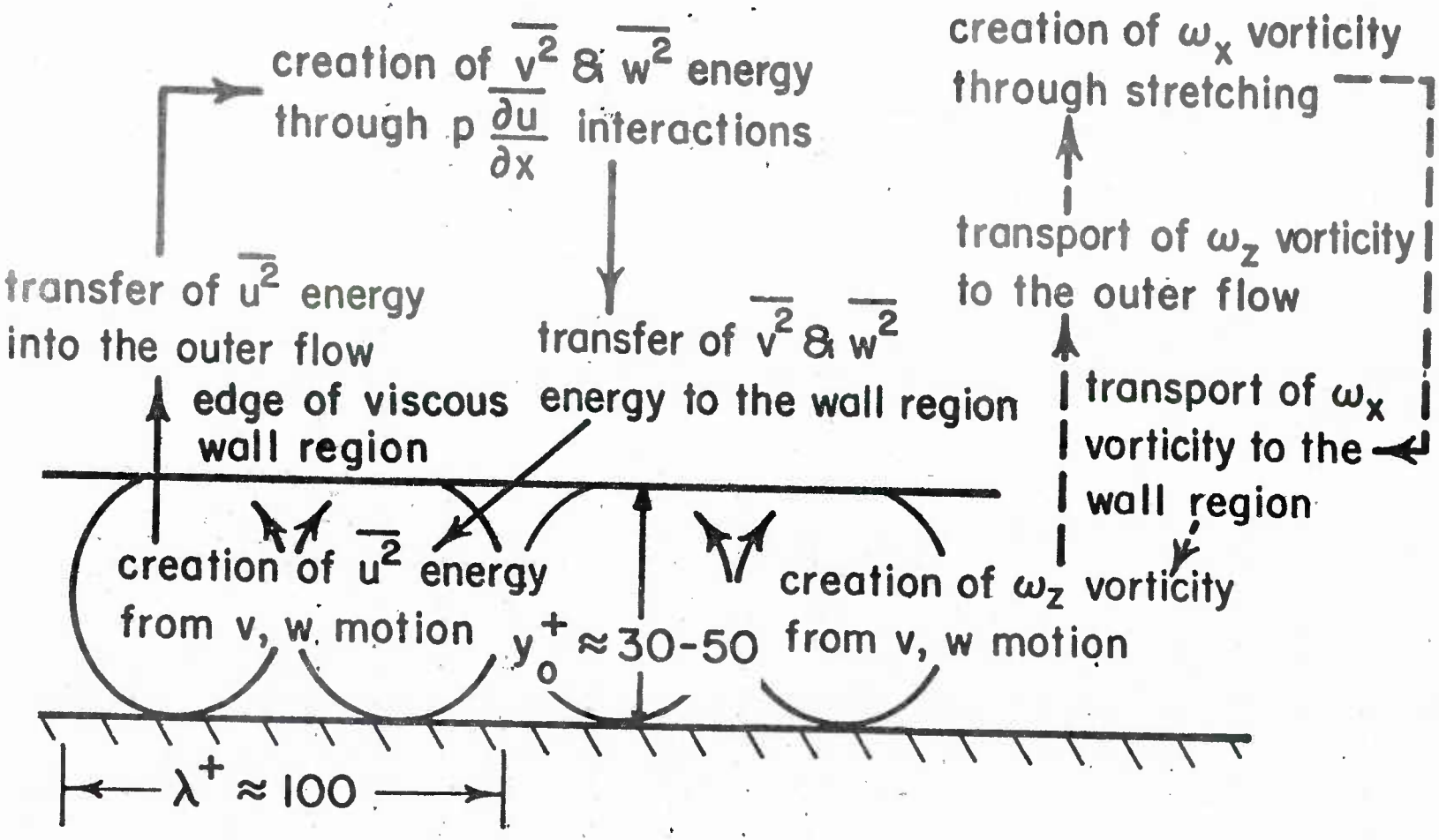

Figure 116 Energy and vorticity transport from interaction of the wall and the outer layer.

is $\overline{w^2}$ energy transferred in this region. It is not clear, however, whether this comes from the outer flow or from the flow in $0 \leq y^+ \leq 35$, where this term is negative. The v–w field that is, thus, set up creates $\overline{u^2}$ energy by producing Reynolds stresses and mean shear. The $\overline{u^2}$ energy produced is transferred to the outer flow by turbulent transport. In this region energy is transferred from the u to the v and w components of the velocity through $\overline{p\frac{\partial u}{\partial x}}$ interactions. As discussed in Chapter 4, these interactions are absent in the viscous wall region due to the homogeneity assumption. The subsequent transfer of $\overline{v^2}$ and possibly $\overline{w^2}$ energy from the outer flow into the wall region closes the cycle of events.

An analogous picture for the interaction of the wall layer with the outer flow can be constructed in terms of vorticity and is also shown in Figure 116. As discussed in Chapter 4 there is no production of streamwise vorticity in the wall region. The v–w motion creates spanwise vorticity $\left(-\frac{dU}{dy}\right)$ which is transported to the outer flow. In this region streamwise vorticity is produced by the stretching of the spanwise vorticity and is subsequently transported into the wall layer. In the wall layer the streamwise vorticity induces a v–w field that produces spanwise vorticity and the cycle of events is completed.

CHAPTER 9

CONCLUSIONS

Conditionally averaged measurements of the flow in the viscous wall region showed that strong spanwise flows at $y^+=40$ are related to strong spanwise flows at the wall that are of opposite sign. At $y^+=20$ the spanwise flows are always in phase with the flows at the wall.

The characteristics of the dominant eddies at the wall were explored by performing numerical computations using a fixed cell in space. Close to the edge of the viscous sublayer ($y^+=15$) the use of a single spatial harmonic ($\lambda^+=100$) was found to be adequate in predicting all the important features of turbulence.

At the edge of the viscous wall layer two spatial harmonics were found to be necessary for the description of the flow field. The longer scale outer flow eddies produce most of the spanwise mixing in the wall region. The smaller scale $\lambda^+=100$ eddies can account for momentum transport, Reynolds stress production and the creation of $\overline{u^2}$ and $\overline{v^2}$ energy in this region.

A mechanism for the generation of smaller scales at the wall appears to be the separation of the flow in the spanwise direction. This convective type of motion creates small scales by the non-linear interaction of larger eddies.

Evidence for a frequency filtering process results from calculations where a wide range of frequencies is used to describe the flow on the plane perpendicular

to the mean flow direction. According to this process the streamwise velocity fluctuations are of much lower frequency content than the fluctuations of the normal and spanwise components of the velocity.

The physical picture of the flow that results from the interaction of the wall with the outer layer is the following: The mean flow energy is primarily produced in the outer layer by the mean pressure gradient and is subsequently transferred into the viscous wall region. All the turbulent kinetic energy is produced by the v–w flow in the wall layer and is concentrated in the streamwise component of the velocity. This energy is convected out of the wall layer into the core region, where part of it is transferred to the motion on the y–z plane. The cycle of events completes with the transport of $\overline{v^2}$ energy into the wall region and the set-up of the v–w field, whereby energy is transferred from the v to the w component of the velocity by means of pressure-velocity gradient interactions.

LIST OF REFERENCES

1. Antonia, R.A. and Atkinson, J.D., J. Fluid Mech., 58, 581 (1973)

2. Antonia, R.A., Danh, H.Q. and Prabhu A., Phys. Fluids, 19, 1680 (1976)

3. Badri Narayanan, M.A. and Marvin, J.G., NASA TM 78477 (1978)

4. Bakewell, H.P. and Lumley, J.L., Phys. Fluids, 10, 1880 (1967)

5. Batchelor, G.K. and Proudman, I., Quart. J. Mech. Appl. Math., 7, 83 (1954)

6. Bull, M.K., J. Fluid Mech., 28, 719 (1967)

7. Blackwelder, R.F. and Eckelmann, H., Structure and Mechanisms of Turbulence I, Lecture Notes in Physics, Vol. 75, p.190, Springer Verlog (1978)

8. _____, J. Fluid Mech., 94, 577 (1979)

9. Blackwelder, R.F. and Haritonidis, J.H., Bull. Amer. Phys. Soc., Vol.25, No.9, p. 1094 (1980)

10. Blackwelder, R.F. and Kaplan, R.E., J. Fluid Mech., 76, 89 (1976)

11. Brodkey, R.S., Nychas, S.G., Taraba, J.L. and Wallace, J.M., Phys. Fluids, 16, 2010 (1973)

12. Chapman, D.R. and Kuhn, G.D., AIAA Paper 81-1024, Proc. AIAA 5th CFD Conference, Palo Alto, California (1981)

13. Clark, J.A., J. Basic Engrg., 90, 455 (1968)

14. Coantic, M., Comptes Rendus, 20, 849 (1967)

15. Comte-Bellot, G., Comptes Rendus, 253, 2846 (1961)

16. _____, Doctoral Thesis, University of Grenoble (1963)

17. _____, Publ. Sci. et Techn. du Ministere de l'Air, No. 419 (1965)

18. Corino, E.R. and Brodkey, R.S., J. Fluid Mech., 37, 1 (1969)

19. Corrsin, S.,Symp. On Naval Hydrodyn., 373 (1956)

20. Davies, P.O.A.L. and Yule, A.J., J. Fluid Mech., 69, 513 (1975)

21. Deardorff, J.W., J. Fluid Mech., 41, 453 (1970)

22. Donohue, G.L., Tiederman, W.G. and Reischman, M.M., J. Fluid Mech., 56, 559 (1972)

23. Dorodnitsyn, A.A. and Meller, N.A., U.S.S.R. Comput. Math. and Math. Phys., 8, 205 (1968)

24. Eckelmann, H., J. Fluid Mech., 65, 439 (1974)

25. Eckelmann, H., Nychas, S.G., Brodkey, R.S. and Wallace, J.M., Phys. Fluids, 20, S225 (1977)

26. Eckelman, L.D., Ph.D. Thesis, University of Illinois, Urbana, Illinois (1971)

27. Elena, M., Fulachier, L. and Dumas, R., AGARD CPP271, 2-1 (1979)

28. Emmerling, R., Max-Planck Institut fur Stromungforschung, Gottingen (1973)

29. Favre, A.J., Gaviglio, J.J. and Dumas, R., J. Fluid Mech., 2, 313 (1957)

30. _____, J. Fluid Mech., 3, 344 (1958)

31. Fortuna, G., Ph.D. Thesis, University of Illinois, Urbana, Illinois (1971)

32. Grant, H.L., J. Fluid Mech., 4, 149 (1958)

33. Gupta, A.K., Ph.D. Thesis, University of Southern California (1970)

34. Gupta, A.K. and Kaplan, R.E., Phys. Fluids, 15, 981 (1972)

35. Gupta, A.K., Laufer, J. and Kaplan, R.E., J. Fluid Mech., 50, 493 (1971)

36. Gurkham, A.A. and Kader, B.A., Paris Heat Transfer Conf., FC 2.5 (1970)

37. Hanratty, T.J., Chorn, L.G. and Hatziavramidis, D.T., Phys. Fluids, 20, S112 (1977)

38. Hatziavramidis, D.T., Ph.D. Thesis, University of Illinois, Urbana, Illinois (1978)

39. Hatziavramidis, D.T. and Hanratty, T.J., J. Fluid Mech., 95, 655 (1979)

40. Head, M.R. and Bandyopadhyay, P., J. Fluid Mech., 107, 297 (1981)

41. Hinze, J.O., Turbulence, 2nd Edition, McGraw-Hill (1975)

42. Hogenes, J.H.A., Ph.D. Thesis, University of Illinois, Urbana, Illinois (1979)

43. Hogenes, J.H.A. and Hanratty, T.J., J. Fluid Mech., 124, 363 (1982)

44. Hussain, A.K.M.F. and Reynolds, W.C., J. Fluids Engr., 97, 568 (1975)

45. Israeli, M., Studies in Appl. Math., 49, 327 (1970)

46. _____, Studies in Appl. Math., 51, 67 (1972)

47. Kaplan, R.E., Turbulence in Liquids (ed. Patterson, G.K. and Zakin, J.L.), University of Missouri-Rolla, 274 (1973)

48. Kaplan, R.E. and Laufer, J., Proc. 12th Int. Cong. Appl. Mech., Stanford, Springer, 236 (1969)

49. Kim, J., Phys. Fluids, 26, 2088 (1983)

50. Kim, J. and Moin, P., NASA TM 78619 (1979)

51. Kim, H.T., Kline, S.J. and Reynolds, W.C., J. Fluid Mech., 50, 133 (1971)

52. Klebanoff, P.S., NACA TN 3178 (1954)

53. Kline, S.J., Sum. of the 1st Res. Spec. Workshop on Coh. Str. in Turb. Bound. Layers, Stanford University (1978)

54. Kline, S.J. and Falco, R.E., Sum. of the 2nd Res. Spec. Workshop on Coh. Str. in Turb. Bound. Layers, Stanford University (1979)

55. Kline, S.J., Reynolds, W.C., Schraub, F.A. and Runstadler, P.W., J. Fluid Mech., 30, 741 (1967)

56. Kline, S.J. and Runstadler, P.W., J. Appl. Mech., 2, 166 (1959)

57. Kreplin, H.P., Max-Planck Institut fur Stromungforschung, Gottingen, Bericht 2/1973 (1973)

58. Kreplin, H.P. and Eckelmann, H., J. Fluid Mech., 95, 305 (1979a)

59. _____, Phys. Fluids, 22, 1233 (1979b)

60. _____, Phys. Fluids, 22, 1210 (1979c)

61. Kovasznay, L.S.G., Kibens, V. and Blackwelder, R.F., J. Fluid Mech., 41, 283 (1970)

62. Kutateladze, S.S., Khabakhpasheva, E.M., Orlov, V.V., Pereplitsa, B.V. and Mikhailova, E.S., Proc. Symp. on Turbulent Shear Flows, Penn. State Univ., 17-13 (1977)

63. Lau, K.K., Ph.D. Thesis, University of Illinois, Urbana, Illinois (1980)

64. Laufer, J., NACA TN 2123 (1950)

65. _____, NACA TN 1174 (1954)

66. _____, Recent Developments in Turbulent Boundary Layer Research, Ist. Naz. Alta Mat., Symp. Math., 9 (1972)

67. Lee, M.K., Ph.D. Thesis, University of Illinois, Urbana, Illinois (1975)

68. Lee, M.K., Eckelmann, L.D. and Hanratty, T.J., J. Fluid Mech., 66, 17 (1974)

69. Leith, C.E., Methods in Comp. Physics, 4, New York: Academic (1965)

70. Leonard, A., Adv. in Geophysics, A18, 237 (1973)

71. Lilly, D.K., Month. Weath. Rev., 93, 11 (1965)

72. _____, Proc. of the IBM Sci. Comp. Symp. on Environ. Sci., IBM Form No. 320-1951, 195 (1967)

73. Lighthill, M.J., Laminar Boundary Layers, p.99 (ed. L. Rosenhead), Oxford: Clarendon Press (1963)

74. Moin, P. and Kim, J., NASA TM 81309 (1981)

75. Moin, P., Reynolds, W.C. and Ferziger, J.H., Rep. No TF-12, Thermosci. Div., Dept. of Mech. Eng., Stanford University (1978)

76. Morrison, W.R.B., Bullock, K.J. and Kronauer, R.E., J. Fluid Mech., 47, 639 (1971)

77. Morrison, W.R.B., and Kronauer, R.E., J. Fluid Mech., 39, 117 (1969)

78. Nikolaides, C., M.S. Thesis, University of Illinois, Urbana, Illinois (1981)

79. Nikolaides, C., Lau, K.K. and Hanratty, T.J., J. Fluid Mech., 130, 91 (1983)

80. Norris, L.H. and Reynolds, W.C., Rep. No. FM-10, Mech. Engrg. Dept., Stanford University (1975)

81. Nychas, S.G., Hershey, H.C. and Brodkey, R.S., J. Fluid Mech., 61, 513 (1973)

82. Offen, G.R. and Kline, S.J., J. Fluid Mech., 62, 223 (1974)

83. _____, J. Fluid Mech., 70, 209 (1975)

84. Peaceman, D.W. and Rachford, H.H., Jr., J. Soc. Ind. Appl. Math., 3, 28 (1955)

85. Praturi, A.K. and Brodkey, R.S., J. Fluid Mech., 89, 251 (1978)

86. Py, B., Int. J. Heat Mass Transfer, 16, 129 (1973)

87. Rao, K.N., Narasimha, R. and Badri Narayanan, M.A., J. Fluid Mech., 48, 339 (1971)

88. Reynolds, O., Phil. Trans., A186, 123 (1895)

89. Reynolds, W.C., Ann. Rev. Fluid Mech., 8, 183 (1976)

90. Rice, S.O., Selected Papers on Noise and Stochastic Processes (ed. Wax, N.), Dover Publ., New York (1954)

91. Roache, P.J., Computational Fluid Dynamics, Hermosa Publishers (1982)

92. Runstadler, P.W., Kline, S.J. and Reynolds, W.C., Rep. No. MD-8, Thermosci. Div., Mech. Eng. Dept., Stanford University (1963)

93. Schildnecht, M., Miller, J.A. and Meier, G., J. Fluid Mech., 90, 67 (1979)

94. Schraub, F.A. and Kline, S.J., Rep. No. MD-12, Thermosci. Div., Mech. Eng. Dept., Stanford University (1965)

95. Schubert, G. and Corcos, G.M., J. Fluid Mech., 29, 113 (1967)

96. Schumann, U., J. Comp. Physics, 18, 376 (1975)

97. Sirkar, K.K., Ph.D. Thesis, University of Illinois, Urbana, Illinois (1969)

98. Sirkar, K.K. and Hanratty, T.J., J. Fluid Mech., 44, 589 (1970a)

99. _____, J. Fluid Mech., 44, 605 (1970b)

100. Smagorinsky, J., Manabe, S. and Holloway, J.L., Mon. Weath. Rev., 93, 727 (1965)

101. Smith , C.R., AFOSR/Lehigh University Workshop (1978)

102. Spalding, D.B., J. Appl. Mech., 28E, 455 (1971)

103. Sreenivasan, K.R., Prabhu, A., Narasimha, R. and Shivaprasad, B.G., Rep. 77 FM13, Dept. of Aeronautical Eng., Indian Inst. of Science (1977)

104. Sternberg, J., J. Fluid Mech., 13, 241 (1962)

105. Swartztrauber, P., SIAM J. Numer. Anal., 11, 1136 (1974)

106. Sweet, R.A., SIAM J. Numer. Anal., 14, 706 (1977)

107. Taylor, G.I., Proc. Roy. Soc., A156, 307 (1936)

108. Tennekes, H. and Lumley, J.L., A First Course in Turbulence, MIT Press (4th Printing) (1977)

109. Theodorsen, T., Mechanism of Turbulence, Proc. of the 2nd Midwestern Conf. on Fluid Mech., Ohio State Univ. (1952)

110. Townsend, A.A., The Structure of Turbulent Shear Flow, Cambridge University Press (1956)

111. _____ ,Boundary Layer Research, IUTAM Symposium (ed H. Gortler), 1 (1957)

112. _____, J. Fluid Mech., 11, 97 (1961)

113. _____, J. Fluid Mech., 41, 13 (1970)

114. Tritton, D.J., J. Fluid Mech., 28, 439 (1967)

115. Tu, B.J. and Willmarth, W.W., Tech. Rep. No. 02920-3-T, Dept. of Aerosp. Eng., University of Michigan, Ann Arbor (1966)

116. Ueda, H. and Hinze, J.O., J. Fluid Mech., 67, 125 (1975)

117. Ueda, H. and Mitzushina, T., Proc. Symp. on Turbulence in Liquids, 41, Univ. of Missouri-Rolla (1977)

118. Van Atta, C.W., Ann. Rev. of Fluid Mech., 6, 75 (1974)

119. Van Driest, E., J. Aero Sci., 23, 1007 (1956)

120. Wallace, J.M. and Brodkey, R.S., Phys. Fluids, 20, 351 (1977)

121. Wallace, J.M., Brodkey, R.S. and Eckelmann, H., J. Fluid Mech., 83, 673 (1977)

122. Wallace, J.M., Eckelmann, H. and Brodkey, R.S., J. Fluid Mech., 54, 39 (1972)

123. Willmarth, W.W., Structure of Turbulence in Boundary Layers, Adv. in Appl. Mech., 15, 159 (1975)

124. Willmarth, W.W. and Lu, S.S., J. Fluid Mech., 55, 65 (1972)

125. Zaric, Z., 4th All Union Heat Mass Transfer Conference (1972)

NOMENCLATURE

Symbol	Description	Units
C	Courant number	
C_{uv}	Reynolds stress correlation coefficient	
c_x	Convection velocity in the x-direction	cm/sec
c_y	Convection velocity in the y-direction	cm/sec
$D(t)$	Dectection function	
D_{ij}	Rate of strain tensor	sec^{-1}
D_{is}	Isotropic dissipation	cm^2/sec^3
D_k	Difference $s_{z_4}(t_k)-s_{z_6}(t_k)$	sec^{-1}
E_1, E_2	Voltage drops across resistors 1 and 2	Volt
E_{u1}, E_{v1}, E_{w1}	Percentage of energy in the u,v and w components of the $\lambda^+ = 100$ eddies	
$f(t)$	Detection function	
F	Number of bursts per unit	

	span per unit time	$cm^{-1}\text{sec}^{-1}$
H	Convective terms in the vorticity transport equation; channel half-height	
$I(t)$	Indicator function	
J_{ijl}	Transport of $\overline{u_i u_j}$	
$\underline{k}$	Wavenumber vector	
k_x, k_z	Wavenumber components in the x and z directions	cm^{-1}
K	Von-Karman constant; SGS eddy -coefficient	
l	Length scale	cm
M	Number of panels in the z-direction	
n	Frequency	sec^{-1}
N	Number of panels in the y-direction; percentage of closed flow	
N_o	Frequency of zero-crossings	sec^{-1}
O	Order of magnitude	
p	Fluctuating pressure	dyn/cm^2

$p(\cdot,\cdot)$	Joint probability density function	
P	Power spectral function; production of turbulent kinetic energy	
$\overline{P}$	Mean pressure	dyn/cm^2
P_{ij}	Production of $\overline{u_i u_j}$	
P_k	Product $s_{z_k}(t_k)\cdot s_{z_\ell}(t_k)$	$\sec^{-2}$
P_x, P_y, P_z	Production of $\omega_x, \omega_y, \omega_z$	
q^2	Instantaneous turbulent kinetic energy	$cm^2/\sec^2$
Q	Defined in equation (4.23)	
$\hat{Q}$	Conditionally averaged	Q
r	Relaxation constant for the iteration on the boundary vorticity	
$\underline{r}$	Physical space vector	
R_{AB}	Correlation coefficient between A and B	
R_l	Turbulent Reynolds number $(\frac{u\cdot l}{\nu})$	
Re	Reynolds number	

Re_θ	Momentum thickness Reynolds number	
s_x	Streawise component of the fluctuating velocity gradient at the wall	sec^{-1}
s_z	Spanwise component of the fluctuating velocity gradient at the wall	sec^{-1}
S	Source term defined in equation (4.24); slope of the $(v')^+$ intensity profile	
$\tilde{S}_d$	Threshold level for $\hat{S}_{d_t}$	
$\hat{S}_{d_{av}}$	Average value of $\hat{S}_{d_t}$	
$\hat{S}_{d_t}$	Detection function	
S_x	Instantaneous streamwise velocity gradient at the wall	sec^{-1}
t	Time	sec
t_o	Time reference point for conditional averaging	sec
T	Period of velocity fluctuations	sec
T_{u1}, T_{v1}, T_{w1}	Periods for the velocity fluctuations of the $\lambda^+ = 100$ eddies	sec
T_{u2}, T_{v2}, T_{w2}	Periods for the velocity fluctuations of the outer flow eddies	sec

T_B	Bursting period	sec
T_S	Period of time for conditional averaging	sec
u	Fluctuating velocity component in the x-direction	cm/sec
u_*	Friction velocity $(\sqrt{\frac{\tau_w}{\rho}})$	cm/sec
u_1, u_2, u_3	Fluctuating velocity components in directions 1, 2 and 3	cm/sec
$\hat{u}_{L1}, \hat{u}_{L2}$	Amplitudes of $u_{L1}(t), u_{L2}(t)$	cm/sec
U	Instantaneous streamwise velocity	cm/sec
U_1, U_2, U_3	Instantaneous velocity components in directions 1, 2 and 3	cm/sec
U_∞	Streamwise velocity at infinity	cm/sec
U_c	Characteristic velocity; centerline velocity	cm/sec
v	Fluctuating velocity component in the y-direction; Kolmogorov velocity scale	cm/sec
$\hat{v}_{L1}, \hat{v}_{L2}$	Amplitudes of $v_{L1}(t), v_{L2}(t)$	cm/sec
V_{1l}, V_{2l}	Linearized voltages	

w	Fluctuating velocity component in the z-direction	cm/sec
$\hat{w}_{L1}, \hat{w}_{L2}$	Amplitudes of $w_{L1}(t), w_{L2}(t)$	cm/sec
x	Coordinate in the mean flow direction; fraction of Reynolds stress contributed by the $\lambda^+ = 100$ eddies at $y_o^+ = 40$	
$\underline{x}$	Position vector	
y	Coordinate in the direction normal to the wall	cm
y_o	Edge of the viscous wall region	cm
z	Coordinate in the spanwise direction	cm
z_o	Length of computational domain in the spanwise direction	cm

Greek Letters

α	Angle between w and the flow direction	
β	Angle between v and the flow direction	
γ	Average value of $I(t)$	
δ	Boundary layer thickness	cm

δ^*	Displacement thickness	cm
δ_{ij}	Kronecker delta	
Δ	Length scale for LES	
Δ_y, Δ_z	Space increments in computations	cm
Δt	Time increment in computations	sec
ϵ	Dissipation rate	cm^2/sec^3
ϵ_{RS}	Resolvable-scale dissipation rate in LES	cm^2/sec^3
ς	Streamwise vorticity	sec^{-1}
η	Kolmogorov length scale	cm
λ	Wavelength	cm
$\lambda_{u1}, \lambda_{v1}, \lambda_{w1}$	Wavelengths for the $\lambda^+ = 100$ eddies	cm
$\lambda_{u2}, \lambda_{v2}, \lambda_{w2}$	Wavelengths for the outer flow eddies	cm
λ_T	Taylor microscale	cm
Λ	Zero-crossing scale	cm
μ_{ij}	Isotropic eddy-viscosity coefficient	

$^{ij}\mu^*$	Inhomogeneous eddy-viscosity coefficient	
ν	Kinematic viscosity	cm^2/sec
ν_T	Eddy viscosity	cm^2/sec
ρ	Density	g/cm^3
Σ	Summation sign	
τ	Time delay for correlation coefficients; Kolmogorov time scale	sec
τ_{ij}	Stress tensor	
ϕ_{ij}	Pressure-strain "redistribution" tensor	
$\phi_{u1},\phi_{u2},\phi_{v1}$ ϕ_{v2},ϕ_{w2}	Phases relative to the phase of $w_{L1}(t)$	
Φ	Power spectra density function	
Ψ	Stream function	
ω	Frequency , $2\pi n$	sec^{-1}
$\omega_x,\omega_y,\omega_z$	Instantaneous vorticity components	sec^{-1}

Subscripts, superscripts, and overhead symbols

$\bar{}$	Space and time average quantity
$'$	Root-mean-squared quantity
$+$	Quantity made dimensionless with wall parameters, u_* and ν
o	Quantity calculated at the upper boundary of the computational domain
w	Quantity calculated at the wall
$\hat{}$	Conditional average

APPENDIX A

COMPUTER PROGRAM

```
      PROGRAM CLADIR(INPUT,OUTPUT,TAPE2,TAPE4,TAPE5,TAPE21,
     $TAPE24,TAPE7,TAPE8,TAPE9,TAPE13,TAPE15,TAPE16,TAPE17,
     $TAPE18,TAPE19,TAPE20,TAPE22,TAPE23,TAPE25,TAPE26,TAPE27,
     $TAPE28,TAPE29,TAPE30,TAPE31,TAPE32,TAPE88)
C
C
C*****************************************************************
C                                                                *
C   THIS PROGRAM CALCULATES THE STREAMLINES PATTERN              *
C      FOR A FIXED CELL OF THE MODEL FLOW IN THE                 *
C                VISCOUS WALL REGION                             *
C                                                                *
C*****************************************************************
C
C   BOUNDARY CONDITIONS AT Y=Y0:
C
C   W=W0(Z,T)    V=V0(Z,T)
C
C   INPUT FILES
C*****************************************************************
C   TAPE2=PSI(NBEF): CONTAINS PSI,ZETA AND UCOM FROM
C                    PREVIOUS RUN
C   TAPE4=UVWINP: CONTAINS THE THREE FLUCTUATING
C                 COMPONENTS OF THE VELOCITY AT THE
C                 UPPER BOUNDARY
C   TAPE5=DAT(NBEF): CONTAINS STATISTICAL STORAGE
C                    ARRAYS FROM THE PREVIOUS RUN
C   TAPE21=PAR(NBEF): CONTAINS THE COORDINATES OF THE
C                     PARTICLES IN THE BEGINNING OF THE
C                     RUN
C   TAPE24=STK(NBEF): CONTAINS THE ENDPOINTS OF THE
C                     PATH-LINES IN THE BEGINNING OF
C                     THE RUN
C*****************************************************************
C   OUTPUT FILES
C*****************************************************************
C   TAPE7=RES(NTOT): CONTAINS INFORMATION RELATED TO THE
C                    EXECUTION OF THIS RUN
C   TAPE8=PSI(NTOT): CONTAINS PSI,ZETA AND UCOM AT THE
```

```
C                       END OF THIS RUN
C     TAPE9=DAT(NTOT): CONTAINS UPDATED STATISTICAL STORAGE
C                       ARRAYS
C     TAPE13=DPL(NTOT): CONTAINS STATISTICAL QUANTITIES
C                        THAT ARE TO BE PLOTTED USING GCS
C     TAPE15=UVE: CONTAINS THE STREAMWISE VELOCITY
C                 COMPONENT AT YPLUS=(J1-1)*DY,(J2-1)*DY,(J3-1)*DY
C     TAPE16=PIE: CONTAINS THE WALL PRESSURE
C     TAPE17=UVG: CONTAINS THE STREAMWISE VELOCITY
C                 GRADIENTS AT THE WALL
C     TAPE18=WVG: CONTAINS THE SPANWISE VELOCITY
C                 GRADIENTS AT THE WALL
C     TAPE19=WVE: CONTAINS THE SPANWISE VELOCITY
C                 COMPONENT AT YPLUS=(J1-1)*DY,(J2-1)*DY,(J3-1)*DY
C     TAPE20=VVE: CONTAINS THE LATERAL VELOCITY
C                 COMPONENT AT YPLUS=(J1-1)*DY,(J2-1)*DY,(J3-1)*DY
C     TAPE22=TRA: CONTAINS THE COORDINATES OF THE
C                 PARTICLE TRAJECTORIES THROUGHOUT
C                 THE RUN
C     TAPE23=PAR(NTOT): CONTAINS THE COORDINATES OF THE
C                        PARTICLES AT THE END OF THIS RUN
C     TAPE25=STR: CONTAINS THE COORDINATES OF THE PATH
C                 LINES THAT START FROM THE INJECTION
C                 POINT
C     TAPE26=STK(NTOT): CONTAINS THE ENDPOINTS OF THE PATH-
C                        LINES AT THE END OF THIS RUN
C     TAPE27=UTA: CONTAINS THE STREAMWISE VELOCITY COMPONENT
C                 AT ZPLUS=(I1-1)*DZ,(I2-1)*DZ,(I3-1)*DZ,(I4-1)*DZ
C     TAPE28=VTA: CONTAINS THE LATERAL VELOCITY COMPONENT
C                 AT ZPLUS=(I1-1)*DZ,(I2-1)*DZ,(I3-1)*DZ,(I4-1)*DZ
C     TAPE29=WTA: CONTAINS THE SPANWISE VELOCITY COMPONENT
C                 AT ZPLUS=(I1-1)*DZ,(I2-1)*DZ,(I3-1)*DZ,(I4-1)*DZ
C     TAPE30=ZET: CONTAINS THE STREAMWISE VORTICITY
C                 AT YPLUS=(J1-1)*DY,(J2-1)*DY,(J3-1)*DY
C     TAPE31=VOR: CONTAINS THE STREAMWISE VORTICITY
C                 AT ZPLUS=(I1-1)*DZ,(I2-1)*DZ,(I3-1)*DZ,(I4-1)*DZ
C     TAPE32=PLO: CONTAINS PSI AND/OR U AND/OR ZETA
C                 AND/OR PIESH DATA WHICH ARE TO BE PLOTTED
C                 USING CONREC FROM NCAR
```

```
C   TAPE88=CON: CONTAINS NUMBER OF ITERATIONS PER TIME
C               STEP AND ACCURACY OF CONVERGENCE
C*****************************************************************
C
      DIMENSION PSI(26,33),PSI1(26,33),ZETA(26,33),ZETA1(26,33)
      DIMENSION ZETA2(26,33),WTAX(26),UTAX(26),PSIUP(26),DVDZ(26)
      DIMENSION WORK(600),WGR(26),UGR(26),DUDZ(26)
      DIMENSION UCOM(26,33),VBEF(26)
      DIMENSION XS(250),YS(250),ZS(250),BDA(33),BDB(33),VTAX(26)
      DIMENSION X1(20),Y1(20),Z1(20),Y(33),Z(26),DWDZ(26)
      DIMENSION UAVE(33),VAVE(33),WAVE(33)
      DIMENSION UINTY0(33),VINTY0(33),WINTY0(33)
      COMMON/AREA1/R,FOVRE,FOVRE1,BETAP,BETAM,GAMAP,GAMAM
      COMMON/AREA2/A,B,C,D,IDIMF
      COMMON/AREA3/M,MP1,MM1,MM2,N,NP1,NM1,NM2
      COMMON/AREA4/WORK,BDA,BDB
      COMMON/AREA5/CHARVEL,CHARLEN,ACON,ALPHA
      COMMON/AREA6/RE,DY,DZ,DT,TDY,TDZ,DY2,DZ2
      COMMON/AREA7/NCTOT,SXBAR,SZBAR,SXSB,SZSB
      COMMON/AREA8/X1,Y1,Z1,MPAR
      COMMON/AREA9/NCB,NINDEX
      COMMON/AREA10/Y,Z,KSTAT,DTE
      COMMON/AREA11/XS,YS,ZS,MSF,NST,KST
      COMMON/AREA12/J1,J2,J3,I1,I2,I3,I4
      COMMON/AREA13/SZBARA,SZBARB,SZSBA,SZSBB
      COMMON/ONE/PSI1
      COMMON/TWO/ZETA1
      COMMON/THREE/ZETA2
      COMMON/FOUR/UAVE,VAVE,WAVE,UINTY0,VINTY0,WINTY0
      PRINT*,"ENTER B,D,NBEF,NCB,NINDEX,ITERM,E,NPLOT,KPLOT,NPLOTZ"
      PRINT*,"KPLOTZ,NPLOTU,KPLOTU,NPLOTP,KPLOTP,NSTAT KSTAT NPRES"
      PRINT*,"KPRES ULPLUS NU,CU1,CU2,CV1,CV2 CW  CW2 ALU1 AL 2,ALV1"
      PRINT*,"ALV2,ALW1,ALW2,NRT2,VELINT,DTE,MPAR,NSB,NST,KST"
      PRINT*,"YINJ,ZINJ,RELCON"
      PRINT*,"J1,J2,J3,I1,I2,I3,I4"
C
C
C   READS INPUT PARAMETERS
C
```

```
C   B: DIMENSIONLESS LENGTH OF THE COMPUTATIONAL
C      DOMAIN IN THE SPANWISE DIRECTION
C   D: DIMENSIONLESS LENGTH OF THE COMPUTATIONAL
C      DOMAIN IN THE LATERAL DIRECTION
C   NBEF: NUMBER OF TIME STEPS IN PREVIOUS RUN
C   NCB: TOTAL NUMBER OF POINTS USED FOR
C        STATISTICAL CALCULATIONS IN PREVIOUS
C        RUN
C   NINDEX: NUMBER OF TIME STEPS IN THIS RUN
C   ITERM: MAXIMUM NUMBER OF ITERATIONS OF ADI
C          SCHEME AT EACH TIME STEP
C   E: ACCURACY OF CONVERGENCE OF ADI SCHEME
C   NPLOT: TIME STEP WHERE PLOTTING OF PSI STARTS
C   KPLOT: TIME STEP INCREMENT FOR PLOTTING OF PSI
C   NPLOTZ: TIME STEP WHERE PLOTTING OF ZETA STARTS
C   KPLOTZ: TIME STEP INCREMENT FOR PLOTTING OF ZETA
C   NPLOTU: TIME STEP WHERE PLOTTING OF U STARTS
C   KPLOTU: TIME STEP INCREMENT FOR PLOTTING OF U
C   NPLOTP: TIME STEP WHERE PLOTTING OF PIESH STARTS
C   KPLOTP: TIME STEP INCREMENT FOR PLOTTING OF PIESH
C   NSTAT: TIME STEP WHERE STATISTICAL
C          CALCULATIONS START
C   KSTAT: TIME STEP INCREMENT FOR STAT.CALCS
C
C *NOTE* THE PRESSURE FIELD HAS TO BE CALCULATED AT LEAST
C        AS OFTEN AS THE STATISTICS ARE CALCULATED
C
C   NPRES: TIME STEP WHERE PRESSURE FIELD
C          CALCULATIONS START
C   KPRES: TIME STEP INCREMENT FOR PRESSURE
C          FIELD CALCULATIONS
C   ULPLUS: MEAN STREAMWISE VELOCITY AT Y=Y0
C           IN WALL PARAMETERS
C   NU: PARAMETER THAT FIXES THE WAVELENGTH OF THE
C       LARGE SCALE U-EDDIES AT Y=Y0
C       IF NU=0   ALU2=FINITE
C       IF NU=1   ALU2=INFINITE
C   CU1,CU2: CONSTANTS THAT ADJUST THE STREAMWISE
C            INTENSITY AT THE UPPER BOUNDARY
```

```
C    CV1,CV2: CONSTANTS THAT ADJUST THE LATERAL
C             INTENSITY AT THE UPPER BOUNDARY
C    CW1,CW2: CONSTANTS THAT ADJUST THE SPANWISE
C             INTENSITY AT THE UPPER BOUNDARY
C    ALU1,ALU2: DIMENSIONLESS WAVELENGTHS OF THE U-FLUCTUATIONS
C    ALV1,ALV2: DIMENSIONLESS WAVELENGTHS OF THE V-FLUCTUATIONS
C    ALW1,ALW2: DIMENSIONLESS WAVELENGTHS OF THE W-FLUCTUATIONS
C    NRT2: CONSTANT FOR THE CHARACTERISTIC VELOCITY
C    VELINT: INTENSITY OF CHARACTERISTIC VELOCITY
C            AT Y0 IN WALL PARAMETERS
C    DTE: EXPERIMENTAL TIME STEP IN WALL PARAMETERS
C    MPAR: NUMBER OF FLUID PARTICLES WHOSE TRAJECTORIES
C          ARE TO BE CALCULATED
C    NSB: THE NUMBER OF PATH LINES FROM THE PREVIOUS RUN
C         IF NSB=0 THEN A NEW STREAKLINE CALCULATION
C         STARTS
C    NST: TIME STEP WHERE STREAKLINE CALCULATIONS START
C    KST: TIME STEP INCREMENT FOR STREAKLINE CALCULATIONS
C    YINJ: Y-COORDINATE OF INJECTION POINT
C    ZINJ: Z-COORDINATE OF INJECTION POINT
C    RELCON: RELAXATION CONSTANT FOR THE ITERATION ON THE
C            ADI-SCHEME
C    J1,J2,J3: Y-COORDINATE FOR THE ROWS OF THE DATA TO BE
C              PRINTED
C    I1,I2,I3,I4: Z-COORDINATE FOR THE COLUMNS OF THE DATA
C                 TO BE PRINTED
C
C
      READ*,B,D,NBEF,NCB,NINDEX,ITERM,E,NPLOT,KPLOT,NPLOTZ,KPLOTZ,
     $NPLOTU,KPLOTU,NPLOTP,KPLOTP,NSTAT,KSTAT,NPRES,KPRES,ULPLUS,NU,CU1,
     $CU2,CV1,CV2,CW1,CW2,ALU1,ALU2,ALV1,ALV2,ALW1,ALW2,NRT2,VELINT,DTE,
     $MPAR,NSB,NST,KST,YINJ,ZINJ,RELCON,J1,J2,J3,I1,I2,I3,I4
C
C    PARAMETERS FOR THE MODEL FLOW
C
      A=0.0
      C=0.0
      M=25
      N=32
```

```
      IDIMF=M+1
      MP1=M+1
      FMP1=FLOAT(MP1)
      MM1=M-1
      NP1=N+1
      NM1=N-1
      NM2=N-2
      MM2=M-2
      CHARVEL=SQRT(2.)**NRT2*VELINT
      CHARLEN=100.
      RE=CHARVEL*CHARLEN
      ACON=CHARVEL/CHARLEN
      ALPHA=1./(0.4*D*CHARVEL)
      UL=ULPLUS/CHARVEL
      WRITE(7,101) M,N,RE
  101 FORMAT(29X,"M=",I3,2X,"N=",I3,5X,"RE=",F7.2,///)
      DZ=(B-A)/FLOAT(M)
      DY=(D-C)/FLOAT(N)
      TDY=2.*DY
      TDZ=2.*DZ
      DY2=DY**2
      DZ2=DZ**2
      R=DZ/DY
      PI=4.*ATAN(1.)
      TPI=2.*PI
      DTV=RE*DZ2/(2.*(1.+R**2))
      DTE=DTE*ACON
      DT=DTE
      DTS=FLOAT(NBEF)*DTE
      BETAM=8.*(1./RE-DZ**2./DT)
      BETAP=8.*(1./RE+DZ**2./DT)
      GAMAP=8.*(R**2./RE+DZ**2./DT)
      GAMAM=8.*(R**2./RE-DZ**2./DT)
      FOVRE=4./RE
      FOVRE1=R**2*FOVRE
      IF(NSB.EQ.0) GO TO 333
C
C     READS COORDINATES OF THE END POINTS OF
C     ALL THE PATH LINES FROM THE PREVIOUS RUN
```

```
C    AND COORDINATES OF THE INJECTION POINT
C
       READ(24)  (XS(K),K=1,NSB)
       READ(24)  (YS(K),K=1,NSB)
       READ(24)  (ZS(K),K=1,NSB)
 333   NSB1=NSB+1
       DO 338 INR=NSB1,250
       XS(INR)=0.
       YS(INR)=YINJ
       ZS(INR)=ZINJ
 338   CONTINUE
C
C    READS PARTICLE COORDINATES IN THE
C    BEGINNING OF THE RUN
C
       READ(21)  (X1(K),K=1,MPAR)
       READ(21)  (Y1(K),K=1,MPAR)
       READ(21)  (Z1(K),K=1,MPAR)
C
C   GENERATES MESH COORDINATES
C
       DO 543 I=1,MP1
       Z(I)=A+FLOAT(I-1)*DZ
 543   CONTINUE
       DO 544 J=1,NP1
       Y(J)=C+FLOAT(J-1)*DY
 544   CONTINUE
C
C    READS TEMPORAL PART OF THE
C    VELOCITY COMPONENTS FROM
C    UVWINP FILE
C
       VPRIN1=1.
       VPRIN2=0.
       IF(NBEF.EQ.0) GO TO 788
       NSKIP=NBEF-1
       DO 671 NB=1,NSKIP
       READ(4,787)
 787   FORMAT()
```

```
  671  CONTINUE
       READ(4,789) WPRIN1,UPRIN1,VPRIN1,WPRIN2,UPRIN2,VPRIN2
       VPRIN1=CV1*VPRIN1
       VPRIN2=CV2*VPRIN2
  788  READ(4,789) WVEL1,UVEL1,VVEL1,WVEL2,UVEL2,VVEL2
       UVEL1=CU1*UVEL1
       UVEL2=CU2*UVEL2
       VVEL1=CV1*VVEL1
       VVEL2=CV2*VVEL2
       WVEL1=CW1*WVEL1
       WVEL2=CW2*WVEL2
  789  FORMAT(6E14.7)
C
C    READS STREAM FUNCTION,VORTICITY AND
C    STREAMWISE VELOCITY FROM TIME STEP N.
C
       READ(2) PSI,ZETA,UCOM
C
C   ZEROES ALL THE COUNTERS
C
C    THE VALUE OF IFLAG DENOTES WHETHER
C    THE SENSE-SWITCH 1 HAS BEEN TURNED
C    ON BY THE OPERATOR
C        IF IFLAG=2   SWITCH IS OFF
C        IF IFLAG=1   SWITCH IS ON
C
     .  IFLAG=2
       MSF=NSB
       IFL=0
       NC=0
       ITERS=0
       MPL=0
       MPLU=0
       MPLZ=0
       MPLP=0
       MPRES=0
       NCOUNT=0
C
C    NEW TIME STEP
```

```
C
  33  NCOUNT=NCOUNT+1
      NTOT=NBEF+NCOUNT
      DTS=DTS+DT
C
C   CALCULATION OF V AT THE UPPER
C   BOUNDARY FOR TIME STEP N.
C
      DO 11 I=1,MP1
      VBEF(I)=VPRIN1*COS(TPI*Z(I)/ALV1)+VPRIN2*COS(TPI*Z(I)/ALV2)
  11  CONTINUE
C
C   CALCULATION OF U,PSI,W AND DV/DZ
C   AT THE UPPER BOUNDARY FOR TIME STEP N+1.
C
      DO 10 I=1,MP1
      WTAX(I)=WVEL1*SIN(TPI*Z(I)/ALW1)+WVEL2*SIN(TPI*Z(I)/ALW2)
      UTAX(I)=UL+UVEL1*COS(TPI*Z(I)/ALU1)+UVEL2*(NU+(1-NU)*
     $COS(TPI*Z(I)/ALU2))
      PSIUP(I)=-(VVEL1*ALV1*SIN(TPI*Z(I)/ALV1)+VVEL2*ALV2*
     $SIN(TPI*Z(I)/ALV2))/TPI
      DVDZ(I)=-TPI*(VVEL1*SIN(TPI*Z(I)/ALV1)/ALV1+VVEL2*
     $SIN(TPI*Z(I)/ALV2)/ALV2)
  10  CONTINUE
C
C   GUESS FOR STREAM FUNCTION AND BOUNDARY VORTICITY
C   IN THE FIRST ITERATION OF THE CURRENT TIME STEP.
C
      DO 922 I=1,MP1
      DO 923 J=1,NP1
      PSI1(I,J)=PSI(I,J)
 923  CONTINUE
 922  CONTINUE
      DO 701 J=2,N
      ZETA1(1,J)=ZETA(1,J)
      ZETA1(MP1,J)=ZETA(MP1,J)
 701  CONTINUE
      DO 702 I=2,M
      ZETA2(I,1)=ZETA(I,1)
```

```
      ZETA2(I,NP1)=ZETA(I,NP1)
  702 CONTINUE
      ITER=0
C
C   NEW ITERATION AT THE CURRENT TIME STEP
C
   34 ITER=ITER+1
C
C   ADI-SOLVER FOR THE V-W VELOCITY FIELD
C
      CALL VWSOL2(PSI,PSI1,ZETA,ZETA1,ZETA2,IER)
      IF(IER.EQ.129) GO TO 136
C
C   POISSON-SOLVER FOR THE STREAM FUNCTION
C
      DO 441 I=2,M
      DO 442 J=1,NP1
      ZETA1(I,J)=ZETA2(I,J)
  442 CONTINUE
  441 CONTINUE
      DO 801 I=2,M
      ZETA2(I,1)=0.
      ZETA2(I,NP1)=PSIUP(I)
  801 CONTINUE
      DO 802 J=1,NP1
      ZETA2(1,J)=0.
      ZETA2(MP1,J)=0.
  802 CONTINUE
      CALL HWSCRT(A,B,M,1,BDA,BDB,C,D,N,1,BDC,BDD,0.,ZETA2,IDIMF,
     1PERTRB,IERROR,WORK)
      IF(IERROR.GT.0) GO TO 55
      IF(ITER.EQ.1) GO TO 131
      AMAXI=0.
      DO 401 I=1,MP1
      DO 402 J=1,NP1
      DEV=ABS(ZETA2(I,J)-PSI1(I,J))
      AMAXI=AMAX1(AMAXI,DEV)
  402 CONTINUE
  401 CONTINUE
```

```
      IF(AMAXI.LE.E) GO TO 132
      IF(ITER.EQ.ITERM) GO TO 135
C
C   STORES ESTIMATE OF STREAM FUNCTION AND UPDATES
C   BOUNDARY VORTICITY FOR THE NEXT ITERATION
C
 131  DO 501 I=1,MP1
      DO 502 J=1,NP1
      PSI1(I,J)=ZETA2(I,J)
 502  CONTINUE
 501  CONTINUE
      DO 901 J=2,N
      ZETA1(1,J)=0.
      ZETA1(MP1,J)=0.
 901  CONTINUE
      DO 902 I=2,M
      ZETA2(I,1)=RELCON*ZETA1(I,1)+(1.-RELCON)*(8.*PSI1(I,2)-PSI1(I,3))
     $/(2.*DY2)
      ZETA2(I,NP1)=RELCON*ZETA1(I,NP1)+(1.-RELCON)*(2.*((PSI1(I,N)-
     $PSI1(I,NP1))/DY2+WTAX(I)/DY)-DVDZ(I))
 902  CONTINUE
       GO TO 34
 132  ITERS=ITERS+ITER
      WRITE(88) ITER,AMAXI
C
C   ADI-SOLVER FOR THE U-VELOCITY FIELD
C
      CALL USOL3(PSI,ZETA2,UCOM,UTAX,IER)
      IF(IER.EQ.129) GO TO 137
C
C   UPDATES THE VORTICITY FOR THE NEXT TIME STEP
C
      DO 473 I=2,M
      DO 474 J=2,N
      ZETA(I,J)=ZETA1(I,J)
 474  CONTINUE
 473  CONTINUE
      DO 475 J=1,NP1
      ZETA(1,J)=0.
```

```
      ZETA(MP1,J)=0.
  475 CONTINUE
      DO 476 I=2,M
      ZETA(I,1)=(8.*ZETA2(I,2)-ZETA2(I,3))/(2.*DY2)
      ZETA(I,NP1)=2.*((ZETA2(I,N)-ZETA2(I,NP1))/DY2+WTAX(I)/DY)-DVDZ(I)
  476 CONTINUE
C
C   UPDATES THE STREAM FUNCTION FOR THE
C   NEXT TIME STEP
C
      DO 471 I=1,MP1
      DO 472 J=1,NP1
      PSI(I,J)=ZETA2(I,J)
  472 CONTINUE
  471 CONTINUE
C
C   CALCULATES THE PRESSURE FIELD IF NCOUNT=NPRES
C
      IF(NCOUNT.EQ.NPRES) GO TO 3077
      GO TO 3078
 3077 NPRES=NCOUNT+KPRES
C
C   CALCULATION OF V AND DW/DZ AT
C   THE UPPER BOUNDARY FOR TIME STEP N+1.
C
      DO 294 I=1,MP1
      VTAX(I)=VVEL1*COS(TPI*Z(I)/ALV1)+VVEL2*COS(TPI*Z(I)/ALV2)
      DWDZ(I)=TPI*(WVEL1*COS(TPI*Z(I)/ALW1)/ALW1+WVEL2*
     $COS(TPI*Z(I)/ALW2)/ALW2)
  294 CONTINUE
      CALL PRES(PSI,ZETA,VTAX,WTAX,DVDZ,DWDZ,
     $VBEF,IERROR,DEVMAX)
      IF(IERROR.GT.0) GO TO 56
      MPRES=MPRES+1
      WRITE(88) DEVMAX
C
C   PRINTS FILE PIE
C
      WRITE(16) (PSI1(L,1),L=1,MP1)
```

```
C
C    CALCULATES THE STREAMWISE VELOCITY GRADIENT
C    AT THE WALL AND PRINTS FILES UVE,UVG,WVG,
C    UTA,ZET AND VOR
C
 3078 DO 675 I=1,MP1
      UGR(I)=(4.*UCOM(I,2)-UCOM(I,3))/TDY
      WGR(I)=ZETA(I,1)
 675  CONTINUE
      WRITE(15)  (UCOM(L,J1),L=1,MP1)
      WRITE(15)  (UCOM(L,J2),L=1,MP1)
      WRITE(15)  (UCOM(L,J3),L=1,MP1)
      WRITE(17)  (UGR(L),L=1,MP1)
      WRITE(18)  (WGR(L),L=1,MP1)
      WRITE(27)  (UCOM(I1,L),L=1,NP1)
      WRITE(27)  (UCOM(I2,L),L=1,NP1)
      WRITE(27)  (UCOM(I3,L),L=1,NP1)
      WRITE(27)  (UCOM(I4,L),L=1,NP1)
      WRITE(30)  (ZETA(L,J1),L=1,MP1)
      WRITE(30)  (ZETA(L,J2),L=1,MP1)
      WRITE(30)  (ZETA(L,J3),L=1,MP1)
      WRITE(31)  (ZETA(I1,L),L=1,NP1)
      WRITE(31)  (ZETA(I2,L),L=1,NP1)
      WRITE(31)  (ZETA(I3,L),L=1,NP1)
      WRITE(31)  (ZETA(I4,L),L=1,NP1)
C
C    STORES PSI IF NCOUNT=NPLOT
C
      IF(NCOUNT.EQ.NPLOT) GO TO 998
      GO TO 999
 998  NPLOT=NCOUNT+KPLOT
      WRITE(32) PSI
      MPL=MPL+1
C
C    STORES U IF NCOUNT=NPLOTU
C
 999  IF(NCOUNT.EQ.NPLOTU) GO TO 8881
      GO TO 8882
 8881 NPLOTU=NCOUNT+KPLOTU
```

```
      WRITE(32) UCOM
      MPLU=MPLU+1
C
C   STORES ZETA IF NCOUNT=NPLOTZ
C
 8882 IF(NCOUNT.EQ.NPLOTZ) GO TO 8883
      GO TO 8884
 8883 NPLOTZ=NCOUNT+KPLOTZ
      WRITE(32) ZETA
      MPLZ=MPLZ+1
C
C   STORES PIESH IF MPRES=NPLOTP
C
 8884 IF(MPRES.EQ.NPLOTP) GO TO 8885
      GO TO 8886
 8885 NPLOTP=MPRES+KPLOTP
      WRITE(32) PSI1
      MPLP=MPLP+1
C
C   CALCULATES STATISTICS IF NCOUNT=NSTAT
C
 8886 IF(NCOUNT.EQ.NSTAT) GO TO 1110
      GO TO 2077
 1110 NSTAT=NCOUNT+KSTAT
      NC=NC+1
C
C   CALCULATION OF DU/DZ AT THE UPPER
C   BOUNDARY FOR TIME STEP N+1.
C
      DO 297 I=1,MP1
      DUDZ(I)=-TPI*(UVEL1*SIN(TPI*Z(I)/ALU1)/ALU1+UVEL2*(1-NU)*
     $SIN(TPI*Z(I)/ALU2)/ALU2)
 297  CONTINUE
      CALL SSWTCH(1,IFLAG)
      CALL STATIS(PSI,ZETA,UCOM,DUDZ,VTAX,DVDZ,WTAX,DWDZ,
     $UGR,WGR,NC,NSTAT,IFLAG)
      IF(IFLAG.EQ.1) GO TO 134
 2077 IF(NCOUNT.EQ.NINDEX) GO TO 134
      VPRIN1=VVEL1
```

```
      VPRIN2=VVEL2
      READ(4,789) WVEL1,UVEL1,VVEL1,WVEL2,UVEL2,VVEL2
      UVEL1=CU1*UVEL1
      UVEL2=CU2*UVEL2
      VVEL1=CV1*VVEL1
      VVEL2=CV2*VVEL2
      WVEL1=CW1*WVEL1
      WVEL2=CW2*WVEL2
      GO TO 33
C
C   PRINTS FILE RES
C
 134  WRITE(7,533) NCOUNT,NTOT
 533  FORMAT(//////,2X,"NUMBER OF TIME STEPS IN THIS RUN=",I5,
     $//,2X,"TOTAL NUMBER OF TIME STEPS=",I5)
      DT=DT/ACON
      DTS=DTS/ACON
      WRITE(7,597) ITERS,DT,DTS
 597  FORMAT(//,2X,"TOTAL # OF ITERATIONS=",I5,//,2X,"TIME STEP=",F12.5,
     $2X,"TOTAL TIME ELAPSED=",F12.5//)
      WRITE(7,849) MPL,MPLU,MPLZ,MPLP
 849  FORMAT(///,2X,"NUMBER OF PSI PLOTS=",I3,//,2X,
     $"NUMBER OF  U  PLOTS=",I3,//,2X,"NUMBER OF ZETA PLOTS=",I3,//,2X,
     $"NUMBER OF PIESH PLOTS=",I3,///)
C
C   PRINTS FILE PSI
C
      WRITE(8) PSI,ZETA,UCOM
      IF(NC.EQ.0) GO TO 17
C
C   PRINTS FILE STK
C
      WRITE(26) (XS(K),K=1,MSF)
      WRITE(26) (YS(K),K=1,MSF)
      WRITE(26) (ZS(K),K=1,MSF)
C
C   PRINTS FILE PAR
C
      WRITE(23) (X1(K),K=1,MPAR)
```

```
      WRITE(23)  (Y1(K),K=1,MPAR)
      WRITE(23)  (Z1(K),K=1,MPAR)
      IF(IFL.EQ.1) GO TO 17
      WRITE(7,443) NC,NCTOT,SXBAR,SZBAR,SZBARA,SZBARB,SXSB,
     $SZSB,SZSBA,SZSBB,UINTY0(33),VINTY0(33),WINTY0(33)
  443 FORMAT(/////,5X,"NUMBER OF POINTS FOR STAT.CALC. IN THIS RUN=",I5,
     $//,5X,"TOTAL NUMBER OF POINTS FOR STAT.CALC.=",I5,///,5X,
     $"STREAMWISE VELOCITY GRADIENT AT THE WALL=",E12.5,//,
     $5X,"SPANWISE VELOCITY GRADIENT AT THE WALL=",3E12.5,//,5X,
     &"STREAMWISE WALL INTENSITY=",E12.5,//,5X,
     &"SPANWISE WALL INTENSITY=",3E12.5,//,5X,
     $"STREAMWISE INTENSITY AT Y0=",E12.5,//,5X,
     $"LATERAL INTENSITY AT Y0=",E12.5,//,5X,
     $"SPANWISE INTENSITY AT Y0=",E12.5,///)
      WRITE(7,445)
  445 FORMAT(5X,"AVERAGE VELOCITY DISTRIBUTIONS",//,5X,
     $"STREAMWISE VELOCITY",//)
      WRITE(7,446)  (UAVE(L),L=1,NP1)
      WRITE(7,448)
  448 FORMAT(//,5X,"LATERAL VELOCITY",//)
      WRITE(7,446)  (VAVE(L),L=1,NP1)
  446 FORMAT(8E12.5)
      WRITE(7,447)
  447 FORMAT(//,5X,"SPANWISE VELOCITY",//)
      WRITE(7,446)  (WAVE(L),L=1,NP1)
      WRITE(7,670)
  670 FORMAT(///,5X,"VELOCITY R.M.S. VALUES IN WALL PARAMETERS",
     $//,5X,"STREAMWISE R.M.S. VALUES",//)
      WRITE(7,446)  (UINTY0(L),L=1,NP1)
      WRITE(7,672)
  672 FORMAT(//,5X,"LATERAL R.M.S. VALUES",//)
      WRITE(7,446)  (VINTY0(L),L=1,NP1)
      WRITE(7,673)
  673 FORMAT(//,5X,"SPANWISE R.M.S. VALUES",//)
      WRITE(7,446)  (WINTY0(L),L=1,NP1)
      GO TO 17
C
C   ERROR MESSAGES
C
```

```
  135  WRITE(7,598) NCOUNT
       ITERS=ITERS+ITER
       IFL=1
  598  FORMAT(2X,"ADI SCHEME DID NOT CONVERGE AT NCOUNT=",I5,///)
       GO TO 134
   55  WRITE(7,888) NCOUNT,ITER,IERROR
  888  FORMAT(5X,"ERROR DETECTED WHEN CALLING HWSCRT FOR THE SOLUTION",
      $" OF THE PSI FIELD",//,5X,"NCOUNT=",I3,2X,"ITER=",I2,2X,"IERROR=",
      $I5,///)
       ITERS=ITERS+ITER
       IFL=1
       GO TO 134
  136  WRITE(7,997) NCOUNT,ITER,IER
  997  FORMAT(5X,"ERROR DETECTED WHEN CALLING LEQT1B FOR THE V-W FIELD",
      $" ADI-SOLVER",//,5X,"NCOUNT=",I3,2X,"ITER=",I2,2X,"IER=",I5,///)
       ITERS=ITERS+ITER
       IFL=1
       GO TO 134
  137  WRITE(7,996) NCOUNT,IER
       IFL=1
  996  FORMAT(5X,"ERROR DETECTED WHEN CALLING LEQT1B FOR THE U-FIELD",
      $" ADI-SOLVER",//,5X,"NCOUNT=",I3,2X,"IER=",I5,///)
       GO TO 134
   56  WRITE(7,887) NCOUNT,IERROR
       IFL=1
  887  FORMAT(5X,"ERROR DETECTED WHEN CALLING HWSCRT FOR THE SOLUTION",
      $" OF THE PIESH FIELD",//,5X,"NCOUNT=",I3,2X,"IERROR=",I5,///)
       GO TO 134
   17  STOP
       END
       SUBROUTINE VWSOL2(PSI,PSI1,ZETA,ZETA1,ZETA2,IER)
C
C
C*************************************************************
C                                                            *
C   THIS SUBROUTINE CALCULATES THE VORTICITY                 *
C   FIELD USING A CONSERVATIVE FINITE-DIFFERENCE             *
C   SCHEME AND  * LEQT1B *  FOR THE INVERSION                *
C   OF THE RESULTING TRIDIAGONAL MATRICES                    *
```

```
C   BOUNDARY CONDITION AT Y=Y0  ZETA=ZETA0(Z,T)                    *
C                                                                  *
C******************************************************************
C
C
      DIMENSION PSI(26,33),PSI1(26,33),ZETA(26,33)
      DIMENSION ZETA1(26,33),ZETA2(26,33),P(31,3),Q(31),XL(80)
      COMMON/AREA1/R,FOVRE,FOVRE1,BETAP,BETAM,GAMAP,GAMAM
      COMMON/AREA3/M,MP1,MM1,MM2,N,NP1,NM1,NM2
      COMMON/SCRA/P,Q,XL
      DO 40 J=2,N
      DO 30 K=1,MM1
      PSIM1DJ=(PSI(K,J+1)-PSI(K,J-1)+PSI1(K,J+1)-PSI1(K,J-1))*0.5
      PSIP1DJ=(PSI(K+2,J+1)-PSI(K+2,J-1)+PSI1(K+2,J+1)-
     $PSI1(K+2,J-1))*0.5
      PSIM1DI=(PSI(K+2,J-1)-PSI(K,J-1)+PSI1(K+2,J-1)-PSI1(K,J-1))*0.5
      PSIP1DI=(PSI(K+2,J+1)-PSI(K,J+1)+PSI1(K+2,J+1)-PSI1(K,J+1))*0.5
      P(K,1)=R*PSIM1DJ+FOVRE
      P(K,3)=-R*PSIP1DJ+FOVRE
      P(K,2)=-BETAP
      Q(K)=(R*PSIM1DI-FOVRE1)*ZETA(K+1,J-1)+GAMAM*ZETA(K+1,J)-
     $(R*PSIP1DI+FOVRE1)*ZETA(K+1,J+1)
30    CONTINUE
      Q(1)=Q(1)-P(1,1)*ZETA1(1,J)
      Q(MM1)=Q(MM1)-P(MM1,3)*ZETA1(MP1,J)
      P(1,1)=0.
      P(MM1,3)=0.
      CALL LEQT1B(P,MM1,1,1,31,Q,1,31,0,XL,IER)
      IF(IER.EQ.129) GO TO 136
      DO 50 I=2,M
      IA=I-1
      ZETA1(I,J)=Q(IA)
50    CONTINUE
40    CONTINUE
      DO 60 I=2,M
      DO 70 K=1,NM1
      PSIM1DI=(PSI(I+1,K)-PSI(I-1,K)+PSI1(I+1,K)-PSI1(I-1,K))*0.5
      PSIP1DI=(PSI(I+1,K+2)-PSI(I-1,K+2)+PSI1(I+1,K+2)-
     $PSI1(I-1,K+2))*0.5
```

```
      PSIM1DJ=(PSI(I-1,K+2)-PSI(I-1,K)+PSI1(I-1,K+2)-PSI1(I-1,K))*0.5
      PSIP1DJ=(PSI(I+1,K+2)-PSI(I+1,K)+PSI1(I+1,K+2)-PSI1(I+1,K))*0.5
      P(K,1)=-R*PSIM1DI+FOVRE1
      P(K,3)=R*PSIP1DI+FOVRE1
      P(K,2)=-GAMAP
      Q(K)=-(R*PSIM1DJ+FOVRE)*ZETA1(I-1,K+1)+BETAM*ZETA1(I,K+1)+
     $(R*PSIP1DJ-FOVRE)*ZETA1(I+1,K+1)
   70 CONTINUE
      Q(1)=Q(1)-P(1,1)*ZETA2(I,1)
      Q(NM1)=Q(NM1)-P(NM1,3)*ZETA2(I,NP1)
      P(1,1)=0.
      P(NM1,3)=0.
      CALL LEQT1B(P,NM1,1,1,31,Q,1,31,0,XL,IER)
      IF(IER.EQ.129) GO TO 136
      DO 80 J=2,N
      JA=J-1
      ZETA2(I,J)=Q(JA)
   80 CONTINUE
   60 CONTINUE
  136 RETURN
      END
      SUBROUTINE USOL3(PSI,ZETA2,UCOM,UTAX,IER)
C
C   THIS SUBROUTINE CALCULATES THE STREAMWISE
C   VELOCITY FIELD USING A CONSERVATIVE
C   FINITE-DIFFERENCE SCHEME AND  * LEQT1B *
C   FOR THE INVERSION OF THE RESULTING
C   TRIDIAGONAL MATRICES
C   BOUNDARY CONDITION AT Y=Y0 IS   U=U0
C
      DIMENSION PSI(26,33),ZETA2(26,33),UCOM(26,33),UHAL(26,33)
      DIMENSION P(31,3),Q(31),XL(80),UTAX(26)
      COMMON/AREA1/R,FOVRE,FOVRE1,BETAP,BETAM,GAMAP,GAMAM
      COMMON/AREA3/M,MP1,MM1,MM2,N,NP1,NM1,NM2
      COMMON/AREA5/CHARVEL,CHARLEN,ACON,ALPHA
      COMMON/AREA6/RE,DY,DZ,DT,TDY,TDZ,DY2,DZ2
      COMMON/SCRA/P,Q,XL
      COMMON/ONE/UHAL
      DO 161 J=2,N
```

```
      DO 162 K=1,MM1
      PSIM1DJ=(PSI(K,J+1)-PSI(K,J-1)+ZETA2(K,J+1)-
     $ZETA2(K,J-1))*0.5
      PSIP1DJ=(PSI(K+2,J+1)-PSI(K+2,J-1)+ZETA2(K+2,J+1)-
     $ZETA2(K+2,J-1))*0.5
      PSIM1DI=PSI(K+2,J-1)-PSI(K,J-1)
      PSIP1DI=PSI(K+2,J+1)-PSI(K,J+1)
      P(K,1)=R*PSIM1DJ+FOVRE
      P(K,3)=-R*PSIP1DJ+FOVRE
      P(K,2)=-BETAP
      Q(K)=(R*PSIM1DI-FOVRE1)*UCOM(K+1,J-1)+GAMAM*UCOM(K+1,J)-
     $(R*PSIP1DI+FOVRE1)*UCOM(K+1,J+1)
162   CONTINUE
      P(1,2)=P(1,2)+4.*P(1,1)/3.
      P(1,3)=P(1,3)-P(1,1)/3.
      P(MM1,1)=P(MM1,1)-P(MM1,3)/3.
      P(MM1,2)=P(MM1,2)+4.*P(MM1,3)/3.
      P(1,1)=0.
      P(MM1,3)=0.
      CALL LEQT1B(P,MM1,1,1,31,Q,1,31,0,XL,IER)
      IF(IER.EQ.129) GO TO 136
      DO 163 I=2,M
      IA=I-1
      UHAL(I,J)=Q(IA)
163   CONTINUE
161   CONTINUE
      DO 194 J=2,N
      UHAL(1,J)=(4.*UHAL(2,J)-UHAL(3,J))/3.
      UHAL(MP1,J)=(4.*UHAL(M,J)-UHAL(MM1,J))/3.
194   CONTINUE
      DO 164 I=2,M
      DO 165 K=1,NM1
      PSIM1DI=ZETA2(I+1,K)-ZETA2(I-1,K)
      PSIP1DI=ZETA2(I+1,K+2)-ZETA2(I-1,K+2)
      PSIM1DJ=(PSI(I-1,K+2)-PSI(I-1,K)+ZETA2(I-1,K+2)-
     $ZETA2(I-1,K))*0.5
      PSIP1DJ=(PSI(I+1,K+2)-PSI(I+1,K)+ZETA2(I+1,K+2)-
     $ZETA2(I+1,K))*0.5
      P(K,1)=-R*PSIM1DI+FOVRE1
```

```
      P(K,3)=R*PSIP1DI+FOVRE1
      P(K,2)=-GAMAP
      Q(K)=-(R*PSIM1DJ+FOVRE)*UHAL(I-1,K+1)+BETAM*UHAL(I,K+1)+
     $(R*PSIP1DJ-FOVRE)*UHAL(I+1,K+1)
  165 CONTINUE
      Q(1)=Q(1)-P(1,1)*UCOM(I,1)
      Q(NM1)=Q(NM1)-P(NM1,3)*UTAX(I)
      P(1,1)=0.
      P(NM1,3)=0.
      CALL LEQT1B(P,NM1,1,1,31,Q,1,31,0,XL,IER)
      IF(IER.EQ.129) GO TO 136
      DO 166 J=2,N
      JA=J-1
      UCOM(I,J)=Q(JA)
  166 CONTINUE
  164 CONTINUE
      DO 718 I=2,M
      UCOM(I,NP1)=UTAX(I)
  718 CONTINUE
      DO 719 J=1,NP1
      UCOM(1,J)=(4.*UCOM(2,J)-UCOM(3,J))/3.
      UCOM(MP1,J)=(4.*UCOM(M,J)-UCOM(MM1,J))/3.
  719 CONTINUE
  136 RETURN
      END
      SUBROUTINE PRES(PSI,ZETA,VTAX,WTAX,DVDZ,DWDZ,
     $VBEF,IERROR,DEVMAX)
C
C*****************************************************************
C                                                                *
C   THIS SUBROUTINE CALCULATES THE PRESSURE FIELD                *
C        FOR A FIXED CELL OF THE MODEL FLOW                      *
C          IN THE VISCOUS WALL REGION                            *
C                                                                *
C*****************************************************************
C
C
      DIMENSION PSI(26,33),ZETA(26,33),VTAX(26),WTAX(26),Y(33)
      DIMENSION PIESH(26,33),BDA(33),BDB(33),BDC(26),BDD(26),VBEF(26)
```

```
      DIMENSION WORK(600),RHS(26,33),DVDZ(26),DWDZ(26),Z(26)
      COMMON/AREA2/A,B,C,D,IDIMF
      COMMON/AREA3/M,MP1,MM1,MM2,N,NP1,NM1,NM2
      COMMON/AREA4/WORK,BDA,BDB
      COMMON/AREA6/RE,DY,DZ,DT,TDY,TDZ,DY2,DZ2
      COMMON/AREA10/Y,Z,KSTAT,DTE
      COMMON/ONE/PIESH
      COMMON/TWO/RHS
      TWDELZ=2./DZ
      TWDELY=2./DY
C
C   BOUNDARY CONDITIONS FOR THE
C   PRESSURE FIELD
C
      DO 10 I=2,M
      BDC(I)=(-1./RE)*(ZETA(I+1,1)-ZETA(I-1,1))/TDZ
   10 CONTINUE
      BDC(1)=(-1./RE)*(-3.*ZETA(1,1)+4.*ZETA(2,1)-ZETA(3,1))/TDZ
      BDC(MP1)=(-1./RE)*(ZETA(MM1,1)-4.*ZETA(M,1)+3.*ZETA(MP1,1))/TDZ
      DO 20 J=1,NP1
      BDA(J)=0.
      BDB(J)=0.
   20 CONTINUE
      DO 30 I=2,M
      BDD(I)=(-1./RE)*(ZETA(I+1,NP1)-ZETA(I-1,NP1))/TDZ-(VTAX(I)-
     $VBEF(I))/DTE-(-VTAX(I)*DWDZ(I)+WTAX(I)*DVDZ(I))
   30 CONTINUE
      BDD(1)=(-1./RE)*(-3.*ZETA(1,NP1)+4.*ZETA(2,NP1)-ZETA(3,NP1))/TDZ-
     $(VTAX(1)-VBEF(1))/DTE-(-VTAX(1)*DWDZ(1)+WTAX(1)*DVDZ(1))
      BDD(MP1)=(-1./RE)*(ZETA(MM1,NP1)-4.*ZETA(M,NP1)+3.*ZETA(MP1,NP1))
     $/TDZ-(VTAX(MP1)-VBEF(MP1))/DTE-(-VTAX(MP1)*DWDZ(MP1)+WTAX(MP1)*
     $DVDZ(MP1))
C
C   CALCULATION OF THE SOURCE TERM
C   IN THE POISSON EQUATION FOR
C   THE PRESSURE FIELD
C
      DO 40 I=2,M
      DO 50 J=2,N
```

```
      PIESH(I,J)=2.*((PSI(I,J+1)-2.*PSI(I,J)+PSI(I,J-1))*
     $(PSI(I+1,J)-2.*PSI(I,J)+PSI(I-1,J))/(DY2*DZ2)-((PSI(I+1,
     $J+1)-PSI(I+1,J-1)-PSI(I-1,J+1)+PSI(I-1,J-1))/(TDY*TDZ))**2)
   50 CONTINUE
   40 CONTINUE
      DO 60 I=1,MP1
      PIESH(I,1)=0.
   60 CONTINUE
      DO 70 J=2,N
      PIESH(1,J)=-2.*((-3.*(PSI(1,J+1)-PSI(1,J-1))+4.*(PSI(2,J+1)-
     $PSI(2,J-1))-(PSI(3,J+1)-PSI(3,J-1)))/(TDY*TDZ))**2
      PIESH(MP1,J)=-2.*(((PSI(MM1,J+1)-PSI(MM1,J-1))-4.*(PSI(M,
     $J+1)-PSI(M,J-1))+3.*(PSI(MP1,J+1)-PSI(MP1,J-1)))/
     $(TDY*TDZ))**2
   70 CONTINUE
      DO 80 I=1,MP1
      PIESH(I,NP1)=-2.*(DWDZ(I)**2+DVDZ(I)*(ZETA(I,NP1)+DVDZ(I)))
   80 CONTINUE
      DO 310 I=1,MP1
      DO 320 J=1,NP1
      RHS(I,J)=PIESH(I,J)
  320 CONTINUE
  310 CONTINUE
      DO 311 J=1,NP1
      RHS(1,J)=PIESH(1,J)+BDA(J)*TWDELZ
      RHS(MP1,J)=PIESH(MP1,J)-BDB(J)*TWDELZ
  311 CONTINUE
      DO 312 I=1,MP1
      RHS(I,1)=PIESH(I,1)+BDC(I)*TWDELY
      RHS(I,NP1)=PIESH(I,NP1)-BDD(I)*TWDELY
  312 CONTINUE
C
C   POISSON-SOLVER FOR THE PRESSURE FIELD
C
      CALL HWSCRT(A,B,M,3,BDA,BDB,C,D,N,3,BDC,BDD,0.,PIESH,IDIMF,
     $PERTRB,IERROR,WORK)
      RHSAVE=0.
      DO 90 I=1,MP1
      DO 100 J=1,NP1
```

```
      RHSAVE=RHSAVE+ABS(RHS(I,J))
  100 CONTINUE
   90 CONTINUE
      RHSAVE=RHSAVE/FLOAT(MP1*NP1)
      DEVMAX=ABS(PERTRB)*100./RHSAVE
      PCON=(PIESH(13,1)+PIESH(14,1))/2.
      DO 313 I=1,MP1
      DO 314 J=1,NP1
      PIESH(I,J)=PIESH(I,J)-PCON
  314 CONTINUE
  313 CONTINUE
      RETURN
      END
```

APPENDIX B

PULSATING FLOW AT THE UPPER BOUNDARY OF THE VISCOUS WALL REGION
(Moving cell runs)

The difference between this approach and the one described in Chapter 4 is the form of the boundary conditions at $y=y_o$. The outer flow eddies are visualized to have infinite wavelengths on a plane parallel to the wall and negligible amount of energy in the normal component of the velocity. The boundary conditions that are consistent with this picture at $y_o^+=40$ are the following

$$w=\hat{w}_{L1}\cos\frac{2\pi t}{T_{w1}}\sin\frac{2\pi z}{\lambda_{w1}}+\hat{w}_{L2}\cos\left(\frac{2\pi t}{T_{w2}}+\phi_{w2}\right) \tag{B.1}$$

$$v=\hat{v}_L\cos\left(\frac{2\pi t}{T_v}+\phi_v\right)\cos\frac{2\pi z}{\lambda_v} \tag{B.2}$$

$$u=\hat{u}_{L1}\cos\left(\frac{2\pi t}{T_{u1}}+\phi_{u1}\right)\cos\frac{2\pi z}{\lambda_{u1}}+\hat{u}_{L2}\cos\left(\frac{2\pi t}{T_{u2}}+\phi_{u2}\right) \tag{B.3}$$

and $U=\overline{U}(y_o)+u$ where $\lambda_{w1}^+=\lambda_v^+=\lambda_{u1}^+=100$, $T_{w1}^+=T_v^+=T_{u1}^+=100$ and $\phi_v=\pi\left(1-\frac{N_1}{100}\right)$ where N_1 is the percentage of closed flow of the $\lambda^+=100$ wall eddies. It can be seen from (B.2) and (B.3) that all the Reynolds stress at $y_o^+=40$ is produced by the $\lambda^+=100$ eddies and this can be used to specify the phase ϕ_{u1} and the energy E_{u1} of these eddies. The periods T_{u2}^+ and T_{w2}^+ can not be determined from scaling arguments since the wavelength of the outer flow eddies is assumed to be infinite. For the calculations described below these periods were selected as $T_{u2}^+=T_{w2}^+=400$ as in the case of finite wavelengths and

ϕ_{u2} was taken to be 150^o as in the case of the single harmonic runs.

The boundary conditions used at the sides of the computational domain are periodic conditions for all three velocity components and at the wall the no-slip condition is enforced. These boundary conditions along with (B.1) through (B.3) can be translated for the stream function-vorticity formulation as follows:

$$\Psi=0,\ \varsigma=\frac{\partial^2\Psi}{\partial y^2}\ \text{at}\ y=0 \qquad \Psi(z_o)=\Psi(0),\ \varsigma(z_o)=\varsigma(0)\ \text{at}\ \begin{cases} z=0 \\ z=z_o \end{cases}$$

$$\frac{\partial\Psi}{\partial y}=w(z,y_o,t),\quad \varsigma=\frac{\partial^2\Psi}{\partial y^2}-\frac{\partial v}{\partial z}\ \text{at}\ y=y_o$$

It is to be noted that a Dirichlet boundary condition cannot be used for the stream function at $y=y_o$ in the moving cell runs because the mass flow rate in the z-direction at $z=0$ is not known. The stream function at $y=y_o$ is given by: $\Psi=-\int_0^z v(\xi,y_o,t)d\xi+\Psi_o$ which at $z=o$ becomes $\Psi=\Psi_o=\int_o^y w(0,\xi,t)d\xi$. For a fixed cell $w(0,y,t)=0$ for $0\leq y\leq y_o$; so $\Psi_o=0$. Since Ψ_o is not known a priori for a moving cell, a Newmann condition is necessary.

It was found during the calculations that the energy E_{w1} in the spanwise component of the velocity of the $\lambda^+=100$ eddies had to be greater than 60%, otherwise the calculated s_z-intensity at the wall was too large. This value is higher than the value of 40% that was used in the case of finite wavelengths described in Chapter 5 and appears to contradict the experimental results of Tritton (1967). Evenmore, the calculated $R_{s_z s_z}(\Delta z)$ correlation at the wall indicated that the pulsating spanwise flow at $y=y_o$ affects greatly the wall s_z-

patterns in a manner inconsistent with available experimental data (Lau 1980). A plot of the calculated $R_{v_1 v_1}(\Delta z)$ correlation for a case where E_{w1}=60% and N_1=70% is shown in Figure B-1. It can be seen from this plot that the correlation exhibits no zero-crossing and assumes large values for large separations. This means that the pulsating spanwise flow imposed at $y=y_o$ has a very big effect right down to the wall, which contradicts the experimental observations that the λ^+=100 eddies are the dominant eddies at the wall.

The statistically averaged results of the calculations are shown in Figures B-2 through B-6 . It can be seen that the agreement with experimental data is satisfactory. The important difference between these calculations and the double harmonic runs is that, even though the "pulsating" spanwise flows at y_o^+=40 give the correct magnitude of spanwise mixing throughout the wall layer, they wipe out the importance of the λ^+=100 eddies close to the wall in contradiction to experimental measurements.

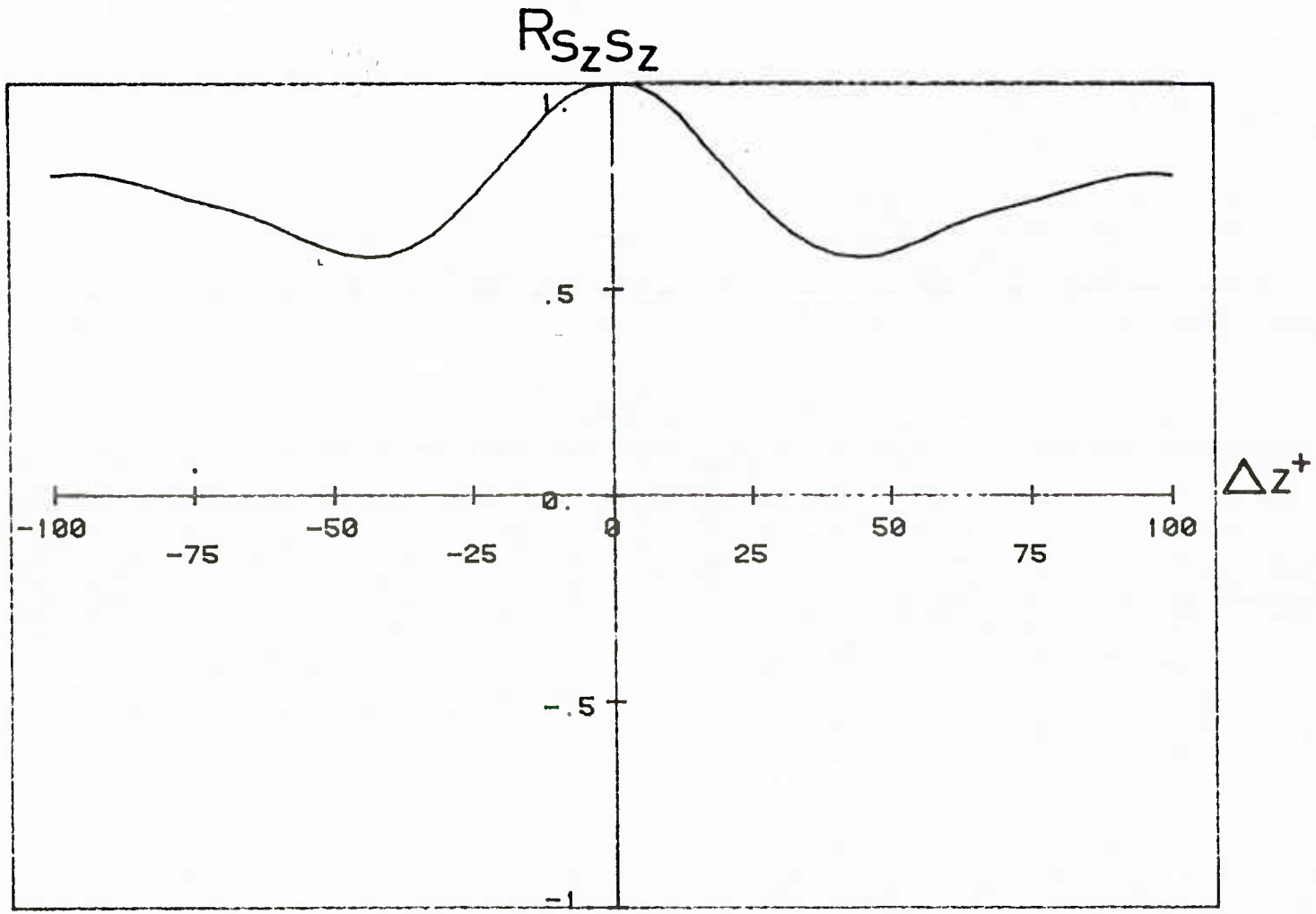

Figure B-1 Plot of the $R_{s_z s_z}(\Delta z)$ correlation versus Δz^+. Moving cell run; upper boundary at $y_o^+ = 40$

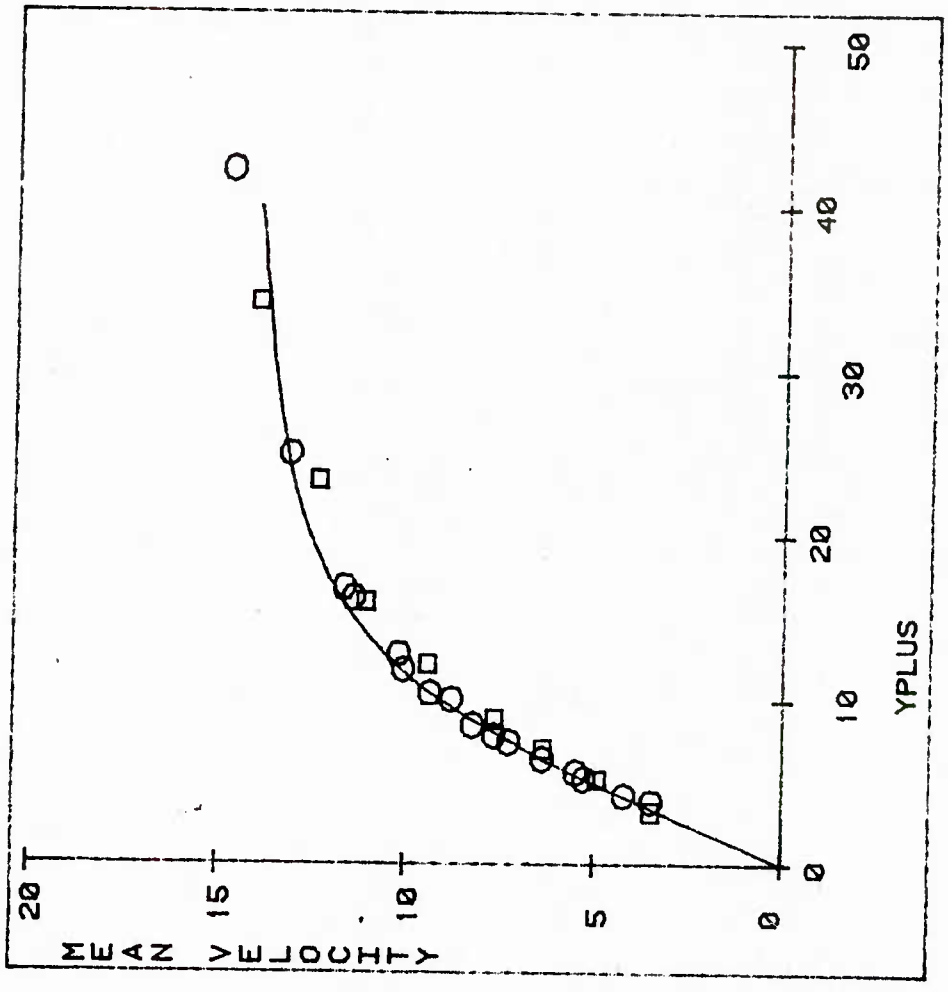

Figure B-2 Mean streamwise velocity for a moving cell run; upper boundary at $y_o^+ = 40$

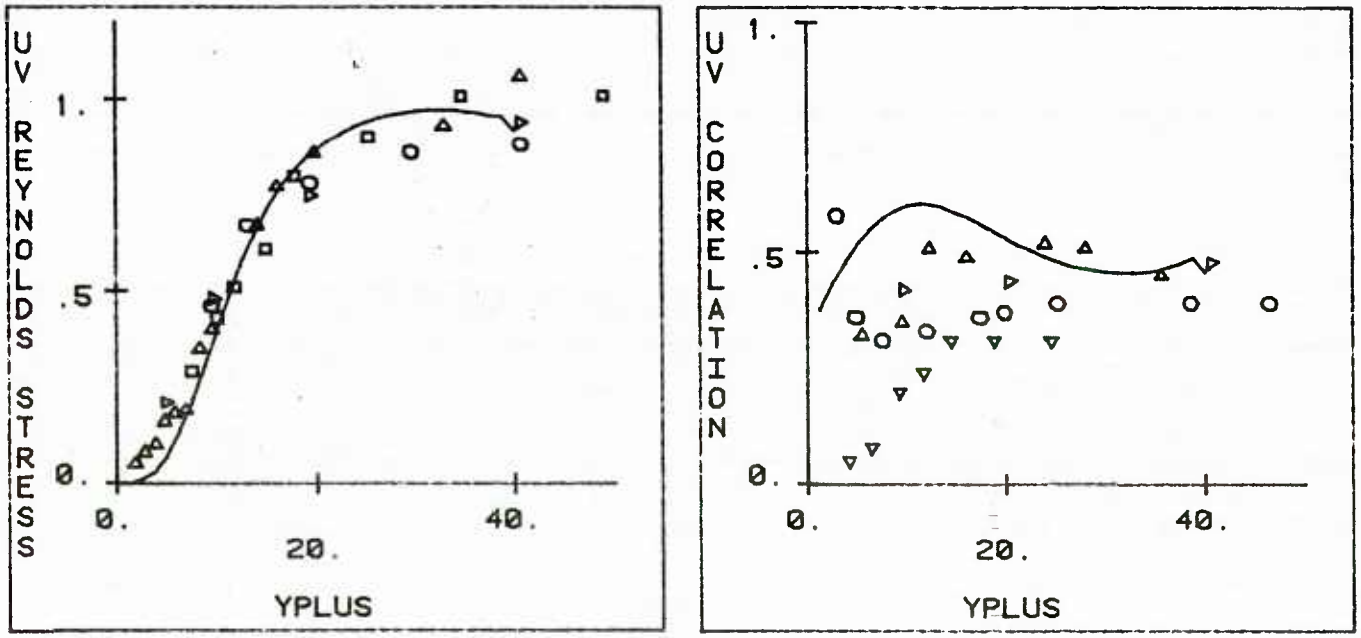

Figure B-3 Reynolds stress and $-\overline{uv}/u'v'$ correlation for a moving cell run; upper boundary at $y_o^+ = 40$

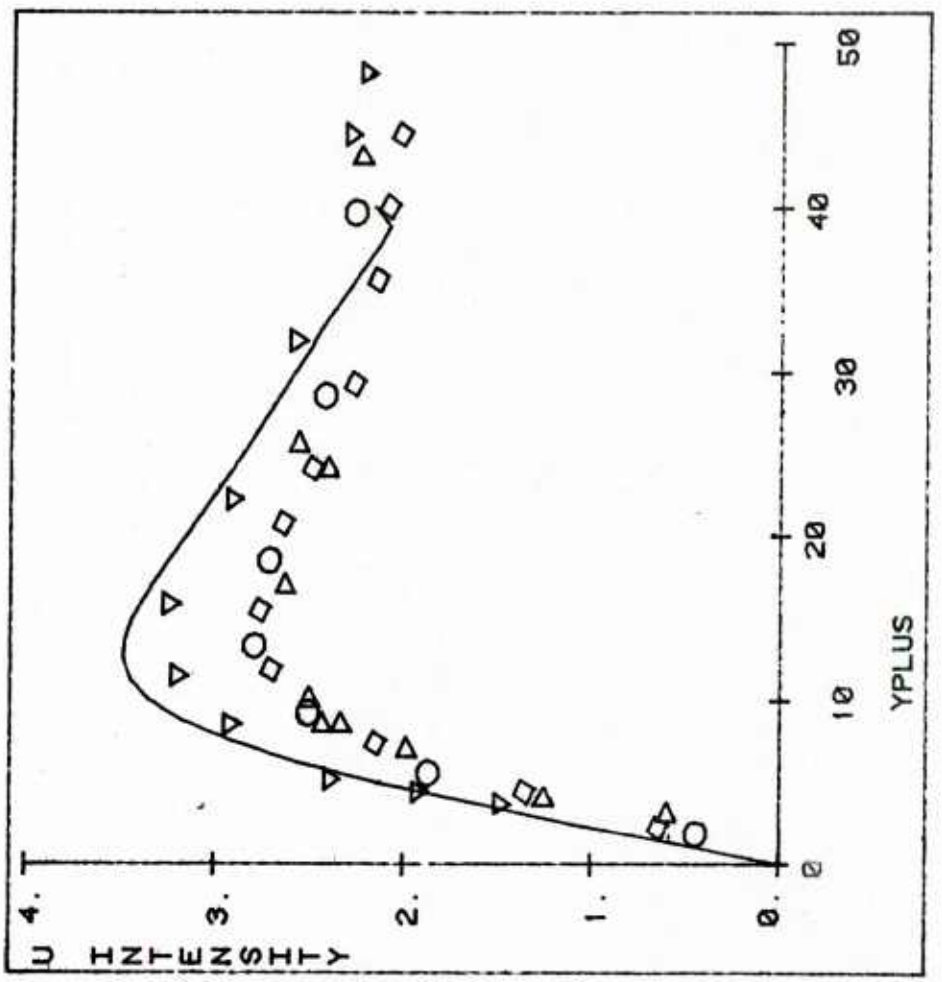

Figure B-4 Intensity of streamwise velocity fluctuations for a moving cell run; upper bounday at $y_o^+ = 40$

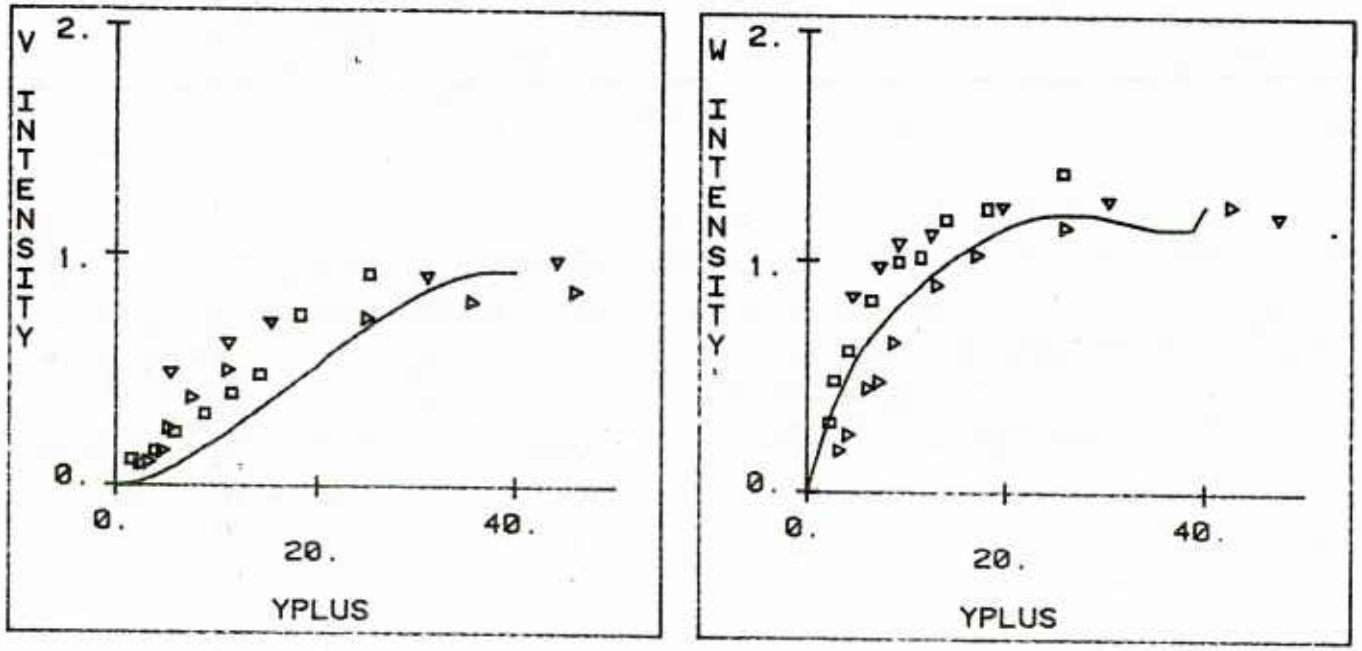

Figure B-5 Intensities of the normal and spanwise components of the velocity for a moving cell run; upper boundary at $y_o^+ = 40$

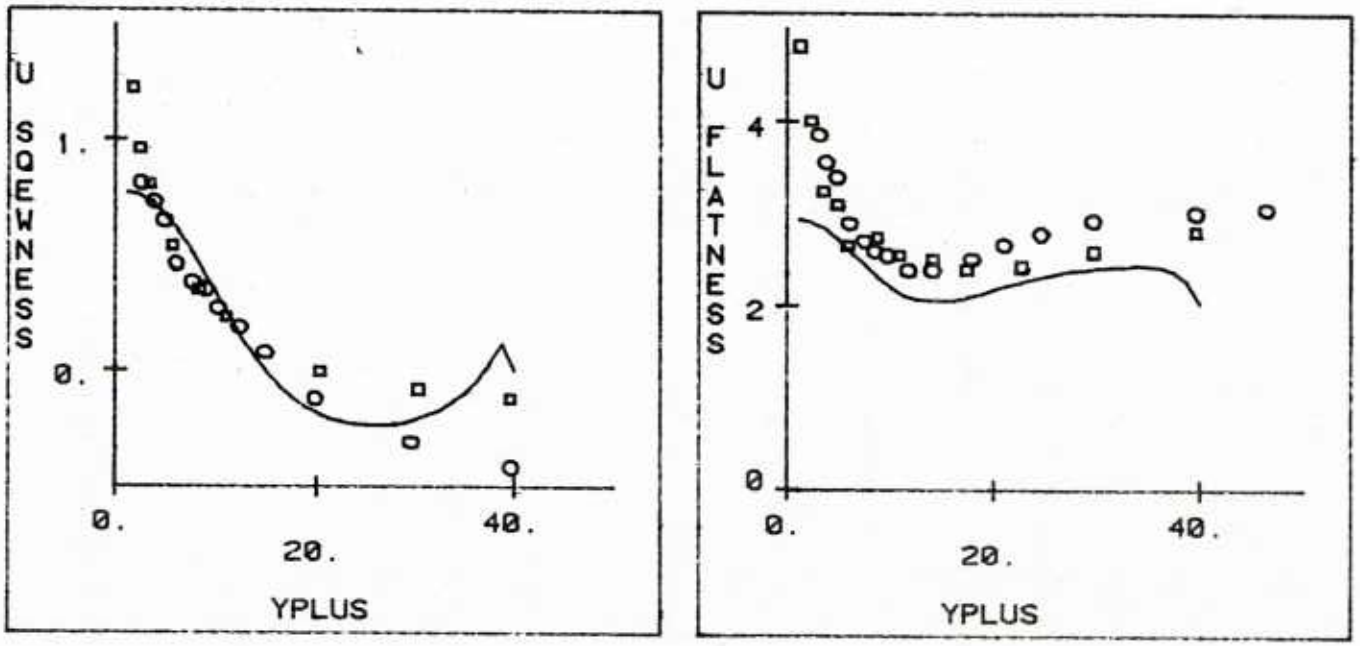

Figure B-6 Skewness and flatness of the streamwise velocity fluctuations for a moving cell run; upper boundary at $y_o^+ = 40$

APPENDIX C

SHIFTING OF THE $\lambda^+=100$ WALL EDDIES

(Moving cell runs)

In these calculations a random phase $\phi(t)$ was used in order to shift the spanwise profiles of the three velocity components at $y=y_o$. The boundary conditions at $y=y_o$ in this case have the following form:

$$w=\hat{w}_L \cos\frac{2\pi t}{T}\sin[\frac{2\pi z}{\lambda} - \phi(t)] \tag{C.1}$$

$$v=\hat{v}_L \cos(\frac{2\pi t}{T} + \phi_v)\cos[\frac{2\pi z}{\lambda} - \phi(t)] \tag{C.2}$$

$$u=\hat{u}_L \cos(\frac{2\pi t}{T} + \phi_{u1})\cos[\frac{2\pi z}{\lambda} - \phi(t)] + \hat{u}_{L2}\cos(\frac{2\pi t}{T} + \phi_{u2}) \tag{C.3}$$

It turns out that the phase $\phi(t)$ does not influence the selection of the relevant parameters, therefore these were selected to be the same as the ones used in the single harmonic fixed cell runs. In order to specify a realistic signal for $\phi(t)$ the experimental measurements of Lau (1980) were used. These measurements provide instantaneous spanwise s_z-profiles at the wall. As mentioned in Chapter 4, the s_z-patterns evolve both in time and space and shift in the spanwise direction. These patterns were fitted with sine waves $\lambda^+=100$ and $\phi(t)$ was adjusted at each instant of time so that the error was minimum in the least-squares sense.

The purpose of these calculations was to assess the effect of the shifting of $\lambda^+=100$ wall eddies on the calculated profile of the w-intensity. The calculated

statistically averaged flow variables showed no difference from the single harmonic runs. In particular, the profile of the spanwise intensity attained, again, low-values in the region $10 \leq y^+ \leq 25$ and was not affected by the shifting of the cells. That leads us to the conclusion that the shifting of the $\lambda^+ = 100$ wall eddies is not enough to account for the spanwise mixing observed experimentally in the viscous wall region.

Professor W. W. Willmarth
The University of Michigan
Department of Aerospace Engineering
Ann Arbor, MI 48109

Office of Naval Research
Code 481
800 N. Quincy Street
Arlington, VA 22217

Professor Richard W. Miksad
The University of Texas at Austin
Department of Civil Engineering
Austin, TX 78712

Professor Stanley Corrsin
The Johns Hopkins University
Department of Mechanics and
Materials Sciences
Baltimore, MD 21218

Professor Paul Lieber
University of California
Department of Mechanical Engineering
Berkeley, CA 94720

Professor P. S. Virk
Massachusetts Institute of Technology
Department of Chemical Engineering
Cambridge, MA 02139

Professor E. Mollo-Christensen
Massachusetts Institute of Technology
Department of Meteorology
Room 54-1722
Cambridge, MA 02139

Professor Patrick Leehey
Massachusetts Institute of Technology
Department of Ocean Engineering
Cambridge, MA 02139

Professor Eli Reshotko
Case Western Reserve University
Department of Mechanical and
Aerospace Engineering
Cleveland, OH 44106

Professor S. I. ai
University of Ma yland
Institute of Flu d Dynamics
and Applied Mathematics
College Park, MD 20742

Computation and Analyses Laboratory
Naval Surface We pons Center
Dahlgren Laboratory
Dahlgren, VA 22 18

Dr. Robert H. Kr chnan
Dublin, NH 03444

Professor Robert E. Falco
Michigan State Un versity
Department of Me hanical Engineering
East Lansing, MI 48824

Professor E. Run Lindgren
University of Fl rida
Department of En ineering Sciences
231 Aerospace En ineering Building
Gainesville, FL 32611

Mr. Dennis Bushn l
NASA Langley Res arch Center
Langely Station
Hampton, VA 23365

Dr. A. K. M. Faz Hussain
University of Houston
Department of Mechanical Engineering
Houston, TX 77004

Professor John L. Lumley
Cornell Universit
Sibley School of echanical
and Aerospace Engineering
Ithaca, NY 14853

Professor K. E. Shuler
University of Cal fornia, San Diego
Department of Chemistry
La Jolla, CA 92093

Dr. E. W. Montroll
Physical Dynamics, Inc.
P. O. Box 556
La Jolla, CA 92038

Dr. Steven A. Orszag
Cambridge Hydrodynamics, Inc.
54 Baskin Road
Lexington, MA 02173

Professor Tuncer Cebeci
California State University
Mechanical Engineering Department
Long Beach, CA 90840

Dr. C. W. Hirt
University of California
Los Alamos Scientific Laboratory
P. O. Box 1663
Los Alamos, NM 87544

Professor Frederick K. Browand
University of Southern California
University Park
Department of Aerospace Engineering
Los Angeles, CA 90007

Professor John Laufer
University of Southern California
University Park
Department of Aerospace Engineering
Los Angeles, CA 90007

Professor T. R. Thomas
Teesside Polytechnic
Department of Mechanical Engineering
Middlesbrough TS1 3BA, England

Dr. Arthur B. Metzner
University of Delaware
Department of Chemical Engineering
Newark, DE 19711

Professor Harry E. Rauch
The Graduate School and University
Center of the City University of
New York
Graduate Center: 33 West 42 Street
New York, NY 10036

Mr. Norman M. Nilsen
Dyntec Company
5301 Laurel Canyon Blvd., Suite 201
North Hollywood, CA 91607

Professor L. Gary Leal
California Institute of Technology
Division of Chemistry and Chemical
Engineering
Pasadena, CA 91125

Professor H. W. Liepmann
California Institute of Technology
Graduate Aeronautical Laboratories
Pasadena, CA 91125

Professor A. Roshko
California Institute of Technology
Graduate Aeronautical Laboratories
Pasadena, CA 91125

Dr. Leslie M. Mack
Jet Propulsion Laboratory
California Institute of Technology
Pasadena, CA 91103

Professor K. M. Agrawal
Virginia State College
Department of Mathematics
Petersburg, VA 23803

Technical Library
Naval Missile Center
Point Mugu, CA 93041

Professor Francis R. Hama
Princeton University
Department of Mechanical and
Aerospace Engineering
Princeton, NJ 08540

Dr. Joseph H. Clarke
Brown University
Division of Engineering
Providence, RI 02912

Professor J. T. C. Liu
Brown University
Division of Engineering
Providence, RI 02912

Chief, Document Section
Redstone Scientific Information Center
Army Missile Command
Redstone Arsenal, AL 35809

Dr. Jack W. Hoyt
Naval Ocean Systems Center
Code 2501
San Diego, CA 92152

Professor Richard L. Pfeffer
Florida State University
Geophysical Fluid Dynamics Institute
Tallahassee, FL 32306

Defense Technical Information Center
Cameron Station
Alexandria, VA 22314 12 copies

Professor Bruce Johnson
U.S. Naval Academy
Engineering Department
Annapolis, MD 21402

Library
U.S. Naval Academy
Annapolis, MD 21402

Technical Library
David W. Taylor Naval Ship Research
and Development Center
Annapolis Laboratory
Annapolis, MD 21402

Professor C. -S. Yih
The University of Michigan
Department of Engineering Mechanics
Ann Arbor, MI 48109

Professor T. Francis Ogilvie
The University of Michigan
Department of Naval Architecture
and Marine Engineering
Ann Arbor, MI 48109

Office of Naval Research
Code 200B
800 N. Quincy Street
Arlington, VA 22217

Office of Naval Research
Code 438
800 N. Quincy Street
Arlington, VA 22217 3 copies

Office of Naval Research
Code 473
800 N. Quincy Street
Arlington, VA 22217

NASA Scientific and Technical
Information Facility
P. O. Box 8757
Baltimore/Washington International
Airport
Maryland 21240

Professor Paul M. Naghdi
University of California
Department of Mechanical Engineering
Berkeley, CA 94720

Librarian
University of California
Department of Naval Architecture
Berkeley, CA 94720

Professor John V. Wehausen
University of California
Department of Naval Architecture
Berkeley, CA 94720

Library
David W. Taylor Naval Ship Research
and Development Center
Code 522.1
Bethesda, MD 20084

Mr. Justin H. McCarthy, Jr.
David W. Taylor Naval Ship Research
and Development Center
Code 1552
Bethesda, MD 20084

Dr. William B. Morgan
David W. Taylor Naval Ship Research
and Development Center
Code 1540
Bethesda, MD 20084

Director
Office of Naval Research Eastern/Central
Building 114, Section D Regional Office
666 Summer Street
Boston, MA 02210

Library
Naval Weapons Center
China Lake, CA 93555

Technical Library
Naval Surface Weapons Center
Dahlgren Laboratory
Dahlgren, VA 22418

Technical Documents Center
Army Mobility Equipment Research Center
Building 315
Fort Belvoir, VA 22060

Technical Library
Webb Institute of Naval Architecture
Glen Cove, NY 11542

Dr. J. P. Breslin
Stevens Institute of Technology
Davidson Laboratory
Castle Point Station
Hoboken, NJ 07030

Professor Louis Landweber
The University of Iowa
Institute of Hydraulic Research
Iowa City, IA 52242

R. E. Gibson Library
The Johns Hopkins University
Applied Physics Laboratory
Johns Hopkins Road
Laurel, MD 20810

Lorenz G. Straub Library
University of Minnesota
St. Anthony Falls Hydraulic Laboratory
Minneapolis, MN 55414

Library
Naval Postgraduate School
Monterey, CA 93940

Technical Library
Naval Underwater Systems Center
Newport, RI 02840

Engineering Societies Library
345 East 47th Street
New York, NY 10017

The Society of Naval Architects and
Marine Engineers
One World Trade Center, Suite 1369
New York, NY 10048

Technical Library
Naval Coastal System Laboratory
Panama City, FL 32401

Professor Theodore Y. Wu
California Institute of Technology
Engineering Science Department
Pasadena, CA 91125

Director
Office of Naval Research Western Regional
1030 E. Green Street Office
Pasadena, CA 91101

Technical Library
Naval Ship Engineering Center
Philadelphia Division
Philadelphia, PA 19112

Army Research Office
P. O. Box 12211
Research Triangle Park, NC 27709

Editor
Applied Mechanics Review
Southwest Research Institute
8500 Culebra Road
San Antonio, TX 78206

Technical Library
Naval Ocean Systems Center
San Diego, CA 92152

ONR Scientific Liaison Group
American Embassy - Room A-407
APO San Francisco 96503

Librarian
Naval Surface Weapons Center
White Oak Laboratory
Silver Spring, MD 20910

Defense Research and Development Attache
Australian Embassy
1601 Massachusetts Avenue, NW
Washington, DC 20036

Librarian Station 5-2
Coast Guard Headquarters
NASSIF Building
400 Seventh Street, SW
Washington, DC 20591

Library of Congress
Science and Technology Division
Washington, DC 20540

Dr. A. L. Slafkosky
Scientific Advisor
Commandant of the Marine Corps
Code AX
Washington, DC 20380

Maritime Administration
Office of Maritime Technology
14th & E Streets, NW
Washington, DC 20230

Maritime Administration
Division of Naval Architecture
14th & E Streets, NW
Washington, DC 20230

Dr. G. Kulin
National Bureau of Standards
Mechanics Section
Washington, DC 20234

Naval Research Laboratory
Code 2627
Washington, DC 20375 6 copies

Library
Naval Sea Systems Command
Code 09GS
Washington, DC 20362

Mr. Thomas E. Peirce
Naval Sea Systems Command
Code 03512
Washington, DC 20362

Dr. Gary Chapman
Ames Research Center
Mail Stop 227-4
Moffett Field, CA 94035

Dr. Louis Schmidt
Assistant for Engineering Technology
Assistant Secretary of the Navy (RE&S)
Department of Navy
Washington, D.C. 20310

Mr. Stanley W. Doroff
Mechanical Technology, Inc.
2731 Prosperity Avenue
Fairfax, VA 22031

Dr. Charles Watkins
Head, Mechanical Engineering Department
Howard University
Washington, DC 20059

Dr. Denny R. S. Ko
Dynamics Technology, Inc.
22939 Hawthorne Boulevard, Suite 200
Torrance, CA 90505

Professor Thomas J. Hanratty
University of Illinois at Urbana-Champaign
Department of Chemical Engineering
205 Roger Adams Laboratory
Urbana, IL 61801

Air Force Office of Scientific Research/NA
Building 410
Bolling AFB
Washington, DC 20332

Professor Hsien-Ping Pao
The Catholic University of America
Department of Civil Engineering
Washington, DC 20064

Dr. Phillip S. Klebanoff
National Bureau of Standards
Mechanics Section
Washington, DC 20234

Dr. G. Kulin
National Bureau of Standards
Mechanics Section
Washington, DC 20234

Dr. J. O. Elliot
Naval Research Laboratory
Code 8310
Washington, DC 20375

Mr. R. J. Hansen
Naval Research Laboratory
Code 8441
Washington, DC 20375

U211412